Three-wave mixing in semiconductor whispering gallery mode microcavities

Silvia Mariani

UNIVERSITÉ PARIS DIDEROT - PARIS 7

LABORATOIRE
MATÉRIAUX ET PHÉNOMÈNES QUANTIQUES

ÉCOLE DOCTORALE 564 :
PHYSIQUE EN ÎLE-DE-FRANCE

UFR DE PHYSIQUE

THÈSE

présentée par
Silvia MARIANI

pour obtenir le grade de
Docteur en Sciences de l'Université Paris Diderot

Three-wave mixing in semiconductor whispering gallery mode microcavities

Soutenue publiquement le 9 octobre 2014,
devant la commission d'examen composée de :

M.	Marc DE MICHELI,	Rapporteur
M.	Olivier GAUTHIER-LAFAYE,	Rapporteur
M.	Jean-Michel GÉRARD,	Invité
M.	Riad HAIDAR,	Examinateur
M.	Aristide LEMAÎTRE,	Examinateur
M.	Giuseppe LEO,	Directeur de thèse
M.	Carlo SIRTORI,	Président

Contents

List of Figures

List of Tables

List of Acronyms

1D	Unidimensional
2D	Bidimensional
3D	Three-dimensional
Al	Aluminum
AlAs	Aluminium Arsenide
AlGaAs	Aluminum Gallium Arsenide
Al$_x$Ga$_{1-x}$As	Aluminum Gallium Arsenide ($0 < x < 1$)
Au	Gold
BCK	Mixture of HBr, CH_3OOH and $K_2Cr_2O_7$
CCD	Charge-Coupled Device
CH$_3$COOH	Acetic Acid
C$_6$H$_8$O$_7$	Citric Acid
CMOS	Complementary Metal-Oxide-Semiconductor
CMT	Coupled-Mode Theory
CROW	Coupled Resonator Optical Waveguide
CW	Continuous Wave
DI	Deionized
DFG	Difference Frequency Generation
e-beam	Electron beam
ECR	Electron Cyclotron Resonance
EIM	Effective-Index Method
FCA	Free Carrier Absorption
FDFD	Finite-Difference Frequency-Domain
FF	Fundamental Frequency
FIB	Focused Ion Beam

FSR	Free Spectral Range
FTIR	Fourier-Transform Infra-Red
FWHM	Full Width at Half-Maximum
FWM	Four-Wave Mixing
GaAs	Gallium Arsenide
GaP	Gallium Phosphide
Ge	Germanium
GVD	Group-Velocity Dispersion
HBr	Hydrobromic Acid
HMDS	HexaMethylDiSilazane
HNO_3	Nitric Acid
H_2O	Water
H_2O_2	Hydrogen Peroxide
ICP	Inductively Coupled Plasma
InAs	Indium Arsenide
InGaAs	Indium Gallium Arsenide
IPA	Isopropanol
IR	Infrared
$K_2Cr_2O_7$	Potassium Dichromate
$LiNbO_3$	Lithium Niobate
MBE	Molecular Beam Epitaxy
MIR	Mid IR
N_2	Nitrogen
NH_4OH	Ammonium Hydroxide
Ni	Nickel
NIR	Near IR
O_2	Dioxygen
OPA	Optical Parametric Amplification
PPLN	Periodically Poled Lithium Niobate
Pt	Platinum
QCL	Quantum Cascade Laser
QD	Quantum Dot

QPM	Quasi-Phase Matching
RIE	Reactive-Ion Etching
SFG	Sum Frequency Generation
Si	Silicon
SiO_2	Silica
SH	Second Harmonic
SHG	Second Harmonic Generation
SEM	Scanning Electron Microscope
SPDC	Spontaneous Parametric Down-Conversion
TDS	Time-Domain Spectroscopy
TE	Transverse Electric
THG	Third Harmonic Generation
TM	Transverse Magnetic
TPA	Two-Photon Absorption
VIS	Visible
WGM	Whispering Gallery Mode
ZnSe	Zinc Selenide

Acknowledgements

La rédaction de ce manuscrit et les travaux effectués pendant mes trois ans de thèse n'auraient pas été possibles sans le support d'un grand nombre de personnes. Dès mon arrivée au laboratoire Matériaux et Phénomènes Quantiques, j'ai eu la chance d'être entourée de scientifiques intelligents, créatifs et dynamiques, que je souhaite remercier ici.

Un grand merci va tout d'abord à mon directeur de thèse Giuseppe Leo, qui n'a pas trop regardé mon passé de physicienne des particules et qui m'a fait confiance dès les premiers jours. Difficilement j'oublierai ton énergie, tes milles idées de projets et la motivation que tu as toujours su m'insuffler. Durant ces années j'ai appris combien le partage, la communication et la réactivité sont des instruments indispensables pour avancer rapidement dans n'importe quel domaine de la vie.

Je voudrais également remercier tous les membres de mon jury pour l'intérêt qu'ils ont porté à mon travail. Les rapporteurs Marc De Micheli et Olivier Gauthier-Lafaye, pour avoir accepté de lire aussi attentivement mon manuscrit pendant leurs vacances d'été. Riad Haidar, pour avoir été aussi enthousiaste de la soutenance au pot. Aristide Lemaître, pour les croissances effectuées tout le long de ma thèse, sans lesquelles je n'aurais jamais pu obtenir mes résultats. Jean-Michel Gérard, pour avoir accepté de participer à mon jury malgré une date déjà établie, et pour les encouragements donnés avant les réunions du projet TREASURE et surtout avant la soutenance. Carlo Sirtori, pour avoir présidé le jury et pour tous les échanges riches et intéressants que nous avons eus pendant ces trois ans.

Trois ans de thèse peuvent être très durs si on n'a pas les bonnes personnes à ses côtés. Merci donc à toute l'équipe DON, dont chaque membre a laissé une marque.
Après des longues journées de travail on a souvent envie de "vider son sac" et de raconter ce qui de bien ou de mal s'est passé. Merci Sara, qui ayant la (mal)chance d'avoir le bureau juste en face de la porte de la salle de manip, m'as vue sortir avec des belles et des mauvaises nouvelles, as toujours été à l'écoute et prête à me donner des conseils sages et appropriés. S'il est vrai que la patience

est la vertu des forts, Alessio est champion toutes compétitions ! Merci pour avoir répondu à toutes mes nombreuses questions et pour m'avoir aidée dans la compréhension des modes de galerie. Via Mario Borsa est un peu plus vide sans nous ! Je tiens à remercier aussi Ivan, les échanges avec toi ont toujours été intéressants, il y a toujours une manip de plus que l'on peut faire pour vérifier un certain effet.

Une mention spéciale va aux protagonistes de notre thèsarium, duquel je suis sortie tous les jours avec au moins un sourire. Je commence avec l'ancienne génération : merci à Alex, pour les nombreuses discussions profondes faites quand je parlais à peine français ; à Adeline, pour avoir partagé des regards de "désespoir" quand les discours des garçons prenaient un pli bizarre ; à Marc, pour m'avoir appris certains secrets de l'optique et pour avoir échangé autour du sujet "Polaroïd" ; merci Chris, pour tes "perles de sagesse" dans n'importe quel domaine ! Je continu avec la génération présente : merci à David, pour tous les trois ans, mais surtout pour avoir partagé les joies et les douleurs de la rédaction et de la soutenance. Aux autres opto-mécaniciens, Trung, Eduardo, William et Biswarup, pour avoir aussi bien discuté de nos magnifiques disques ; rappelez-vous, si vous êtes les beaux gosses, la dernière techno que j'ai faite montre que je reste toujours la seule belle gosse jusqu'à présent ! Merci aux photons jumeaux Guillaume, Claire, le premier pour avoir partagé des blagues de très haut niveau, la deuxième pour avoir été l'interlocutrice parfaite de mon côté créatif très souvent réprimé par la physique. Un merci spécial à Fabien, qui m'a poussée à mesurer le second harmonique et qui y a cru plus que moi. Il paraitraît que l'on forme un "duo de choc" : merci Cécile, tout d'abord parce je trouve que cet appellation nous convient très bien, et ensuite pour tous les papotages et les conseils de différente nature tout au long de ces années. Pour finir, la nouvelle génération : bon courage à Natalia, qui reprend la "lourde" tâche de l'étude des modes de galerie. Bonne chance aussi à Alice, Qifeng et Oleksandr, que votre vie scientifique puisse être riche en résultats.

Les bons moments ne sont pas liés qu'à l'équipe DON : merci aux membres de MPQ qui ont tous ajouté une brique à ma thèse ou à ma personnalité. Aux nombreux QUAD : Margaux, Benjamin, Thibault, Maria, Ariane, Anna et Giulia F. Mention très spéciale pour Giulia P. : merci d'avoir toujours été là pour moi. Merci à Angela pour les petits papotages du soir avant de partir. Merci aux autres doctorants que j'ai eu le plaisir de croiser sur mon chemin : Charlotte, Siham, Hélène, Loïc, Philippe.

Merci Thomas, les discussions avec toi ont toujours été fructueuses, surtout pour comprendre qu'un docteur n'a pas nécessairement un futur lié à l'université.

Le travail en salle blanche est souvent difficile, les temps d'attente sont longs

et les déceptions peuvent se cacher dans n'importe quelle étape du protocole technologique. Mais quand les joies arrivent, c'est génial de pouvoir les partager avec des personnes avec beaucoup d'expérience et d'humour ! Tout d'abord merci à Christophe, qui m'a initiée à ce monde magnifique en m'expliquant les secrets d'une lithographie bien faite ; les déplacements à l'Ecole Normale Supérieure ont été nombreux pendant ma première année de thèse : merci à Michael pour m'avoir appris à utiliser la lithographie électronique et pour avoir toujours répondu à mes appels désespérés quand à 22h je me retrouvais en salle blanche sans pouvoir avancer. Enfin, les derniers mais non les moindres, Pascal et Stéphan, merci à vous pour toutes les discussions de techno ou autre qui ont fait que le temps passe beaucoup plus rapidement.

Quand le travail est fait efficacement et précisément, on va beaucoup plus vite : merci Joëlle et Jocelyne (bon courage pour le poids double que tu ports sur tes épaules en ce moment !) pour votre rapidité "administrative". Un immense merci à Anne, pour avoir été aussi disponible : combien ma thèse aurait été plus dure sans toi ? Sans Martial et Patrick ma table optique n'aurait pas eu le même aspect : un grand merci et bravo pour votre travail précis.

La réalisation personnelle passe aussi à travers les beaux moments au dehors du laboratoire, loin de la physique. Merci Michèle et Chagny, entre un canard et un plongeon vous m'avez soutenue et faite rigoler les jeudis et les lundis pendant la rédaction et juste avant la soutenance.

Un grazie mille à mes copines et copains italiens, qui de près ou de loin ont enrichie ma vie pendant ces dernières années. Merci à Lan, Priscilla et Silvia, Giulio, Matteo, Riccardo et Riccardo pour tout, depuis le temps que l'on se connaît. À Marta, une bombe de bonne humeur qui a rendu spéciales pas mal d'occasions.

Merci à la famille Szymanski : à Thérèse et François, pour m'avoir toujours accueillie et chouchoutée ; à Alice et Cécile, pour les moments partagés et les encouragements pré-soutenance très appréciés.

Tous les mercis du monde ne suffiraient pas pour ma famille : à mes grand-mères, qui avec leur amour ont toujours veillé sur moi, et de près ou de loin continuent à le faire. À Ela et Gianni, parce qu'il n'y a rien de plus beau qu'avoir une sœur et un (presque) frère sur lesquels compter en n'importe quel moment, toujours avec une blague ou un sourire. Et surtout, grazie à maman et papa, qui m'ont toujours et depuis toujours soutenue dans n'importe quelle direction j'aie décidé de choisir. Merci parce que sans vous je n'aurais jamais pu faire ce que j'ai fait jusqu'à aujourd'hui. Merci parce que mes rêves ont toujours été aussi un peu les vôtres, et c'est pourquoi vous en êtes et en serez toujours partie.

Et pour finir, merci à Benjamin, la plus belle découverte faite dans ce pays, pour avoir été là en tout moment, du début à la fin.

General introduction

Science and technology are two distinct, but indissolubly interlaced, fields of study. We often tend to overlook that the technological progress experienced in the last century bases on complex and sometimes obscure scientific discoveries, tracing back mostly to the XVIII and XIX centuries.

Many direct technological applications stem from the several results achieved in laboratories all around the world. For instance, the discovery of the electron and the consequent revolution brought into our lives with the electronic devices.

Among the numerous possible examples of connection between science and technology, the laser demonstration easily finds a place of paramount importance [1]. Indeed, it corresponds to the birth of photonics as a field of research. In this technological dualism, we can certainly assert that photonics plays a central role. By extending its meaning, we can refer to this branch of science while dealing with linear, nonlinear, and quantum optics, or optical and optoelectronic engineering. Moreover, the development and the improvement of increasingly advanced fabrication procedures, in particular in the semiconductor field, has enabled to fine-tune the basic structure of what we call "photonic device", i. e. the optical cavity, which holds a relevant task in nowadays technology [2].

Optical cavities allow to investigate different − more or less fundamental − aspects of physics, as quantum information [3,4] or optical communication [5]. Strong spatial confinement and long photon storage times are necessary for a highly performing cavity, and these requirements are fulfilled by Whispering Gallery Mode (WGM) microcavities. In fact, such kind of resonators can store electromagnetic energy in the form of optical rays trapped in a circling path via total internal reflection. Light is vertically confined by standard dielectric guiding, while in the horizontal plane it is provided by the bent semiconductor-air interface. The interest drawn by WGM microcavities originates from their high quality factors and promise of applications for fundamental science and engineering purposes. Thanks to their versatility and high performances, they can be integrated on a photonic chip and involved in a wide set of applications, such as quantum-dot lasers [6], optomechanics [7], nanosensing [8], or quantum optics [9].

For telecom applications, optoelectronics industry or spectroscopy purposes, we deal with two main alternatives: the silicon (Si) platform and the III-V semiconductor family. Regarding nonlinear optics, Si compounds offer their long-standing technological maturity and CMOS compatibility. Besides the demonstration of Raman lasing in a photonic crystal structure [10], silica [11] and silicon nitride [12] WGM microcavities have been employed for the investigation of third-order nonlinear effects. Their high $\chi^{(3)}$ is also exploited for frequency conversion [13] and parametric oscillation [14].

Analogous results for the III-V semiconductor family are still lacking, despite the advantages offered by this platform (e. g. fabrication of monolithic laser sources, low losses, broad transparency window, high $\chi^{(2)}$, ...). With their continuing development, Aluminum Gallium Arsenide (AlGaAs) waveguides have allowed the achievement of important results, in terms of, e.g., tunable sources [15] or quantum optics and information [16, 17]. Despite their relatively early stage of technological evolution, AlGaAs WGM resonators stand out as good candidates for the study of quadratic nonlinear effects. In fact, their high quality factors result in a strong field enhancement inside the cavity, possibly giving rise to efficient Second Harmonic Generation (SHG) [18], Difference Frequency Generation (DFG) [19], and entangled photon generation [20].

Of course, a large number of applications might benefit from the merger of silicon and III-V platforms. Device integration and in particular in the telecom range, the convergence between electronics and photonics circuits represent a topical challenge in materials and electronics research. To date, the different approaches and material technologies developed for the two platforms constitute the main obstacle for implementing their hybridization.

As far as nonlinear conversion is concerned, among the most employed media we can find Lithium Niobate ($LiNbO_3$), Si, Gallium Arsenide (GaAs) and compounds, or Zinc Selenide (ZnSe). For our purposes, the material has to offer the highest possible nonlinear efficiency, operate in wavelength ranges of interest, be integratable and electrically pumpable. First of all, such crystal has to be non-centrosymmetric, so as to avoid a null second-order nonlinearity. It has to be transparent at the wavelengths involved in the nonlinear process and its $\chi^{(2)}$ has to be strong. A large thermal conductivity is a good feature for devices exposed to strong luminous intensity, toward an on-chip integration. Table 1 summarizes the main properties of the nonlinear materials that can be employed for the fabrication of optical devices [1].

III-V semiconductors have a wider transparency range, a higher refractive index n, a larger second-order nonlinear coefficient d_{il} and a better thermal

1. Refractive indices and nonlinear coefficient are provided for $\lambda = 1064$ nm [21]. d_{il} values at different wavelengths can be inferred with the Miller's rule [22].

Material	Transparency (μm)	n (@ 1064 nm)	$\mathbf{d}_{il}$ (pm/V)	κ_{th} (W/m K)
$LiNbO_3$	$0.4 \rightarrow 4.5$	2.2	$d_{33} = 25$	5.6
Si	$1.2 \rightarrow 10$ $48 \rightarrow > 100$	3.5	0	130
GaAs	$0.9 \rightarrow 17$	3.5	$d_{14} = 170$	55
GaP	$0.6 \rightarrow 11$	3.1	$d_{14} = 71$	110
ZnSe	$0.5 \rightarrow 20$	2.5	$d_{14} = 30$	18

TABLE 1 – Relevant physical properties of a few nonlinear materials employed for the fabrication of challenging optical devices.

conductivity κ_{th}. This is why all the samples conceived and characterized in this thesis are based on GaAs/AlGaAs. In fact, despite the advantages illustrated above, Si is not suitable for second-order nonlinear processes and Si-based light emitters exhibit lower efficiency due to the indirect bandgap of this material. Moreover, III-V materials are widely employed in conventional photonic devices, thanks to their excellent optical properties and well-developed platform.

AlGaAs WGM microresonators as frequency converters

Despite the complex phase-matching schemes required by the III-V semiconductors [23], the crystal symmetry of zincblend crystals such as GaAs and compounds, together with the circular shape of a $\langle 100 \rangle$-grown WGM cavity result in an azimuthal modulation of the effective $\chi^{(2)}$. It constitutes a significant advantage from a technological point of view, since it enables the achievement of the phase-matching condition without any technological effort in terms of domain-inversion engineering [19, 20, 24]. Once phase matching and energy conservation are fulfilled, we can have several second-order nonlinear processes: Sum Frequency Generation (SFG), DFG, SHG or its reverse process, the Spontaneous Parametric Down-Conversion (SPDC).

Although WGM are known since the beginning of the XX century, the first application of WGM microresonators traces back to the early '90s. For instance, the first semiconductor microring laser was demonstrated in 1992 [25] and at that time the main use of such cavities was as highly selective add-drop

filters [26]. Only in the last decade they have drawn the attention as nonlinear converters, initially in periodically poled $LiNbO_3$ cavity [27], and recently in the III-V platform [28, 29]. The interest for this field of research is due to their particular feature of boosting the nonlinear conversion efficiency. In fact, the high Q-factors grant a long nonlinear interaction within the cavity, enhancing the generated nonlinear signal. Moreover, WGM resonators offer the opportunity of shrinking the device dimension from the millimetric to the micrometric scale, the key toward on-chip integration.

By exploiting second-order nonlinearities, WGM resonators open great possibilities of study for the realization of new optical devices.

Near-IR and visible regions: second harmonic generation

To date, SHG integrated emitters in the near IR have been proposed and demonstrated mostly in waveguides, with their simple geometry, or in photonic crystals [30,31], thanks to their light confining capability. While the latter require special fabrication efforts, the former are widely used ; with more than 20 years of expertise, they have led to the exploitation of various phase-matching techniques for frequency doubling or other nonlinear processes. From the proof of concept to the demonstration, we can mention frequency doubling obtained with form-birefringence phase matching [32, 33], non-collinear phase-matching [34, 35], modal phase matching [36,37], and, finally, quasi-phase matching (QPM) [38,39].

Concerning the latter technique, the fabrication of WGM microdisks has been concurrently developed and improved ; today it has reached its maturity, and such structures can now compete with the other geometries, as shown in the comparative table of Ref. [40]. To date, besides the results obtained in PPLN [41] and $LiNbO_3$ [42] WGM resonators, SHG has been experimentally demonstrated in WGM semiconductor microcavities at two different input wavelengths. Kuo and coworkers have employed GaAs microdisks with a pump throughput around 2 μm [43], while we have fabricated and characterized AlGaAs microdisks with a pump wavelength around 1.55 μm [44]. These results allow an optimistic view on future applications, because a wide set of monolithic active devices can be fabricated starting from these structures. For example, integrating an active layer emitting around 780 nm [45] would provide an on-chip, optically pumped, nonlinear source. The WGM nature of these structures could even lead to an electrically pumped microcavity, operating at room temperature in the continuous-wave (CW) regime. Thanks to the enhancement of the nonlinear efficiency in these cavities, it might become possible to conceive and fabricate marketable devices for environmental sensing or spectroscopy applications.

THz region: Difference Frequency Generation

During the last years, several paths toward the nonlinear generation of THz frequencies have been explored in different materials, mostly based on DFG, optical rectification or parametric generation. However, until recently THz nonlinear sources were passive, bulky, and pulsed.

In 2007, Capasso's group demonstrated for the first time THz emission via intracavity DFG from a dual-wavelength QCL [46]. However, their parametric process was not phase-matched and the coherence length was limited by free-carrier absorption in the THz. Considerable technological efforts and improvements made by researchers at Northwestern and Austin Universities enabled an efficient pulsed THz generation at room temperature. Both these groups recently reached DFG output powers above 100 μW around 4 THz [47,49,48]. The potential of the above QCL-based nonlinear devices is indisputable and the scientific environment very competitive. Indeed, they can be exploited for a wide set of purposes (security and screening, biomedical applications, non-destructive evaluation and testing, THz wireless communication technology, ...). However, it would be very attractive to have a semiconductor THz source, operating at room temperature, in CW regime, broadly tunable, electrically pumped and very compact.

A few years ago G. Leo and coworkers proposed a novel nonlinear THz source [50]. The resulting project was ambitious: active WGM microring-like cavities might provide some advantages concerning CW operation and device compactness. In fact, with a proper design, it is possible to fabricate a very small array of microresonators, with a layer of embedded QD lasers providing the two input wavelengths for the emission of THz radiation by DFG. Such a device can hence operate at room temperature, in CW regime, under electrical pumping. Although the development of our source has been delayed due to the required technological effort, the interest for the fabrication of this alluring THz emitter is still deep. In fact, very recently Razeghi and coworkers demonstrated room temperature continuous wave THz sources based on intracavity DFG from mid-IR QCLs [51].

Thesis outline

The manuscript is organized as follows:

– **Chapter 1** firstly recalls the basics of second-order nonlinear optics, with a focus on SHG and DFG, the two frequency-conversion processes studied in this doctoral work. Then it provides the main elements to deal with WGM microcavities: the Coupled-Mode Theory (CMT) description of the

fiber-to-disk evanescent coupling, as well as WGM fundamental properties. Finally, it illustrates the phase-matching technique employed for zincblend crystals.

– **Part I**: this part of the manuscript describes the work carried out for designing, fabricating and characterizing an original WGM AlGaAs microcavity suspended by a GaAs pedestal, for SHG with a pump input in the third telecom fiber window. It is divided into three chapters.
  - **Chapter 2** goes from the concept of this new resonator to its complete design with a view on fabrication. In particular, it deals with the modeling required to find cavity and optical parameters giving rise to SHG.
  - **Chapter 3** is a detailed discussion about the fabrication procedure that I have developed to obtain our suspended AlGaAs microdisks.
  - **Chapter 4** presents the optical measurements that I have carried out on the fabricated samples, with the various steps leading to the demonstration of SHG from $\sim$1.58 µm to $\sim$0.79 µm ;
– **Part II**: this part of the manuscript treats the experimental work conducted within the framework of the EU FET project TREASURE, having as final goal the demonstration of an integrated THz emitter at room temperature, based on DFG in AlGaAs devices. It is divided into two chapters.
  - **Chapter 5** first provides the general context of the project. Then, it summarizes the choices made by the project partners all along the way to develop and improve the final device.
  - **Chapter 6** reports on the results obtained from the characterization of the first passive samples received from our partners. I performed a few experiments on microresonators arrays in the near IR and on microresonators matrices in the THz range.
– A few perspectives on future research will be given in the **conclusion**.

For the sake of clarity I decided to present the results in logical order rather than chronological. This stems from the will of guiding the comprehension of our work from the easiest second-order nonlinear process, i. e. the SHG, toward the DFG in a more complex structure and context. However, it is worth highlighting that TREASURE, first project dealt with during this thesis, has allowed the development of several simulation codes and the assembly of two optical benches. Such hard work, together with fruitful exchanges with national and international partners, turned out to be very useful for the SHG experiment.

Collaborations

The work presented in this thesis was performed under the direction of G. Leo, in collaboration with the partners listed hereafter:

– A. Lemaître at the "Laboratoire de Photonique et Nanostructures" for the SHG samples growths ;
– the group of J.-M. Gérard at CEA for the TREASURE samples ;
– the group of M. Kamp at the University of Würzburg for the TREASURE samples ;
– the group of P. U. Jepsen at the Technical University of Denmark for the TDS characterization of the double-metal TREASURE samples ;
– the group of C. Sirtori at the University Paris Diderot for the FTIR characterization of the double-metal TREASURE samples.

Chapter 1

Nonlinear processes

1.1 Introduction

The aim of this chapter is to recall the basis required to discuss about three wave mixing in semiconductor cylindrical micro-structures. This will help to understand the interest of merging second-order nonlinear optics and WGM resonators. Firstly, we shall review the fundamentals of nonlinear optics, focusing on second-order nonlinear processes. Then, we shall present the basic properties of WGM cavities, showing how to find the microdisk resonance frequencies. We shall also explain the approach needed to study the coupling between waveguide and disk resonator fields, specifying how to improve it and reduce the main loss causes. Finally, we shall show how and why WGMs can be exploited to enhance optical nonlinearities.

1.2 Elements of second-order nonlinear optics

Nonlinear optical processes originate from the feature of some materials to be polarized by the presence of light, depending in a nonlinear manner on the applied optical field amplitude.

Historically, the origins of nonlinear optics date back to the 1960s: just one year after the very first realization of a working laser by T. H. Maiman [1], P. A. Franken and coworkers, at the University of Michigan, observed for the first time the second-harmonic generation in a quartz crystal [52]. That experiment was made possible thanks to the important progress achieved in the development of the first high intensity lasers, allowing the scientists of those days to study the nonlinear response of different media under the application of strong electromagnetic fields. Since then, the nonlinear interaction between lasers and materials has led to the discovery of plenty of new effects and phenomena.

Electric polarization $\vec{P}(\vec{r},t)$

Before describing part of the various nonlinear processes, it may be useful to introduce a parameter playing a central role in this respect, i.e. the electric polarization $\vec{P}(\vec{r},t)$ induced in the medium; in a linear regime, it is proportional to the amplitude of the applied optical field $\vec{E}(\vec{r},t)$. Let us consider a dielectric, homogeneous and time-invariant medium, having a local response in time and space. The electrons can oscillate harmonically around their position of equilibrium. These small elementary displacements translate into induced electric dipole moment. It means that by applying an electric field on a lossless and dispersionless dielectric medium, it is possible to induce a polarization, defined as:

$$\vec{P}(\vec{r},t) = \epsilon_0 \chi^{(1)} \cdot \vec{E}(\vec{r},t)\,, \tag{1.1}$$

where ϵ_0 and $\chi^{(1)}$ are the permittivity of free space and the linear susceptibility, respectively, and $\vec{E}(\vec{r},t)$ is the applied electric field, represented as:

$$\vec{E}(\vec{r},t) = \frac{1}{2}\{\hat{e}E(\vec{r},t)\exp\left[i(\omega t - \vec{k}\cdot\vec{r})\right] + c.c.\}\,. \tag{1.2}$$

In this equation $\hat{e}$ is the unit vector depicting the polarization of the wave, $E(\vec{r},t)$ the wave amplitude, $\vec{k}$ the wave vector and ω the angular frequency, while $c.c.$ stands for "complex conjugate", ensuring that $\vec{E}(\vec{r},t)$ is a real quantity.

If we consider now a stronger incident wave, such as a laser beam [1], the regime is not linear anymore, and an additional polarization term arises. The response is then described by a power series expansion in the field amplitude $\vec{E}(\vec{r},t)$. It is therefore possible to rewrite Eq. 1.1 as:

$$\vec{P}(\vec{r},t) = \overbrace{\epsilon_0\chi^{(1)}\cdot\vec{E}(\vec{r},t)}^{\vec{P}_L} + \overbrace{\epsilon_0\chi^{(2)} : \vec{E}(\vec{r},t)^2 + \epsilon_0\chi^{(3)}\vdots\vec{E}(\vec{r},t)^3 + \dots}^{\vec{P}_{NL}}\,. \tag{1.3}$$

In the right hand side of Eq. 1.3, $\vec{P}_L$ and $\vec{P}_{NL}$ describe the linear and the nonlinear polarization, respectively. Regarding the nonlinearities, the $\chi^{(2)}$ term depicts three-wave mixing processes, while the $\chi^{(3)}$ term represents third-order optical effects, such as Four-Wave Mixing (FWM), Third Harmonic Generation (THG), Kerr effect, Two-Photon Absorption (TPA), Raman processes, ...

Several mechanisms can induce a nonlinear polarization in a medium [53], and depending on the intensity of the applied optical field, the relevance of each mechanism can vary. The one that enters in any nonlinear process and that is important for most optical frequency-mixing effects, is the *distortion of electronic cloud*. This contribution consists of a distortion of the outer electronic level of the atoms of the medium, induced by the applied optical field. The response is

1. Typically of the order of $\sim 10^{10-11}$ V/m.

fast enough ($\sim 10^{-15} - 10^{-16}$ s) with respect to the time variation of the optical frequency, to neglect the other possible mechanisms [2].

From Maxwell's equations, it is also possible to notice that the nonlinear polarization acts as a source of new components of the electromagnetic field [54]. For a non-magnetic, isotropic and dielectric optical medium with no free charges or currents, we can write:

$$\begin{cases} \vec{\nabla} \times \vec{E} = -\dfrac{\partial \vec{B}}{\partial t}\,, & \text{(1.4a)} \\ \vec{\nabla} \times \vec{H} = \dfrac{\partial \vec{D}}{\partial t}\,, & \text{(1.4b)} \end{cases}$$

where $\vec{B} = \mu_0 \vec{H}$ and $\vec{D} = \epsilon_0 \vec{E} + \vec{P}$, with μ_0 permittivity of free space. In terms of nonlinear polarization, this leads to the wave equation, which describes the coupling between the electric field and the induced polarization:

$$\vec{\nabla}^2 \vec{E} - \frac{n^2}{c^2} \frac{\partial^2 \vec{E}}{\partial t^2} = \mu_0 \frac{\partial^2 \vec{P}_{NL}}{\partial t^2}\,, \tag{1.5}$$

where n is the refractive index and c is the speed of light in vacuum.

The i^{th} cartesian component of the nonlinear polarization can be written as:

$$P^i_{NL} = \epsilon_0 \sum_{j,k} \chi^{(2)}_{ijk} E_j E_k + \epsilon_0 \sum_{j,k,l} \chi^{(3)}_{ijkl} E_j E_k E_l + \dots\,, \tag{1.6}$$

from where we notice that the susceptibility $\chi^{(n)}$ is a $(n+1)$th-rank tensor (with $i, j, k, l = x, y, z$).

Since in this thesis work we focus on second-order nonlinear media, we shall only deal with the second term of the right hand side in Eq.1.6; the Fourier component of the second-order nonlinear polarization is a complex value and can be written as:

$$P^{(2)}_i(\omega_3 = \omega_1 + \omega_2) = \frac{\epsilon_0 D^{(2)}}{2} \sum_{j,k} \chi^{(2)}_{ijk}(-\omega_3; \omega_1, \omega_2) \cdot E_j(\omega_1) \cdot E_k(\omega_2)\,, \tag{1.7}$$

where ω_3 is the oscillation frequency of $\vec{P}^{(2)}$, due to the presence of fields oscillating at frequencies ω_1 and ω_2, $D^{(2)}$ is a degeneracy factor [3] and $\chi^{(2)}$ is the second-order nonlinear susceptibility, representing the most relevant quantity in three-wave mixing processes. This tensor owns a large number of symmetry properties, and the knowledge of some of them is essential to simplify the mathematical expressions and have a better insight of the nonlinear processes.

2nd-order nonlinear susceptibility $\chi^{(2)}$

2. The other possible mechanisms are the *intermolecular motion*, the *molecular orientation*, the *induced acoustic motion* and the *induced polarization change* [53].

3. $D^{(2)} = 1$ (2) for indistinguishable (distinguishable) fields.

In general, the $\chi^{(2)}$ is a 27-element tensor, but many of these can be reduced by symmetry arguments. In fact, for a lossless medium, far from any resonance frequency, the Kleinman symmetry condition [55] is valid; by exploiting it and by introducing the tensor d:

$$d_{ijk} = \frac{1}{2}\chi^{(2)}_{ijk}\,, \tag{1.8}$$

together with the intrinsic permutation symmetry [4], the number of independent elements drops to 10. We can then write the second-order nonlinear polarization [5] as follows:

$$\begin{pmatrix} P_x^{(2)}(\omega_3) \\ P_y^{(2)}(\omega_3) \\ P_z^{(2)}(\omega_3) \end{pmatrix} =$$

$$= 2\epsilon_0 \begin{pmatrix} d_{11} & d_{12} & d_{13} & d_{14} & d_{15} & d_{16} \\ d_{16} & d_{22} & d_{23} & d_{24} & d_{14} & d_{12} \\ d_{15} & d_{24} & d_{33} & d_{23} & d_{13} & d_{14} \end{pmatrix} \begin{pmatrix} E_x(\omega_1)E_x(\omega_2) \\ E_y(\omega_1)E_y(\omega_2) \\ E_z(\omega_1)E_z(\omega_2) \\ E_y(\omega_1)E_z(\omega_2) + E_z(\omega_1)E_y(\omega_2) \\ E_x(\omega_1)E_z(\omega_2) + E_z(\omega_1)E_x(\omega_2) \\ E_x(\omega_1)E_y(\omega_2) + E_y(\omega_1)E_x(\omega_2) \end{pmatrix}. \tag{1.9}$$

For materials owning the $\bar{4}3m$ crystallographic symmetry, such as GaAs and compounds, the only non-zero element is d_{14}, which enables them to have a non-vanishing second-order nonlinear optical response [56]:

$$\begin{pmatrix} P_x^{(2)}(\omega_3) \\ P_y^{(2)}(\omega_3) \\ P_z^{(2)}(\omega_3) \end{pmatrix} = 2\epsilon_0 d_{14} \begin{pmatrix} E_y(\omega_1)E_z(\omega_2) + E_z(\omega_1)E_y(\omega_2) \\ E_x(\omega_1)E_z(\omega_2) + E_z(\omega_1)E_x(\omega_2) \\ E_x(\omega_1)E_y(\omega_2) + E_y(\omega_1)E_x(\omega_2) \end{pmatrix}. \tag{1.10}$$

1.3 Overview of $\chi^{(2)}$ processes

The second-order nonlinearity triggers three-wave mixing processes, i.e. the coupling among three coherent monochromatic waves: three photons of different angular frequencies ω_1, ω_2 and ω_3 interact with each other. While from Eq. 1.10, we notice that the $\chi^{(2)}$ combines the different field components, energy and momentum conservation is ensured by the following relations:

$$\hbar\omega_3 = \hbar\omega_1 + \hbar\omega_2\,, \tag{1.11a}$$

$$\hbar k_3 = \hbar k_1 + \hbar k_2\,, \tag{1.11b}$$

4. The intrinsic permutation ($d_{\mathbf{ijk}} = d_{i\mathbf{kj}}$) allows to introduce the contracted matrix $d_{ijk} \rightarrow d_{il}$, considerably simplifying the notation [54].

5. The degeneracy factor in the expression of the nonlinear polarization is due to the intrinsic permutation symmetry: $\chi^{(2)}_{ijk}(-\omega_m - \omega_n; \omega_m, \omega_n) = \chi^{(2)}_{ikj}(-\omega_n - \omega_m; \omega_m, \omega_n)$.

where $\hbar$ is the Planck constant over 2π. As we will see later on, while energy must be conserved, the condition on the momentum conservation can be relaxed.

In the following, we shall present the primary second-order non-resonant nonlinear interactions (Figure 1.1). Depending on the main oscillation frequency of $\vec{P}^{(2)}$, we have different frequency conversion processes:

- Sum Frequency Generation (SFG): two pump fields of frequency ω_1 and ω_2 incident on a nonlinear medium generate another field with $\omega_3 = \omega_1 + \omega_2$ (Figure 1.1a); ***SFG***
- Second Harmonic Generation (SHG): it is a special case of SFG. Two waves at fundamental frequency $\omega = \omega_1 = \omega_2$ incident on a nonlinear medium generate a wave with oscillation frequency $\omega_3 = 2\omega$ (Figure 1.1b); ***SHG***
- Difference Frequency Generation/Optical Parametric Amplification (DFG/OPA): a photon of frequency ω_1 interacts with a photon of frequency ω_2 (with $\omega_1 > \omega_2$). The system partially relaxes, parametrically amplifying a photon at ω_2. Moreover, a third photon is generated at the difference frequency $\omega_3 = \omega_1 - \omega_2$ to fulfill the energy conservation (Figure 1.1c); ***DFG - OPA***
- Spontaneous Parametric Down-Conversion (SPDC): it corresponds to the annihilation of a pump photon of frequency ω_1, with the simultaneous generation of two lower frequency photons at ω_2 and ω_3, triggered by vacuum fluctuations (Figure 1.1d). ***SPDC***

The photons involved in the different nonlinear processes can then either be annihilated (upward arrows) or created (downward arrows) during the conversion, which is allowed if the condition in Eq. 1.11a is fulfilled. The excited levels are virtual: after the interaction, the electrons of the medium occupy the same energy level as the beginning.

Let us associate a monochromatic plane wave to each of these three oscillation frequencies, and from now on we shall consider them propagating primarily along the z direction:

$$\vec{E}_j(z,t) = \frac{1}{2}\{\hat{e}_j E_j(z)\exp[i(\omega_j t - k_j z)] + c.c.\}\,, \tag{1.12}$$

where $j = (1,2,3)$ and $k_j = n_j\omega_j/c$, with n_j refractive index at ω_j. In the case of SFG, with $\omega_3 = \omega_1 + \omega_2$, for each ω_j the form of the nonlinear polarization is the following:

$$P^{(2)}(z,\omega_3) = 2\epsilon_0 d_{\text{eff}} E_1(z)E_2(z)e^{-i(k_1+k_2)z}\,, \tag{1.13a}$$

$$P^{(2)}(z,\omega_1) = 2\epsilon_0 d_{\text{eff}} E_2^*(z)E_3(z)e^{-i(k_3-k_2)z}\,, \tag{1.13b}$$

$$P^{(2)}(z,\omega_2) = 2\epsilon_0 d_{\text{eff}} E_1^*(z)E_3(z)e^{-i(k_3-k_1)z}\,, \tag{1.13c}$$

where d_{eff} is a scalar effective nonlinear coefficient. Now we have all the information required to look at the propagation of the different spectral components of the electric field. Under the slowly-varying envelope approximation, we can

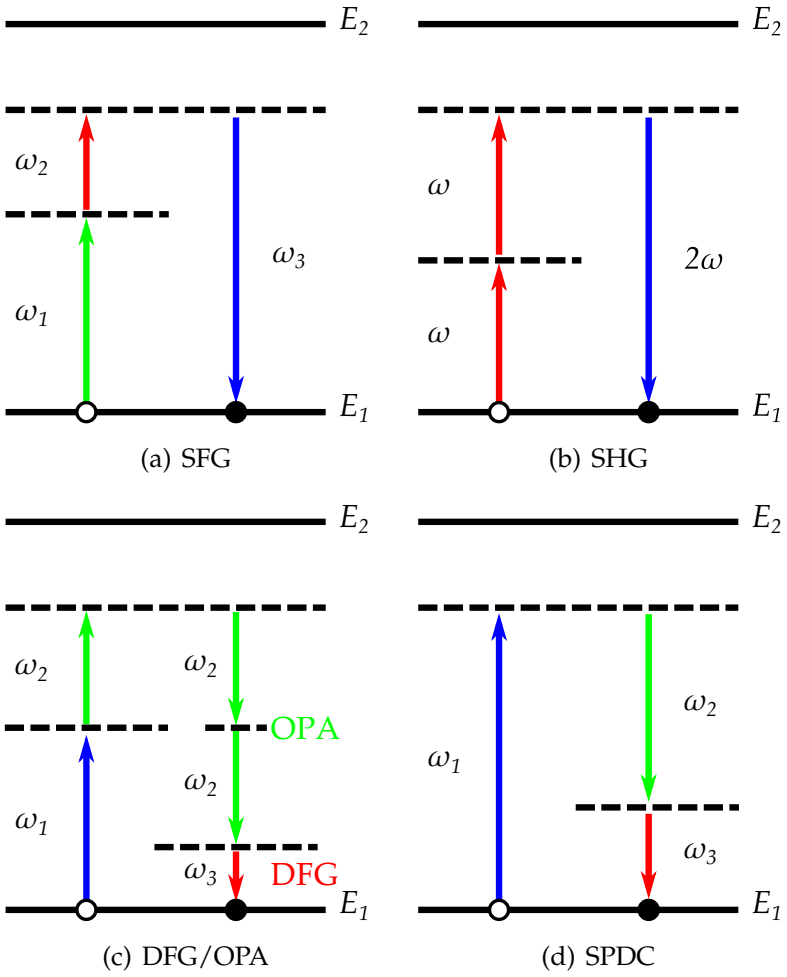

Figure 1.1: Energy level description of the primary second-order nonlinear processes. Black solid lines correspond to real energy levels, while black dashed lines represent the states of the virtual transitions.

write:

$$\frac{\mathrm{d}E_1}{\mathrm{d}z} = -i\frac{\omega_1}{n_1 c} d_{\text{eff}} E_2^*(z) E_3(z) e^{-i\Delta k z}\,, \tag{1.14a}$$

$$\frac{\mathrm{d}E_2}{\mathrm{d}z} = -i\frac{\omega_2}{n_2 c} d_{\text{eff}} E_1^*(z) E_3(z) e^{-i\Delta k z}\,, \tag{1.14b}$$

$$\frac{\mathrm{d}E_3}{\mathrm{d}z} = -i\frac{\omega_3}{n_3 c} d_{\text{eff}} E_1(z) E_2(z) e^{i\Delta k z}\,. \tag{1.14c}$$

where $\Delta k = k_3 - k_1 - k_2$ is the phase mismatch.

In the following subsections we shall focus on the SHG and on the DFG, the two nonlinear processes dealt with in this thesis work.

1.3.1 Second-harmonic generation

A simple case of three-wave mixing is SHG, for which we have $\omega_1 = \omega_2 = \omega$ and $\omega_3 = 2\omega$. In this case, the system of coupled equations in 1.14 can be simplified as follows:

$$\frac{\mathrm{d}E_\omega}{\mathrm{d}z} = -i\frac{\omega}{n_\omega c} d_{\text{eff}} E_\omega^*(z) E_{2\omega}(z) e^{-i(k_{2\omega}-2k_\omega)z}\,, \tag{1.15a}$$

$$\frac{\mathrm{d}E_{2\omega}}{\mathrm{d}z} = -i\frac{\omega}{n_{2\omega} c} d_{\text{eff}} E_\omega^2(z) e^{i(k_{2\omega}-2k_\omega)z}\,, \tag{1.15b}$$

where E_ω and $E_{2\omega}$ are the envelopes of the fundamental frequency (FF) and of the second harmonic one (SH), respectively. Equation 1.15a represents the process of two fundamental waves interacting with a nonlinear medium and generating the SH wave, as graphically shown in Figure 1.2.

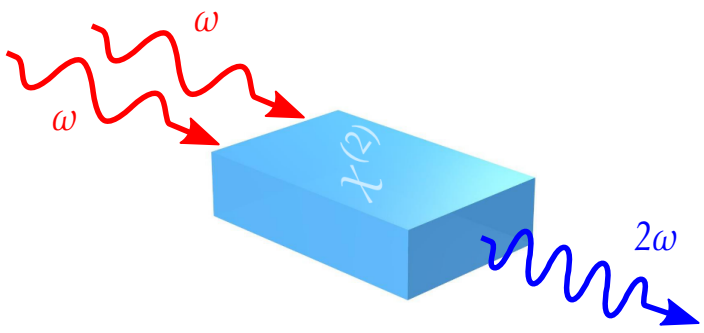

Figure 1.2: Schematic representation of the SHG process.

In the non-depleted pump approximation [6], we can obtain the optical power generated by SHG just by solving Eq. 1.15b and integrating the resulting wave intensity over the effective area $\mathcal{A}$ of the beam. We then obtain:

$$\mathcal{P}_{2\omega}(L) = \frac{8\pi^2}{\epsilon_0 c \lambda^2 n_\omega^2 n_{2\omega} \mathcal{A}} d_{\text{eff}}^2 L^2 \mathcal{P}_\omega^2 \text{sinc}^2\left(\frac{\Delta k L}{2}\right), \tag{1.16}$$

where λ is the wavelength of the FF, $\mathcal{P}_\omega$ is its optical power and L is the length of the nonlinear medium

The conversion efficiency of the nonlinear process η_{SHG} is defined as the ratio between the generated second-harmonic power and the square of the incident wave power:

Conversion efficiency η_{SHG}

$$\eta_{\text{SHG}} = \frac{\mathcal{P}_{2\omega}}{\mathcal{P}_\omega^2} \quad [\text{W}^{-1}]\,. \tag{1.17}$$

6. For a low conversion efficiency ($< 10\%$), it is possible to neglect the depletion of the pump power, which can be considered to be constant. This approximation is very often experimentally verified.

From Eq. 1.16 we can notice that, for an efficient frequency conversion process, Δk has to be null. This means that, in order to have a constructive interaction between the three coexistent waves, they have to propagate at the same speed and be phase-matched. This condition can also be seen in terms of momentum and, for the SHG, Eq. 1.11b becomes:

$$\hbar k_{2\omega} = 2\hbar k_{\omega} \,. \tag{1.18}$$

Unlike energy conservation, momentum conservation is not automatically fulfilled. For exemple, Eq. 1.18 implies $n(2\omega) = n(\omega)$, which is not possible because of the dispersion of the media. So when $\Delta k \neq 0$, the conversion efficiency η_{SHG} evolves periodically with the length of the nonlinear medium L; its maximum is reached when:

$$L = L_c = \pi/\Delta k \,, \tag{1.19}$$

where L_c is the coherent length, the maximal distance over which the nonlinear interaction is constructive. The more Δk differs from 0, the shorter L_c and the weaker the maximal value of η_{SHG}. On the contrary, when $\Delta k = 0$ the nonlinear interaction depends quadratically on L. In section 1.5 we shall see how WGM microcavities can increase L_c so as to have higher η_{SHG} values.

SHG is probably the most common and exploited second-order nonlinear process, thanks to its relative ease of demonstration. The field of applications is wide: frequency doubling can be used in surface nonlinear optics [57], in nonlinear optical microscopy [58] or for generating light with short wavelengths, as in the case of green laser pointers [59].

1.3.2 Difference frequency generation

If we consider now $\omega_1 \neq \omega_2$, with $\omega_1 > \omega_2$, the three interacting waves inside the nonlinear medium can create a radiation by DFG, with $\omega_3 = \omega_1 - \omega_2$, as schematically represented in Figure 1.3. In this case, the second-order nonlinear

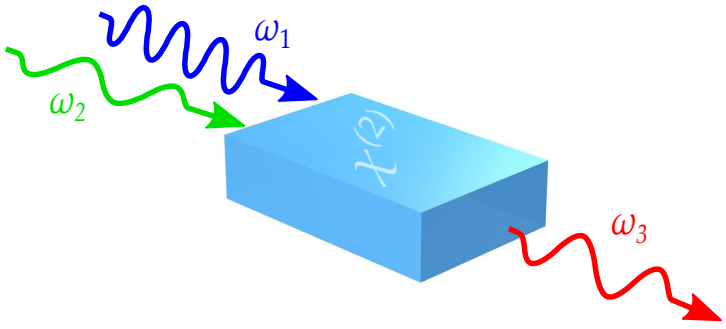

Figure 1.3: Schematic representation of the DFG process.

polarization oscillating at ω_3 can be rewritten as:

$$P^{(2)}(z,\omega_3) = 2\epsilon_0 d_{\text{eff}} E_1(z) E_2^*(z) e^{-i(k_1-k_2)z} \,. \tag{1.20}$$

Under the same hypotheses that led us to Eq. 1.16, we obtain the optical power generated by DFG:

$$\mathcal{P}_3(L) = \frac{8\pi^2}{\epsilon_0 c \lambda_3^2 n_1 n_2 n_3 \mathcal{A}} d_{\text{eff}}^2 L^2 \mathcal{P}_1 \mathcal{P}_2 \text{sinc}^2\Big(\frac{\Delta k L}{2}\Big) \,, \tag{1.21}$$

and the DFG conversion efficiency:

$$\eta_{\text{DFG}} = \frac{\mathcal{P}_3}{\mathcal{P}_1 \mathcal{P}_2} \quad [\text{W}^{-1}] \,. \tag{1.22}$$

Conversion efficiency η_{DFG}

For η_{DFG} to be non negligible, $\Delta k = k_3 - (k_1 - k_2)$ must be null. As for the SHG, this requirement is not automatically satisfied due to the dispersion of the nonlinear medium. However, in some special cases (particular material, direction or temperature) momentum conservation can be fulfilled.

In the complete picture of this nonlinear process, the incident high-frequency wave $E(z,\omega_1)$ weakens while propagating along the z direction, and at the same time, the two low-frequency waves $E(z,\omega_2)$ and $E(z,\omega_3)$ arise, resulting in a transfer of optical power from $E(z,\omega_1)$ to $E(z,\omega_2)$ and $E(z,\omega_3)$.

DFG is mostly exploited to obtain a long idler wavelength (ω_3) starting from pump (ω_1) and signal (ω_2) waves of similar values. For example, it is possible to obtain mid-infrared wavelengths starting from ω_1 and ω_2 in the near IR, useful for gas spectroscopy [60]. Another important application field for DFG processes is the generation of THz waves [61], interesting for a wide set of purposes, such as security, screening and biomedical applications. In chapters 5 and 6 we shall treat the subject, showing some recent achievements in this domain.

1.4 Phase matching

As we have seen in sections 1.3.1 and 1.3.2, phase matching can be a real issue for an efficient frequency conversion process. Although the phase-matching condition expressed by Eq. 1.11b is not automatically verified, it is still possible to fulfill it even when $\Delta k \neq 0$. This stems from the dependence of the refractive index on both wavelength and polarization; on this basis, we can rewrite Eq. 1.11b as:

$$\omega_3 n(\omega_3) = \omega_1 n(\omega_1) + \omega_2 n(\omega_2) \,. \tag{1.23}$$

For an efficient nonlinear process, we need at least $\omega_3 n(\omega_3) \simeq \omega_1 n(\omega_1) + \omega_2 n(\omega_2)$ and, for instance, polarization can be used as an adjusting parameter. There are

main principal ways to achieve phase matching in nonlinear crystals [62]: for two of them exact phase matching is required; for the third one, condition 1.23 can be relaxed.

The first two methods, used with birefringent crystals, are listed hereafter. For both of them temperature and crystal orientation can be used as adjusting parameters.

Type I phase matching
- Type I phase matching: it is attained when the two low-frequency fields own the same polarization and the high-frequency field is orthogonally polarized to them;

Type II phase matching
- Type II phase matching: it is obtained when the two low-frequency fields are orthogonally polarized and the high-frequency field owns the same polarization as one of the other two fields.

Their drawback is that optically isotropic second-order nonlinear materials, such as III-V semiconductors, lack birefringence. However, it is possible to circumvent these strict conditions by using:

Quasi-phase matching
- Quasi-Phase Matching (QPM): this method consists in a periodic modulation of the effective nonlinear coefficient of the medium, by reversing the sign of the $\chi^{(2)}$. This also results in an inversion of the nonlinear interaction at positions where otherwise it would be destructive. As shown in Figure 1.4, the generated power of a QPM process evolves quasi-quadratically with the propagation distance. In section 1.5.4 we shall see how to obtain the QPM in WGM microcavities.

It is possible to show that the reduced tensor $\chi^{(2)}$ (Eq. 1.10) defines the polarization of the waves interacting inside the resonator. In the case of three-wave mixing in zincblend crystals with the growth axis along the $\langle 100 \rangle$ direction, there must be two TE-polarized waves and one TM-polarized.

For the following, it is helpful to look at the phase matching also in terms of nonlinear overlap integral between the interacting electric fields: we can impose a condition on Δk starting from the oscillating terms of the fields expression. Then the picture is that of a volume overlap between the three fields:

3D nonlinear overlap integral

$$I_{\mathrm{ov}} = 2\epsilon_0 \int_V d_{\mathrm{eff}}(\vec{r}) E^*_{\omega_3}(\vec{r}) E_{\omega_1}(\vec{r}) E^*_{\omega_2}(\vec{r}) \mathrm{d}\vec{r}, \tag{1.24}$$

where V is the cavity volume.

1.5 Nonlinear optics in WGM microcavities

To appreciate the definition of WGM resonators, we have to trace back to the end of the XIX century: many scientists were fascinated by the possibility of evenly hearing some whispers around the gallery of the St. Paul cathedral, in

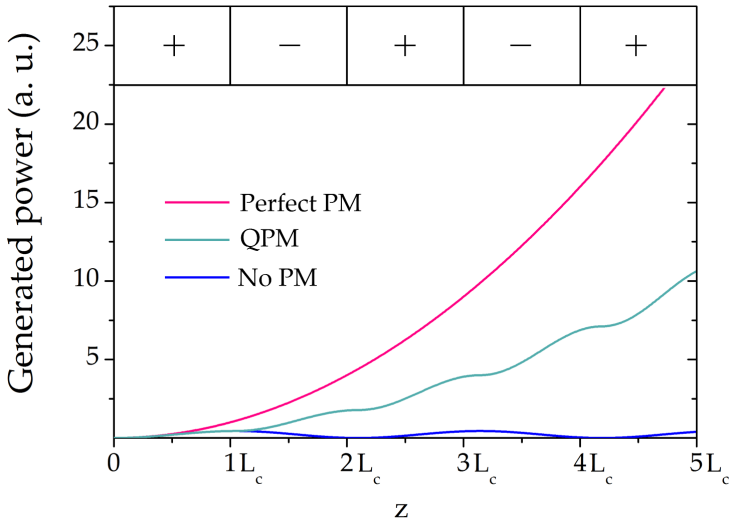

Figure 1.4: Generated power vs propagation distance. Power transfer changes sign for each coherence length L_c if phase matching does not occur. On the contrary, evolution is quadratic for perfect phase matching and quasi-quadratic for QPM.

London. After several studies and tests, Lord Rayleigh finally explained and named this peculiar phenomenon [63], which results from the propagation of acoustic waves thanks to successive reflections all along the gallery walls. In the same way, in an optical cavity with cylindrical symmetry, a WGM resonance corresponds to the propagation of an electromagnetic wave, which closes on itself in phase after a round trip thanks to total internal reflection. This results in an intensity enhancement due to constructive interference.

WGM resonators are employed in a wide set of domains [6,7,8,9], thanks to their intrinsic property of light confinement. The strong technological development carried out in the last decades has allowed to reach very high values of quality factors. This has made them even more popular and exploited than in the early '90s, when they were mostly employed as micro-ring lasers [25] and add-drop filters [26].

In the next sections we shall give a rapid overview of the WGM properties, useful for the understanding of the following chapters. More details can be found e. g. in other PhD dissertations [61,64,65].

1.5.1 Microdisk cavity modes

To describe the eigenvalues of a microdisk, we start by recalling Maxwell's equations 1.4 in the absence of free charges and currents in the material. By

taking the curl of both Eqs. 1.4a and 1.4b, we obtain again the wave equation:

$$\vec{\nabla}^2\vec{F} + \frac{n^2\omega^2}{c^2}\vec{F} = 0\,, \tag{1.25}$$

where $\vec{F}$ can be either $\vec{E}$ or $\vec{H}$. If we write the Laplacian operator in the cylindrical coordinates (ρ, θ, x) represented in Fig. 1.5b, Eq. 1.25 becomes:

$$\left(\frac{\partial^2}{\partial\rho^2} + \frac{1}{\rho}\frac{\partial}{\partial\rho} + \frac{1}{\rho^2}\frac{\partial^2}{\partial\theta^2} + \frac{\partial^2}{\partial x^2} + \frac{n^2\omega^2}{c^2}\right)\vec{F} = 0\,. \tag{1.26}$$

Let us assume that it is possible to separate the microdisk modes into two

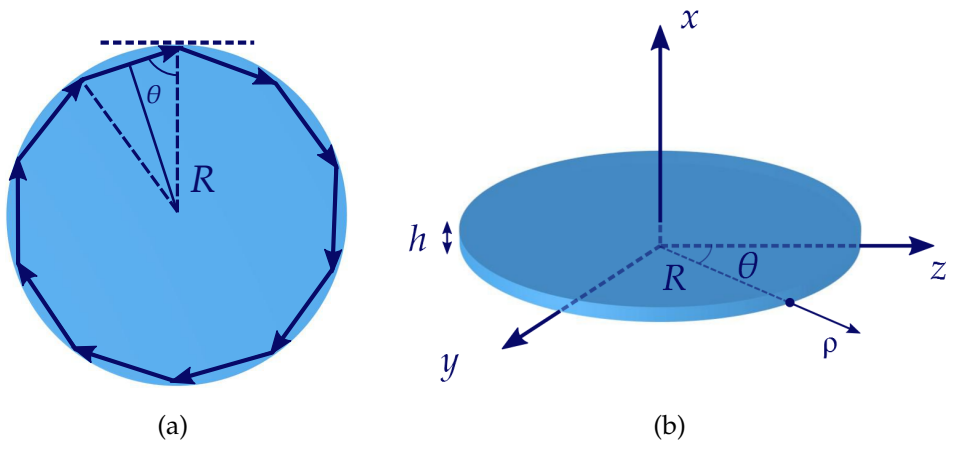

Figure 1.5: (a) Ray of light propagating by total internal reflection inside a cavity of radius R (top view); (b) General 3D scheme of a microdisk of radius R and thickness h. The cylindrical reference system used in the text is shown.

uncoupled sets with orthogonal polarizations, TM and TE respectively, using the Effective-Index Method (EIM)[7]. In this case, we can say that:

- for a TM mode[8] the non-vanishing mode components are E_x, H_ρ and H_θ;
- for a TE mode[9] the non-vanishing mode components are H_x, E_ρ and E_θ.

Then Eq. 1.26 becomes a linear equation in F_x and it can be factorized as $F_x = \Psi(\rho)\Theta(\theta)X(x)$. This assumption leads to a set of three equations describing

7. This is an approximation that allows to simplify the problem: the field is strongly vertically confined due to the index contrast at the interface semiconductor/air, so in-plane and vertical dependences can be decoupled [66].

8. Transverse Magnetic mode (relative to x): electric field orthogonally polarized to the disk plane and magnetic field lying in the plane of the cavity.

9. Transverse Electric mode (relative to x): magnetic field orthogonally polarized to the disk plane and electric field lying in the plane of the cavity.

the axial, azimuthal and radial properties of the WGM, respectively:

$$\begin{cases} \dfrac{\mathrm{d}^2 X}{\mathrm{d}x^2} + \dfrac{\omega^2}{c^2}(n^2 - n_{\text{eff}}^2)X = 0 & \text{(1.27a)} \\ \dfrac{\mathrm{d}^2 \Theta}{\mathrm{d}\theta^2} + m^2 \Theta = 0 & \text{(1.27b)} \\ \dfrac{\mathrm{d}^2 \Psi}{\mathrm{d}\rho^2} + \dfrac{1}{\rho}\dfrac{\mathrm{d}\Psi}{\mathrm{d}\rho} + \left(\dfrac{n_{\text{eff}}^2\,\tilde{\omega}^2}{c^2} - \dfrac{m^2}{\rho^2}\right)\Psi = 0 & \text{(1.27c)} \end{cases}$$

Eq. 1.27a is the equation of a slab waveguide with effective index n_{eff}; Eq. 1.27b can be analytically solved, giving $\Theta(\theta) = e^{-im\theta}$, with m the azimuthal (integer) number. Eq. 1.27c enables to know the electromagnetic field radial dependence; the solutions of this equation can be written in terms of first-kind Bessel functions inside the cavity ($\rho \leq R$) and second-kind Hankel functions outside the cavity ($\rho > R$):

$$\Psi(\rho) = \begin{cases} N J_m(\tilde{k}\, n_{\text{eff}}\, \rho) & \rho \leq R \quad \text{(1.28)} \\ N \dfrac{J_m(\tilde{k}\, n_{\text{eff}}\, R)}{H_m^{(2)}(\tilde{k}\, R)} H_m^{(2)}(\tilde{k}\, \rho) & \rho > R \quad \text{(1.29)} \end{cases}$$

where N is a normalization constant and $\tilde{k} = \tilde{\omega}/c$.

If we impose the continuity of field tangential components (E_x and H_θ for the TM modes and H_x and E_θ for the TE modes) at the dielectric/air interface, we obtain the following dispersion relations:

$$n_{\text{eff}} \frac{\dot{J}_m(\tilde{k}\, n_{\text{eff}}\, R)}{J_m(\tilde{k}\, n_{\text{eff}}\, R)} - \frac{\dot{H}_m^{(2)}(\tilde{k}\, R)}{H_m^{(2)}(\tilde{k}\, R)} = 0 \qquad \text{TM modes} \qquad \text{(1.30a)}$$

$$\frac{\dot{J}_m(\tilde{k}\, n_{\text{eff}}\, R)}{J_m(\tilde{k}\, n_{\text{eff}}\, R)} - n_{\text{eff}} \frac{\dot{H}_m^{(2)}(\tilde{k}\, R)}{H_m^{(2)}(\tilde{k}\, R)} = 0 \qquad \text{TE modes} \qquad \text{(1.30b)}$$

The numerical solultion of Eqs. 1.30 for the wave vector $\tilde{k}$ provides the complex WGM eigenfrequency $\tilde{\omega} = c\,\tilde{k}$ of the cavity. Note that $\mathrm{Im}(\tilde{\omega})$ derives from the bent interface dielectric/air: the curved geometry of the disk causes energy dissipation, resulting in radiative losses and, therefore, in a broadening of the resonance linewidth (see section 1.5.2). Once radius, thickness and effective index are set, multiple solutions of Eqs. 1.30 exist for a given azimuthal number m; these are labeled by another integer, the radial number p, which indicates the number of field maxima along $\hat{\rho}$ (Figure 1.6).

Once Eqs. 1.30 are solved, we can use Eq. 1.28 to find F_x. At that point, the other field components are directly obtained from Maxwell's equations.

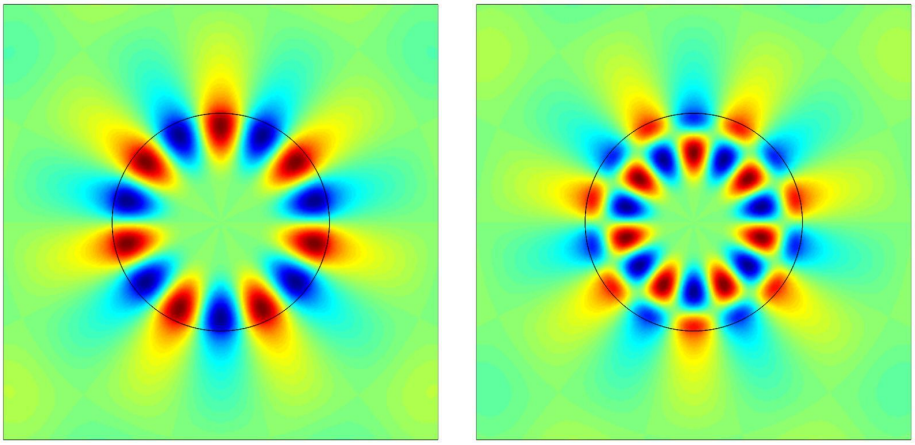

(a) (b)

Figure 1.6: 2D mode profile of a WGM microdisk. (a) WGM with azimuthal number $m = 7$ and radial number $p = 1$; f(b) WGM with azimuthal number $m = 7$ and radial number $p = 2$. The black line represents the disk boundary.

For the TM modes we have:

$$\begin{cases} H_\rho = \dfrac{m}{\mu_0\,\rho\,\tilde{\omega}} E_x \\ H_\theta = -\dfrac{i}{\mu_0\,\tilde{\omega}} \dfrac{\partial E_x}{\partial \rho} \end{cases} \tag{1.31}$$

while for the TE modes:

$$\begin{cases} E_\rho = -\dfrac{m}{\epsilon_0\,\epsilon_r\,\rho\,\tilde{\omega}} H_x \\ E_\theta = \dfrac{i}{\epsilon_0\,\epsilon_r\,\tilde{\omega}} \dfrac{\partial H_x}{\partial \rho} \end{cases} \tag{1.32}$$

1.5.2 WGM properties

If we consider a microdisk of radius R, thickness h, and refractive index n surrounded by air, with $R \gg h$ and $n > n_{\text{air}}$, the index contrast strongly confines the electromagnetic field in both vertical and radial direction. WGMs are guided along the cavity circumference by total internal reflection (Fig. 1.5a); at each bounce, thanks to the cavity rotational invariance, the incidence angle is the same, so that the photon passes by the same point many times, being trapped in the microdisk. This resonance condition can be expressed by:

WGM resonance condition

$$2\pi n_{\text{eff}} R = m\lambda_0\,, \tag{1.33}$$

with λ_0 the free-space wavelength, and the effective index $n_{\text{eff}} = \beta\lambda/2\pi$ (with $n_{\text{air}} < n_{\text{eff}} < n$), being β the mode propagation constant.

Quality factor and losses

Even though light is initially trapped inside the cavity, the electromagnetic energy stored inside it decays away, due to the imperfect optical confinement. The temporal energy dissipation for a resonant cavity is described by:

$$\frac{\mathrm{d}U}{\mathrm{d}t} = -\frac{\omega_0}{Q}U\,, \tag{1.34}$$

where $U = U_0 e^{-\omega_0 t/Q}$ is the energy stored in the cavity and U_0 the initial amount of energy in it, ω_0 its resonance frequency and Q the quality factor, defined as [67]:

$$Q = \omega_0 \frac{U}{\mathcal{P}_d}\,, \tag{1.35}$$

with $\mathcal{P}_d$ the dissipated power. The energy decay rate is inversely proportional to Q, and so is the electric field inside the cavity. Due to the damping, the electric field does not oscillate at the single resonance frequency ω_0; to take into account this broadening, it can be useful to express the electric field in the Fourier domain:

$$E(t) = \frac{1}{\sqrt{2\pi}} \int_{-\infty}^{\infty} E(\omega) e^{-i\omega t} \mathrm{d}\omega\,. \tag{1.36}$$

It is possible to show that the frequency distribution of the energy in the cavity has a Lorentzian line shape, with a full width at half-maximum (FWHM) ω_0/Q. This tells us that the Q-factor of a WGM can be expressed as:

$$Q = \frac{\omega_0}{\Delta\omega}\,, \tag{1.37}$$

WGM quality factor Q

where $\Delta\omega$ is the frequency separation between half-power points.

The energy dissipation can be ascribed to the following primary effects:

- radiative losses: the energy inside the cavity tends to leak out because of the bent edges. It is possible to reduce this kind of losses as long as the resonator diameter and the effective index are large enough; (Q^{rad})
- surface scattering, due to the roughness of the cavity edge. This is set by the quality of the fabrication process and, in general, the smaller the disk, the larger the effect; (Q^{Rayl})
- bulk absorption, due to material imperfections and impurities; (Q^{bulk})
- coupling losses, due to the presence of other resonators or a waveguide close to the disk, as sketched in Figure 1.7 (Q^{cpl}). In section 1.5.3 we shall give more details about it.

Another term to take into account while dealing with semiconductors, is the one linked to:

- surface absorption, due to the presence of a layer of native oxide at the interface nonlinear medium/air; (Q^{ox})

The overall quality factor Q can be expressed as the sum of the reciprocal of the all quality factors listed above:

Overall quality factor Q

$$1/Q = \underbrace{1/Q^{\mathrm{rad}} + 1/Q^{\mathrm{Rayl}} + 1/Q^{\mathrm{bulk}} + 1/Q^{\mathrm{ox}}}_{\mathbf{1/Q^{intr}}} + \underbrace{1/Q^{\mathrm{cpl}}}_{\mathbf{1/Q^{extr}}}, \tag{1.38}$$

where Q^{intr} stands for *intrinsic* quality factor and is related to the inherent physical properties of the resonator, while Q^{extr} stands for *extrinsic* quality factor and describes the external coupling.

Finesse

The finesse $\mathcal{F}$ of an optical resonator is defined as the ratio between the Free Spectral Range (FSR) and the FWHM bandwidths of its resonances:

$$\mathcal{F} = \frac{\Delta\omega_{\mathrm{FSR}}}{\Delta\omega}\,, \tag{1.39}$$

where the FSR of an optical cavity is the frequency (wavelength) spacing $\Delta\omega_{\mathrm{FSR}}$ ($\Delta\lambda_{\mathrm{FSR}}$) between its modes; generally speaking, the smaller the disk, the larger the FSR.

$\mathcal{F}$ is determined by the resonator losses; moreover, it is proportional to the mean number of round trips of a photon inside the cavity, linking it to an enhancement of the power circulating inside the resonator. By injecting Eq. 1.37 into Eq. 1.39, we can write:

$$\mathcal{F} = Q\frac{\Delta\omega_{\mathrm{FSR}}}{\omega_0}\,. \tag{1.40}$$

If we express the cavity round trip time as $\tau_{\mathrm{RT}} = 2\pi/\Delta\omega_{\mathrm{FSR}}$, and recall Eq. 1.35, we obtain:

$$\mathcal{F} = 2\pi\frac{U}{\mathcal{P}^d\tau_{\mathrm{RT}}} = 2\pi\frac{U}{\mathcal{P}^d_{\mathrm{RT}}}\,, \tag{1.41}$$

where $\mathcal{P}^d_{\mathrm{RT}}\cdot\tau_{\mathrm{RT}}$ is the dissipated energy per round trip.

For a WGM resonance, we can also simply write [10]

$$\mathcal{F} = \frac{Q}{m}\,. \tag{1.42}$$

High $\mathcal{F}$-valued microresonators are much exploited in nonlinear optics, since hundreds of watts can be obtained inside them for low incident powers.

10. Let us consider $Q = \omega\tau_{\mathrm{ph}}$, with $\tau_{\mathrm{ph}} = L_{\mathrm{ph}}n_g/c = 1/\Delta\omega$ the photon lifetime, L_{ph} the cavity decay length and $n_g = c/v_g$ the group index within the cavity. If we take Eq. 1.33 and replace n_{eff} with n_g, we get $Q = c\tau_{\mathrm{ph}}m/n_gR$. By expressing the propagation constant as $\beta = m/R$, we can write $v_g \equiv \partial\omega/\partial\beta = \Delta\omega_{\mathrm{FSR}}R$. Therefore, we obtain $Q/m = \Delta\omega_{\mathrm{FSR}}/\Delta\omega = \mathcal{F}$.

Effective mode volume

Among the fundamental properties of a WGM resonator, the mode volume is important for nonlinear optics applications. It provides a measure of the volume that a given mode physically occupies, and it is defined as the ratio between the total energy stored inside the resonator by that mode and its maximum energy density:

$$V_{\text{eff}} = \frac{\int n^2(\mathbf{r})|\vec{E}(\mathbf{r})|^2 \mathrm{d}V}{\max(n^2(\mathbf{r})|\vec{E}(\mathbf{r})|^2)} \,. \tag{1.43}$$

Large energy densities are associated to small effective-volume modes, and this plays a key role for nonlinear processes.

1.5.3 Fiber-to-disk coupling

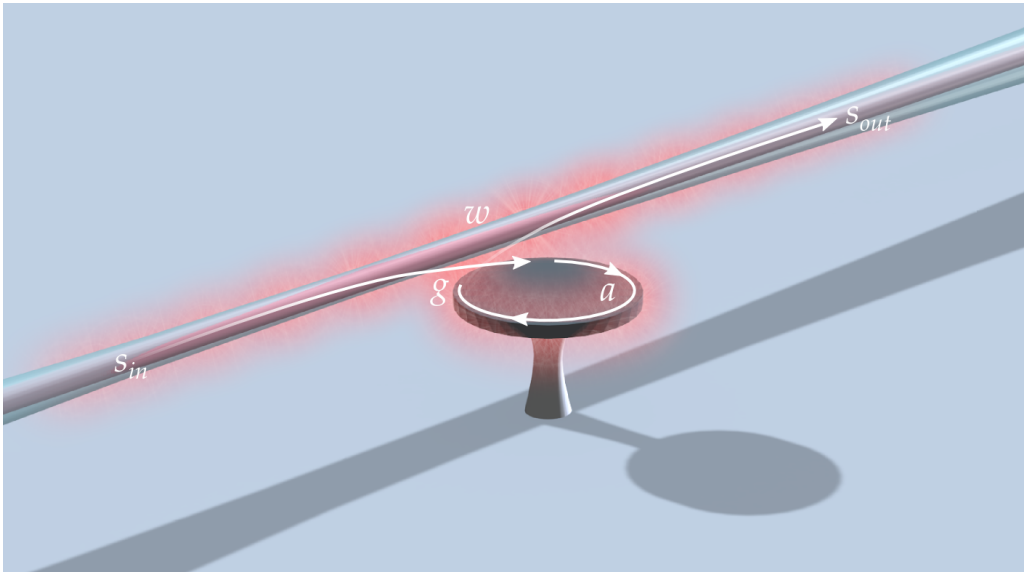

Figure 1.7: Evanescent coupling of a WGM cavity with a bus waveguide of width w. s_{in} is the injected mode amplitude, s_{out} the transmitted one, a is the WGM amplitude and g is the distance between the cavity and the waveguide.

As far as experiments are concerned, it is important to effectively couple optical energy into a WGM microcavity. In our case, this is done via evanescent coupling, by approaching a tapered silica fiber [11] to the microdisk, as we shall see in chapter 4.

11. Even if all the relations presented in this chapter are obtained for and referred to a waveguide, they also hold for a fiber.

In this section we refer to Haus' textbook [68] for the coupled-mode theory (CMT) by recalling only the results that help to understand how the evanescent coupling takes place. The following analysis provides us with further information to more easily perform the experimental tests.

Figure 1.7 shows an input fiber mode of amplitude s_{in} coupled to the cavity WGM of amplitude a, and the output fiber mode of amplitude s_{out}. If we assume that the power exchange between the disk and the fiber occurs without losses and in an adiabatic way (slowly-varying amplitude approximation), then the presence of the fiber in the proximity of the resonator does not change the cavity resonances, but only the photon lifetime inside it [12].

Besides the properties listed in section 1.5.2, two additional quantities are relevant for the study of WGM resonances: the coefficient κ^{cpl} describing the coupling between the disk and the fiber, and the transmission T. The former, proportional to the overlap integral between the resonator WGM and fiber mode fields, is defined as:

Coupling coefficient κ^{cpl}

$$\kappa^{\text{cpl}} = -i\frac{\omega\epsilon_0}{4}\int_{\text{disk}}(n_{\text{air}}^2 - n^2)\hat{e}_r^* \cdot \hat{e}_+ e^{i(m\theta-\beta z)}\mathrm{d}S\,, \tag{1.44}$$

where $\hat{e}_r^*$ is the uncoupled resonator mode field normalized to unit energy, and $\hat{e}_+$ is the unperturbed fiber mode profile normalized to unit power [69]. Moreover, κ^{cpl} allows to rewrite the coupling quality factor Q^{cpl} as [68]:

$$Q^{\text{cpl}} = \frac{\omega}{|\kappa^{\text{cpl}}|^2}\,, \tag{1.45}$$

For the transmission we have:

Transmission T

$$T = \frac{(\Delta\omega\,\tau^{\text{cpl}})^2 + (1 - Q^{\text{cpl}}/Q^{\text{intr}})^2}{(\Delta\,\omega\,\tau^{\text{cpl}})^2 + (1 + Q^{\text{cpl}}/Q^{\text{intr}})^2}\,, \tag{1.46}$$

where $\Delta\omega = \omega - \omega_0$ and $\tau^{\text{cpl}} = 2Q^{\text{cpl}}/\omega_0$ is the photon escape time from the cavity, due to the coupling. At resonance ($\Delta\omega = 0$), we have:

$$T = \left(\frac{1-K}{1+K}\right)^2\,, \tag{1.47}$$

where $K = Q^{\text{cpl}}/Q^{\text{intr}}$. The ratio K is useful to distinguish the three possible coupling schemes:

- $K > 1$, undercoupling: the intrinsic losses prevail on the coupling losses, resulting in a weak coupling ($Q^{\text{cpl}} > Q^{\text{intr}}$). Therefore, for the overall quality factor we have $Q^{\text{intr}}/2 < Q < Q^{\text{intr}}$;

12. A mathematical explanation for the injected, intracavity and output mode amplitudes can be found in other PhD theses [61, 64].

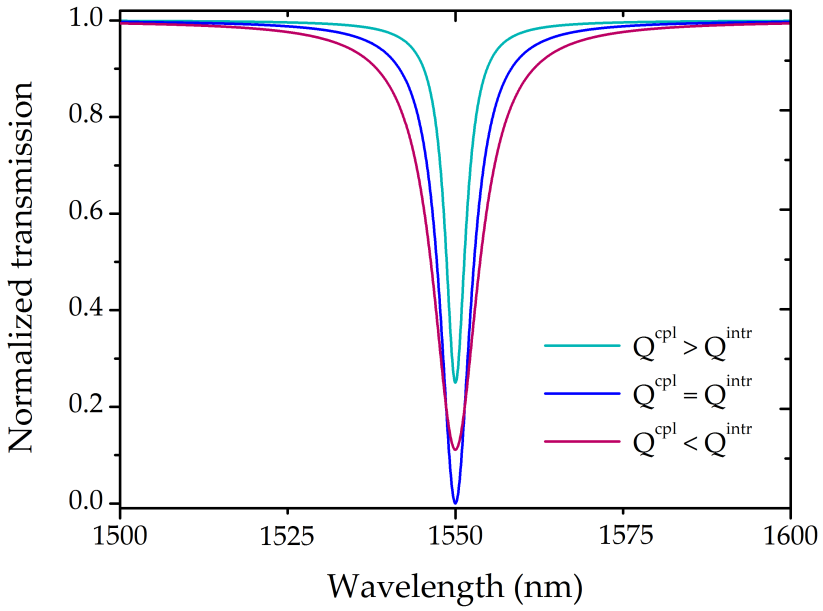

Figure 1.8: Numerical plot showing the three possible coupling regimes: under coupling (green), over coupling (carmine) and critical coupling (blue).

- $K = 1$, critical coupling: the coupling losses equal the intrinsic ones, $Q = Q^{\text{intr}}/2 = Q^{\text{cpl}}/2$ and the s_{out} drops to zero, resulting in a total power transfer from the fiber to the resonator;
- $K < 1$, over coupling: the coupling losses exceed the intrinsic losses ($Q^{\text{cpl}} < Q^{\text{intr}}$), and, as we shall see in chapter 4, the resonance linewidth increases, since the input power is not promptly dissipated.

Figure 1.8 illustrates the three regimes. Even though the critical coupling is the most desirable case, over coupling can be exploited to inject and/or extract the maximum power from the resonator.

Evanescent coupling

Our experiments are carried out by exploiting the evanescent coupling technique. This requires an overlap between the evanescent tails of the WGM and of the fiber mode in the coupling region.

To have an efficient coupling between the WGM and the fiber fields, the respective phases must match, i. e. $m\,\theta = \beta\,z$ in Eq. 1.44. Two degrees of freedom are available to enhance the coupling: the fiber diameter and the distance between the fiber and the disk (see also chapters 2 and 4).

Backscattering

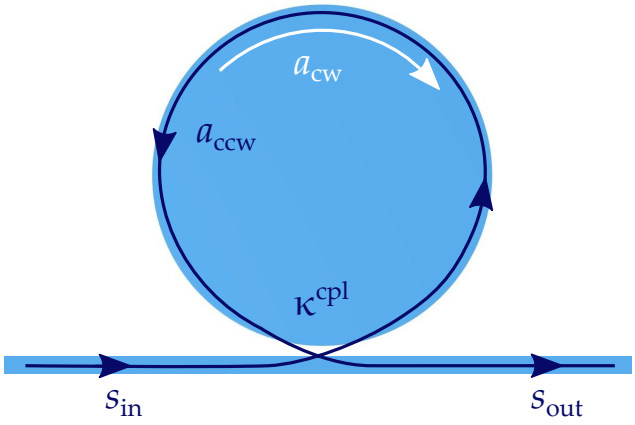

Figure 1.9: Schematic representation of the backscattering due to surface roughness. A coupling between clockwise (a_{cw}) and counter-clockwise (a_{ccw}) WGMs occurs.

Thanks to the rotational invariance, WGM resonators support two frequency-degenerate modes, for each (p, m) pair: the clockwise and the counterclockwise waves (Figure 1.9). However, while fabricating a microresonator, small imperfections can be created on the surface, resulting in roughnesses that break the symmetry. This experimentally gives rise to a splitting of the WGM resonance [70]. Figure 1.10 shows a numerical plot representing the splitting due to a weak (carmine line) and a strong (green line) backscattering.

1.5.4 QPM in WGM microcavities

In section 1.4 we mentioned that in isotropic media it is not possible to obtain a perfect phase matching. To get rid of the nonzero Δk, the QPM scheme was proposed just after the first nonlinear optics discoveries [71], and it consists in a periodical modulation of the effective second-order nonlinear coefficient of the medium. The QPM condition becomes:

$$\Delta k = \frac{2\pi}{\Lambda}\,, \tag{1.48}$$

where Λ is the $\chi^{(2)}$ grating period.

Well established for $LiNbO_3$ waveguides since the early '90s thanks to ferroelectric poling, the first application of this method on the III-V semiconductors had to wait until the late '90s, after important technological developments [72]. This modulation can be achieved in several ways [73, 74], and nowadays the

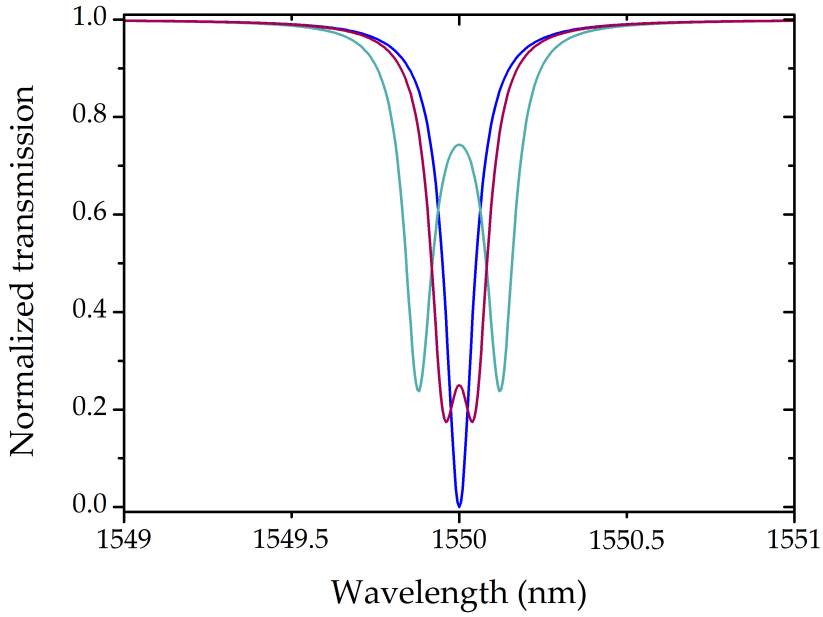

Figure 1.10: Normalized optical transmission in the case of weak (carmine) and strong (green) backscattering caused by surface roughness. The blue line represents the ideal case (no backscattering) at critical coupling.

most common technique is the "sublattice reversal epitaxy" [75], resulting in a change of the sign of the $\chi^{(2)}$ (Figure 1.11a).

The geometry of zincblende [13] cavities can be engineered so as to automatically obtain the periodic modulation. By fabricating cylindrically symmetric structures, as the one of Figure 1.11b, QPM is attainable thanks to the crystallographic symmetry of these materials. The $\langle 001 \rangle$ axes have $\bar{4}$ symmetry, which means that a rotation of 90° about it corresponds to an inversion in terms of conventional QPM (Figg. 1.11c-e) [24, 18]. In a WGM microresonator, the field propagating inside the cavity comes upon the equivalent of four domain inversions per round trip. This clearly represents a fabrication advantage, because QPM can be achieved with geometrical considerations and without resorting to any epitaxial effort.

As we saw by solving Eq. 1.27b, the electric field has an angular dependence $e^{-im\theta}$, where m is the azimuthal number; if we compare this oscillating term with the one of the linear geometry e^{-ikz}, we can state that m plays the same role as the wavevector k. In fact, we can write:

$$e^{-im\theta} = e^{-i(m/R)(R\theta)}\,, \tag{1.49}$$

13. GaAs, GaP, ZnSe, ...

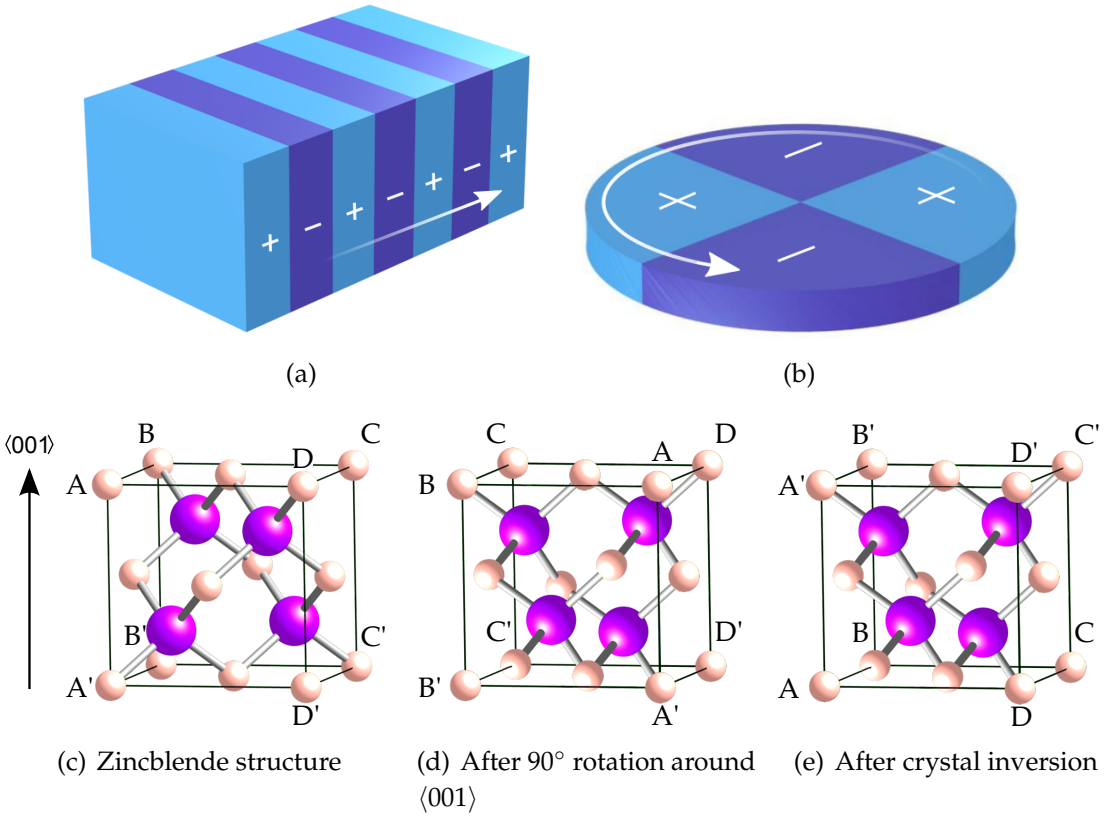

(c) Zincblende structure

(d) After 90° rotation around ⟨001⟩

(e) After crystal inversion

Figure 1.11: (a) Standard QPM obtained by physically inverting the $\chi^{(2)}$ of the crystal; (b) Effective QPM in WGM resonators. $-/+$ represent the $\chi^{(2)}_{\text{eff}}$ sign. The rotation around the $\langle 001 \rangle$ axis is equivalent to a crystal inversion.

where $R\,\theta$ can be interpreted as a propagation distance and $m/R = \beta_m$ as the propagation constant. So, if we express Eq. 1.48 in terms of β_m, with $\Lambda = \pi\, R = 2L_c$, and L_c the coherence length, we can see that:

$$\Delta\beta = \beta_3 - \beta_1 - \beta_2 = \frac{1}{R}(m_3 - m_1 - m_2) = \pm\frac{2\pi}{\pi R}\,, \tag{1.50}$$

from which we obtain the QPM condition that we shall use in all the thesis:

QPM condition for WGM cavities

$$\Delta m = m_3 - m_1 - m_2 = \pm 2\,. \tag{1.51}$$

1.6 Summary

In this chapter, we briefly recalled the nonlinear optics formalism, highlighting the main second-order nonlinear processes. We derived the main relations required for second-harmonic generation and difference frequency generation, the conversion processes studied in this thesis. We also presented the basic

equations and characteristics of the WGM resonators, of crucial importance for the modeling and experimental work described in the following. Moreover, we discussed the coupling between a resonator and a waveguide, which, as we shall see in the next chapters, plays an essential role in the optical characterization of our microcavities.

Part I

AlGaAs microcavities for SHG

Chapter 2

Concept and design of an AlGaAs WGM microcavity

2.1 Introduction

The first part of the thesis deals with the study of an AlGaAs WGM microcavity for SHG in the telecom band.

As we pointed out in the previous chapter, such WGM microresonators can exhibit several advantages. The $\bar{4}-$symmetry of III-V zincblende crystals allows the azimuthal modulation of the effective second-order nonlinear coefficient $\chi^{(2)}_{\text{eff}}$, attaining the QPM without resorting to domain inversions. Moreover, their possibly high quality factors result in a strong field enhancement inside the cavity, crucial for high nonlinear conversion efficiencies. All these properties might lead to new compact devices, with a view to the possible monolithic integration on a photonic chip for classical and quantum applications.

III-V semiconductors are well suited for providing compact and potentially inexpensive sources for room-temperature applications in the IR range. In particular, GaAs has gained a prominent position thanks to its large $\chi^{(2)}_{\text{eff}}$, low losses, broad transparency window in the NIR-MIR, and a mature technology.

On one hand, GaAs WGM microcavities can be exploited for frequency mixing, such as SHG or DFG. On the other hand, the demonstration of spontaneous parametric down-conversion (SPDC) would have an important impact for quantum light sources on chip [76], and an operation range in the telecom band would provide even more possibilities of applications [77,78,79].

Kuo and coworkers have recently demonstrated SHG in GaAs WGM microdisks, with a pump wavelength around 2 μm [43]. Although this certainly represents an important achievement for nonlinear optics, if the challenge is to develop integrated photonic devices, it would be interesting to work with a pump wavelength around 1.55 μm. Unfortunately, GaAs does not allow to

employ a fundamental frequency (FF) in this range, since the corresponding second harmonic (SH) photon energy exceeds the material bandgap [1]. Moreover, the two-photon absorption (TPA) coefficient β_{TPA} is quite large up to 1.7 μm [80,81,82], which represents a limit for application purposes (Figure 2.1).

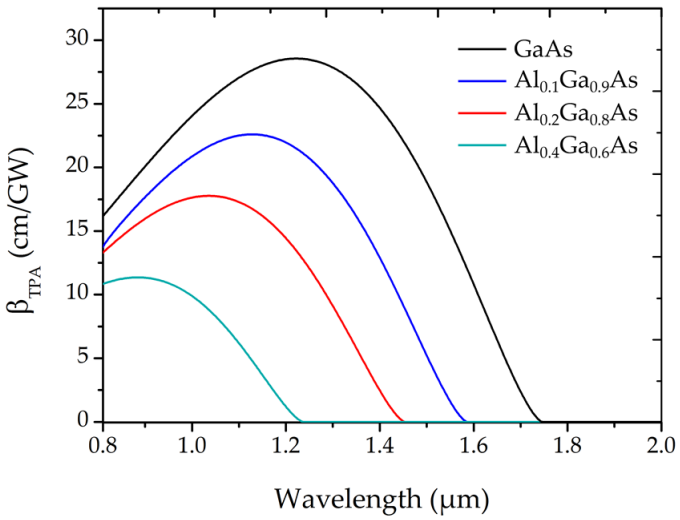

Figure 2.1: Wavelength dependence of the TPA coefficient β_{TPA} for AlGaAs at four concentration of Al: 0% (black), 10% (blue), 20% (red), and 40% (green).

Therefore $Al_xGa_{1-x}As$ (with $x > 0.28$) microdisks are suitable to circumvent these issues; in this chapter we shall describe the simulations that have guided us towards the fabrication and characterization of these original microresonators.

The codes employed for the modeling presented hereafter are one of the results stemming from the efforts of the DON group within the TREASURE project. In this case the values for the material parameters are taken form the model presented by Gehrsitz et al. [83] (e. g. for $T = 23°C$ $n(Al_{0.4}Ga_{0.6}As)$ = 3.17 @ 1.55 μm, $n(Al_{0.4}Ga_{0.6}As)$ = 3.37 @ 0.775 μm).

2.2 Design

The goal of our AlGaAs WGM structure is the demonstration of SHG from the near IR (∼1550 nm) to the visible (∼775 nm) with the QPM scheme.

A crucial step in the design of the cavity is finding the two WGMs (at FF and SH) that conserve the energy and fulfill the QPM condition (Eqs. 1.11a and 1.51):

1. We recall that the energy gap is 1.425 eV (870 nm) for GaAs, 1.92 eV (649 nm) for $Al_{0.4}Ga_{0.6}As$, and that the second harmonic photon energy is $\mathcal{E}_{\mathrm{SH}} = 1.6$ eV (775 nm).

$$\Delta\lambda = \lambda_{\mathrm{FF}} - 2\lambda_{\mathrm{SH}} = 0\,, \tag{2.1a}$$

$$\Delta m = m_{\mathrm{SH}} - 2m_{\mathrm{FF}} = \pm 2\,. \tag{2.1b}$$

As mentioned in section 1.4, a microdisk with perfect cylindrical symmetry supports both TE- and TM- polarized modes. In zincblende crystal, such as GaAs and AlGaAs, the only non-zero elements in $\chi^{(2)}_{xyz}$ (Eq. 1.10). Therefore in the case of $\langle 100 \rangle$-wafer-based devices one of the three interacting fields must be TM-polarized, while the other two must be TE-polarized. In our case (type I phase matching) the two pump photons must have the same TE polarization, implying the TM-polarization of the SH field.

In order to fabricate a performant device, we need to know the following cavity design parameters: :

Cavity design parameters

- Al molar fraction (x) in $Al_xGa_{1-x}As$;
- disk height (h);
- disk radius (R);
- pedestal radius (R_p).

The Al concentration is somehow fixed by three main reasons. Firstly, for $x < 0.28$ the known etchant solutions are not selective between the GaAs sacrificial layer and the $Al_xGa_{1-x}As$ microdisks. Secondly, for $x > 0.5$ the AlGaAs gap becomes indirect, which is not interesting for our purposes [2]. Thirdly, $x = 0.4$ is a stop etch value for some etchant solutions, making the fabrication much easier [3]. Following these considerations, we opt for $x = 0.4$.

Afterwards, we proceed with finding the height of the $Al_{0.4}Ga_{0.6}As$ layer that ensures a single-mode vertical confinement [4]. To do so, we perform a 1D finite-difference frequency-domain (FDFD) simulation. By studying both TE- and TM-polarized modes for FF and SH fields, we can infer the lower and the upper limits $h_{\min} = 130$ nm and $h_{\max} = 260$ nm.

By varying h between $h_{\min}$ and $h_{\max}$, we can find the disk radius R for which the cavity will sustain the phase-matched WGMs. In the DON group, WGMs are simulated with an in-house code based on the Effective-Index Method (EIM) [61]. Due to its analytic nature, it is a very convenient method to test several configurations. Moreover, it allows to quickly find all the WGMs of any polarization in a given range (either 1500-1600 nm or 750-800 nm) for a cavity of fixed height h and radius R. We select the radial orders p to be simulated: high-p order modes have their "center of mass" displaced towards the microdisk

2. An indirect band gap would prevent the realization of efficient light-emitting devices.
3. More details can be found in chapter 3.
4. The coupled-mode theory (CMT) allows to decouple the in-plane and the vertical problems, and therefore consider the disk along the z direction as an - air/AlGaAs/air - waveguide. See Figure 1.5b for the reference system.

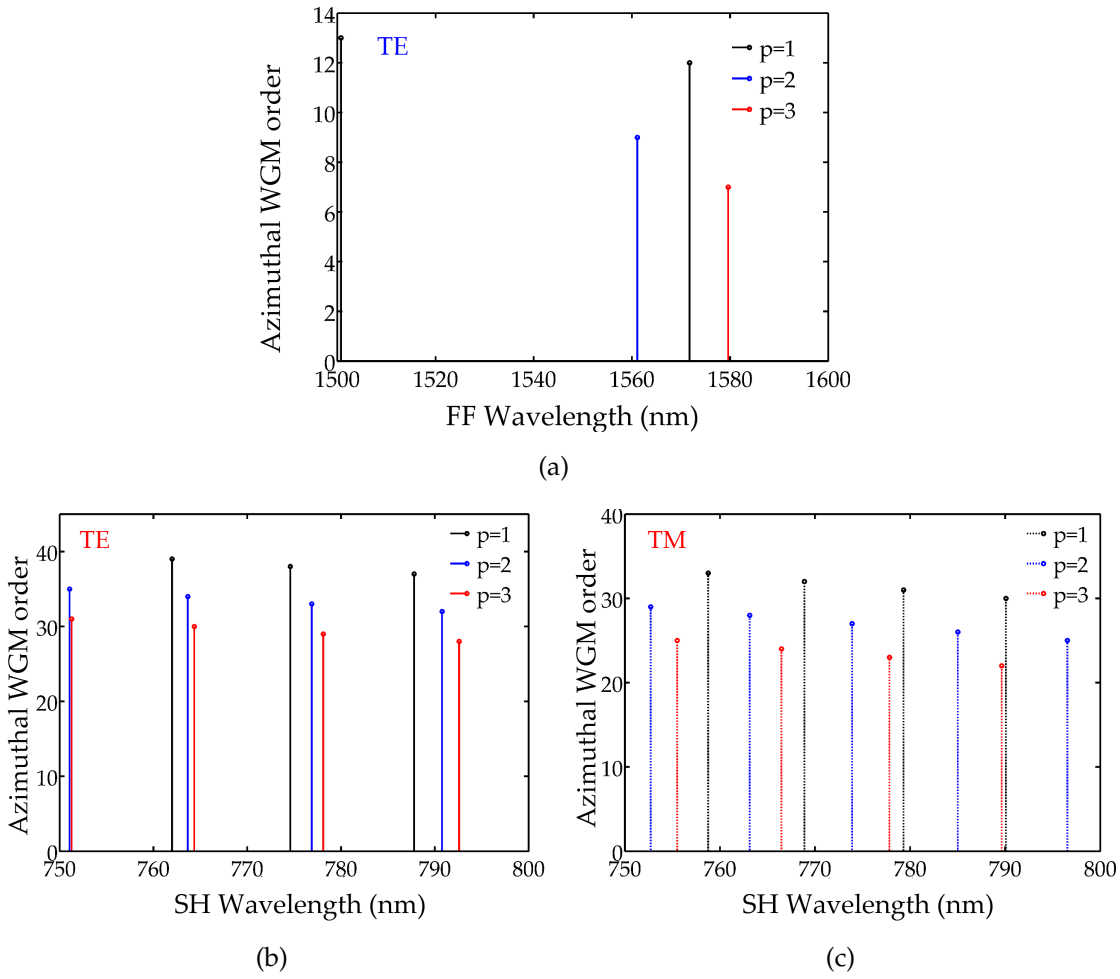

Figure 2.2: Labeling of WGMs having different radial orders, for a cavity with radius $R = 1.903$ µm and height $h = 155$ nm. At the FF, we find only TE-polarized modes (a), while in the second case we find both TE- (b) and TM-polarized (c) WGMs.

center, resulting in a difficult coupling and a possible leakage into the pedestal. Therefore, we start from the lower radial numbers ($p = 1, 2, \dots$) and for each p we look at the azimuthal order values of the resonant modes lying in the wavelength ranges of interest. Among these resonances we shall find the modes fulfilling QPM and energy conservation for SHG. The best results compatible with our constraints are obtained for $h = 155$ nm and $R = 1.903$ µm. The simulations of WGMs between 1500 and 1600 nm indicate that only TE modes exist at the FF (Figure 2.2a). The resonant TE- and TM- polarized WGMs between 750 and 800 nm are illustrated in Figs. 2.2b and 2.2c. Although we know that the SH signal will be TM-polarized, it is helpful, from an experimental point of view, to have the complete picture of the existing modes.

	FF (TE)	
$p = 1$	$m = 13$	$\lambda = 1500.7$ nm
	$\mathbf{m = 12}$	$\boldsymbol{\lambda = 1571.3}$ **nm**
$p = 2$	$m = 9$	$\lambda = 1561.1$ nm
$p = 3$	$m = 7$	$\lambda = 1579.6$ nm
	SH (TM)	
$p = 1$	$m = 33$	$\lambda = 758.8$ nm
	$m = 32$	$\lambda = 768.9$ nm
	$m = 31$	$\lambda = 779.39$ nm
	$m = 30$	$\lambda = 790.1$ nm
$p = 2$	$m = 29$	$\lambda = 753.7$ nm
	$m = 28$	$\lambda = 764.1$ nm
	$m = 27$	$\lambda = 774.9$ nm
	$\mathbf{m = 26}$	$\boldsymbol{\lambda = 785.7}$ **nm**
	$m = 25$	$\lambda = 796.5$ nm
$p = 3$	$m = 25$	$\lambda = 755.5$ nm
	$m = 24$	$\lambda = 766.5$ nm
	$m = 23$	$\lambda = 777.8$ nm
	$m = 22$	$\lambda = 789.6$ nm

Table 2.1: Summary of the WGM resonances for the TE FF field and the TM SH field, for an $Al_{0.4}Ga_{0.6}As$ cavity with radius $R = 1.903$ µm and height h =155 nm. The highlighted lines represent the phase-matched modes that conserve the energy and that could give rise to a SHG process.

Table 2.1 shows the modes that could fulfill Eqs. 2.1, i. e. the TE-polarized for the FF field and the TM-polarized for the SH field. The FF WGM with (p_{FF}, m_{FF}) = (1, 12) at $\lambda_{FF} = 1571.3$ nm and the SH mode with (p_{SH}, m_{SH}) = (2, 26) at $\lambda_{SH} = 785.7$ nm are the two phase-matched WGMs that conserve the energy and, therefore, are needed for a SHG process. Their intrinsic quality factors, taking into account radiation losses, are $Q_{FF}^{intr} = 1.1 \times 10^5$ and $Q_{SH} = 5.4 \times 10^9$, respectively.

By now, the last unknown parameter is R_p: the pedestal radius is less critical than h or R, since its possible values span over a wide range before affecting the two chosen WGMs. Despite that, one should avoid a detrimental mode leakage into the substrate. Figure 2.3a shows how the resonant wavelength (in this case λ_{FF}) changes when R_p increases. $\Delta\lambda$ represents the discrepancy between the

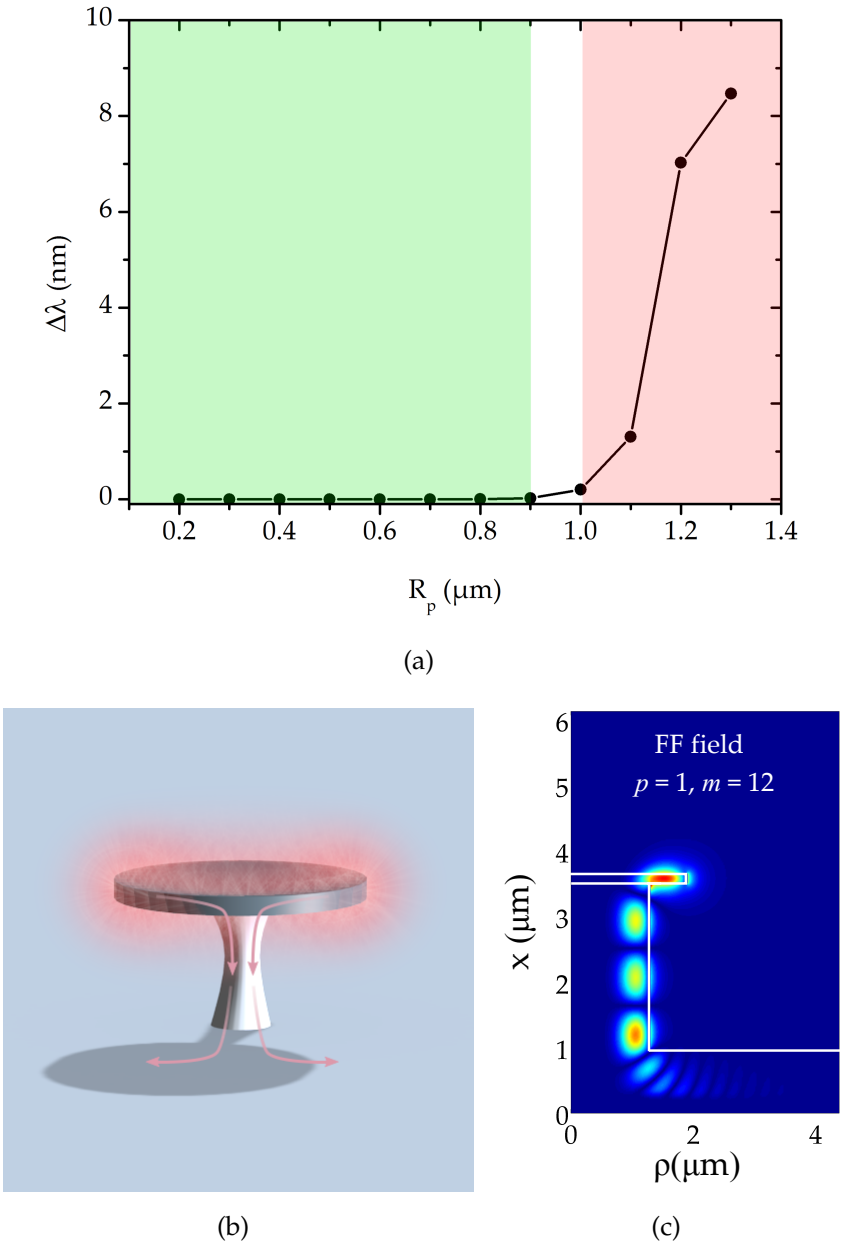

Figure 2.3: Issues related to the pedestal width, for an $Al_{0.4}Ga_{0.6}As$ cavity with radius $R = 1.903$ μm and height $h = 155$ nm, at $\lambda_{FF} = 1571.3$ nm. (a) Wavelength vs. pedestal radius R_p. Up to $R_p \sim 1$ μm the wavelength is not much affected, while for $R > 1$ μm, the WGM starts to leak into the pedestal towards the substrate (b) and (c).

nominal resonance wavelength and the wavelength of the mode affected by too large a pedestal. We note that for $R_p < 1$ μm, the mode is negligibly affected; conversely, when $R_p > 1$ μm, the mode tends to leak into the pedestal and then in the substrate (Figures 2.3b and 2.3c). Note that we do not consider $R_p < 0.2$

µm, because for too small pedestal radii the disks risk to collapse.

We did not mention the pedestal height h_p, since its lower value is fixed by the tapered fiber diameter needed for the experiments (∼1 µm). To easily move the fiber around the microcavity, we need at least $h_p = 2.5$ µm. According to our simulation, this seems sufficient to avoid any mode leakage into the substrate.

Once the basic parameters have been established, we need to evaluate the tolerances of FF and SH phase-matched wavelengths with respect to some crucial quantities, such as h, x, R and temperature T. The results of this study are reported in Figure 2.4, resulting from an in-house FDFD code developed in our group [61] following [84]; these simulations are performed with a 2D axi-symmetric layout.

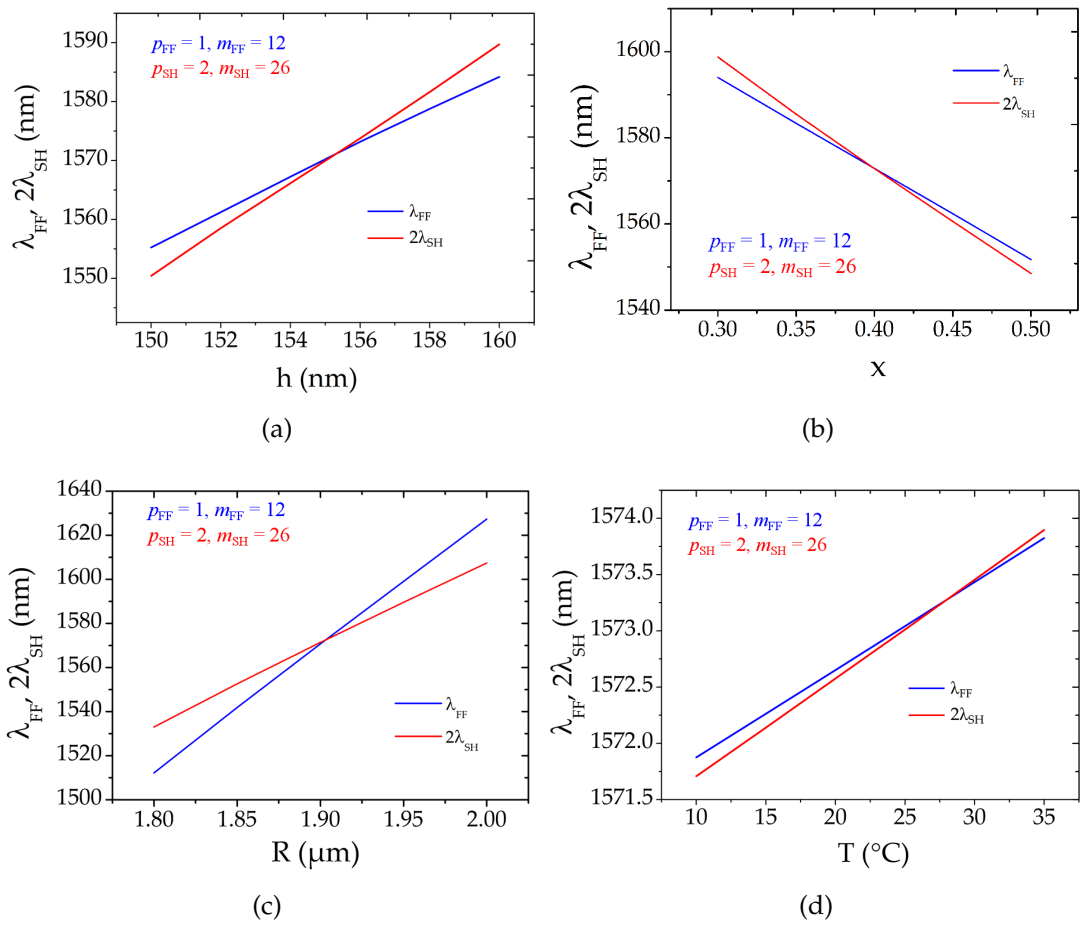

Figure 2.4: Study of the sensitivity of the FF and SH phase-matched mode wavelengths to the (a) cavity thickness h, (b) Al concentration x, (c) radius R, and (d) temperature T.

From these plots we can: 1) infer the impact of an error in the radius value, the epitaxied AlGaAs layer thickness or the Al molar fraction on the resonance

wavelength; and 2) assess the possible use of the temperature T as a tuning parameter to correct the possible wavelength shift. Table 2.2 shows the tolerance on the height h, Al concentration x, radius R and temperature T, for both FF and SH wavelengths. Apparently, the most critical parameters are the thickness and the Al concentration of the AlGaAs layer. Unfortunately, these are set by the epitaxial growth and an error on their values cannot be removed. However, it is possible to effectively compensate a potential mistake on h or x, by varying the cavity radius during the fabrication step. T can be used as a tuning parameter in case of slight mismatch of the FF and SH wavelengths caused by a non-optimal cavity radius.

FF	SH
$\mathrm{d}\lambda_{\mathrm{FF}}/\mathrm{d}h = 2.71$	$\mathrm{d}(2\lambda_{\mathrm{SH}})/\mathrm{d}h = 4.07$
$\mathrm{d}\lambda_{\mathrm{FF}}/\mathrm{d}x$ = -2.01 nm/%	$\mathrm{d}(2\lambda_{\mathrm{SH}})/\mathrm{d}x$ = -2.41 nm/%
$\mathrm{d}\lambda_{\mathrm{FF}}/\mathrm{d}R = 0.57$	$\mathrm{d}(2\lambda_{\mathrm{SH}})/\mathrm{d}R = 0.39$
$\mathrm{d}\lambda_{\mathrm{FF}}/\mathrm{d}T = 0.077$ nm/°C	$\mathrm{d}(2\lambda_{\mathrm{SH}})/\mathrm{d}T = 0.088$ nm/°C

Table 2.2: Tolerance on h, x, R and T values for both FF and SH wavelengths.

To summarize, in order to demonstrate SHG with pump wavelength around 1550 nm and SH around 775 nm, we need an $Al_{0.4}Ga_{0.6}As$ microdisk, of height $h = 155$ nm and radius $R = 1.903$ µm, lying on a pedestal of radius $R_p \sim 0.5$ µm and height $h_p \sim 2.5$ µm. In this case, the two phase-matched WGMs susceptible to give rise to an efficient frequency mixing are $(p_{\mathrm{FF}}, m_{\mathrm{FF}})$ = (1, 12) at $\lambda_{\mathrm{FF}} =$ 1571.3 nm (Figure 2.5a), and $(p_{\mathrm{SH}}, m_{\mathrm{SH}})$ = (2, 26) at $\lambda_{\mathrm{SH}} = 785.7$ nm (Figure 2.5b). Table 2.3 summarizes the related relevant quantities for our experiments.

Overall cavity and WGM parameters

Cavity Parameters	**Phase-matched modes**	
$h = 155$ nm	FF (TE)	SH (TM)
$x = 0.4$	$p_{\mathrm{FF}} = 1$	$p_{\mathrm{SH}} = 2$
$R = 1.903$ µm	$m_{\mathrm{FF}} = 12$	$m_{\mathrm{SH}} = 26$
$R_p = 0.5$ µm	$\lambda_{\mathrm{FF}} = 1571.3$ nm	$\lambda_{\mathrm{SH}} = 785.7$ nm

Table 2.3: Summary of the important quantities playing a crucial role for our SHG experiment.

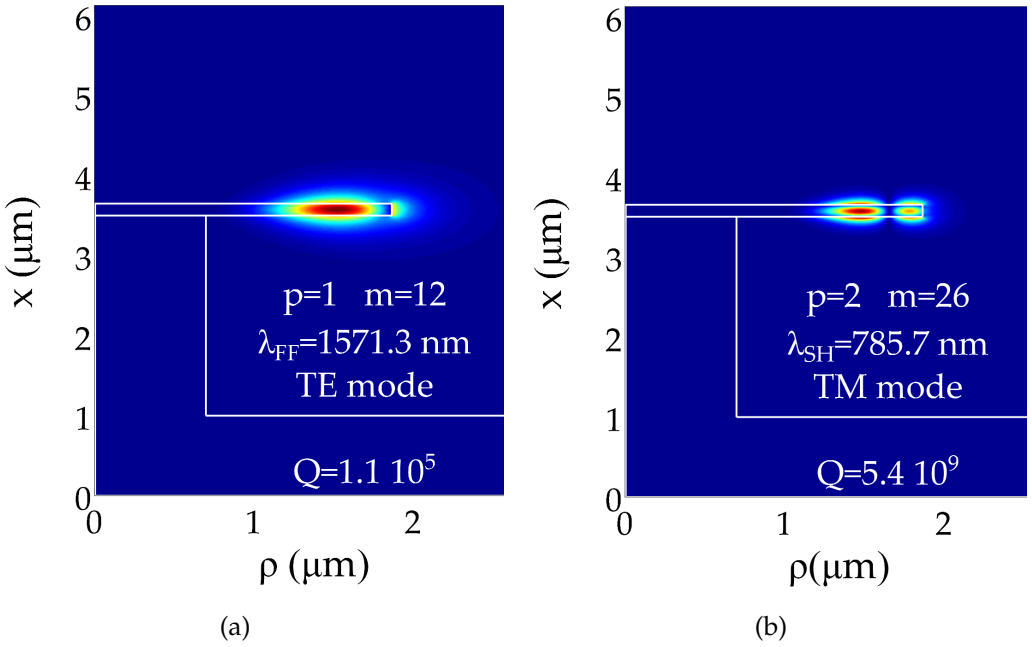

Figure 2.5: Transverse section of an $Al_{0.4}Ga_{0.6}As$ suspended microdisk of radius $R = 1.903$ μm, height $h = 155$ nm and pedestal radius $R_p = 0.5$ μm, showing the 2D radial profile of the WGMs that are phase-matched and that conserve the energy, for the FF (a) and the SH (b) fields.

2.3 Nonlinear conversion efficiency

The computation of the expected conversion efficiency η_{SHG} enables to know the value of the generated SH power. The expression of η_{SHG} (Eq. 1.17) is deduced from CMT and it is possible to show that it can also be written as:

$$\eta_{\mathrm{SHG}} = \frac{\mathcal{P}_{\mathrm{SH}}^{\mathrm{out}}}{\left(\mathcal{P}_{\mathrm{FF}}^{\mathrm{in}}\right)^2} = 4\frac{\omega_{\mathrm{SH}}}{(\omega_{\mathrm{FF}})^2}|I_{\mathrm{ov}}|^2 \left[\frac{Q_{\mathrm{FF}}^{\mathrm{cpl}}}{\left(1+Q_{\mathrm{FF}}^{\mathrm{cpl}}/Q_{\mathrm{FF}}^{\mathrm{intr}}\right)^2}\right]^2 \left[\frac{Q_{\mathrm{SH}}^{\mathrm{cpl}}}{\left(1+Q_{\mathrm{SH}}^{\mathrm{cpl}}/Q_{\mathrm{SH}}^{\mathrm{intr}}\right)^2}\right], \tag{2.2}$$

where $\mathcal{P}_{\mathrm{FF}}^{\mathrm{in}}$ and $\mathcal{P}_{\mathrm{SH}}^{\mathrm{out}}$ are the injected power into the fiber at λ_{FF} and the SH generated power coupled into the fiber, respectively; $\omega_i = 2\pi c/\lambda_i$, I_{ov} the overlap integral, and Q_i^{cpl} and Q_i^{intr} the coupling and the intrinsic quality factors, respectively ($i =$ FF or SH).

In case of critical coupling ($Q^{\mathrm{cpl}} = Q^{\mathrm{intr}}$), Eq. 2.2 can be expressed as:

$$\eta_{\mathrm{SHG}} = \frac{1}{16}\frac{\omega_{\mathrm{SH}}}{(\omega_{\mathrm{FF}})^2}|I_{\mathrm{ov}}|^2 \left(Q_{\mathrm{FF}}^{\mathrm{intr}}\right)^2 Q_{\mathrm{SH}}^{\mathrm{intr}}\,. \tag{2.3}$$

Therefore, via an EIM approach, it is possible to compute I_{ov} to estimate η_{SHG}. For $Q^{\mathrm{cpl}} = Q^{\mathrm{intr}} = 10^4$ at both wavelengths, we predict $\eta_{\mathrm{SHG}} = 0.21\ \mathrm{W}^{-1}$.

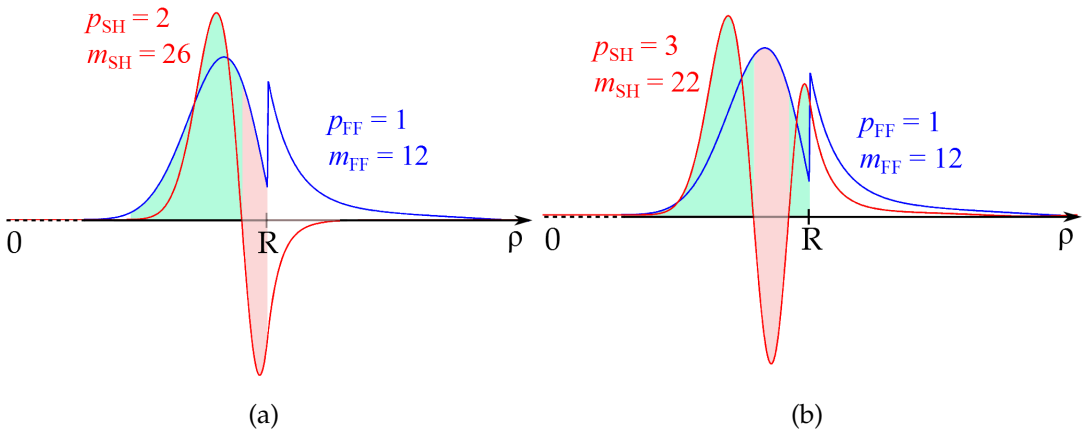

Figure 2.6: 1D radial overlap between two different pairs of phase-matched WGMs, normalized to have unity intensity. The red area corresponds to the zone where the two fields have opposite sign.

To provide a qualitative physical picture of the nonlinear conversion efficiency, we can interpret it in terms of 1D radial overlap [5], closely related to the 3D nonlinear overlap integral I_{ov} (Eq. 1.24). If we assume (p_{FF}, m_{FF}) = (1, 12) and (p_{SH}, m_{SH}) = (2, 26), i. e. for the phase-matched and energy-conserving WGMs of our SHG experiment, we find a 1D radial overlap of 55%. This value stems from the product of the two mode contributions, corresponding to the difference between the green and red areas of Figure 2.6a. For (p_{FF}, m_{FF}) = (1, 12) and (p_{SH}, m_{SH}) = (3, 22) [6], the only other two phase-matched modes, we obtain a 1D radial overlap of 17% (Figure 2.6b). From the latter, we can notice that the maximum of the FF field occurs when the SH field has a minimum, giving rise to a lower spatial overlap with respect to the first case.

2.4 Fiber-to-disk coupling

After setting the right cavity parameters, in order to optimize the SHG process we need to design the the optimal evanescent coupling between the tapered fiber and the disk. To this end, we use again the EIM.

The coupling between a WGM and a fiber can be tuned by changing two independent parameters: the fiber diameter w, and the distance g between the microdisk and the fiber. In fact, for each experiment, w is fixed by the fabrication of the tapered fiber and g can be finely tuned during the measurements. In

5. The 1D radial overlap should not be confused with the nonlinear overlap I_{ov} of Eq. 1.24.
6. The comparison between these pairs of modes only aims at exemplifying the meaning of the 1D radial overlap.

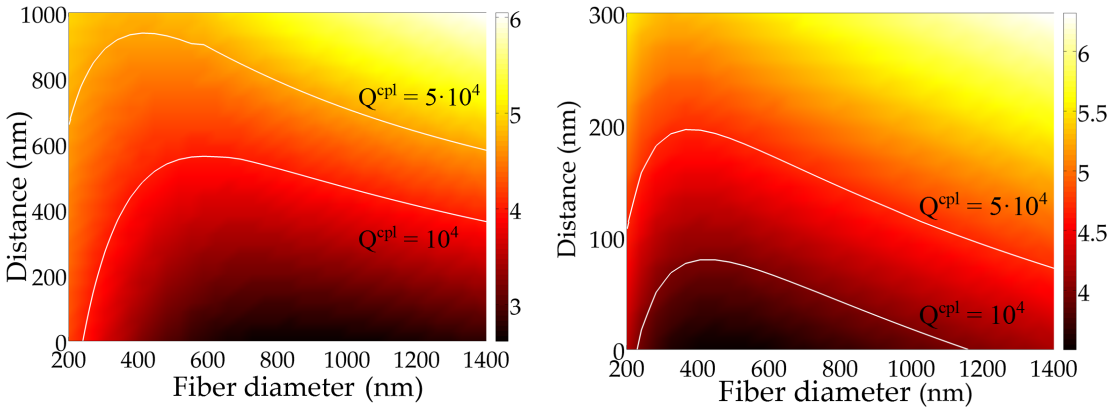

(a) 1500 nm $< \lambda_{FF} <$ 1600 nm

(b) 750 nm $< \lambda_{SH} <$ 800 nm

Figure 2.7: Logarithm of the calculated coupling quality factor Q^{cpl} as a function of the fiber diameter w and the fiber-to-disk distance g, for a cavity height $h = 155$ nm and radius $R = 1.903$ µm.

principle, we can find a high number of combinations of values for w and g providing the expected coupling quality factor Q^{cpl}. However, we can take into account neither too low ($w < 800$ nm) nor too large ($w > 1.2$ µm) fiber diameters. The lower limit is due to fabrication issues[7]. The upper limit is chosen so as to avoid a too confined optical mode. Moreover, we cannot consider too large fiber-to-disk distances, because this would provide a poor overlap between the WGMs and the fiber mode.

Figures 2.7 is the result of the calculation of Q^{cpl}, based on Eqs. 1.44 and 1.45, as a function of w and g, for a cavity of radius $R = 1.903$ µm and thickness $h = 155$ nm. In Fig. 2.7a, the surface plot displays the logarithm of the calculated Q^{cpl} for the FF WGM, while Fig. 2.7b represents the calculated Q^{cpl} for the SH WGM. The white curves delimit the ensemble of points $\{w, g\}$ for which $1 \times 10^4 < Q^{cpl} < 5 \times 10^4$. These values are dictated by the desire of attaining the critical coupling regime in the experiments, assuming that the cavity has an intrinsic quality factor $Q^{intr} \sim 10^4$. While GaAs microcavities exhibit $Q^{intr} > 10^5$ yet, a Q^{intr} of a few tens of 10^4 would be already satisfactory for AlGaAs microcavities, whose fabrication is less mature. The differences between Figure 2.7a and 2.7b are due to the mode confinement inside the fiber at the two wavelengths: in the visible range, the mode radius is smaller than in the IR[8], as shown in Figure 2.8. With our fiber fabrication technique, we obtain good quality fibers

7. See chapter 4 for more details.

8. The mode radius is ∼5.6 µm @ 830 nm and ∼10.5 µm @ 1550 nm (*source: Thorlabs fiber specification sheets*).

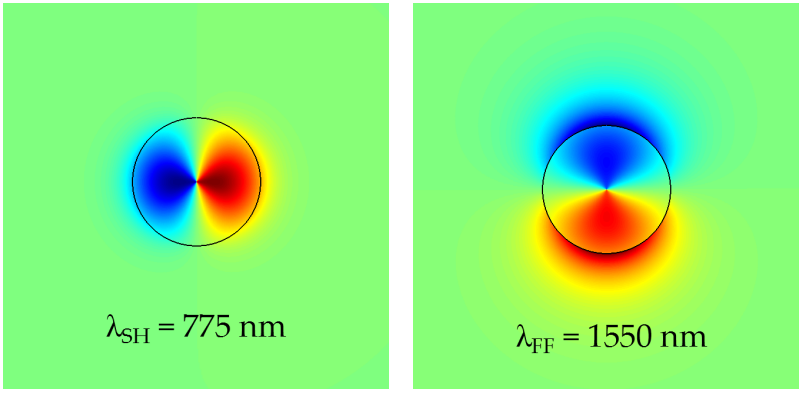

(a) (b)

Figure 2.8: Transverse profile of the radial component of the electromagnetic field inside the fiber ($w = 1$ µm), calculated with the EIM. The black line depicts the fiber transverse section.

(transmission $T > 95\%$) for $w \sim 1$ µm. Therefore, since the fiber used for the disk characterization is the same for both wavelengths, at $\lambda \sim 775$ nm (Fig. 2.8a) the field is less evanescent than the one at $\lambda \sim 1550$ nm (Fig. 2.8b). Figure 2.7 provides a quantitative indication for w and g. Starting from these data, more precise values to be used in our experiments are inferred with a 2D EIM approach. The results, obtained by plugging the values reported in Table 2.3, are shown in Figure 2.9.

The latter shows two different pictures of the mode matching, for both FF and SH modes. In Figs. 2.9a and 2.9c WGM and fiber fields are plotted for optimal fiber diameter (1 µm) and fiber-to-disk distance (540 nm for the FF and 50 nm for the SH); these values hold for a $Q^{\text{cpl}} = 10^4$, $R = 1.903$ µm and $h = 155$ nm. Figures 2.9b and 2.9d represent the real part of the oscillatory term of the integrand in Eq. 1.44. The blue part between the disk and the fiber represents the region where $\text{Re}[e^{i(m\theta-\beta z)}]$ is constant, resulting in $\kappa_{\text{cpl}} \neq 0$, mandatory to have an efficient coupling. All these plots exemplify what we have illustrated above: the coupling in the IR range can be efficient even at moderately large fiber-to-disk distances, while to get $Q^{\text{cpl}} = 10^4$ at λ_{SH} we need to be far closer to the disk, with a few issues from an experimental point of view. A zoom on the proximity zone between the resonator and the fiber can give a better insight of the field evanescent tails for both modes. This is presented in Figure 2.10: the left part of the pictures (red) stands for the disk edge, while the right part (blue) represents the fiber ($w = 1$ µm).

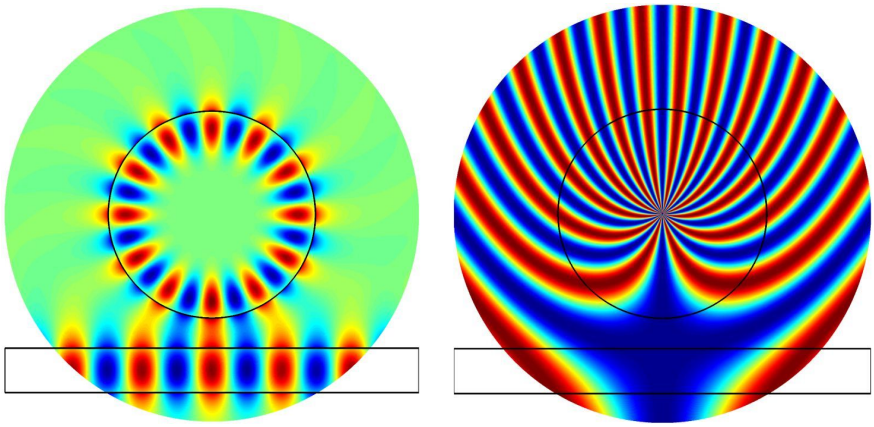

(a) FF: $w = 1$ µm, $g = 540$ nm (b) FF: $w = 1$ µm, $g = 540$ nm

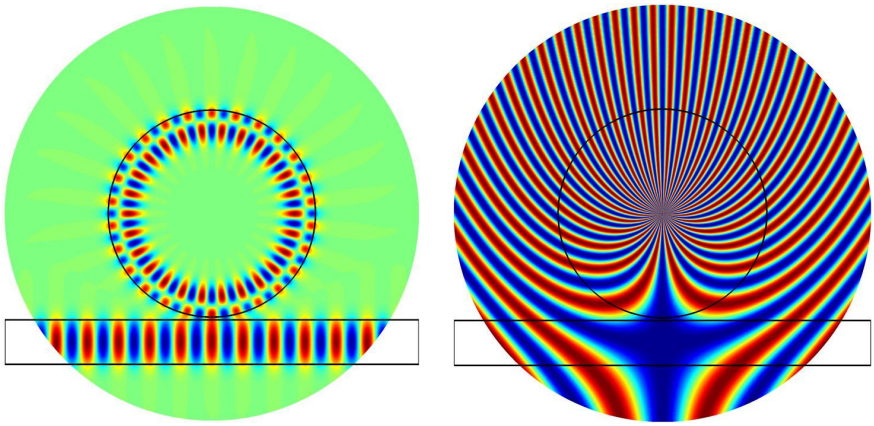

(c) SH: $w = 1$ µm, $g = 50$ nm (d) SH: $w = 1$ µm, $g = 50$ nm

Figure 2.9: Different pictures of the mode matching. (a) and (c) EIM plots of WGMs and fiber fields for optimal fiber width and fiber-to-disk distance: in red $\mathrm{Re}\,[E] \geq 0$, in blue $\mathrm{Re}\,[E] < 0$; (b) and (d) EIM plots of $\mathrm{Re}\left[e^{i(m\theta-\beta z)}\right]$: in blue $\mathrm{Re}\left[e^{i(m\theta-\beta z)}\right] = 1$, in red $\mathrm{Re}\left[e^{i(m\theta-\beta z)}\right] = -1$. The black lines represent disk and fiber boundaries.

2.5 Summary

In this chapter we described the goal of the first part of the thesis, illustrating the road leading to the concept of an original suspended $Al_{0.4}Ga_{0.6}As$ microcavity, for SHG from ∼1550 nm to ∼775 nm. For the comprehension of our final cavity design, we listed the important parameters and the methods to obtain them. We also reported on our approach to select the two energy-conserving and phase-matched WGMs needed for our experiment. Then we illustrated how to compute the nonlinear conversion efficiency, which is important to assess the experiment feasibility. Finally, we gave an overview on how to control and

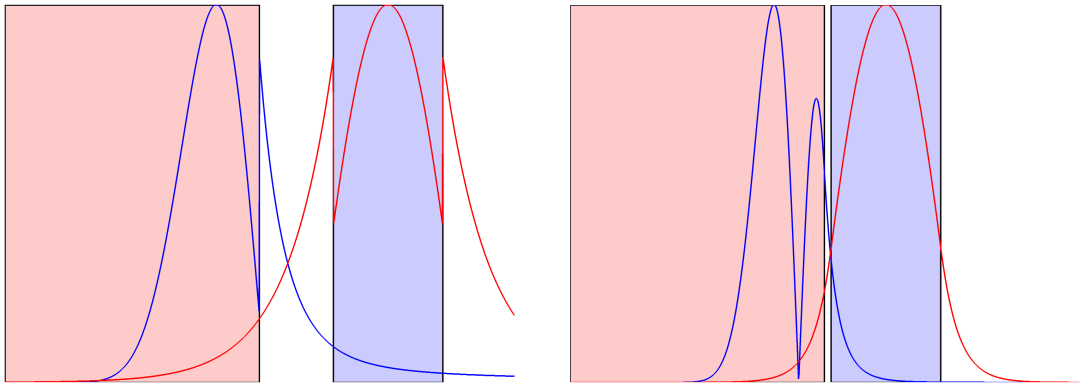

(a) FF WGM + fundamental fiber mode (b) SH WGM + fundamental fiber mode

Figure 2.10: Zoom on the proximity zone between the resonator ($h = 155$ nm, $R = 1.903$ µm) and the fiber ($w = 1$ µm), representing the field evanescent tails of the interacting modes.

adjust the coupling strength between the microcavity and the fiber, to optimize the experimental conditions.

In the next chapters we shall use the information drawn from the simulations presented here, in order to fabricate a well-working cavity and, afterwards, characterize it.

Chapter 3

Fabrication

3.1 Introduction

In this chapter we shall describe the fabrication procedure of AlGaAs microdisks on GaAs pedestal. Although suspended GaAs microcavities are well-known and their technology is mature [2,85,86], the demonstration of AlGaAs microresonators required a considerable technological effort, since an adequate protocol did not exist yet. This demanded a significant amount of time: a marge number of tests were performed before getting to the final result.

In the following, we shall show the fabrication procedure step-by-step, including failures and tricks learned on the way, for a complete insight of this new fabrication technique.

The nanofabrication developments were carried out in the clean rooms of the École Normale Supériore and the Université Paris Diderot.

3.2 Employed growths

For this technological development, four different epitaxial structures have been processed. Our samples are grown by Molecular Beam Epitaxy (MBE) on (001) GaAs substrate, with the following vertical layout:

- C2T18: 5 μm GaAs / 198 nm $Al_{0.28}Ga_{0.72}As$ (Fig. 3.1a) − Laboratoire de Photonique et de Nanostructures, Marcoussis, France;
- AS0444: 200 nm GaAs buffer / 3 μm $Al_{0.4}Ga_{0.6}As$ / 2.4 μm GaAs / 150 nm $Al_{0.4}Ga_{0.6}As$ (Fig. 3.1b) − CEA, Grenoble, France;
- CAT104: 5 μm GaAs / 138.6 ÷ 172.2 nm $Al_xGa_{1-x}As$, with 0.39 < x < 0.48 (Fig. 3.1c) − Laboratoire de Photonique et de Nanostructures, Marcoussis, France;
- D8T157: 5 μm GaAs / 155 nm $Al_{0.4}Ga_{0.6}As$ (Fig. 3.1d) − Laboratoire de

Photonique et de Nanostructures, Marcoussis, France.

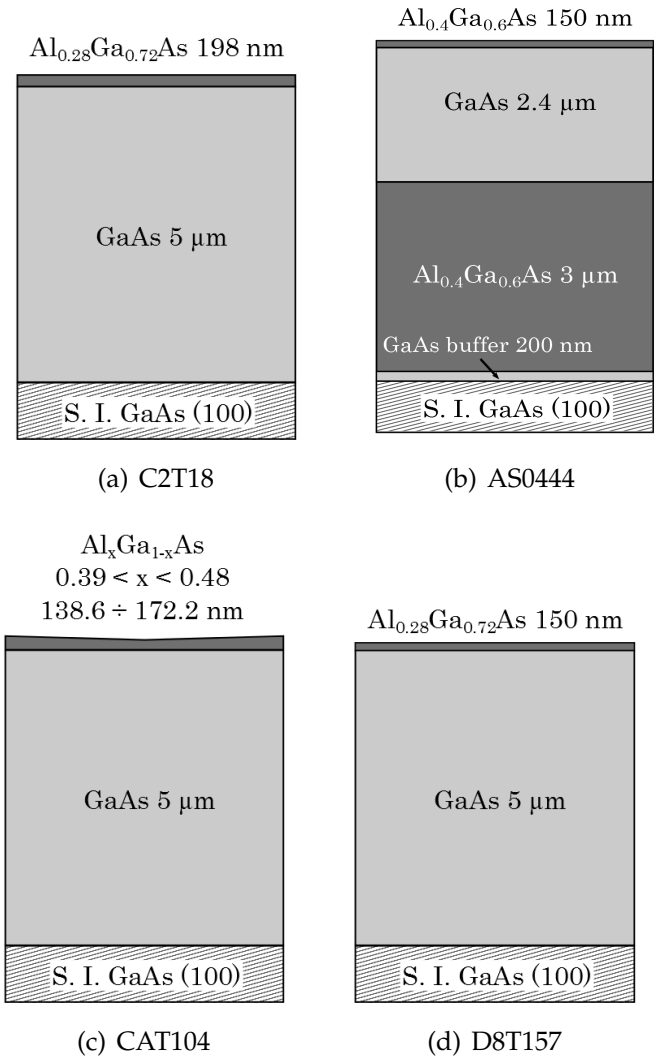

Figure 3.1: Schematic of the four different growths processed during the technological development.

3.3 Fabrication overview

This section provides an overview of the main fabrication steps, reported in Figure 3.2. On a properly cleaned sample chip of wafer (a), negative tone photoresist is spun and then exposed with Raith e-LiNE ultra high resolution electron-beam (e-beam) lithography system (b). The resist is then developed by means of a basic chemical solution (developer). After this step, it is possible to reveal and see the resist pattern, which works as a mask for the etching process

(c). This part of the fabrication is crucial, since the shape of the pattern strongly affects the final disks appearance. In fact, this resist layer protects the AlGaAs from the non-selective etching solution, which will attack everything but the patterned area.

Two main steps are needed to fabricate our microcavities. First, we etch away most of the AlGaAs layer we do not need, i. e. the uncovered one (d), using a non-selective acids mixture. Then, we proceed to under-etch the GaAs sacrificial layer to define small pedestals (e).

Since the total height of the suspended microresonator (disk+pedestal) is about 3 μm, to make the measurement easier (see chapter 4), we decided to put our disks on mesas. In this way we can reasonably isolate the cavities from the rest of the substrate and reduce the possibility of damaging the optical fiber during the experiments. To this end, we perform an optical lithography. Image reversal resist is spun twice on the sample to ensure a covering of the whole disk height, without breaking the structures with the further etching (f). The pattern is then optically exposed using a SUSS MicroTec Manual Mask Aligner and revealed with a different developer (g). After this step, mesas are etched using again the non-selective solution (h).

At the end of the procedure the resist is removed with acetone and isopropanol (IPA). A schematic view of the final sample is shown in (i).

3.4 Electron beam lithography

3.4.1 Why electron beam lithography?

Electron beam lithography is usually employed to draw nanometric patterns. Thus one could ask why we have chosen it to make micrometric cavities, rather than of optical lithography, which is faster and less expensive. Our decision stems from the will of obtaining very smooth sidewalls and shapes as round as possible. The circles patterned on optical-lithography masks are rather polygons with a high number of verteces; the sharp corners coming from the mask (Fig. 3.3a) are then transferred to the resist during the exposure (Fig. 3.3b), making it impossible to achieve good circular structures and thus efficient nonlinear processes. Moreover the e-beam lithography enables to draw and test a wide number of different cavity radii, since, compared to photolithography, it is easier to modify the mask. This degree of freedom provides us with an additional phase-matching parameter.

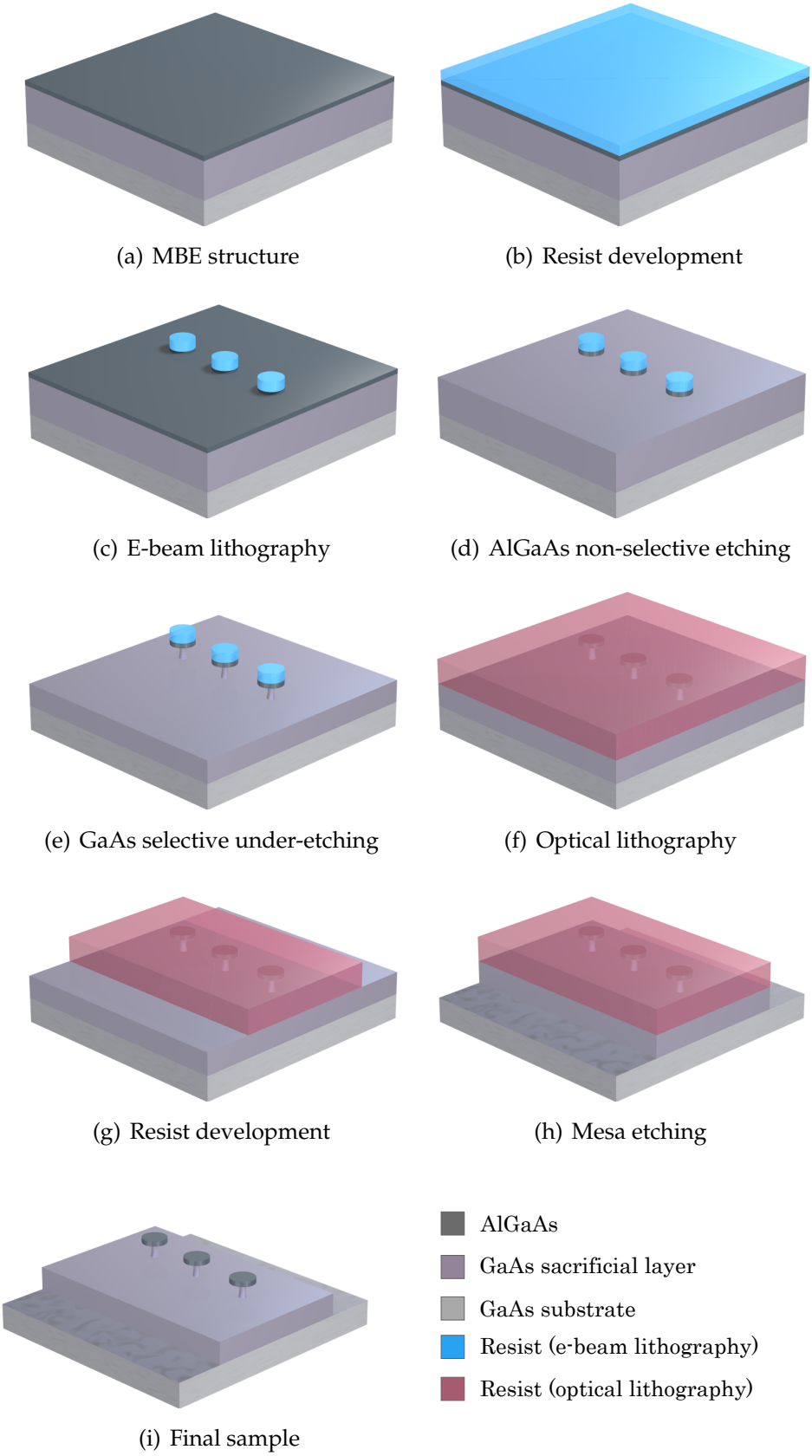

Figure 3.2: Main fabrication steps of AlGaAs microdisks on GaAs pedestals.

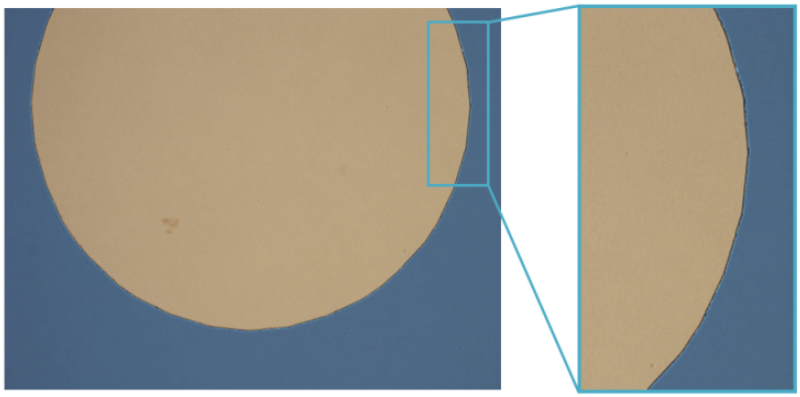

(a)

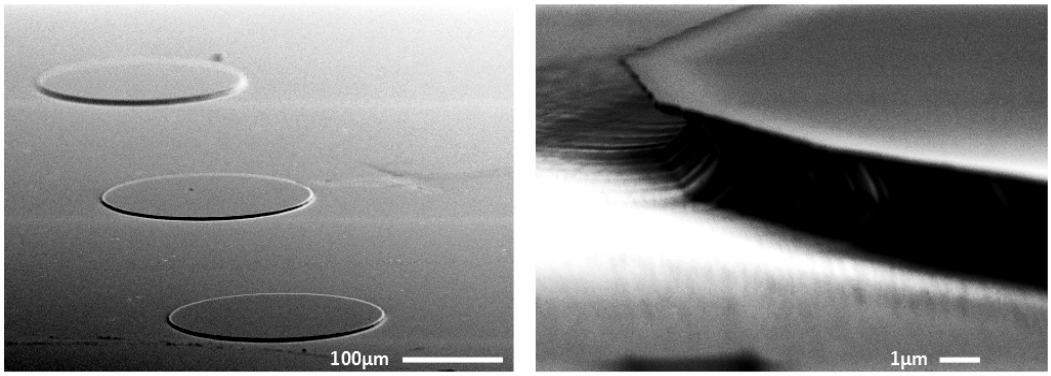

(b)

Figure 3.3: (a) Optical microscope pictures of a round pattern of a mask for optical lithography; (b) SEM pictures of the etched pattern.

3.4.2 Sample preparation

We usually cleave sample chips of less than 1 cm^2 area. Samples of at least 0.5 cm^2 avoid bad resist deposition and large edge effects, thus maximizing the effective area to draw the pattern.

Two different procedures can be adopted to carefully clean the chip before starting the fabrication:

- acetone ultrasound bath for 5 minutes, followed by an IPA bath for 5 additional minutes;
- stir in an acetone bath for 5 minutes, followed by a rinse in IPA for 5 more minutes and by 60 seconds in deionized (DI) water.

In both cases the sample is blow-dried with a N_2 gun.

Anyway, the use of acetone is mandatory to remove the organic impurities and the greasy contaminations from the substrate, while IPA is needed to remove

polluted acetone traces. If after the cleaning the impurities are not totally gone, in general it is possible to use an O_2 plasma cleaner, which breaks the organic bonds of surface contaminants. However, this is not recommended in the presence of Al layers, which can undergo oxidation. A clean substrate, as well as an excellent epitaxial growth, is necessary to avoid any discontinuity on the pattern transfer.

After different tests, we have found out that using the first cleaning method leads to a higher probability of impurities deposit on the sample. In fact, during the ultrasound bath, the sample drifts inside the beaker, damaging the sample chip edges. That is why we decided to use just the second one.

The last step of the cleaning procedure consists in heating the sample on a hotplate at 150°C for 5 minutes to dehydrate the substrate before proceeding with the resist spin-coating. The further preparatory steps should be performed directly after cooling down the sample, to avoid surface re-hydration and poor resist adhesion.

3.4.3 Photoresist spin-coating procedure

A uniform resist layer is also required to have a good result at the end of the fabrication process. Therefore, a proper resist adherence on the surface is necessary and the use of an adhesion promoter is strongly recommended. In fact, between the cooling down of the sample and the beginning of the resist spin-coating, the surface has a few seconds to be naturally re-hydrated by the air. The surface oxide forms hydrogen bonds with water vapor and this thin film of water reduces the resist adherence to the substrate. As a result, the resist pattern could be unintentionally removed after the exposure, during the development. By using an adhesion promoter, it is then possible to turn hydrophilic surfaces into hydrophobic and thus obtain a good resist coating, as shown in Figure 3.4.

The photoresist spin-coating procedure consists of two steps:

– adhesion promoter coating;
– photoresist coating.

As adhesion promoter, we use the HexaMethylDiSilazane (HMDS), which chemically bonds to the oxygen of the native oxide on the surfaces with its Si atom. This produces a release of ammonia, which leads to the rupture of the hydroxyl groups, resulting in hydrophilic surfaces. Just after the dehydration step, the sample is put onto the chuck inside the spin coater and a few drops of HMDS are applied by means of a pipette. All these processes must be really fast to avoid the surface moisturizing. We use the following spin parameters:

– speed: 6000 rpm;
– acceleration: 3000 rpm/s;

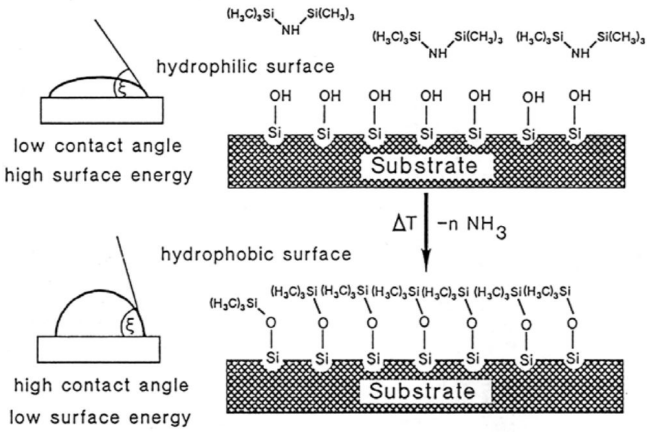

Figure 3.4: Adhesion of resist to a surface after the use of HMDS [87]. The diagram shows the reaction of a hydrophilic surface (top) after the application of the HMDS: the released ammonia breaks the hydroxyl groups, making the surface hydrophobic (bottom).

– time: 30 s.

We wait for 60 seconds before applying the resist: this leads to improve the quality of the whole spin-coating procedure.

We use e-beam photoresists produced by Microresist Technology. The thinner the layer, the more precise the lythography; this basically limits our choice to two different kinds of negative tone-photoresist: the ma-N 2401 and the ma-N 2403 (100 nm and 300 nm nominal thickness, respectively). After several tests, we opted for the second one, since the ma-N 2403 seems to provide a more uniform film, once spun on the surface.

Employed resist: ma-N 2403

To have a layer thickness of 300 nm, the spin coating is carried out following the parameters suggested by Microresist Technology (Fig. 3.5):

– speed: 3000 rpm;
– acceleration: 3000 rpm/s;
– time: 30 s.

After coating, we softbake the sample at 95°C for 60 seconds. This is important since the resist film could contain some residual solvent, and softbaking helps to minimize it, avoiding further problems (poor adhesion, bad development quality, resist dissolving and bubbling, ...).

The sample is now ready to be exposed with the e-beam machine. Since the resist is photosensitive, any light exposure has to be avoided. If it happens, it is not possible to work with the damaged resist film anymore and a new cleaning procedure is required.

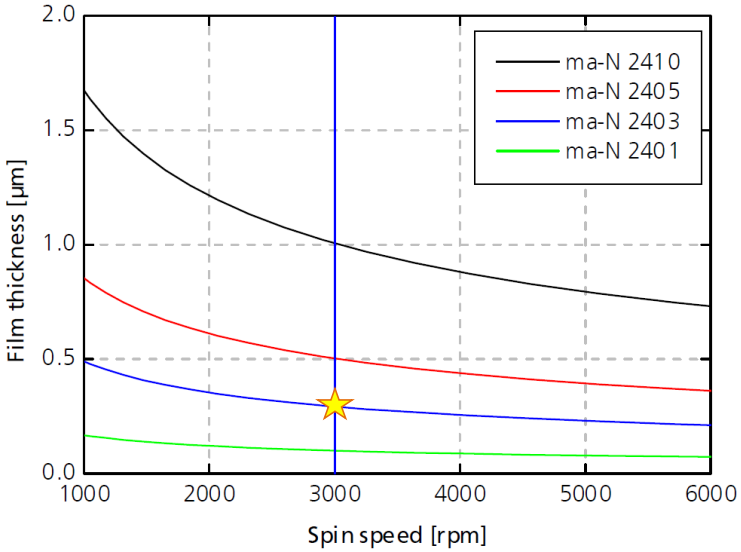

Figure 3.5: Spin curves of ma-N 2400 series, for 30 s spin time. The star points out the right spin speed for ma-N 2403. *Source: Negative Tone Photoresist Series ma-N 2400 - Processing Guidelines*.

3.4.4 Lithography

E-beam lithography procedure

The e-beam lithography machine is essentially a scanning electron microscope (SEM) able to move the electron beam over the surface in order to draw the wanted pattern. The elements contributing to the lithography process (electron gun and lenses) have to be aligned, and it can be directly done by changing a few parameters. Once the vacuum pressure needed by the machine is reached ($\sim 2 \cdot 10^{-5}$ bar), it is possible to switch on the voltage, set it at 20 kV and start the mask drawing. We trace lines of several disks (from 30 to 50), with diameters ranging between 3.4 µm and 4 µm. The spacing between two adjacent disks is 50 µm, large enough not to damage the fiber during the experiments (see chapter 4). We also leave 2 or 3 mm between two adjacent lines so as to have the possibility of cleaving the sample in small bars without breaking them. Cleavage is also helped by the presence of four visible markers (1 mm $\times$ 2 mm) at the beginning and at the end of each line. Another parameter to set is the diaphragm aperture.

Diaphragm aperture

The need for pattern precision made us opt for the smallest possible value (7.5 µm), since such low value provides a high lithography resolution.

To check if the alignment procedure has been carried out properly, we define a row of so-called contamination dots. These are produced leaving the beam switched on for a few seconds on small selected areas ($\sim$100 nm^2) to expose the resist. By looking at the shape of the dots, it is possible to understand if all the parameters have been correctly set. A good alignment should provide a

perfectly circular dot of ∼20 nm of diameter, which means that stigmatism and focus, respectively, have been properly controlled.

Once the procedure is completed, we proceed to the exposure of the resist. During this step, the parameter to take care of is the area dose, which is the quantity of electrons per cm^2 needed to expose the pattern. Normally, a range of possible exposure dose values is provided by the resist producer, and in our case the optimal values range from 170 to 235 $\mu C/cm^2$. To find the best value, we perform a dose test. It consists in making a matrix of disks with the same radius but different dose values. After that, we fabricate a matrix of dummy suspended microdisks. Only at the end of the whole process, it is possible to evaluate the appropriate dose to use. By looking at a close-up of a picture as the one shown in Figure 3.6, it is possible to single out those cavities having smooth edges without a too large diameter. By finding the corresponding disk on the e-beam mask, we can trace back to the specific dose value to use in our lithographies. From this analysis, we deduced an exposure dose $\mathcal{D}$ =192 $\mu C/cm^2$.

Exposure dose

The time required to expose and draw the pattern is directly linked to the employed dose by:

$$t = \frac{\mathcal{D} \cdot \mathcal{A}}{\mathcal{I}} ,$$

where $\mathcal{A}$ and $\mathcal{I}$ are the area to expose and the beam current, respectively [88].

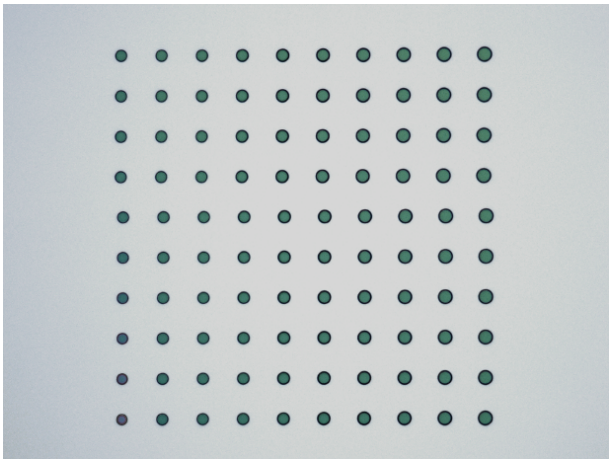

Figure 3.6: Optical microscope picture of a dose testing matrix. It is possible to see that the bottom left disks are smaller (lower dose values) than the top right ones (higher dose values).

In our case, lithographies take less than one hour.

Once the whole pattern has been transferred to the sample chip, the beam is shut down and it is possible to extract the sample from the machine. Even after the lithography process, it is important to avoid any light exposure, in order to exclude accidental over-exposure of the resist before the development.

3.4.5 Development

After the exposure, we develop the resist. When the e-beam draws the chosen pattern onto the substrate, the exposed resist undergoes a cross-link (i. e. a bonding of the resist polymer chains), while the unexposed one stays unchanged. This produces a much slower development rate of the exposed areas with respect to the unexposed ones. Exposure and development are responsible for the reveal of the resist profile. At the end of this process, the etching mask will have completely taken the wanted shape.

We use the AZ 726 MIF developer (from Clariant GmbH) to provide an uniform development on the whole surface.

After developing for 60 seconds, we rinse with DI water for one additional minute, to be sure to stop the development action. Sample agitation during the immersion is recommended: it helps to let fall down and dissolve the developed resist film into the solution, without any surface contamination. The sample is finally blow-dried with a N_2 gun. We check the result by means of an optical microscope provided with an UV filter; the latter is essential especially when the development process is not totally over, since white light would further expose the resist, making impossible any development improvement.

Finding the right development time is crucial, because:

- a resist underdevelopment would originate a patter that is not correctly shaped; the wrong shape would be transmitted to the desired structure during the etching (Fig. 3.7a);
- a resist overdevelopment would erode the pattern edges, transmitting roughness to the structure (Fig. 3.7b).

It is then recommended to start with short-time development steps (5-10 seconds) in order to find the good one (Fig. 3.7c), according to the used resist and exposure dose.

3.5 Microdisks wet etching

To fabricate our microdisks, it is important to respect the whole protocol that we have developed, studied and improved. Any single step is fundamental to get a good quality sample, and our final recipe for this technological process has been finely tuned after a few non-satisfactory tests. First, we use a non-selective solution to define the disks and then we go on with a selective wet under-etching to make the pedestals.

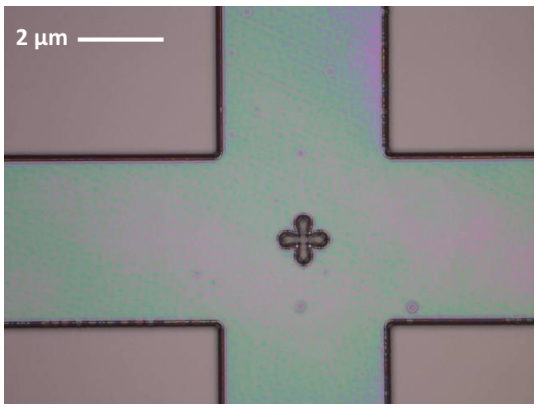

(a) Underdeveloped resist pattern

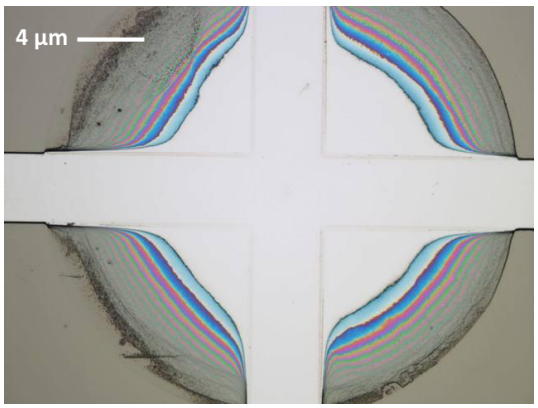

(b) Overdeveloped resist pattern

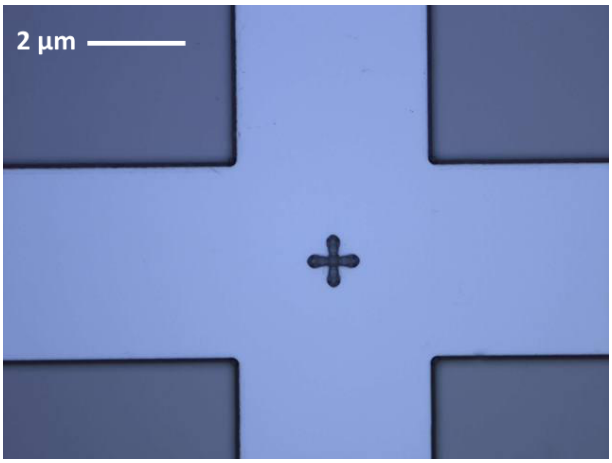

(c) Well-developed resist pattern

Figure 3.7: Optical microscope pictures showing some examples of pattern development corresponding to different agitation times.

3.5.1 Non-selective wet etching

In this case, to define our cavities, we need to transfer the drawn pattern from the resist mask to the AlGaAs layer in an isotropic way. To this end, we etch away the resist-free areas by using an etchant solution able to attack both AlGaAs and GaAs. We made a first attempt with an acid mixture composed of Hydrobromic Acid (HBr), Nitric Acid (HNO_3) and water (H_2O), since the effects of this solution have been thoroughly studied on III-V compound semiconductors [89,90,91]. Since these results were unsatisfactory, we decided to look for a different etchant solution. We opted for an acid mixture composed of HBr, Acetic Acid (CH_3COOH) and Potassium Dichromate ($K_2Cr_2O_7$), as proposed for the first time in 1981 [92]. This solution, called BCK after the name of its principal components (H**Br**, **C**H_3OOH and **K**$_2Cr_2O_7$), has proved much more

effective and appropriate for our purposes.

$HBr/HNO_3/H_2O$

The first tests carried out with this etchant solution have been performed on the structures C2T18 and AS0444 (Fig. 3.1a and 3.1b).

This acid mixture, composed of HBr, HNO_3 and H_2O (1:1:8), dates back to the '80s and is usually employed in GaAs compounds etching [93]. Its action on the AlGaAs layer strongly depends on the agitation and in no case we obtain smooth sidewalls. If agitated, the solution is too aggressive and it tends to

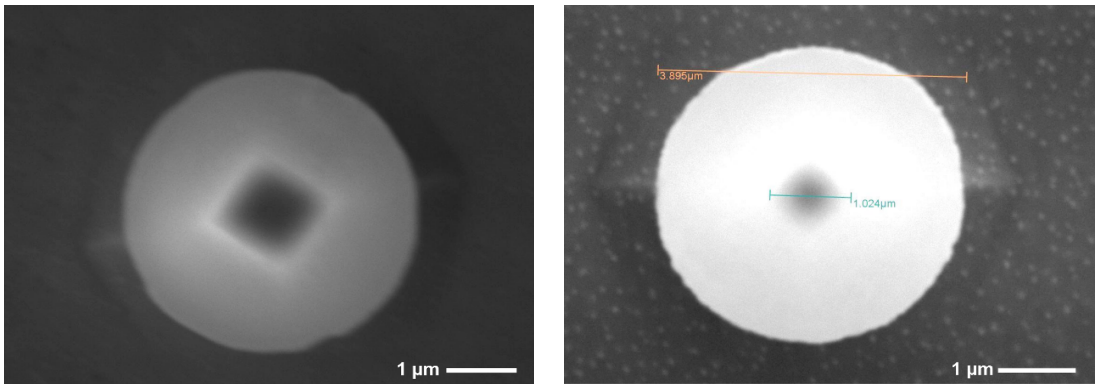

(a) Result from the agitation of the sample inside the solution.

(b) Result without agitating the sample inside the solution.

Figure 3.8: SEM top-view pictures of disks obtained by using the non-selective etchant solution composed of HBr, HNO_3 and H_2O.

remove small parts from the disk edges (Figure 3.8a). If not agitated, the cavity is too rugged to perform any nonlinear optics experiment (Fig. 3.8b).

These preliminary results have induced us to look for a more suitable etchant solution.

$CH_3COOH/HBr/K_2Cr_2O_7$

This test has been performed on the growths AS0444, CAT104 and D8T157 (3.1b, 3.1c and 3.1d). This etchant consists of equal parts (1:1:1) of CH_3COOH, HBr and a saturated solution of $K_2Cr_2O_7$ in DI water (14.7 g $K_2Cr_2O_7$: 100 ml DI water). Its etching behavior is strongly dependent on temperature and agitation. That is why, for our purposes, after several tests we decided to keep the solution at fixed low temperature (4°C using a thermostated bath) without agitating the sample inside the liquid, while etching. By choosing the right etching time, it is

possible to get really smooth surface edges, reducing the roughness which can lower the intrinsic quality factors of the cavities.

To understand how long the sample should be kept inside the mixture of acids, we perform different etchings in order to appreciate the correlation between the roughness and the etching time. In Figure 3.9 we show the different results obtained for etching times of 20 s (a), 30 s (b) and 60 s (c), respectively. It is clear that the best way to proceed is to etch the sample for 60 s. In fact, after 20 s and 30 s the edges are not smoothed at all, even if the round shape is already completely transferred from the resist mask to the surface. The BCK has the time to gradually smooth all the irregularities only after the first minute.

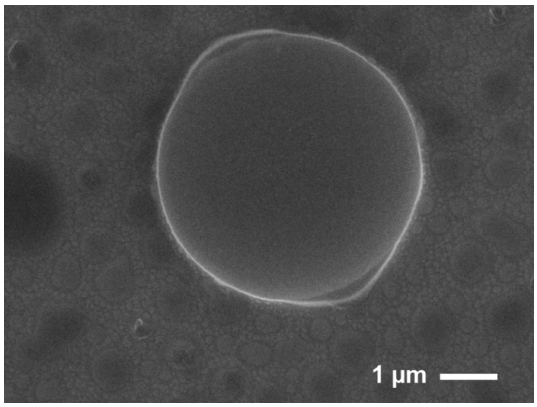

(a) 20 second etching

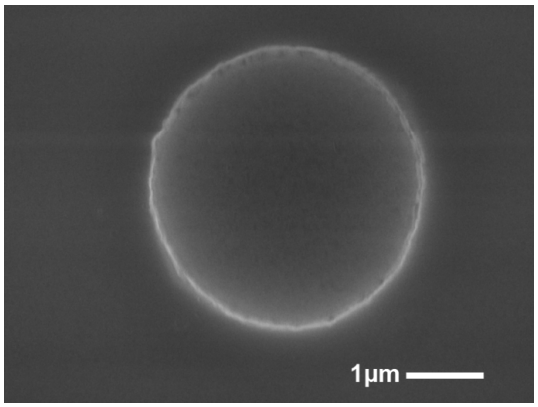

(b) 30 second etching

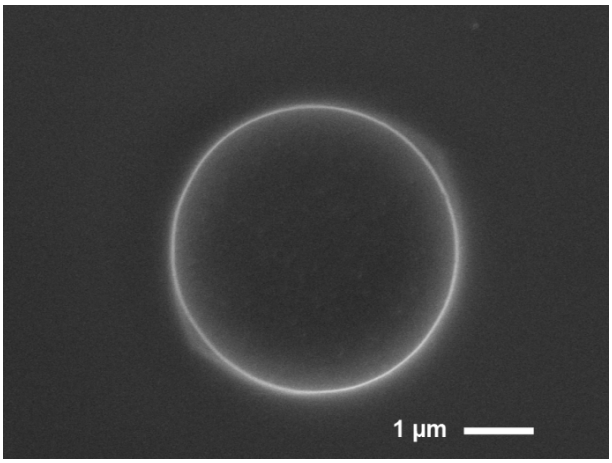

(c) 60 second etching

Figure 3.9: SEM pictures of disks obtained with different etching times, showing the time-dependent action of the BCK solution.

We made also additional tests to study the BCK etching rate. For short times (< 60 s) we found a rate of 27 nm/s. It could seem too long to etch for 60 s just

for attacking 150 nm (AlGaAs layer), since in the end we etch a total thickness of about 1.6 μm. However, this does not have an impact on the further fabrication steps and it gives excellent results in terms of roughness. Nevertheless, it is important not to exceed with the etching time, because after a while the disks are not round anymore.

3.5.2 Selective wet under-etching

Before this thesis, AlGaAs microdisks on GaAs pedestals had never been fabricated. We devoted an important part of our efforts in finding the right etchant solution able to remove the GaAs without damaging the AlGaAs disks.

One of the most common mixture used to etch GaAs over AlGaAs is the citric acid ($C_6H_8O_7$) with the addition of Hydrogen Peroxide (H_2O_2). However, even though the etching rate of AlGaAs is low, it is not zero and it consequently results in insufficiently smooth cavities. Motivated by the will of finding the right way to fabricate our microdisks, we eventually found an Ammonium Hydroxide (NH_4OH) enriched etchant solution suitable for us.

Citric Acid

This selective etchant has been used on the structures C2T18 and AS0444 (3.1a and 3.1b). To prepare it, we first need to blend anhydrous $C_6H_8O_7$ together with DI water (1 g $C_6H_8O_7$: 1 ml H_2O) and leave it for at least 12 hours; in this way, the acid has the time to stabilize and the etching rate will be homogeneous. After that, we add H_2O_2 to the aqueous Citric Acid solution, choosing the most appropriate ratio (5:1) reported in [94] (see Table 3.1).

Although we use the $C_6H_8O_7/H_2O_2$ volume ratio with the highest selectivity between AlGaAs and GaAs, this mixture can slowly etch the AlGaAs layer anyway. After the under-etching, the disks result damaged and not round anymore (Fig. 3.10). Therefore we move on to a different method.

NH_4OH enriched etchant solution

During this thesis, the key point of our technological development was an old article of Logan and Reinhart [95]. The etchant solution studied in their work, mainly composed of H_2O_2 with the addition of NH_4OH, finally enabled us to have round and smooth cavities.

This etchant behaves differently depending on the pH value of the employed solution. According to [95], with a $\sim 6 <$ pH < 7.1 it is possible to obtain smooth etched surfaces, since the etchant has the time to effectively remove the native oxide films and then proceed with the GaAs attack. When pH ~ 7.2, the oxide

Volume ratio of $C_6H_8O_7/H_2O_2$	Etching rate of layers on GaAs substrate (Å/min)	
	GaAs	$Al_{0.3}Ga_{0.7}As$
0	0	0
0.5	60	27
1	69	27
2	85	24
3	2169	24
4	2235	23
5	**3140**	**27**
6	–	30
7	2882	89
8	–	2331
9	–	2297
10	2513	1945
15	1551	1082
20	762	918
50	397	512
∞	0	0

Table 3.1: List of etching rates of GaAs and $Al_{0.3}Ga_{0.7}As$ vs. on the $C_6H_8O_7/H_2O_2$ volume ratio [94]. In green we have highlighted the ratio used for our tests.

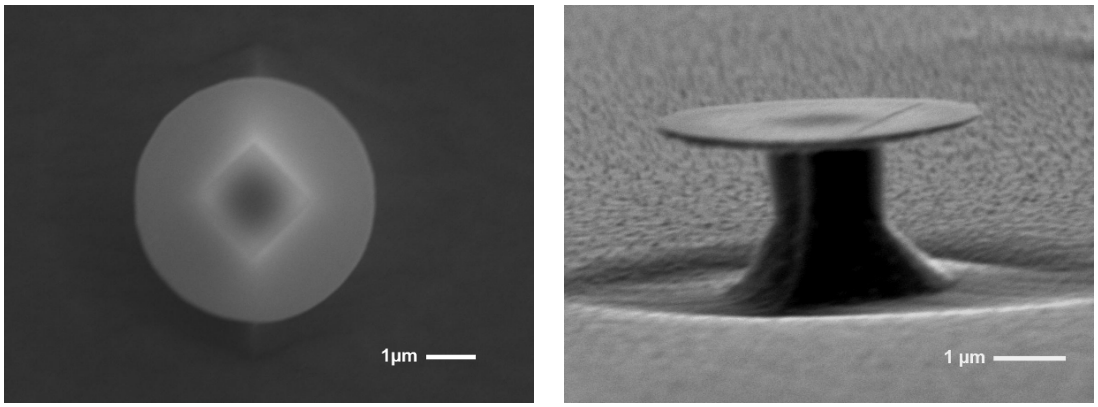

(a) Top view (b) Side view

Figure 3.10: SEM pictures of a suspended microdisk obtained by using the BCK and then the mixture $C_6H_8O_7/H_2O_2$ (5:1). From both pictures it is possible to observe the rugged edges of the disk.

film cannot be totally removed (Fig. 3.11), therefore it acts like a random etching

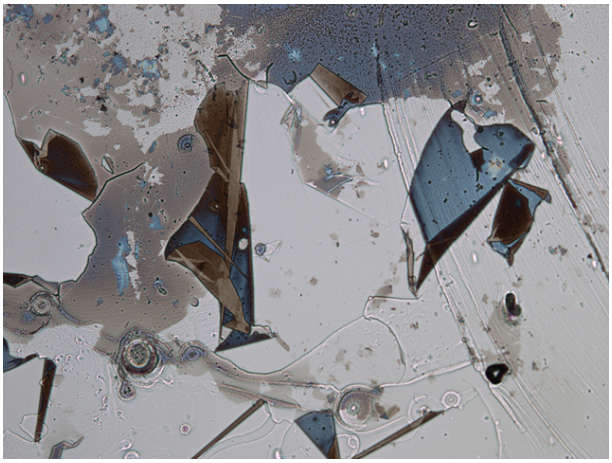

Figure 3.11: Optical microscope picture of a broken oxides film onto a processed sample surface, coming from too high a pH value of the selective solution.

mask and some unwanted features are transferred to the AlGaAs disks. For higher pH values (pH > 7.5) it is impossible to use this mixture to properly etch the AlGaAs, because the result is just a set of holes on the surface.

To prepare the NH_4OH/H_2O_2 mixture, we take a beaker of H_2O_2 and we use a pipette to put a few drops of NH_4OH into the solution, constantly monitoring the pH value with a pH-meter. In general, we use 5 or 6 drops to reach a pH $= 6.95 \pm 0.01$, in order to take into account possible slight imprecisions in the pH measurement and thus staying under the critical value of pH $= 7.1$. While etching, we obtain better results if the sample is stirred inside the solution. To this end, we use a magnetic stirrer and we always set a rotational speed of 325 rpm, for sake of reproducibility. The etching time is of indicatively 40 minutes: less than that leads to a too large pedestal diameter; more than that, to too small ones. It is possible to check its size by transparency through the AlGaAs layer by looking at it under an optical microscope. Moreover, it is important to leave the sample inside the etchant for at least 30 minutes; during this lapse of time, the NH_4OH/H_2O_2 mixture can remove the oxides formed during the whole procedure and etch them away. If the sample is taken out from the beaker earlier, the oxide film is not completely removed and it drops off onto the surface, making it impossible to continue the etching (Fig. 3.12).

Once the etching time is over, we rinse the sample for 3 minutes into three different beakers containing DI water, to be sure to diluite the remaining NH_4OH/H_2O_2 mixture as much as possible. Before blow-drying the sample with the N_2 gun, we pass it into the IPA for about 60 seconds: the use of IPA prevents the disks to collapse, thanks to its lower surface tension with respect to

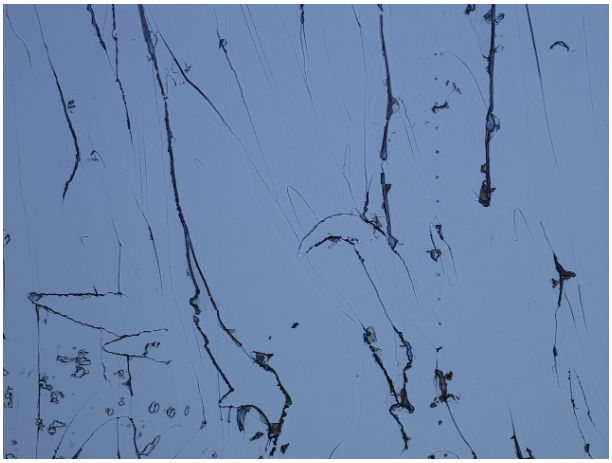

Figure 3.12: Optical microscope picture of a broken oxide film on a processed sample surface, resulting from a too short under-etching time.

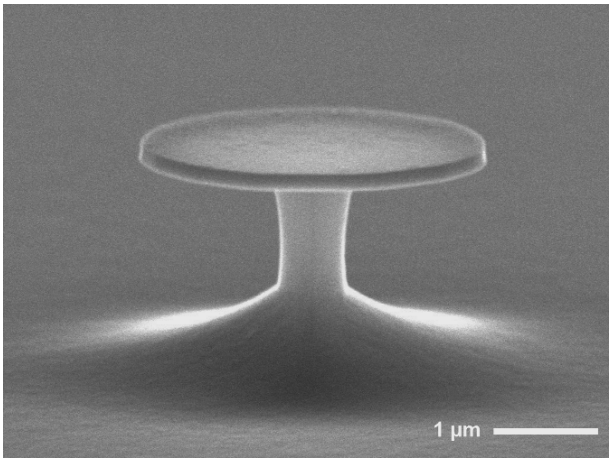

Figure 3.13: SEM side-view picture of a suspended microdisk obtained by using the BCK, followed by the mixture NH_4OH/H_2O_2.

the water one [96].

At the end of this step, we obtain round smooth cavities, as the one shown in Figure 3.13.

3.5.3 E-beam photoresist issues and removal

We have met several problems in removing the e-beam photoresist after the whole procedure. A photoresist crosslink occurs immediately after the first non-selective etching with the BCK, hindering a complete sample cleaning. The resist gets burnt and any attempt to remove it is useless. Figure 3.14 shows the presence of a resist layer despite an accurate cleaning consisting of acetone and

IPA baths, followed by acetone heated at 40°C.

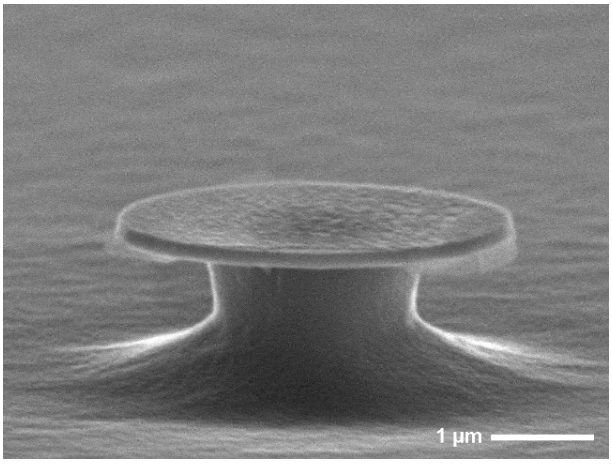

Figure 3.14: SEM side-view picture of a suspendend microdisk with a clear evidence of photoresist crosslink.

These unsatisfactory results have led us to search for a new solution. We faced this problem in two different ways:

- a physical one, by using the O_2 based Reactive-Ion Etching (RIE);
- a chemical one, by using the AZ100 remover from Clariant GmbH.

With the RIE we physically attack the surface (both resist and AlGaAs layer), and the risk of damaging the disk shape is high. From Figure 3.15a, we can see that the edges are smoothed out without completely removing the resist, showing that this method is not adapted to solve our problem.

The AZ100 is a strongly alkaline resist stripper, which can be used on Al-containing substrates only undiluted to avoid any attack [1]. We proceeded with an AZ100 bath at room temperature, but we did not succeed, as shown in Figure 3.15b. The resist film stays on top of the disk, and does not get dissolved even for long baths in the stripper. Since we only need the resist mask to define the cavities, i. e. till the end of the first BCK solution bath, we decide to remove it as soon as possible. After completing the non-selective etching, we strip the resist by means of 5 minutes acetone bath, 1 minute IPA bath and 10 minutes AZ100 bath, all of them with the agitation of the sample inside the beakers to help the resist fall. By doing so, the resist film is effectively removed and dissolved, and the cavities end with being properly cleaned.

1. By adding water, the pH value of AZ100 rises, producing an aqueous alkaline liquid that etches Al.

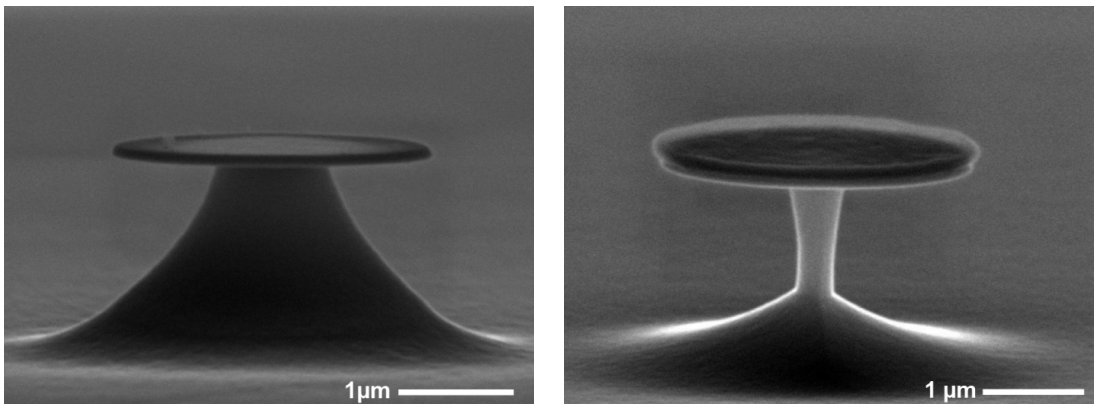

(a) (b)

Figure 3.15: SEM side-view pictures of suspendend microdisks showing the two different methods employed to solve the photoresist crosslink issue: (a) RIE; (b) AZ100 bath.

3.6 Mesa fabrication

During the experiments, we need to be free to approach the tapered fiber as much as possible to our microdisks. Since such fiber has a diameter of only 1 µm, it is likely that it get electrostatically stuck onto the sample substrate (in this case the measurements must be restarted and the fiber gets damaged). To reduce this risk, we slightly modify the design of the sample. By centering each disks line on a 100 µm large mesa, we minimize the possible contact areas between the fiber and the substrate.

3.6.1 Photoresist spin-coating and optical lithography

To prepare the sample for this further step, we heat it on a hotplate at 120°C for 4 minutes to dehydrate the substrate before spin-coating the resist. Then, as in the case of e-beam lithography, we proceed to the resist deposit immediately after cooling down the sample, to avoid surface re-hydration and all the further issues. Again, the photoresist spin-coating procedure consists of the two HMDS-photoresist coating steps.
For the HMDS, we use the following parameters:

- speed: 4000 rpm;
- time: 30 s.

After 60 s we apply the TI 35ES resist from MicroChemicals GmbH. The spin-coating is carried out with the following parameters:

- speed: 4000 rpm;

– time: 30 s.

The resulting thickness being 3.5 μm, it is possible to completely cover the disks (and protect them during the mesa etching) by spinning the resist twice.

After coating, we softbake the sample at 100°C for 3 minutes and then we replicate the photoresist coating and softbake steps, to attain the right resist layer thickness.

Now we can process the sample with the photolitography. First of all, it is crucial to check the cleanliness of the mask to avoid a transfer of residual resist or dust to the sample surface. Then, we place the optical mask inside the lithography machine and we proceed with the parameters settings. A soft contact between the mask and the sample is adequate for our purpose; this procedure does not apply too much force on the sample and, therefore, does not damage the microdisks. This method suites well for large patterns [2], but it might be inaccurate for smaller ones, since the contact could be imperfect in some regions, resulting in pattern transfer imprecisions. In order to draw the pattern on the desired spot, the mask has to be carefully aligned onto the surface. Once all these preliminary steps are set, we just need to select the exposure time and wait for this time lapse, which in our case is 40 s. After that, we develop the photoresist for 50 s and we rinse with DI water. A real-time check of the development is possible by using the optical microscope provided with an UV filter.

From the pre-heating to the end of the development, the sample cannot leave the lithography room, where UV-filters are used to protect the undeveloped resist from accidental light exposure.

3.6.2 Mesa wet etching

Once the mesas are defined by optical lithography and photoresist development, we proceed with the wet etching. Since we want to remove all the GaAs that is not protected by the resist, we do not need a specific etchant solution, but just a non-selective one. Thus we opt for the BCK again, which turns out to be adapted for our intents.

We etch the sample at room temperature for 5 minutes while agitating it inside the beaker. In this way, we create mesas about 20 μm deep, which is enough to use the tapered fiber without problems. We rinse the sample in three different beakers containing DI water and we blow-dry the sample with the N_2 gun. At the end of the process, the mesas are ∼80 μm wide, having been reduced by the etchant solution, and look as in Figure 3.16.

2. The dimensions of the mesa pattern on the optical mask are 100 μm × 1 cm.

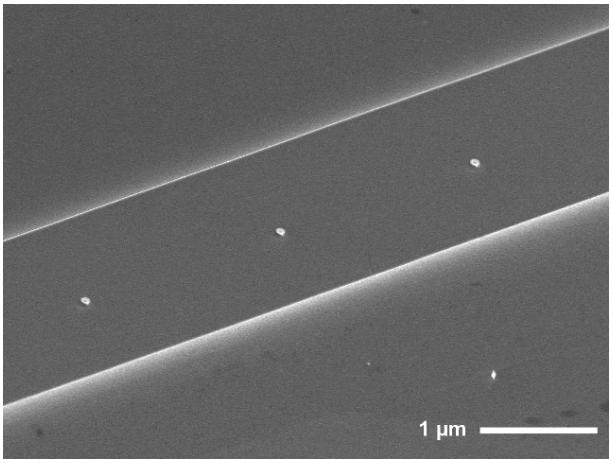

Figure 3.16: SEM picture of a processed sample, showing a line of disks on a mesa.

3.7 Cleaving and cleaning

At the end of fabrication, we cleave as many small bars as disk lines. It is important to remove the resist only after this step, not to contaminate the sample with cleavage dust. Two small notches per line are made onto the sample with a diamond scribe, in correspondence to the bottom markers drawn with the e-beam. The sample is then overturned into a round bottomed box to avoid any contact with the surface (even though covered by resist) and with sharp tweezers we press on the notches. This a thorny and crucial step of the fabrication process: a bad cleavage can waste the whole work.

Now it is possible to remove the resist and reveal the cavities on their mesas. To this end, we proceed with a stir of the cleaved bars in an acetone bath for 3 minutes. Finally, to remove acetone traces we agitate the sample for 60 s in an IPA bath and then let the sample air-dry.

3.8 Summary

In this chapter we detailed the specific technological protocol developed by us to fabricate suspended AlGaAs microdisks. We devoted all our efforts to search for efficient fabrication methods, with the aim of obtaining good quality microcavities. The technological development required an optimization time of almost one year, resulting in resonators suitable for nonlinear process demonstrations.

Chapter 4

Second-Harmonic Generation

4.1 Introduction

In this chapter we shall discuss the nonlinear optics results obtained by probing the AlGaAs WGM suspended microresonators, conceived and fabricated during this doctoral work. In the first part, we shall describe the fabrication of a tapered fiber. Then, we shall present the experimental steps that have led us to the first demonstration of SHG in such microcavities in the telecom range, illustrating the linear and the nonlinear measurements. At the end of the chapter, we shall give an overview of the perspectives that these results have opened.

4.2 Single-mode tapered fibers

As previously mentioned, the coupling scheme consists in approaching a fiber to our microcavities. For the evanescent coupling to occur, we thin the fiber (we *taper* it), passing from a diameter of $\sim$125 µm to $\sim$1 µm, which is essential to let the fiber and the disk share small amounts of power without affecting the mode profiles. This technique is very efficient and well-known by the scientific community since the early '90s, and it is exploited for a wide set of experiments (optics [97], sensing [98], optomechanics [7],...). For all these applications, a low-loss tapered fiber is necessary, so as to make an efficient power transfer at the injection, and to efficiently collect the signal at the output. The requirements for a good tapered fiber are:

- temperature stability;
- clean and dry environment;
- geometric symmetry;
- taper adiabaticity;
- low surface roughness.

The most common procedure to taper a fiber is to melt it by means of a torch [65]. However this method presents some drawbacks, such as possibility of gas impurities or flame instability, resulting in non-uniform temperature and fiber diameter. To get rid of these issues, a different way to obtain better results has been improved and partially developed in the DON group [99], employing a thermoelectric ceramic micro-heater. This approach, which allows obtaining tapered fibers respecting the adiabaticity criteria [100], is described in the following section.

4.2.1 Fabrication of tapered fibers

To prepare our experiments we start from a step-index fiber commonly employed in telecommunications, the SMF-28e+®, which has a Ge-doped SiO_2 core ($w \sim 10$ µm, $n_{\text{core}} = 1.4681$) and a pure SiO_2 cladding ($w \sim 125$ µm, $n_{\text{cladd}} = 1.4675$).

The setup for the fiber pulling is shown in Figure 4.1. The first step of this technique is the micro-oven heating up to 1200°C: the melting point of SiO_2 is around 1600°C, but a temperature of ∼1200°C is sufficient to slowly stretch the fiber without breaking it. Once the micro-heater temperature has stabilized, we reveal the cladding by removing the protective jacket from the portion of fiber we want to stretch (∼3 cm), and we clean it with acetone. Starting from this moment, the uncovered part tends to deteriorate because of the water naturally present in the atmosphere. For a humidity level higher than 40% (monitored with a hygrometer), it is very difficult to end up with a good taper (i. e. transmission grater than 80%). The fiber is fixed on two linear translation stages (Newport UTS 100CC) by two magnetic clamps close to the stripped area, to minimize the vibrations that could make it stick onto the inner walls of the micro-heater, causing its break. Therefore, we put the stripped part inside the oven [1] and we wait for 2 minutes. After this lapse of time, it has become sufficiently soft to be stretched without damages, thus the pulling can be started. It is crucial to constantly check the fiber condition while stretching: this is done by injecting light in it and by monitoring in real time the transmitted power (Fig. 4.2). The fiber is elongated for about 40 mm (20 mm per stage) at the constant speed of 0.04 mm/s, via an electronic controller: during this step, cladding and core merge, resulting in a local multimodal behavior. This is explicated by the presence of large oscillations in the transmission spectrum (Fig. 4.2 - zone 2), representing the interference among the modes. Once these fluctuations are over, the fiber has reached a diameter of about 1 µm and gets back to single-mode:

Tapering procedure

1. The micro-heater is 3 cm wide and 2 cm deep, and the actual cavity where the fiber is placed for the pulling is 3 cm wide and 1 mm deep (see Figure 4.1b).

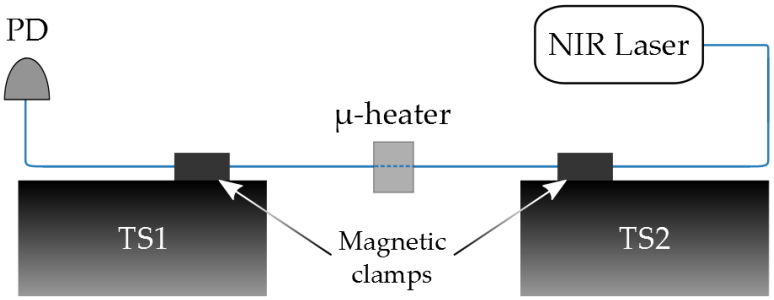

(a)

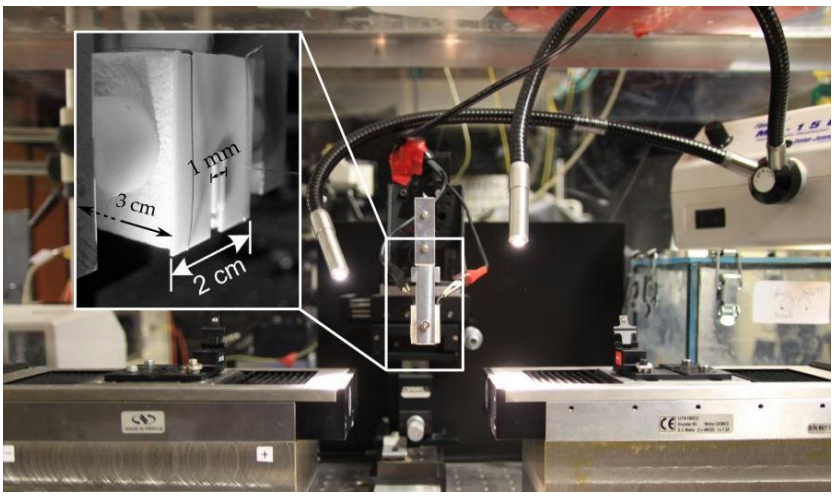

(b)

Figure 4.1: Experimental setup used for the fiber pulling. (a) Schematic of the setup. PD, photodetector; TS, translation stage; (b) Picture of the experimental setup; Inset: close up of the thermoelectric micro-heater.

the pulling can be stopped (Fig. 4.2 - zone 3). At this point, after removing the micro-oven, we wait for about 10 minutes, so that the fiber can solidify and cool down (this step is very delicate: air flows can be fatal as well as small dust particles). After that, it is possible to finely control the fiber tension (neither too strong nor too weak [2]) by means of the electronic controller. The taper is then glued on a holder with an epoxy (Araldite), and after 10 additional minutes it is possible to move it into the protective box of the experimental setup (see Fig. 4.4). However, the epoxy has a curing time of about 60 minutes; only after that, it will be possible to start the experiments.

For a fiber diameter $w = 1$ μm, the reproducibility is relatively high, as shown in Figure 4.3; the success rate is, however, about 50%. Note that fibers

2. If a too strong tension is applied, the fiber will break; on the contrary, if the tension is too feeble, the fiber will be subject to electrostatic charges.

with transmission lower than 80% are discarded to avoid compromising the quality of our measurements.

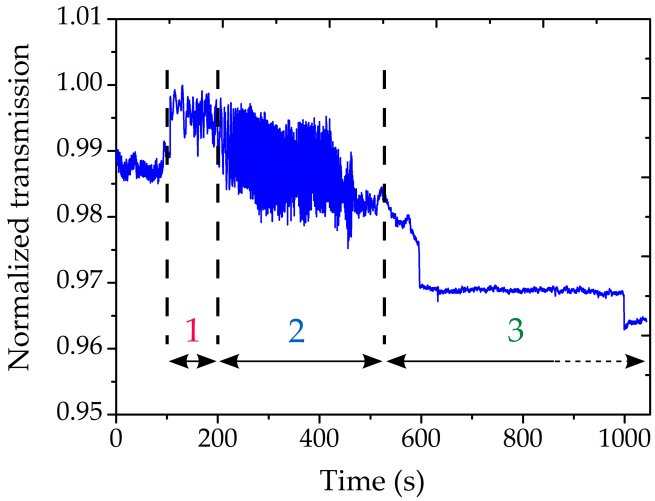

Figure 4.2: Typical transmission spectrum for a fiber pulling experiment, showing the most relevant moments of the fiber tapering: zone 1, 120 second fiber heating; zone 2, pulling; zone 3, end of the pulling and cooling down.

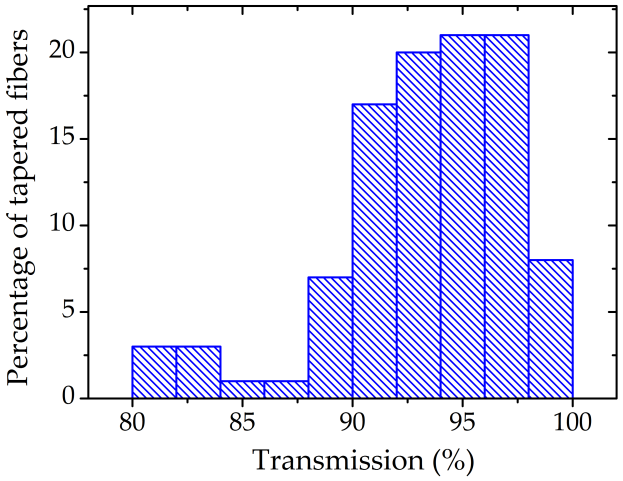

Figure 4.3: Statistic histogram of percentage of fiber tapers with transmission grater than 80% out of 102 samples.

Fiber choice

Since the development of the tapered fiber technique, the researchers of the DON group have employed the SMF-28e+®, adapted for wavelengths in

the telecom range. In our case red visible light has to be used too [3], but below 1260 nm this kind of fiber is multi-mode, which should be avoided in order to maximize the coupling to our microdisks. Unfortunately, the fibers allowing single-mode guidance around 800 nm [4] are not suitable for operating at higher wavelengths.

SM800 fiber

To evaluate the benefits associated to a different fiber, we tested the taper fabrication on the SM800, which is suited for wavelengths around 800 nm. Since the very first step, we noticed that the protocol developed in [99] is not adapted for this fiber. Now a softening time of two minutes is too long: the fiber breaks immediately after the start of the elongation. Also the usual stage speed is too high: the SM800 needs to be pulled less than the SMF-28e+®. These differences makes the completion of the tapering process impossible. Finally, the good protocol is determined by trial and error; we end up with an intact taper by softening it for 95 seconds and with a fiber elongation of 17.8 mm at a speed of 0.03 mm/s. However, at the end of the whole tapering process, the final power transmission is not comparable with the one obtained for the SMF-28e+®. In fact, in the best cases, the tapered SM800 transmits nearly 50% of the injected power. The main differences between the SMF-28e+® and the SM800, and between their fabrication protocols are summarized in Table 4.1. Due to high losses and fabrication difficulties, we decided to keep using the SMF-28e+® for our experiments, with light in both the near-IR (NIR) and the visible (VIS) range.

4.3 Measurements and results

Characteristics and performances of our samples are evaluated via linear and nonlinear measurements. A linear characterization of the microcavities is necessary to investigate the optical properties of the disks; moreover, it enables to compare our simulations with the experimental results, so as to verify the reliability of the modeling in view of the nonlinear measurement. We aim at finding a SH signal coming from our microresonators and studying the characteristics of this light, to validate its nonlinear origin.

The rest of this chapter is dedicated to the description of the measurements performed during several months of this doctoral work, and I have decided to include also the articles that I have co-authored on this subject.

General experimental setup

Both linear and nonlinear characterizations of our samples are performed on an optical table, equipped according to the requirements. Note that the optical bench has been assembled during this doctoral work to enable part of the measurements of the EU FET project TREASURE.

3. See section 4.3.1.
4. The mode radius is ∼5.6 µm @ 830 nm and ∼10.5 µm @ 1550 nm

Fiber characteristics	
SMF-28e+®	SM800
pure SiO_2 cladding	pure SiO_2 cladding
Ge-doped SiO_2 core	Ge-doped SiO_2 core
$2R_{\mathrm{clad}} = 125$ µm	$2R_{\mathrm{clad}} = 125$ µm
$2R_{\mathrm{core}} = 10.5$ µm	$2R_{\mathrm{core}} = 5.6$ µm
$\lambda_{\mathrm{sm}} = 1260 - 1650$ nm	$\lambda_{\mathrm{sm}} = 660 - 800$ nm
Taper fabrication protocols	
SMF-28e+®	SM800
$t_{\mathrm{soft}} = 120$ s	$t_{\mathrm{soft}} = 95$ s
$v_{\mathrm{stage}} = 0.04$ mm/s	$v_{\mathrm{stage}} = 0.03$ mm/s
$l = 40$ mm	$l = 35.6$ mm
Best final power transmission	
SMF-28e+®	SM800
99%	50%

Table 4.1: Analogies between the SMF-28e+® and the SM800, in terms of characteristics, fabrication protocols and final performances. R_{clad}, cladding radius; R_{core}, core radius; λ_{sm}, single-mode wavelength range; t_{soft}, fiber softening time; v_{stage}, stage speed; l, fiber elongation.

The core of the setup is a Plexiglas® box containing the sample and the tapered fiber. Both of them are extremely delicate and sensitive to the environment: air flow, humidity and dust deteriorate them quite quickly. Inside the box, two micro-positioned holders enable to separately adjust the position of both sample and fiber. The former is fixed on an invar [5] holder and has three degrees of freedom (vertical, lateral and axial tilt). The latter is mounted on a support allowing further adjustments of the fiber tension. Also in this case a stage provides a full 3D translation of the system. Moreover, since the optimal coupling of light to our microresonators is a crucial task, the relative position between the probed microcavity and the fiber taper is controlled by means of piezoelectric actuators; they allow a finer control than the micrometric screws, which are mostly used to test a wide set of distances. To facilitate the placement of the fiber with respect to the disk, we use a microscope objective (×50, N. A. =

5. It is a nickel-iron alloy notable for its low coefficient of thermal expansion α. $\alpha_{\mathrm{invar}} = 1.2$ ppm/°C, 11 ppm/°C $< \alpha_{\mathrm{steel}} <$ 15 ppm/°C.

0.5). White light is shined on them and a beam splitter sends half of the radiation to a CCD camera connected to a computer; in this way, it is possible to image on a PC screen the small part of the sample we are interested in, together with the fiber taper nearby. The choice of lasers and detectors depends on the wavelength range that is dealt with in our experiment (either NIR or VIS). Finally a Peltier module allows to control and tune the temperature of the sample, over a span of about 30°C.

In the following, we shall describe the experimental procedures carried out on our samples, discussing the obtained results.

4.3.1 Linear measurements

The first linear measurements have been carried out on samples fabricated starting from the growth CAT104 [6] (Fig. 3.1c). At the beginning, the idea of grading the AlGaAs layer thickness h was dictated by the possibility of exploiting it as an additional free parameter to fulfill the phase-matching condition. In principle, this should help in compensating the tolerances of the MBE growth. However, thickness gradings come together with Al concentration variations. The difficulty of precisely knowing h and x in each point of the wafer has made the fabrication of a nominal-radius cavity quite complex. Therefore, for the second generation of samples, we have opted for the growth D8T157 [7] (Fig. 3.1d). This time, by fixing the two parameters (h and x), finding the right diameter for our resonators has been much easier.

Experimental setup

The experimental setup employed for the linear measurements is shown in Figure 4.4. To investigate the spectral properties of our cavities, we need to search for their resonant modes; by comparing their wavelengths with the ones provided by our simulations (see chapter 2), it is possible to understand if the NIR and VIS modes are phase-matched and, therefore, if they will give rise to a SHG process. To this end, we acquire two separate transmission spectra by injecting the beam emitted by either of two CW, external-cavity, single-mode, tunable laser diodes into the tapered fiber. The former operates between 1490 nm and 1640 nm, with a maximal power of ∼10 mW (Tunics-Plus from Yenista Optics); the latter between 755 nm and 785 nm, with a maximal power of 50 mW (TLK-L780M from Thorlabs). The NIR light is directly injected into the fiber, while for the VIS laser the working beam is obtained after focusing it onto a coupler. To collect the radiation, we use a fast InGaAs detector [8] in both cases.

6. CAT104 composition: GaAs substrate / 5 μm GaAs / 138.6 ÷ 172.2 nm $Al_xGa_{1-x}As$, with $0.39 < x < 0.48$.

7. D8T157 composition: GaAs substrate / 5 μm GaAs / 155 nm $Al_{0.4}Ga_{0.6}As$.

8. Spectral sensitivity: 700 nm $< \lambda <$ 1800 nm; responsivity @ 780 nm: 0.2 A/W, responsivity @ 1550 nm: 1.2 A/W.

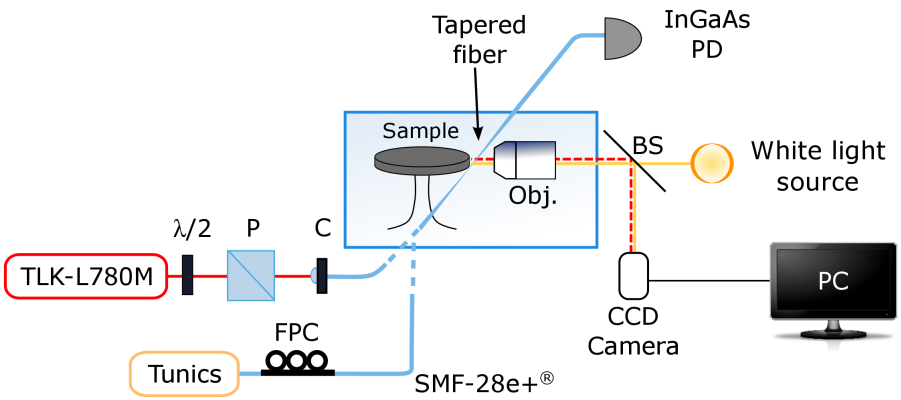

Figure 4.4: Schematic of the experimental setup used for the linear characterization of our samples. $\lambda/2$, half-wave plate; P, polarizer; C, collimator; Obj., microscope objective; BS, beam splitter; FPC, fiber polarization controller; PD, photodiode.

For both NIR and VIS ranges, the first step is to perform a quick scan over the entire wavelength span by exploiting the evanescent coupling technique, to check for the presence of possible resonances. In all spectra and for each scan, the transmission of the fiber coupled to the microdisk is normalized to the transmission of the fiber far from it. Once the resonant WGMs are singled out, we carry out a finer acquisition in proximity of the resonance wavelengths. In this way, the latter are precisely determined and we can also obtain the values of the loaded quality factors; it is worth noting that in this way we can infer the quality of the fabricated structures after a careful spectroscopy of the different cavities. Thanks to these measurements, we were able to verify that the experimental position of the resonances matches very well the results of our modeling.

As already stressed in chapter 2, due to the thin layer of the AlGaAs layer, our cavities support only TE-polarized modes in the telecom band; conversely, both TM- and TE- polarized modes exist in the VIS range. In the first case, a fiber polarization controller is useful to maximize the TE-polarized radiation injected into the fiber, while in the visible range, a half-wave plate and a polarizer are required to select the TM-polarized light.

Linear measurements on CAT104

As far as the first generation of samples is concerned, the best results are obtained for a microdisk with radius $R = 1.85$ µm and Al molar fraction $x \approx 0.47$ [9]; we observe two adjacent TE-polarized modes in the NIR (Fig. 4.5a) and

9. The radius is measured starting from a SEM picture, while the Al molar fraction is estimated from the wafer X-ray analysis.

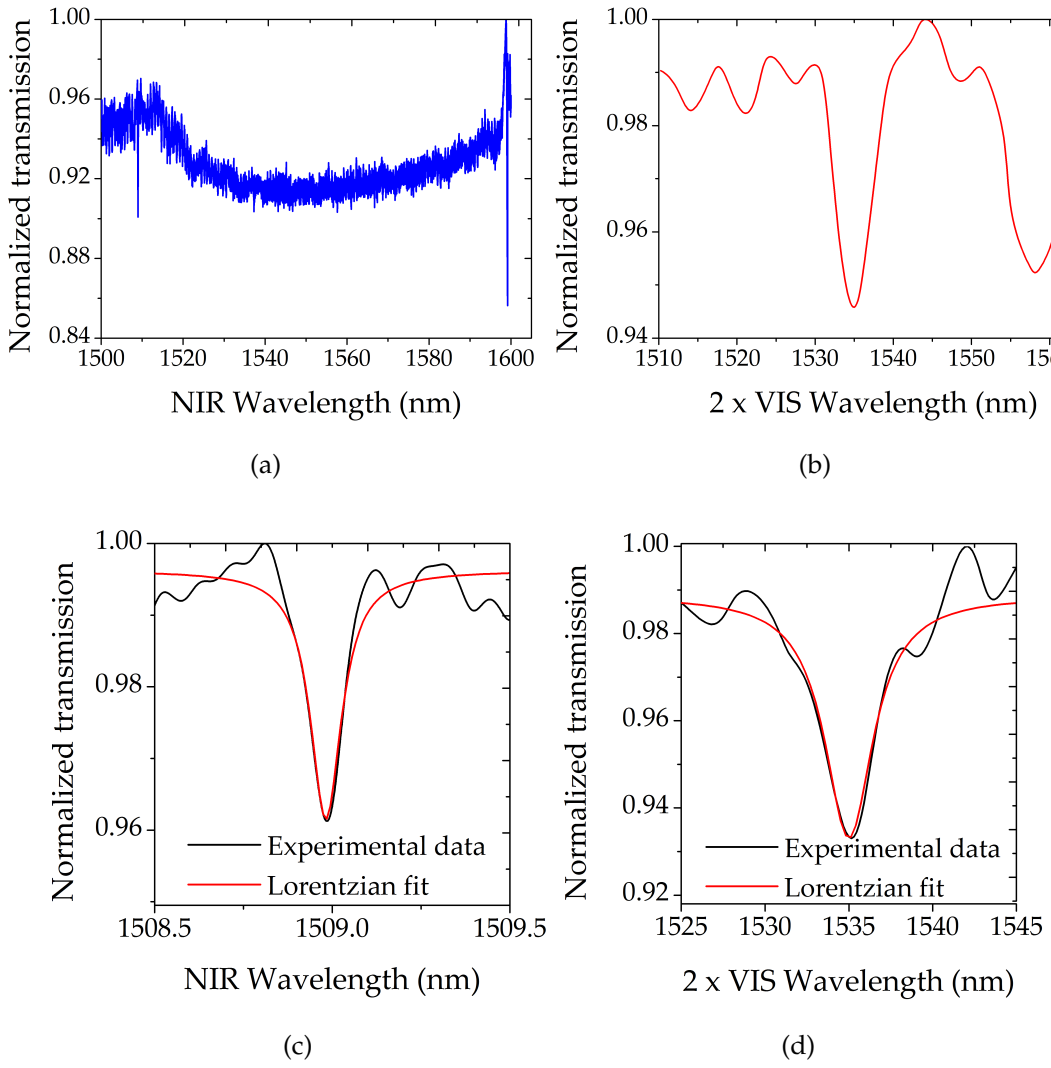

Figure 4.5: Experimental results of the linear measurements on a cavity of radius $R = 1.85$ µm: transmission spectra for λ_{FF}^{res} (a) and $2\lambda_{SH}^{res}$ (b) and details of the resonant WGMs relevant for the SHG process for λ_{FF}^{res} (c) and $2\lambda_{SH}^{res}$ (d).

two adjacent TM-polarized modes in the VIS (Fig. 4.5b). Figure 4.5c details the resonance at $\lambda_{FF}^{res} = 1508.9$ nm, corresponding to the WGM with (p_{FF}, m_{FF}) = (1, 12) and having a loaded quality factor $Q_{FF} = 1.40 \times 10^4$. By repeating the same measurements for different fiber-to-disk distances [101], we estimate its intrinsic quality factor, obtaining $Q_{FF}^{intr} = 1.43 \times 10^4$. We also show the resonant mode at $\lambda_{SH}^{res} = 767.6$ nm (1535.2/2 nm) (Fig. 4.5d), which corresponds to the WGM with (p_{SH}, m_{SH}) = (2, 26), with a loaded quality factor $Q_{SH} = 4.90 \times 10^2$. In this case, the estimated intrinsic quality factor is $Q_{SH}^{intr} = 4.96 \times 10^2$. From these values, we can deduce that the cavity is under-coupled in both NIR and VIS

ranges [10]. Note that, while for the NIR WGM resonances the best Q values are obtained with the fiber far from the disk, for the VIS measurements it is possible to excite the resonant modes only if in contact or very close to the cavities. The discrepancy between λ_{FF}^{res} and $2\lambda_{SH}^{res}$ is due to a non-optimal disk radius. This issue stems from a limitation caused by the wet-etching procedure employed for the fabrication of our cavities; indeed, making disks with radial variations < 20 nm is a very tough task and the cavity radius is a critical parameter to fulfill the energy conservation condition.

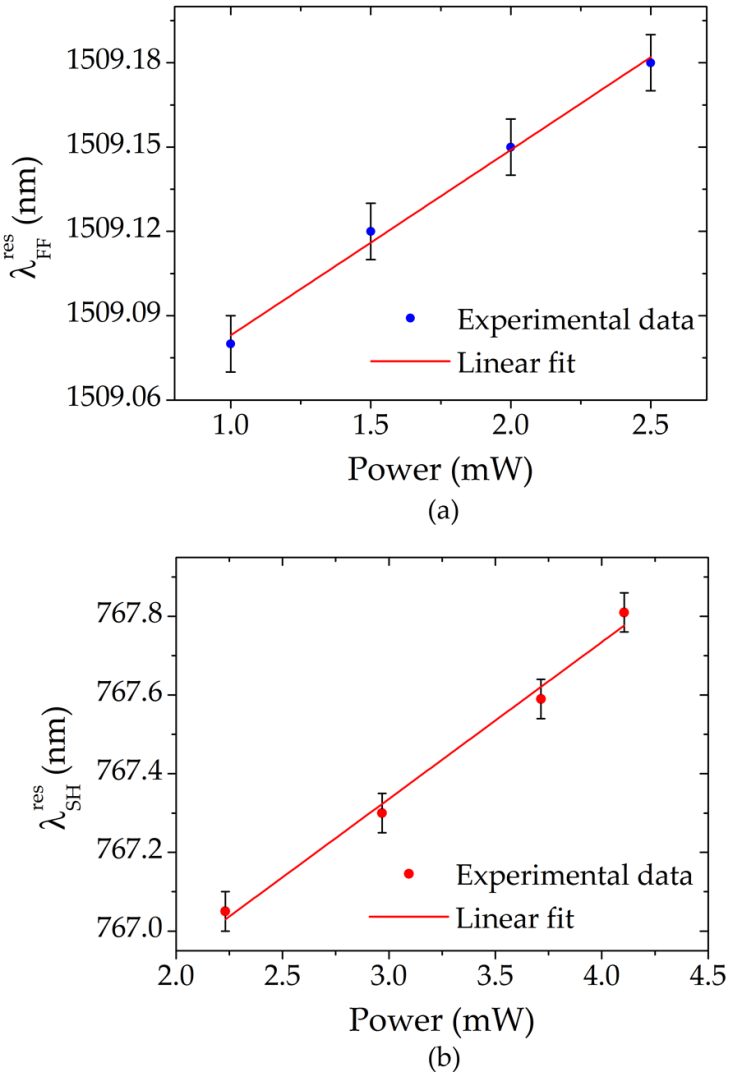

Figure 4.6: Displacement of the resonance wavelength as a function of the external power for λ_{FF}^{res} (a) and λ_{SH}^{res} (b). The linear fits provide the sensitivities of the cavity temperature with respect to the input power.

10. A complete discussion on the quality factors can be found in Appendix A.

During each set of measurements, we observe a displacement and a distortion of the WGM transmission dips following a change of the power in the fiber [102]. To better understand these effects, we monitor the position of the resonance wavelengths while increasing the amount of radiation coupled to the probed resonator. The first effect (wavelength displacement) is shown in Figure 4.6 for both $\lambda_{\mathrm{FF}}^{\mathrm{res}}$ and $\lambda_{\mathrm{SH}}^{\mathrm{res}}$: both wavelengths linearly depend on the power ($\mathrm{d}\lambda_{\mathrm{FF}}^{\mathrm{res}}/\mathrm{d}P_{\mathrm{FF}} = 0.07$ nm/mW, $\mathrm{d}\lambda_{\mathrm{SH}}^{\mathrm{res}}/\mathrm{d}P_{\mathrm{SH}} = 0.41$ nm/mW).

From the data extracted from Figure 4.6 we can also deduce the sensitivities of the cavity temperature with respect to the input power [11]: in the NIR we obtain $\mathrm{d}T/\mathrm{d}P_{\mathrm{FF}} = 0.9$ K/mW, while in the VIS $\mathrm{d}T/\mathrm{d}P_{\mathrm{SH}} = 9.4$ K/mW. More details can be found in Appendix A.

Our first attempt of explanation was based on third-order optical effects, such as the Kerr effect or the TPA. However, according to our calculations, this behavior cannot be ascribed to any of them. In fact, in first place, the Kerr effect would induce a wavelength shift in the NIR of $\mathrm{d}\lambda_{\mathrm{FF}}^{\mathrm{res}}/\mathrm{d}P_{\mathrm{FF}} \sim 0.002$ nm/mW, considerably smaller than what is experimentally observed. Moreover, in the VIS it would even give rise to a negative wavelength shift, not observed during the experiments.

In addition, TPA it is absent in the NIR, while it gives rise to losses of about 25 cm^{-1}/W in the VIS. However, due to the low power circulating in the disk, this has no measurable effect on the VIS field.

Another tentative interpretation of this displacement could be the formation of surface oxides on the disk sidewalls, which might cause surface absorption and deteriorate the intrinsic quality factors, especially in the VIS.

Thermo-optic effect

However, the most suitable explanation for this phenomenon is the thermo-optic effect [103]: the refractive index of bulk AlGaAs is temperature-dependent, so that the effective index n_{eff} of a WGM also displays such dependence, which can be expressed as:

$$\frac{\mathrm{d}n_{\mathrm{eff}}}{\mathrm{d}T} = \frac{n_{\mathrm{eff}}}{n}\frac{\mathrm{d}n}{\mathrm{d}T}\,, \tag{4.1}$$

where n is the refractive index of bulk AlGaAs and $\mathrm{d}n/\mathrm{d}T$ its thermo-optic coefficient [12]. Due to this temperature dependence, we observe a red shift of the resonance wavelength when we repeat a scan at high power around the WGM resonance. Such shift is caused by the important amount of power circulating inside the cavity, which gives rise to an increase of the temperature inside the

11. The sensitivities $\mathrm{d}T/\mathrm{d}P$ for both wavelengths are estimated as:

$$\mathrm{d}T/\mathrm{d}P_i = \mathrm{d}\lambda_i^{\mathrm{res}}/\mathrm{d}P_i \cdot \mathrm{d}T/\mathrm{d}\lambda_i^{\mathrm{res}}\,,$$

with $\mathrm{d}\lambda_i^{\mathrm{res}}/\mathrm{d}T$ simulated in chapter 2, and $\mathrm{d}\lambda_i^{\mathrm{res}}/\mathrm{d}P_i$ obtained from the experiments ($i =$ FF or SH).

12. The AlGaAs thermo-optic coefficient is $\sim$2.3 $\times$ 10^{-4} K^{-1} at room temperature [105].

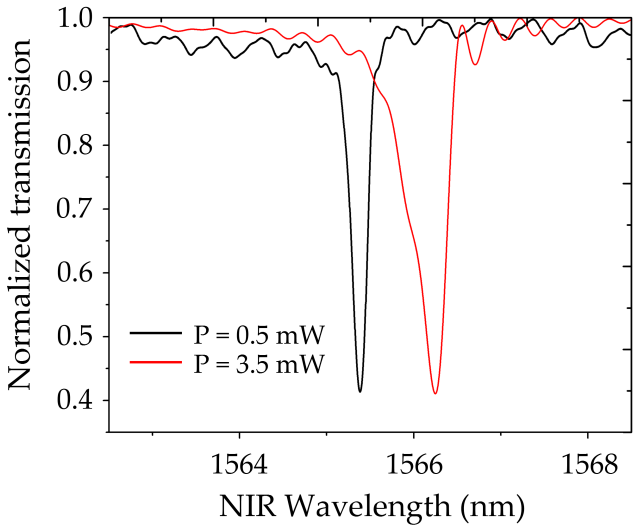

Figure 4.7: Experimental plot showing the difference between a standard lorentzian WGM resonance dip (black line, low power) and a triangular optical resonance profile (red line, high power). The distortion and the wavelength shift of the dip is caused by the thermo-optic effect.

microdisk. This is shown in Figure 4.7, in which the triangular optical resonance profile (red line, high power) instead of the traditional lorentzian dip (black line, low power), can be ascribed to optical bistability [104].

The resonance wavelength shift $\delta\lambda$ is due to a change in the effective refractive index Δn_{eff}:

$$\delta\lambda = \frac{2\pi R}{m}\Delta n_{\text{eff}}\,, \tag{4.2}$$

where m is the azimuthal number of the considered WGM.

We recall that the above measurements were carried out on the growth CAT104. While they proved crucial for a general insight of our work, the mismatch between $\lambda_{\text{FF}}^{\text{res}}$ and $2\lambda_{\text{SH}}^{\text{res}}$ turned out to be too important to even try the SHG experiment.

Linear measurements on D8T157

Further experiments were then carried out on the growth D8T157 (Fig. 3.1d). The procedure is the same as the one described for the growth CAT104. Also for this measurement, the position of the resonant WGMs is in very good agreement with the results of our simulations. However, for some of the disks, the resonance that satisfies the phase-matching condition in the visible range lies outside of the wavelength range spanned by our laser ($\lambda_{\text{SH}}^{\text{res}} > 785$ nm), and the exact resonance position is not found via direct transmission measurements. To circumvent this problem, we search for all the WGMs in the above laser range and we label them by comparing the experimental results to our modeling; finally, we use the cavity free spectral range (always crosschecked with our

theoretical expectations) to establish the position of the resonant mode beyond 785 nm in which we are interested (Fig. 4.8). For a microcavity with radius $R =$

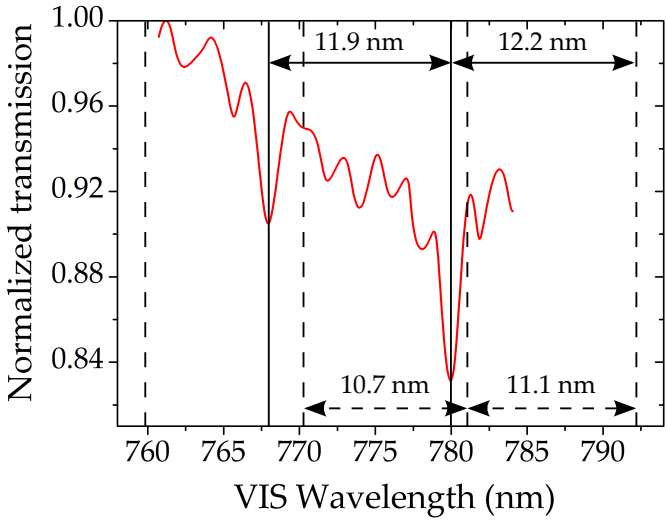

Figure 4.8: Typical transmission spectrum in the VIS. The solid (dashed) vertical lines correspond to the experimental (calculated) FSR. From the comparison between the values obtained in the two ways, we estimate the position of the resonant mode beyond 785 nm in which we are interested.

1.9 µm, the linear measurements allow to separately observe the resonances of the only two WGMs fulfilling the phase-matching condition: TE at $\lambda_{\mathrm{FF}}^{\mathrm{res}} = 1584.3$ nm $(p_{\mathrm{FF}}, m_{\mathrm{FF}}) = (1, 12)$ and TM at $\lambda_{\mathrm{SH}}^{\mathrm{res}} = 793.5$ nm $(p_{\mathrm{SH}}, m_{\mathrm{SH}}) = (2, 26)$. Their loaded quality factors, for measurements with the fiber in contact with the disk, are $Q_{\mathrm{FF}} = 1.5 \times 10^3$ and $Q_{\mathrm{SH}} = 3.2 \times 10^2$. By repeating the same measurements for different fiber-to-disk distances, we also estimate the intrinsic quality factors $Q_{\mathrm{FF}}^{\mathrm{intr}} = 5.3 \times 10^3$ and $Q_{\mathrm{SH}}^{\mathrm{intr}} = 5 \times 10^2$. From these values of Q we infer that the cavity is over-coupled in the NIR and under-coupled in the VIS. Again, the lower quality factors obtained in the visible range stem in part from fabrication issues. From our best disks, we obtain Q^{intr} of a few tens of 10^4, but they show too important a detuning $\Delta\lambda = |\lambda_{\mathrm{FF}}^{\mathrm{res}} - 2\lambda_{\mathrm{SH}}^{\mathrm{res}}|$, which is not really promising in terms of nonlinear conversion efficiencies. For our sample this discrepancy, which can be reduced by choosing the right cavity radius, is minimized for a microresonator of radius $R = 1.9$ µm ($\Delta\lambda = 2.73$ nm). According to our modeling, in order to have zero $\Delta\lambda$ for a disk height $h = 155$ nm, the cavity should have a radius $R = 1.903$ µm. However, with the wet-etching process the minimal tolerance that we achieve to obtain for the cavity radii is around 20 nm, which constitutes our present limitation. In principle, another way to reduce $\Delta\lambda$ could be using a SH mode with a radial number having the same parity as p_{FF},

in order to improve the overlap between the FF and SH fields. Unfortunately, if we consider the WGM at λ_{FF}^{res} with (p_{FF}, m_{FF}) = (1, 12) for a cavity of radius $R =$ 1.9 µm, the only phase-matched resonance with an odd radial number occurs at $\lambda_{SH}^{res} = 752.1$ nm (p_{SH}, m_{SH}) = (3, 26), which corresponds to an even larger $\Delta\lambda$. Moreover, the related overlap integral turns out to be smaller [13]. Despite that, the actual mismatch between λ_{FF}^{res} and λ_{SH}^{res} is small enough to give rise to a SHG process, described in the following section.

To summarize, Figure 4.9 shows the observed coupling regimes for samples CAT104 and D8T157. The relevant figures of merit of our microdisks are listed

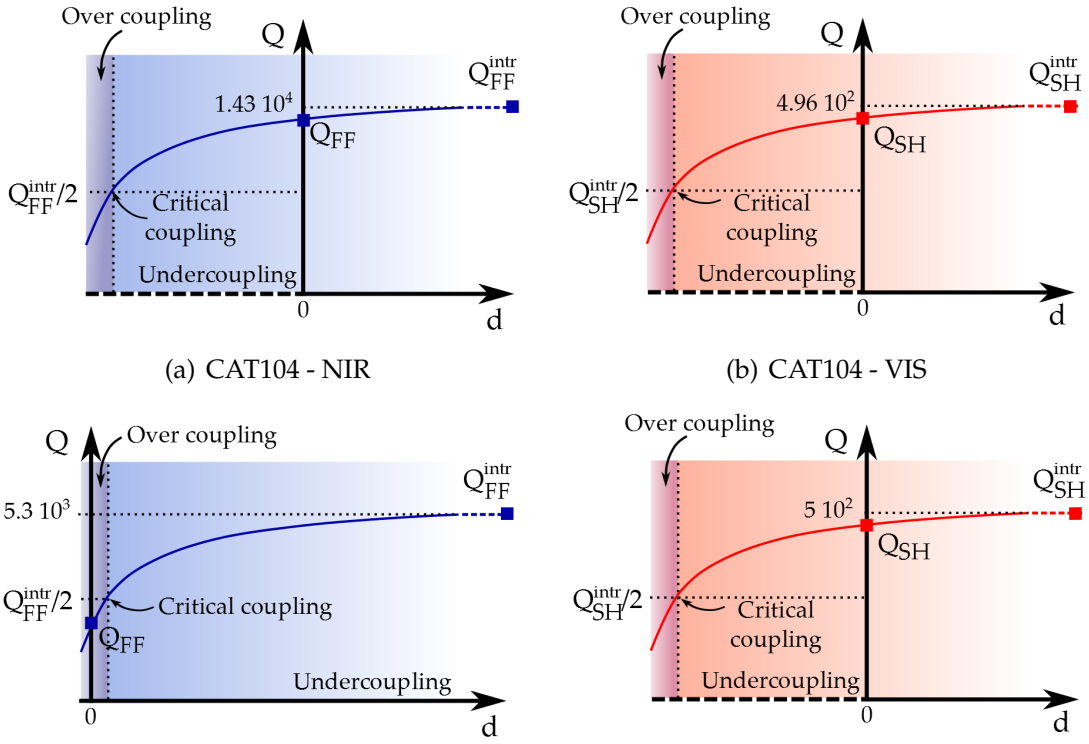

(a) CAT104 - NIR

(b) CAT104 - VIS

(c) D8T157 - NIR

(d) D8T157 - VIS

Figure 4.9: Observed coupling regimes for both NIR and VIS ranges. Solid lines are a guide for the eye and indicate the Q vs d expected behavior. $d < 0$ represents the region inside the disk, $d = 0$ the disk border and $d > 0$ the outside region.

in Table 4.2.

13. The calculated spatial overlap is 23.5% for the couple (p_{SH}, m_{SH}) = (3, 26); (p_{FF}, m_{FF}) = (1, 12)), versus 55.1% for the couple (p_{FF}, m_{FF}) = (1, 12); (p_{SH}, m_{SH}) = (2, 26).

	CAT104		D8T157	
	Employed sample	Sample with the best Q	Employed sample	Sample with the best Q
$Q_{\mathbf{FF}}^{\mathbf{intr}}$	1.43×10^4	3.6×10^4	5.3×10^3	4.1×10^4
$Q_{\mathbf{SH}}^{\mathbf{intr}}$	4.9×10^2	8.1×10^2	5.0×10^2	7.6×10^2
$\boldsymbol{\Delta\lambda}$	25.94 nm	N.A.	2.73 nm	14.6 nm

Table 4.2: Figures of merit of samples CAT104 and D8T157, stemming from the linear characterization. N. A. means that $\Delta\lambda$ was too large to be measured.

4.3.2 Nonlinear measurements

In the experimental setup employed for the nonlinear measurements, shown in Figure 4.10, we need to separately detect two signals: the pump throughput (NIR radiation) and the SHG. The former is focused onto the InGaAs detector, while it is filtered out via a band-pass filter for the SHG measurements. The latter is focused onto a silicon photodiode [14] and detected by a lock-in amplifier preceded by a low-noise transimpedance amplifier with variable gain. The signal modulation required by the lock-in detection is provided by the internal pump laser modulation at 7.2 kHz. To reduce the noise coming from the environmental light and to better detect a SH signal, a black screen is placed all around the detector. As already discussed in chapter 2, temperature can be used as an additional fine-tuning parameter to facilitate the achievement of the phase-matching condition; this is done with a temperature controller (Peltier + thermistor module).

Nonlinear measurement on D8T157

To search for the SH signal, we finely measure the fiber transmission spectrum around the NIR resonance wavelength $\lambda_{\mathrm{FF}}^{\mathrm{res}}$ singled out via the linear characterization. At this stage we use the band-pass filter to reflect the pump radiation thus selecting the SH signal with a wavelength between 700 and 1095 nm. Once the latter is detected, we adjust the fiber position to optimize it; as for the linear measurements, maximum coupling and stability are found when the fiber is in contact with the disk sidewall.

Figure 4.11 shows a typical SH intensity spectrum, obtained by scanning the NIR wavelength.

For the nonlinear results reported in this section, the injected power and the optimal temperature [15] are kept constant at $P_{\mathrm{FF}} = 3.5$ mW and $T = 15°\mathrm{C}$,

14. Spectral sensitivity: 350 nm $< \lambda <$ 1100 nm; responsivity @ 775 nm: 0.5 A/W.
15. The power is measured at the end of the fiber output when the tapered region is close to

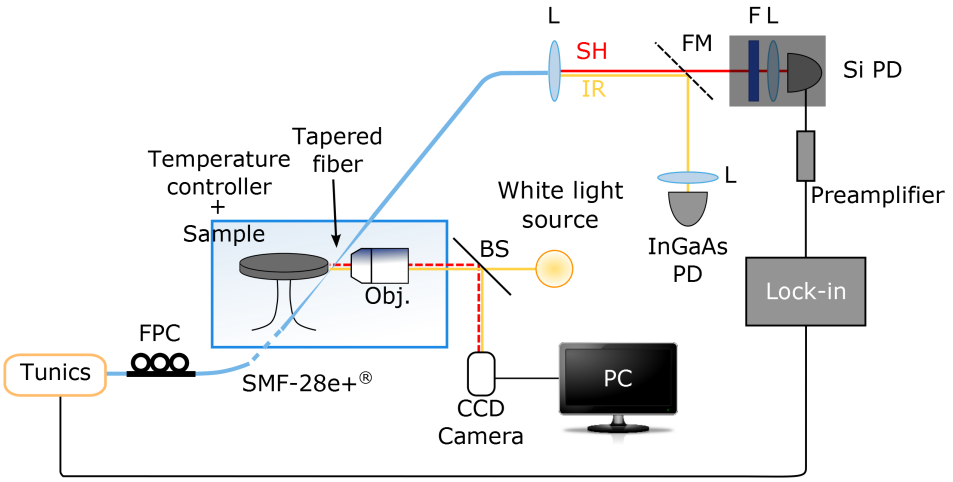

Figure 4.10: Schematic of the experimental setup used for the nonlinear characterization of our samples. $\lambda/2$, half-wave plate; P, polarizer; C, collimator; Obj., microscope objective; BS, beam splitter; FPC, fiber polarization controller; PD, photodiode; L, lens; FM, flip mirror; BPF, band-pass filter.

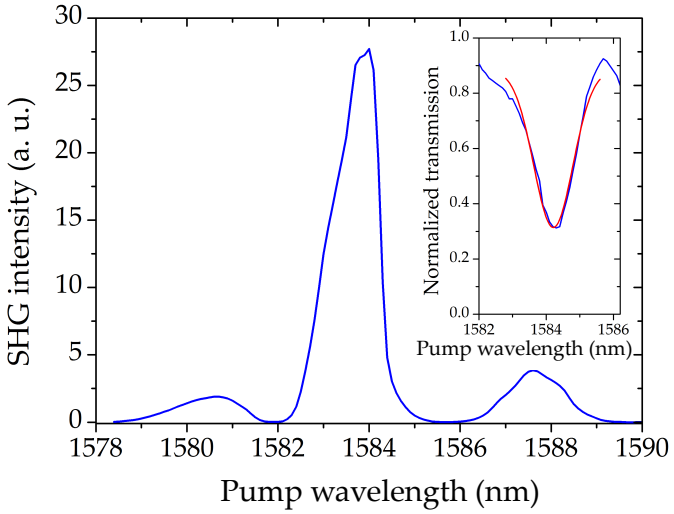

Figure 4.11: SHG spectrum vs. pump wavelength. Inset: observed resonance at $\lambda_{\mathrm{FF}}^{\mathrm{res}} = 1584.29$ nm (blue) and its lorentzian fit (red). The maximum SHG occurs at 1584 nm.

respectively [16]. To maximize the SH signal, the following requirements need to

the disk; the temperature is measured by the thermistor placed inside the holder, right below the sample.

16. $P_{\mathrm{FF}} = 3.5$ mW is the maximum input power delivered by the modulated laser without external amplification.

be fulfilled:

- both FF and SH modes must be resonant within the cavity;
- the two resonances must be perfectly aligned ($\Delta\lambda = |\lambda_{\mathrm{FF}}^{\mathrm{res}} - 2\lambda_{\mathrm{SH}}^{\mathrm{res}}| = 0$);
- critical coupling must be achieved for both FF and SH WGMs ($Q^{\mathrm{intr}} = Q^{\mathrm{cpl}}$).

However, if $\Delta\lambda \neq 0$ it is possible to optimize the SHG by over-coupling the cavity ($Q^{\mathrm{intr}} > Q^{\mathrm{cpl}}$): this produces a broadening of the resonance linewidth and, therefore, a better spectral overlap [28]. We verify this assumption experimentally: while the cavity is under-coupled for resonances in the VIS region, it is over-coupled at the FF wavelength. This results in an increased SH signal that has its maximum in correspondence of the FF wavelength, even if the coupling regime is not the same for both ranges; this is due to the fact that in the NIR the quality factors are higher than in the VIS.

During the data acquisition, we observe a slight blue shift of the resonances while approaching the fiber to the cavities. In fact, sticking the fiber onto the resonator is equivalent to creating a new fiber-disk system, whose modal effective indices are expected to increase. The entity of this effect depends on the tapered fiber width (which slightly changes for each fabricated fiber taper) and results in a NIR and VIS resonance wavelength shift of about 0.2%, close to our simulations predictions. Despite the advantages of the tapered fiber technique, which allows exploiting distance and width as parameters to tune the coupling, this effect constitutes a problem in terms of reproducibility. In order to make the results self-consistent, all the data must be taken during the same run of measurement, at constant fiber-to-disk distance and with the same fiber.

A further step required to fully characterize our samples is the analysis of the behavior of the SH external power as a function of the FF external power. Once the optimal coupling is found, we acquire the SHG intensity spectrum for different values of the injected P_{FF} (Fig. 4.12a). $P_{\mathrm{SH}}^{\mathrm{out}}$ can be expressed as a function of the voltage measured by the lock-in, in the following way:

$$P_{\mathrm{SH}}^{\mathrm{out}} = \frac{\pi}{\sqrt{2}} \frac{V_{\mathrm{lock-in}}}{G_{\mathrm{ampli}}\,\eta_{\mathrm{PD}}\,\eta_{\mathrm{filter}}\,\eta_{\mathrm{lens1}}\,\eta_{\mathrm{lens2}}\,T_{\mathrm{fiber}}}\,, \tag{4.3}$$

where $V_{\mathrm{lock-in}}$ is the voltage measured by the lock-in, $G_{\mathrm{ampli}} = 10^8$ V/A the gain of the transimpedance amplifier, $\eta_{\mathrm{PD}} = 0.5$ A/W the responsivity of the Si photodiode @ 775 nm, $\eta_{\mathrm{filter}} = 0.65$ is the band-pass filter transmission @ 780 nm, $\eta_{\mathrm{lens1}} = \eta_{\mathrm{lens2}} = 0.92$ is the transmission of the two bi-convex lenses used for focusing the SH signal onto the photodiode and T_{fiber} the fiber transmission, varying between 60% and 99%. Figure 4.12b shows a logarithmic plot of the quadratic dependence between P_{SH} and P_{FF}, for the three different peaks visible in Fig. 4.12a. The central peak represents the nonlinear signal corresponding to the resonant mode $p = 1$, $m = 12$. The slope of its linear part is 2.05 ± 0.07,

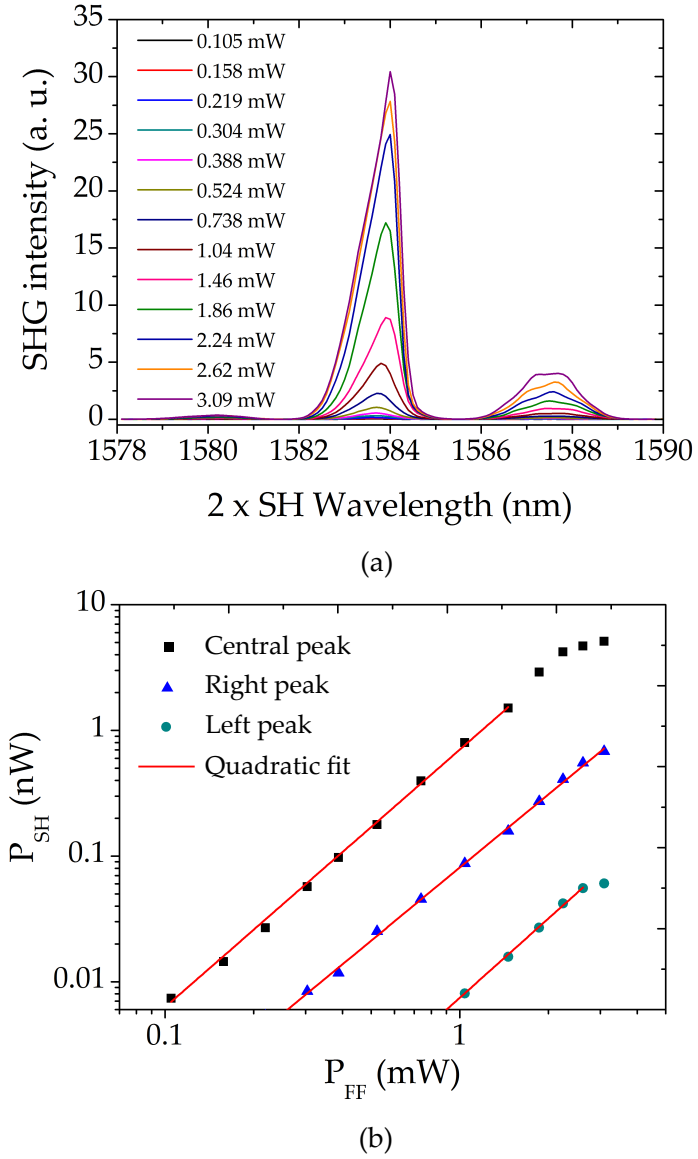

Figure 4.12: (a) SHG intensity vs. 2 × SH wavelength for different FF powers; (b) SH power vs. FF power for the three different peaks (log-log scale).

matching the theoretical quadratic dependence. Starting from this value, we extract the external conversion efficiency $\eta_{\mathrm{SHG}}^{\mathrm{exp}} = P_{\mathrm{SH}}^{\mathrm{out}}/(P_{\mathrm{FF}}^{\mathrm{in}})^2 = (7.04 \pm 0.07) \times 10^{-4}\ \mathrm{W}^{-1}$, $P_{\mathrm{SH}}^{\mathrm{out}}$ and $P_{\mathrm{FF}}^{\mathrm{in}}$ being powers inside the fiber.

To understand the origin of the secondary peaks, we perform the same study as for the primary peak. Again, we observe a quadratic dependence (left peak slope: 2.098 ± 0.068, right peak slope: 1.97 ± 0.08). Such behavior enables us to discard the hypothesis of nonlinear processes with order other than two. For instance, we investigated third-order nonlinear processes such as Brillouin scattering and FWM.

For the former, the distance between the central peak and the other two (about 4 nm) should be 600 GHz, which is at least 60 times higher than what expected as typical frequency shift in Brillouin scattering ($\nu_B = 1 - 10$ GHz [62]). Moreover, both $\chi^{(3)}$ phenomena would be too strong with respect to the frequency doubling. On this basis, we have performed further WGM simulations, looking for higher radial-order modes compatible with the observed scenario. At a result, we have found a couple of phase-matched and energy-conserving WGMs per secondary peak, and this seems to support our interpretation [17].

Coming back to the main peak, by looking at the high-power region of Figure 4.12b for $P_{\mathrm{FF}} > 2$ mW (in the fiber), we observe a roll-off. This effect can be ascribed to a heating of the cavity, due to the high amount of circulating power density. This generates a thermal shift of the FF and SH resonances [18], resulting in a lower spectral overlap as well as a lower $\eta_{\mathrm{SHG}}^{\mathrm{exp}}$. In principle, to reduce this effect we could either decrease the Peltier module temperature or detune the FF wavelength. However, the resulting SHG efficiency decreases in both cases. This stems from the fact that the results have been obtained in optimal experimental conditions for power, Peltier temperature, FF wavelength and fiber-to-disk coupling. Moreover, the data shown in Fig. 4.12 are obtained for $T = 15°\mathrm{C}$, which is very close to the lowest temperature for which our microdisks behave correctly, before that water vapor condensation occurs on their surface.

Differentiating the energy conservation relation, we can roughly check the expected external power $P_{\max}$ at which the thermal roll-off in the SHG efficiency should occur:

$$\left| \frac{\mathrm{d}\lambda_{\mathrm{FF}}^{\mathrm{res}}}{\mathrm{d}T} - 2\frac{\mathrm{d}\lambda_{\mathrm{SH}}^{\mathrm{res}}}{\mathrm{d}T} \right| \frac{\mathrm{d}T}{\mathrm{d}P_{\mathrm{FF}}} P_{\max} \sim \Delta \,, \tag{4.4}$$

where Δ is the VIS resonance width, and $\mathrm{d}T/\mathrm{d}P_{\mathrm{FF}} = 10.5°\mathrm{C/mW}$ obtained experimentally. We find $P_{\max} \sim 7$ mW in the fiber (corresponding to an internal power $P_{\max,\mathrm{int}} \sim 390$ mW). This results is in fair agreement with our experiments.

Two distinct regimes are observed for the wavelength detuning: for a slight FF wavelength detuning of any sign, the SHG signal does not appreciably change; when such detuning becomes more important, the fiber-to-disk coupling is affected. Unfortunately, the latter is extremely critical and cannot be adaptively changed to re-optimize each experimental point of the same curve. Despite the huge difference between the expected SHG conversion efficiency $\eta_{\mathrm{SHG}} = 0.21$ W^{-1} and the experimental one $\eta_{\mathrm{SHG}}^{\mathrm{exp}} = 0.7 \times 10^{-3}$ W^{-1}, we obtain a state-of-the-

Results discussion

17. Left secondary peak: $\lambda_{\mathrm{FF}}^{\mathrm{res}} = 1579.9$ nm, $(p_{\mathrm{FF}}, m_{\mathrm{FF}}) = (2, 9)$, $\lambda_{\mathrm{SH}}^{\mathrm{res}} = 789.2$ nm, $(p_{\mathrm{SH}}, m_{\mathrm{SH}}) = (4, 20)$, right secondary peak: $\lambda_{\mathrm{FF}}^{\mathrm{res}} = 1586.9$ nm, $(p_{\mathrm{FF}}, m_{\mathrm{FF}}) = (3, 7)$, $\lambda_{\mathrm{SH}}^{\mathrm{res}} = 793.9$ nm, $(p_{\mathrm{SH}}, m_{\mathrm{SH}}) = (5, 16)$.

18. We recall the temperature sensitivities for both wavelengths: $\mathrm{d}\lambda_{\mathrm{FF}}^{\mathrm{res}}/\mathrm{d}T = 0.077$ nm/°C and $\mathrm{d}(2\lambda_{\mathrm{SH}}^{\mathrm{res}})/\mathrm{d}T = 0.088$ nm/°C. The difference between these values induces a different displacement of the two resonances.

art result, comparable with other well-known devices, such as semiconductor-based waveguides or photonic crystals [40].

Of course, it is important to try and figure out the possible reasons of this discrepancy. Eq. 2.2 shows that the conversion efficiency depends on the frequencies, on the overlap integral and on the quality factors at both wavelengths. Once the former have been fixed, the latter two quantities are the only ones to affect $\eta_{\mathrm{SHG}}^{\mathrm{exp}}$. Due to the non-zero detuning ($\Delta\lambda \neq 0$), the NIR and VIS resonant modes do not perfectly overlap, thus partly reducing $\eta_{\mathrm{SHG}}^{\mathrm{exp}}$. Additional simulations have therefore been performed to appreciate the connection between wavelength mismatch and conversion efficiency. Figure 4.13 shows η_{SHG}, calcu-

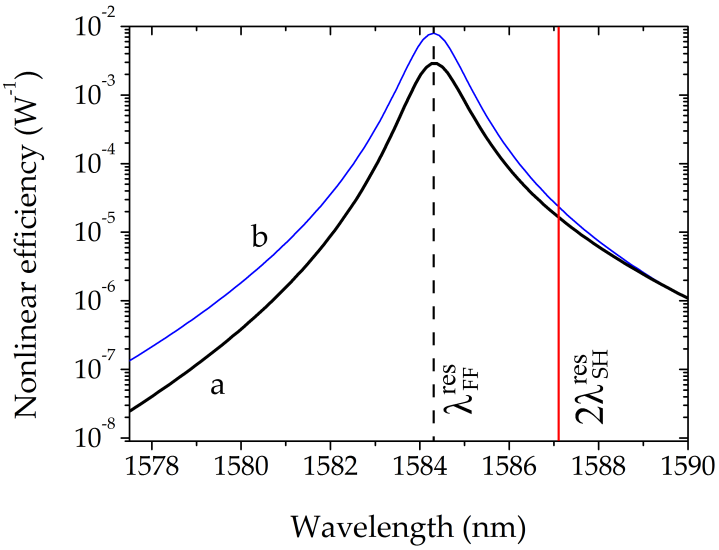

Figure 4.13: Computed nonlinear conversion efficiency η_{SHG} for a detuning $\Delta\lambda =$ 2.73 nm (a, thick black line) and $\Delta\lambda = 0$ (b, thin blue line).

lated according to Ref. [28] and taking into account the measured quality factors. The two curves represent different detunings: the thick black line corresponds to the observed $\Delta\lambda = 2.73$ nm and has a maximum $\eta_{\mathrm{SHG}} = 3.31 \times 10^{-3}$ W^{-1}, in fair agreement with the experimental value; the thin blue one represents the ideal case $\Delta\lambda = 0$, showing the maximum efficiency achievable with the current intrinsic quality factors and coupling conditions. The two peaks differ by less than a factor 3, indicating that the present $\Delta\lambda$ is not the main limiting factor for the nonlinear performance of our disks. Much better conversion efficiencies will be possibly obtained only by improving the quality of our cavities via an optimization of the fabrication process.

Additional measurements

Temperature can be very useful to slightly increase the overlap between the two resonances and, therefore, the conversion efficiency. For a better compre-

hension of the possible role of this parameter, we carried out a further series of measurements, so as to study the SHG peak displacement while changing the temperature (Fig. 4.14a). The measurements are performed as described above, i. e. with the fiber in contact with the disk sidewalls, with FF power fixed at $P_{\mathrm{FF}} = 3$ mW. Figure 4.14b shows a linear dependence of $2\lambda_{\mathrm{SH}}$ relative to T. However, the thermal wavelength displacement of the nonlinear peak does not agree with the one of the NIR resonance, i. e. it does not have the expected slope $\mathrm{d}(2\lambda_{\mathrm{SH}})/\mathrm{d}T = \mathrm{d}\lambda_{\mathrm{FF}}^{\mathrm{res}}/\mathrm{d}T = 0.077 \pm 0.008$ nm/°C. Conversely, from the fit we obtain $\mathrm{d}(2\lambda_{\mathrm{SH}})/\mathrm{d}T = 0.040 \pm 0.003$ nm/°C, which does not correspond to our simulations. This variance can be tentatively ascribed to the reproducibility

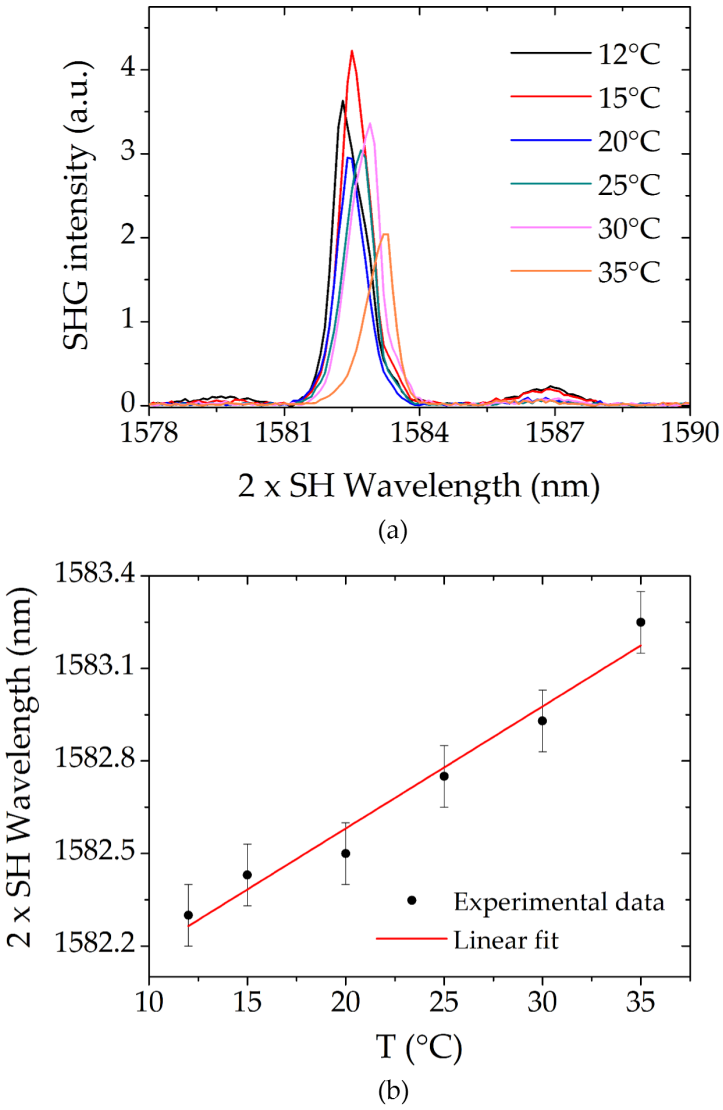

Figure 4.14: (a) SHG intensity vs. 2 × SH wavelength for different values of temperature; (b) 2 × SH wavelength displacement vs. temperature.

issue already mentioned. When modifying the temperature, a dilatation or a contraction of the sample holder occurs; this causes a change of the sample position and the taper generally sticks on a different part of the bar, making a new alignment necessary and modifying the coupling condition. This results in inconsistent sets of measurements, hardly comparable with our simulations

To get rid of these problems, we decided to perform the same study for the linear resonances, with the fiber far from the disks, so as to study the displacement of the NIR and VIS mode wavelengths versus temperature, at fixed FF power $P_{\mathrm{FF}} = 1$ mW. For both $\lambda_{\mathrm{FF}}^{\mathrm{res}}$ and $2\lambda_{\mathrm{SH}}^{\mathrm{res}}$ we observe the expected linear trend: the NIR resonance wavelength has a slope $\mathrm{d}\lambda_{\mathrm{FF}}^{\mathrm{res}}/\mathrm{d}T = 0.077 \pm 0.008$ nm/°C (Fig. 4.15a), while for 2 × VIS WGM wavelength we obtain $\mathrm{d}(2\lambda_{\mathrm{SH}}^{\mathrm{res}})/\mathrm{d}T = 0.083 \pm 0.004$ nm/°C (Fig. 4.15b); these two values are in very good agreement with the results of our simulations: 0.077 nm/°C for the NIR and 0.088 nm/°C for 2 × VIS. With this additional set of measurements, therefore, we can restate that in principle temperature can be used as a fine-tuning parameter to compensate small detunings $\Delta\lambda$.

4.4 Summary

In this chapter we presented the SHG experimental results. First, we discussed the fabrication of fiber tapers, an essential tool for our measurements. Then we described all the steps of the linear characterization, which plays a crucial role in the assessment of modeling reliability and fabrication quality. Finally, we reported on the demonstration of SHG in an AlGaAs suspended WGM microresonator. Although we still have room to improve the SHG efficiency, our microdisks are already at the state-of-the-art of frequency converters in the III-V platform [40].

Our results constitute a significant step toward the fabrication of ultra-compact SPDC sources in the telecom range. To this end, we can still improve on our cavities. For instance, the reproducibility issues associated to the tapered fiber could be overcome by integrating waveguides nearby the microdisks. A new generation of samples would also provide the opportunity to further develop the fabrication process, so as to boost the cavity quality. A monolithic and improved version of the present sample could open a view on other interesting experiments and possible results. Figure 4.16 shows a GaAs sample processed in the DON group, where the waveguides are integrated on the same chip as the GaAs microresonators. Reproducing such integrated system in AlGaAs would provide a compact experimental setup, alleviating also our problems with the tapered fiber.

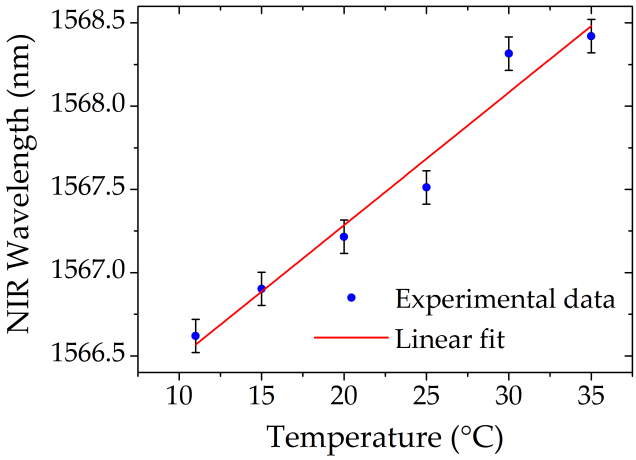

(a)

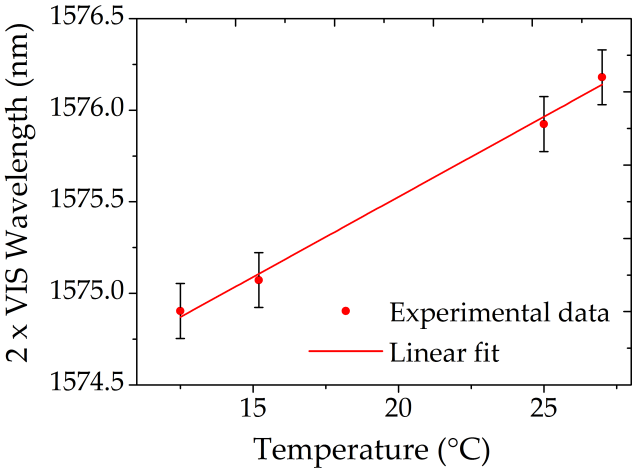

(b)

Figure 4.15: NIR (a) and 2 × VIS (b) mode wavelengths displacement vs. temperature.

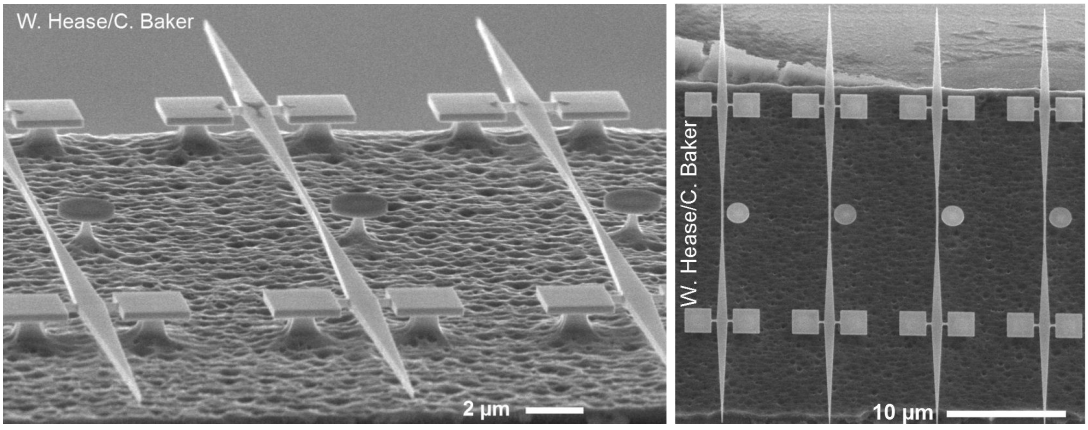

Figure 4.16: SEM pictures of GaAs microdisk resonators with their integrated fully-suspended coupling waveguide.

Part II

Difference Frequency Generation for THz emission

Chapter 5

Terahertz room-temperature integrated parametric source

5.1 Introduction

The second part of this thesis deals with the study of WGM AlGaAs microresonators for the demonstration of an integrated DFG-based THz source, conceived for room-temperature operation. This activity has found its place within the framework of the European project TREASURE (**T**erahertz **r**oom-t**e**mperature integr**a**ted parametric **s**o**ur**c**e**), which consisted in conceiving, designing, fabricating and characterizing this CW, electrically pumped parametric source. Compared to other existing THz sources, the TREASURE source was meant to bring together several crucial advantages that were not simultaneously available in other existing sources at the beginning of my thesis: compact size, room-temperature operation, output power $\sim$1 μW, emission frequency from 2.4 to 6 THz [1], spectral purity, feasibility of multi-spectral array of emitters.

Traditional sources of THz radiation are bulky and expensive. The main techniques exploited to obtain THz emitters (photoconductive dipole antennas [106], photo-mixing [107, 108], THz Quantum Cascade Laser (QCL) [109], ...) are limited by low emission power, pulsed regime, poor tunability or cryogenic temperature operation. To date, the limitations of all these techniques have prevented the large-scale development of THz spectroscopy, even though the interest in both scientific and commercial applications has grown very fast during the last decade. For instance, narrow-band THz systems have found many applications in astronomical spectroscopy. Beyond research, THz spectroscopy has found important applications in security and military perspectives [110]. Despite the considerable demand in terms of applications, today the "ideal"

1. The THz portion of the electromagnetic spectrum, comprised between microwaves and far infrared, goes about from 500 GHz to 5 THz.

THz system (source + coherent detector) is still lacking.

Various routes to THz generation via nonlinear optics have been explored to date in different materials (bulk GaAs [111], ZnSe and $LiNbO_3$ [112, 113], periodically poled $LiNbO_3$ [114]), based on DFG, optical rectification or parametric generation. In the last years, Vodopyanov and coworkers demonstrated the generation of 0.9 to 3 THz radiation in periodically inverted GaAs [115]. Moreover, following Berger and Sirtori [116], Vodopyanov's group has also demonstrated THz DFG in a planar GaAs waveguide [117].

Finally, the most relevant results concerning sources of this type are based on DFG in a dual-wavelength mid-IR QCL. After the first proposal from Capasso's group at at Harvard [46], such devices have been refined concomitantly by the group of Razeghi at Northwestern [47] and by the group of Belkin at the University of Texas at Austin [48], which demonstrated room-temperature single-mode THz emission in pulsed operation. Very recently, Razeghi and coworkers achieved room-temperature CW THz generation based on intracavity DFG from MIR QCLs [51]. This type of THz source takes advantage from the MIR QCLs (room temperature operation, electrical pumping, compact size).

In order to easily obtain efficient THz DFG, the inherently tight optical confinement of semiconductor micro-structures is a great advantage, since it allows the integration of laser pump sources, and can result in a compact device of a few square millimeters in size. In particular, thermal and mechanical properties of GaAs and compounds [119] contribute to better performances with respect to other platforms, such as $LiNbO_3$ [120]. These properties, combined with the strong optical confinement granted by the high refractive index, result in high power levels, stability and mode control in GaAs lasers.

From the need for tight optical confinement, we naturally arrived at the concept of optical microcavities. Therefore, we focused on AlGaAs/GaAs WGM microresonators (Figure 5.1) that vertically confine the NIR WGMs like a standard dielectric waveguide. The cylindrical structure is capped on both sides by metallic mirrors to ensure the vertical confinement of the THz mode. The latter are also conceived as contacts for electrical injection into the doped AlGaAs layers. InAs QD arrays located within the NIR waveguide constitute the active region, allowing a good thermal behavior and low threshold currents. Unlike quantum wells, the gain curve of QD arrays is broadened by shape and size fluctuations (inhomogeneous broadening). This is the key factor for obtaining simultaneous lasing of two NIR WGMs without mode competition. It is important to note that the homogeneous broadening of QDs at 300 K, of the order of 10 meV [121], would allow emission at frequencies down to 2.4 THz. Conversely, an upper limit for DFG is set at 6 THz by GaAs Reststrahlen-band.

In the following sections, we shall give the details needed for having a

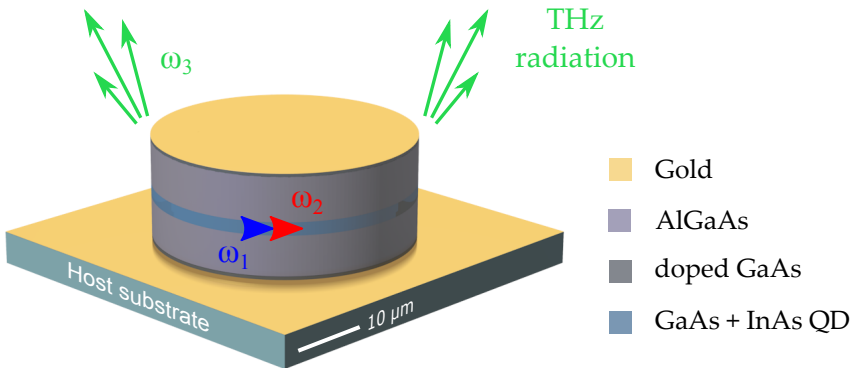

Figure 5.1: 3D view of the TREASURE device on ⟨100⟩-GaAs substrate.

general comprehension of the project and the experimental results shown in chapter 6.

5.1.1 Consortium and tasks

The results of the EU FET project TREASURE stemmed from the collaboration of several renowned, national and international partners over three years (May 2010 – April 2013). Let us state clearly that the main objective of this project, that is the aforementioned TREASURE source, was not achieved. However, besides an invaluable growth of scientific knowledge, these fruitful interactions have also led to the development of state-of-the-art simulation codes and optical benches, which I have had the opportunity to exploit and ameliorate throughout my doctoral work. Each partner of the consortium has made available its expertise. The different contributions are listed below.

Université Paris Diderot (UPD)

The DON and the QUAD groups of the Université Paris Diderot participated to TREASURE with their know-how in: 1) advanced electromagnetic modeling and design; 2) characterization of integrated nonlinear optical devices; 3) evanescent coupling techniques to microcavities; 4) mid-IR detection and imaging and 5) QCLs operating in the mid-IR and THz ranges.

In particular, my thesis work has contributed to the design of such THz source and to the characterization of the passive samples provided by the consortium.

Julius-Maximilians Universitaet Wuerzburg (UW)

The "Technical Physics" group offered its expertise in III-V semiconductor nanotechnology, with an accent on micropillar-based QD lasers. UW identified WGM emission and lasing of the respective modes in micropillar in collaboration with CEA.

Commissariat à l'énergie atomique et aux énergies alternatives (CEA)

CEA participated in TREASURE with the NanoPhysics and SemiConductor laboratory. The know-how of this group relevant to TREASURE project was threefold: 1) growth of self-assembled InAs/GaAs QDs by MBE, 2) top-down nanofabrication of III-V optical microcavities (microcylinders, microdisks, microrings), and 3) advanced optical characterization of QDs and emitters by microphotoluminescence.

Danmarks Tekniske Universitet (DTU)

DTU participated to TREASURE with the research group Terahertz Technologies and Biophotonics. They made available their expertise concerning full 3D modeling capabilities of propagation of electromagnetic radiation at THz frequencies, and capabilities to perform broadband THz transmission and emission spectroscopy.

Alpes Lasers

Alpes Lasers was the industrial partner of TREASURE. It provided its expertise in the transfer of research level technologies to the industrial world and its experience in THz generation and cryogenic QCL sources.

5.2 Microresonators for THz DFG

The THz emission at frequency ω_3 should be obtained through DFG from two near-IR WGMs at frequencies ω_1 and ω_2, for which $\omega_3 = \omega_1 - \omega_2$ holds. These modes, excited by the emission of QDs embedded in the microcavity, should grant efficient THz generation thanks to the Quasi-Phase Matching (QPM).

As for the SHG process, the building block is a WGM microresonator. Therefore the nonlinear interaction among the three WGMs can be described by using the Coupled-Mode Theory (CMT), as shown in chapter 1 and explained in Haus' textbook [68] [2].

2. More details can also be found in Andronico's PhD thesis [61] and in Ref. [19].

Our DFG source is based on AlGaAs and GaAs, which possess a $\bar{4}3m$ symmetry [56] and, therefore, only have one independent nonzero $\chi^{(2)}$ element ($\chi^{(2)}_{ijk} \rightarrow 2d_{14}$). For a growth axis along the $\langle 100 \rangle$ direction, it follows that the nonlinear polarization differs from zero only in two cases:

- two TE pump modes at ω_1 and ω_2 and a TM output at ω_3;
- two orthogonally polarized pump modes at ω_1 and ω_2 and a TE output at ω_3.

An additional constraint comes from the fact that the overlap integral (Eq. 1.24) must be non-negligible and this can be read in terms of phase matching. The general QPM condition for WGM cavities, deduced in section 1.5.4 and expressed by Eq. 1.51, can be rewritten for the particular case of DFG in the following way:

$$\Delta m = m_3 - m_1 + m_2 = \pm 2\,, \tag{5.1}$$

where m_1 and m_2 are the azimuthal numbers of the pump WGMs, and m_3 of the THz mode.

Let us now separately point out a few details for the cases of a passive source (with pump fields coupled from outside) and an active source (with integrated pump lasers).

5.2.1 Passive source

By following the guidelines of the CMT, we start from the expression of the emitted power P_3^{out} at ω_3:

$$P_3^{\text{out}} = 4\frac{\omega_3}{\omega_1\omega_2}\frac{\left(Q_3^{\text{intr}}\right)^2}{Q_3^{\text{rad}}}\prod_{i=1,2}\left[\frac{Q_i^{\text{cpl}}}{(1+Q_i^{\text{cpl}}/Q_i^{\text{intr}})^2}\right]|I_{\text{ov}}|^2 P_1^{\text{in}} P_2^{\text{in}}\,, \tag{5.2}$$

with P_1^{in} and P_2^{in} the injected powers at ω_1 and ω_2, respectively; Q^{intr}, Q^{rad} and Q^{cpl} the intrinsic, radiation-limited and coupling quality factors, respectively; and I_{ov} the nonlinear overlap integral. The DFG conversion efficiency $\eta_{\text{DFG}} = P_3^{\text{out}}/(P_1^{\text{in}} \cdot P_2^{\text{in}})$ has its maximum value at the critical coupling ($Q^{\text{intr}} = Q^{\text{cpl}}$). In this case:

DFG efficiency (critical coupling)

$$\eta_{\text{DFG}} = \frac{1}{4}\frac{\omega_3}{\omega_1\omega_2}\frac{\left(Q_3^{\text{intr}}\right)^2}{Q_3^{\text{rad}}}Q_1^{\text{intr}}Q_2^{\text{intr}}|I_{\text{ov}}|^2\,. \tag{5.3}$$

The conversion efficiency can be optimized by an appropriate design of the cavity that maximizes the overlap integral I_{ov} and/or by changing the coupling geometry, that is by engineering the Q^{cpl}. At critical coupling η_{DFG} is directly related to the overlap between the three interacting fields, and it is enhanced proportionally to the time that the modes spend inside the resonator; higher Q-factors result in a longer interaction time between the fields involved in the nonlinear mixing.

5.2.2 Active source

In the case of the active source, the near-IR fields are generated inside the cavity instead of being in-coupled from outside. Therefore, the expression of the outcoupled power at ω_3 is:

$$P_3^{\text{out}} = \frac{\omega_3}{4} \frac{\left(Q_3^{\text{intr}}\right)^2}{Q_3^{\text{rad}}} |I_{\text{ov}}|^2 U_1 U_2 \,, \tag{5.4}$$

with U_1 and U_2 electromagnetic energies stored in the two pump WGMs. We see that the emitted THz power is proportional to the energy of the pump modes, and, again, it can be increased by maximizing the overlap integral between the interacting WGMs. If we use the definition of WGM quality factor (Eq. 1.35), we can express P_3^{out} as:

$$P_3^{\text{out}} = \frac{1}{4} \frac{\omega_3}{\omega_1 \omega_2} \frac{\left(Q_3^{\text{intr}}\right)^2}{Q_3^{\text{rad}}} Q_1^{\text{intr}} Q_2^{\text{intr}} |I_{\text{ov}}|^2 P_1^L P_2^L \,, \tag{5.5}$$

where P^L is the power emitted due to the lasing of the active medium, which corresponds to the dissipated power $\mathcal{P}_d$. We can note that Eq. 5.5 is the same as that obtained for the passive source at critical coupling (Eq. 5.2), where P_i^{in} is substituted by P_i^L ($i = 1, 2$).

5.2.3 Design

Radius

Materials

In terms of cavity design, the TREASURE source has evolved during the project[3]. At the very beginning of the project, the microresonators consisted of a GaAs core sandwiched between two layers of AlAs and had a radius $R \sim 40.6$ μm. On one side, in an experimental perspective, the aim was to limit the number of lasing modes, i.e. to limit the number of modes whose frequencies fall in the gain band of the QDs. Since the number of modes that a microcavity can accommodate is inversely proportional to the cavity length, the radius was shrunk down to $R \sim 20$ μm. Unfortunately, this had a dramatic drawback in terms of nonlinear efficiency. On the other side, a few attempts to grow such a structure proved that the AlAs layers suffer from oxidation problems under ambient conditions even when the percentage of Al was reduced from 100% to about 90%. This oxidation constitutes a problem for two reasons: first, it introduces surface roughness that degrades the quality factors of all the WGMs (strongly reducing the conversion efficiency); second, it changes the effective indices of the modes, at the expense of the phase-matching condition. For this

3. The simulations that we have carried out to find the best cavity are performed either with an EIM-based code or with a 2D FDFD-based code.

reason, microresonators with $Al_xGa_{1-x}As$ spacers of reduced Al molar fraction x have been considered. However, losses at THz frequencies of the ternary alloy $Al_xGa_{1-x}As$ versus x follow a bell shaped curve with maximum around $x = 0.5$ [122]. Therefore, lowering x (with $x > 0.5$) increases the optical losses for the nonlinearly generated mode. Finally, the problems of oxidation and losses for the THz mode have been bypassed by growing AlGaAs as a superlattice, where layers of GaAs and AlAs − thin enough to avoid oxidation − are alternated so to have the desired mean concentration of Al. The final structure (Fig. 5.2) is mostly made of AlGaAs alloys with an Al composition above 0.4, with a minimum use of GaAs [4]. The latter is only employed for the ohmic contacts and for the barriers of the QDs, which are designed according to a dot-in-a-well scheme, with pure InAs dots embedded in an InGaAs layer. Concerning the cladding layers, a "flat GRINSCH" structure [123] is exploited to minimize the doping, which is kept heavy (10^{19} cm^{-3}) only at the ohmic contacts (10 nm of GaAs and the first 40 nm of the GRINSCH). The rest of the graded regions, with Al composition varying linearly between 0.8 and 0.4, have a 5×10^{16} cm^{-3} doping. This is a reasonable compromise between the minimization of the series resistance and the maximization of laser power in the NIR. Higher doping levels would result in a very weak conversion efficiency (due to increased Free Carrier Absorption (FCA) for the THz mode), while lower levels would not permit to reach sufficient lasing power. Also, a thin layer of platinum (Pt) is needed between the semiconductor structure and the gold (Au) contacts in order to prevent diffusion of gold into the semiconductor during contact annealing. However, the thickness of the Pt layer must be minimized, because it induces additional THz losses.

The choice of the THz portion to generate comes from the analysis of the real part of the nonlinear coefficient d_{14} for GaAs. As shown in Ref. [118], d_{14} changes significantly with the THz frequency and in particular it approaches zero around 5 THz, well before the beginning of the Reststrahlen band ($\sim$ 6 THz). As shown in Eq. 5.3, the nonlinear efficiency scales as the square of the overlap integral (and then as the square of d_{14}). Therefore, even a small reduction of d_{14} significantly affects the THz output power. For our source, THz frequencies are then limited between 1 and 4 THz, assuming that the GaAs nonlinear coefficient is constant in this frequency range ($d_{14} = 46$ pm/V).

Emission frequency

Another key point for a good operation of our device is the impact that Two-Photon Absorption (TPA) can have on input and output powers: in fact, TPA limits the maximum power for the pump modes and must be taken into account for estimating the output THz power. The wavelength dependence of the TPA coefficient β_{TPA} for AlGaAs (shown in chapter 2, Figure 2.1) changes

TPA

4. These choices enable to avoid TPA at the three wavelengths.

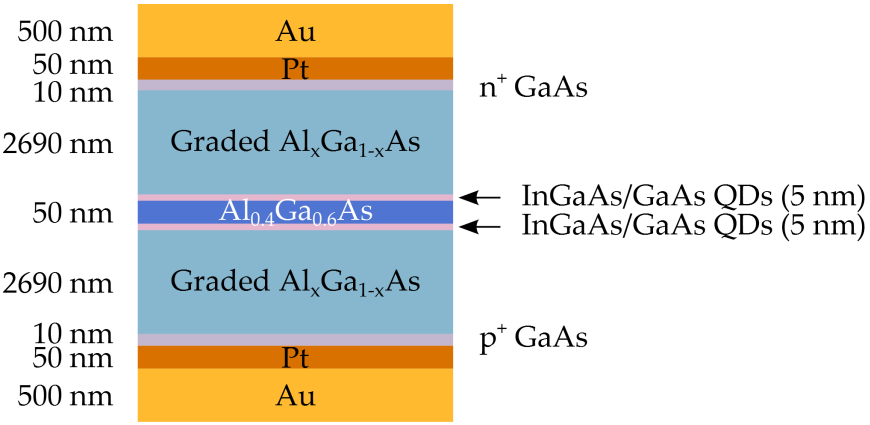

Figure 5.2: Vertical layout of the active device (not to scale). The graded AlGaAs regions have an Al concentration varying linearly from 0.4 (at the interface with the QD layers) to 0.8 (at the interface with the highly doped GaAs layers).

for different concentration of Al. By increasing the Al content, the bandgap of AlGaAs widens and the amount of TPA is reduced. The TREASURE device requires a negligible TPA. In fact, when photons are absorbed due to TPA, they generate free carriers in the conduction band, giving rise to FCA. Since the latter scales as λ^p, with $1.5 < p < 3$ [124], the most affected by FCA is the THz mode; this would have a detrimental effect on the conversion efficiency.

THz output simulations

To calculate the THz output power of our device, the effect of TPA is taken into account by modifying the intrinsic quality factor Q_i^{intr} ($i = 1, 2$) of the pump modes as follows:

$$\frac{1}{Q_i^{\text{intr}}} = \left(\frac{1}{Q_i^{\text{bulk}}} + \frac{1}{Q_i^{\text{rad}}} + \frac{1}{Q_i^{\text{Rayl}}} + \frac{1}{Q_i^{\text{TPA}}} \right) , \tag{5.6}$$

where Q_i^{TPA} depends on the power circulating in each of the pump modes and decreases when the circulating power increases. After a careful modeling, the best performances are obtained for a microresonator with $Al_{0.8}Ga_{0.2}As$ (2.5 µm thick) claddings, $Al_{0.32}Ga_{0.68}As$ (0.4 µm thick) core, and a radius $R = 19.32$ µm. The pump wavelengths are $\lambda_1 = 1.293$ µm ($p_1 = 1$, $m_1 = 281$) and $\lambda_2 = 1.314$ µm ($p_2 = 1$, $m_2 = 276$), while the THz WGM has a frequency $\nu_3 = 3.69$ THz ($p_3 = 1$, $m_3 = 3$). In Figure 5.3 we show the calculated output THz power versus input pump power for such a microcavity; assuming that the pump quality factors are the same $Q_1^{\text{intr}} = Q_2^{\text{intr}} = Q_p$, we show three curves corresponding to $Q_p = 10^4$ (black dots), $Q_p = 10^5$ (red dots) and $Q_p = 5 \times 10^5$ (blue dots). The solid lines reported on the plot stand for the same simulation without considering TPA. From this graphic, we can notice that:

- TPA is completely negligible for $Q_p = 10^4$. Even when $Q_p = 10^5$, its effect becomes relevant only at input pump powers close to 100 mW;

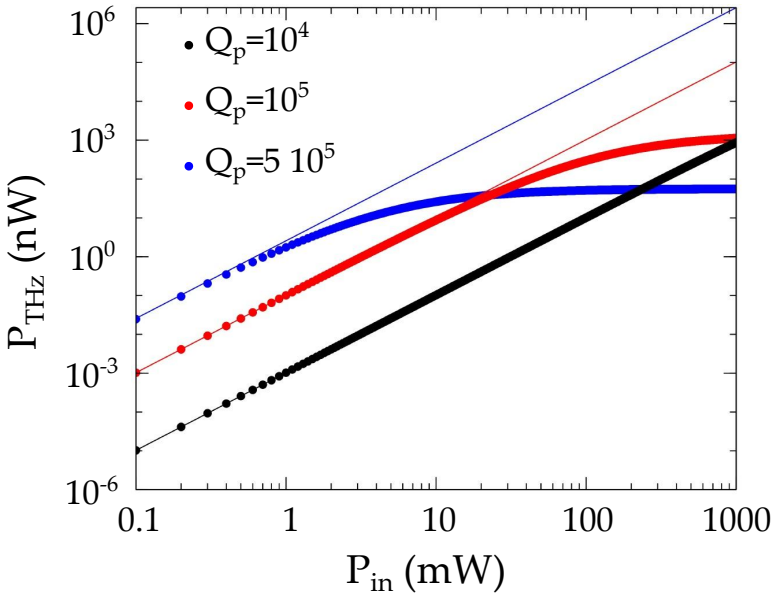

Figure 5.3: Output THz power for a DFG process with pump wavelengths around 1.3 μm. The frequency of the generated WGM is 3.69 THz. The thin solid lines are obtained by neglecting TPA.

– the nonlinear efficiency, calculated for $Q_p = 10^5$ and before the beginning of the saturation due to TPA, is $\eta_{\mathrm{DFG}} = 9.6 \times 10^{-5}$ W^{-1}.

This means that TPA can be effectively controlled via a proper cavity design.

5.3 Microrings for THz DFG

With respect to the above results, a few points to ameliorate have been devised:

1. further reduce the impact of TPA;
2. provide a tuning parameter for the DFG process [5];
3. increase the nonlinear efficiency and the output power provided by a single microresonator emitter.

To do so, we simulate DFG in ring structures (Fig. 5.4) with a core layer slightly richer in Al [125]. The change of Al content allows us to get rid of the TPA altogether (point 1), while the hole radius provides a solution for points 2 and 3. In Table 5.1 we report a triplet of modes sustained by a structure without hole and with the following vertical layout: $Al_{0.34}Ga_{0.66}As$ for the core (0.4 μm

University Paris Diderot - WGM modeling

5. Even if the temperature can certainly be used to shift the resonance frequency of the WGMs involved in the DFG, it is not a selective parameter. A temperature change shifts the frequencies of all the modes and its effect might be difficult to control.

thick) and $Al_{0.8}Ga_{0.2}As$ for the claddings (3.0 μm thick). We deliberately choose three WGMs such that, in an hypothetical DFG process, the energy would not be conserved ($\Delta\omega = \omega_1 - \omega_2 - \omega_3 \neq 0$).

R (μm)	λ_1 (μm)	m_1	λ_2 (μm)	m_2	λ_3 (μm)	m_3
17.48	1.3006	249	1.3194	253	91.79	2

Table 5.1: Triplet of WGMs for the structure with $Al_{0.34}Ga_{0.66}As$ core and $Al_{0.8}Ga_{0.2}As$ spacers. In this case the structure has no hole and the energy is not conserved. DFG is therefore inhibited.

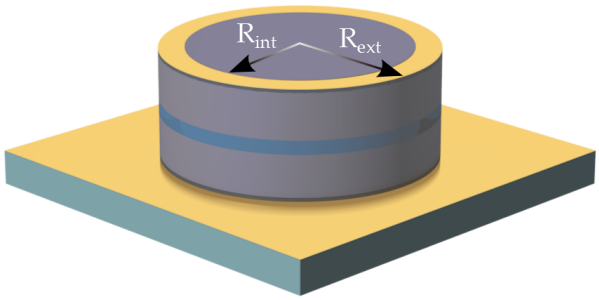

Figure 5.4: 3D schematic of a TREASURE ring-like device.

Figure 5.5 illustrates the effect of opening a central hole in the cavity. The solid black line represents the calculated frequency of the THz mode (the azimuthal order $m_3 = 2$ is fixed) for different values of the hole radius (with R_{int} pillar internal radius). The black dotted line represents the frequency of the mode for a cavity with no hole ($R_{\text{int}} = 0$) and radius $R = R_{\text{ext}} = 17.48$ μm. The blue, dash-dot constant lines represent the spacing between the pump modes $\Delta\omega_p = \omega_1 - \omega_2$, for a few different pairs (m_1, m_2). This is distinctly visible in the close-up panel, which shows the same plot around $R_{\text{int}} = 15.72$ μm. The intersections represent frequency triplets that fulfill the energy conservation condition. The interesting feature is that, by changing the internal radius, not only we can fine tune the THz eigenfrequency (while leaving the pump modes unperturbed) and therefore enforce strict energy conservation for a selected triplet, but the same can be done for different WGMs triplets. Therefore, the central hole can be effectively used as a tuning parameter, with the possibility of implementing it even after processing and testing the sample: the central radius of a chosen microresonator could be adjusted via Focused Ion Beam (FIB) [6]. While any treatment applied to the external boundary would reduce the

6. The Focused Ion Beam is a scientific instrument similar to the Scanning Electron Microscope, but it employs an ion beam rather than an electron beam. Moreover, unlike

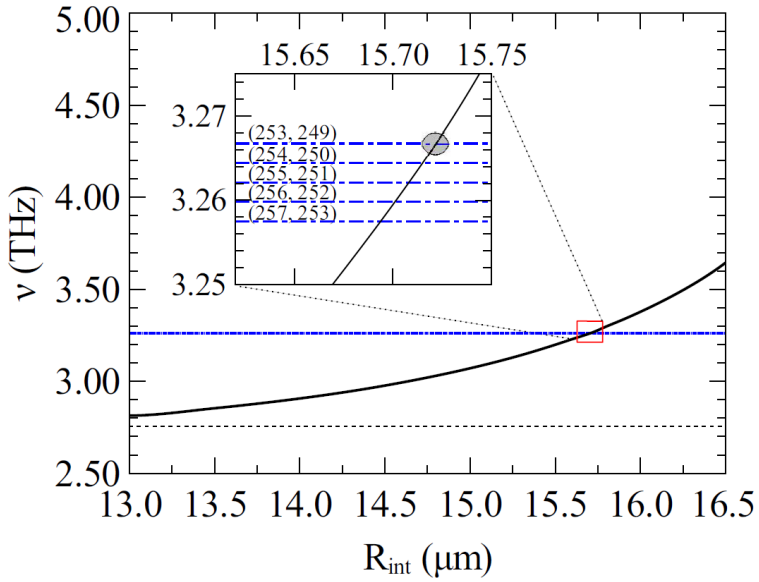

Figure 5.5: THz WGM frequency (solid black curve) and NIR mode spacing (dash-dotted blue curves) versus internal radius of the pillar. The dotted black line corresponds to the THz resonance frequency for a structure without hole. The inset is a zoomed-in view around $R_{\text{int}} = 15.72$ μm.

quality factors of the pump WGMs involved in the DFG, the same does not hold for the internal radius. This is due to the fact that the pump WGMs have their maximum intensity at the periphery of the pillar, while they have negligible intensity close to the pillar axis. By looking at the close-up of Fig. 5.5, if we restrict our attention to the pump modes with $m_1 = 249$ and $m_2 = 253$, we find that the energy is strictly conserved for an internal radius $R_{\text{int}} = 15.72$ μm (gray circle). For such a structure and pump modes, we can compute the THz output power provided by the microring, for pump quality factors $Q_p = 5 \times 10^5$. The result shown in Figure 5.6 reveals that the saturation due to TPA and observed in Fig. 5.3 is absent. Since TPA is negligible, the nonlinear efficiency increases with the pump quality factors (in particular, our simulations predict that an output power of 0.1 μW is reached with input powers slightly below 10 mW).

An additional advantage of the microring with respect to a structure without hole is the increase of the overlap integral between the interacting modes. This is due to the fact that the hole enables to squeeze the THz mode into a smaller volume, and it typically results in an increase of about 50%.

The exploitation of ring-like resonators provides more tuning options. Figure 5.7 shows the effect of a metallic tip placed in the hollow part of the microring.

SEM, FIB is destructive, therefore it is employed for fabrication rather than microscopy.

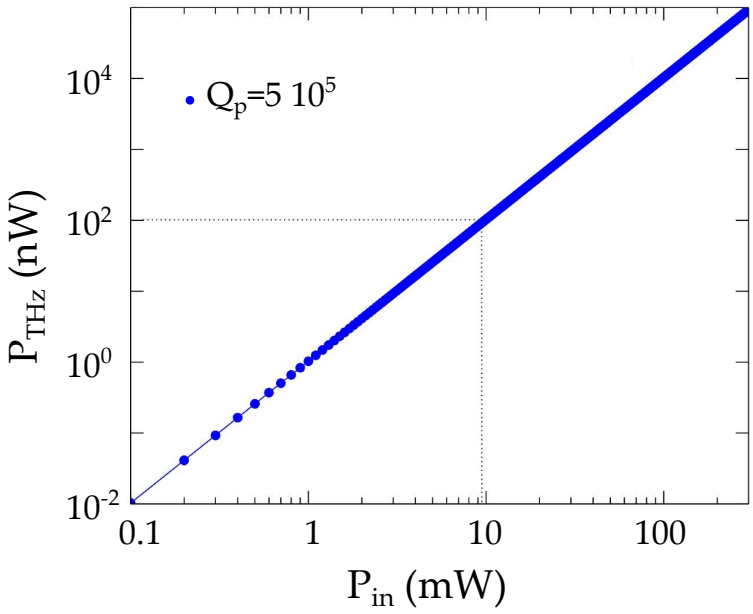

Figure 5.6: Computed THz output power vs input pump power for a microring-like structure. The external (internal) radius is $R_{\text{ext}} = 17.48$ μm ($R_{\text{int}} = 15.72$ μm), respectively. An output power of 0.1 μW can be obtained with a pump power slightly below 10 mW.

In particular, the top panel shows the shift of the THz frequency due to a golden tip with varying radius R_T and height fixed at $h_T = h/2$, with h height of the resonator. It is possible to obtain a shift close to 100 GHz (around 3% of the WGM original frequency) by exploiting large tips ($R_T > 0.8\ R_{\text{int}}$). On the other hand, the bottom panel of Fig. 5.7 shows the shift of the THz frequency due to a golden tip with radius $R_T = 0.9\ R_{\text{int}}$ as a function of the relative tip height h_T/h. By moving the tip closer to the bottom mirror, the frequency of the THz WGM shifts up to 300 GHz (around 9% of the WGM original frequency). The same principle can also be used with a non-metallic tip.

It is interesting to compare the nonlinear efficiencies for the same microresonator before and after opening the hole: if we neglect for a moment that the energy is not conserved for the structure without hole, then we get $\eta(\text{Hole})/(\text{NoHole})$ = 1.6. The nonlinear process benefits of the hole feature for two reasons:

- the THz mode is squeezed into a smaller volume and therefore the overlap integral is increased;
- the radiation-limited quality factor of the THz mode is reduced from $Q_3^{\text{rad}} = 572$ to $Q_3^{\text{rad}} = 376$, i.e. closer to the material quality factor ($Q_3^{\text{bulk}} = 97$).

The microring structures can then be effectively used to introduce a tuning parameter (the internal radius) that selectively acts on the THz WGM.

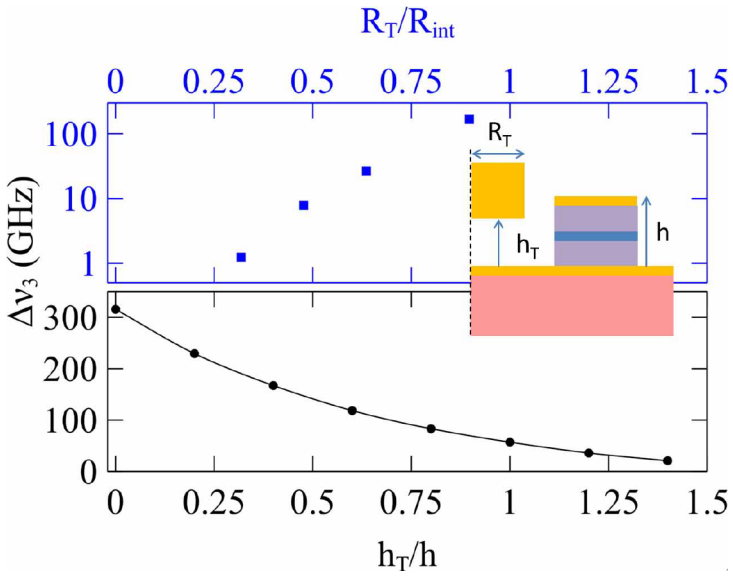

Figure 5.7: Frequency shift of the THz WGM versus: the radius of a metallic tip placed at half pillar height (top panel); the height of a tip with fixed radius $R_T = 0.9\ R_{\rm int}$ (bottom panel). Inset: vertical section of the tip and AlGaAs microring (the dashed line represents the axis of cylindrical symmetry).

5.4 Sample fabrication

Based on our modeling results, a few arrays of microresonators have been fabricated at the University of Würzburg and at CEA.

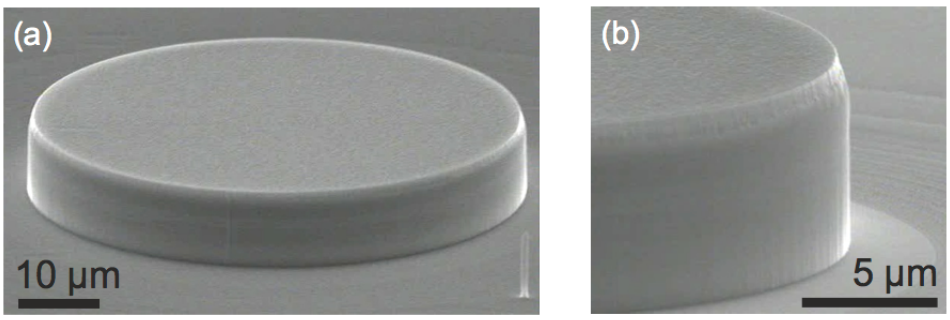

Figure 5.8: SEM pictures of the first microresonators fabricated at the University of Würzburg.

Since the beginning of the project, active samples have been fabricated in order to test their lasing properties and verify their suitability with respect to the final goal. The optimization of all the growth and processing steps has been challenging. In a first phase, microresonators with embedded QDs emitting around 980 nm were fabricated and tested [6, 126] (Fig. 5.8). This process in-

Active samples

volved a number of nanotechnology steps starting from the definition of the circular shape of the resonators into positive resist by either high-resolution electron-beam lithography or optical UV-lithography. The exposed resist was later removed and a metal etch mask deposited on top of the sample. In the subsequent lift-off process, the remaining resist and the metal layer were removed from the unexposed regions of the sample. Finally, Reactive-Ion Etching (RIE) was performed to remove the semiconductor material in the unexposed regions. Figure 5.9 shows the main steps required for the fabrication of the active sample. For the optimization of the dry etching process, standard RIE, Electron Cyclotron Resonance (ECR) plasma etching and Inductively Coupled Plasma (ICP) etching have been used and compared.

After facing several issues related to the etching of Al-rich layers, the etching parameters have been optimized. Then UW and CEA have started to focus on the fabrication of low-threshold electrically pumped QD microring lasers emitting around the target wavelength of ∼1300 nm.

Key to obtain an efficient THz emitter is the suppression of the NIR modes that do not satisfy the phase-matching condition. They might compete for the gain and hence reduce the desired THz output. A special care is therefore devoted to the study of possible ways of obtaining two-color lasing with the required spacing between the two WGMs (i.e. $m_1 - m_2 = 4$) [127]. To this end, UW has performed some tests by making small notches on the sidewalls of the rings (Fig. 5.10), so that modes with a high local intensity at the notch position suffer from losses by scattering. Modes having a node at this position stay more or less unaffected by the notch, contributing to the THz generation. By using two notches and by adjusting their relative position we could therefore select the spacing between the unsuppressed WGMs. The notched ring lasers are fabricated using e-beam lithography and an ECR Cl_2/Ar plasma etching process with a Ni etch mask. Since the notches and the ring ridges are defined in the same lithographic step, a very precise positioning and size control of the notch is guaranteed.

University of Würzburg – Sample development

In Figure 5.11 we show a comparison of laser spectra obtained from rings with 80 μm diameter and with different notch symmetries. All spectra are taken under the same experimental conditions (heat sink temperature of 20°C and injection current of 10 mA). The spectra b) to d) feature successively growing effective Free Spectral Range (FSR) by choosing 90°, 60° and 45° offset angles. These results prove that the notched-ring approach can be effective in providing the required control on the WGM laser spectrum. With one lasing mode every four, the 45° configuration is the one suited for the TREASURE source. Moreover, due to the small notch size with respect to the THz mode wavelength, the latter will not suffer from significant notch-induced losses.

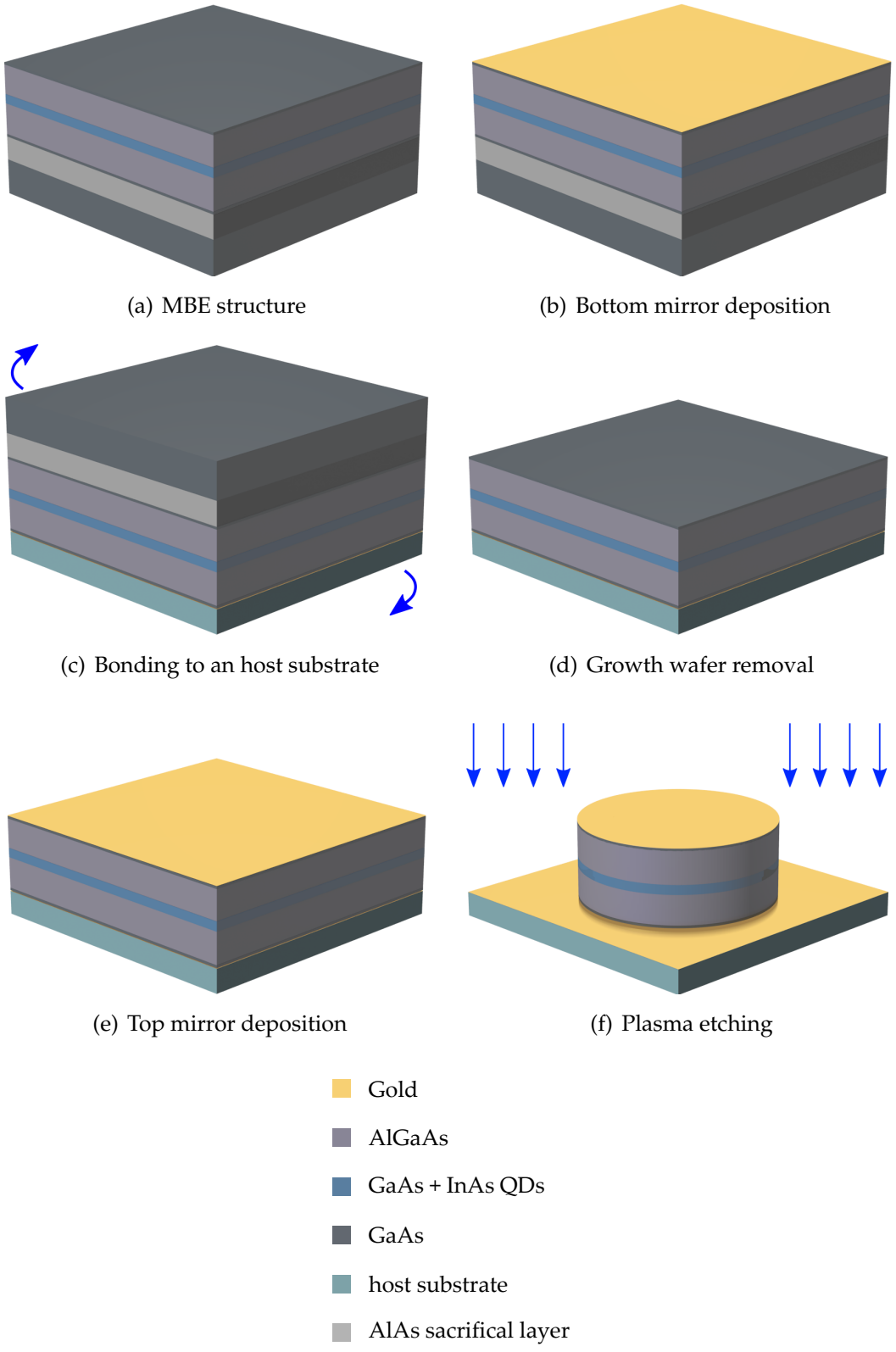

Figure 5.9: Schematics of the main steps required for the fabrication of the active sample.

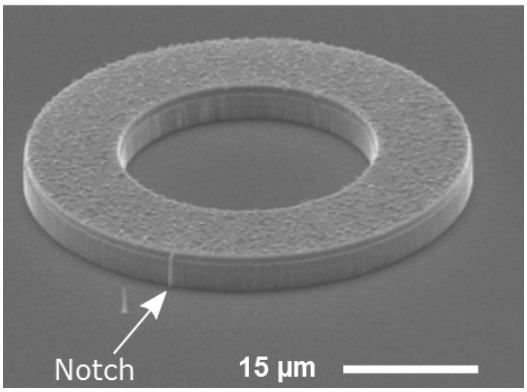

Figure 5.10: SEM picture of a notched microring fabricated at the University of Würzburg.

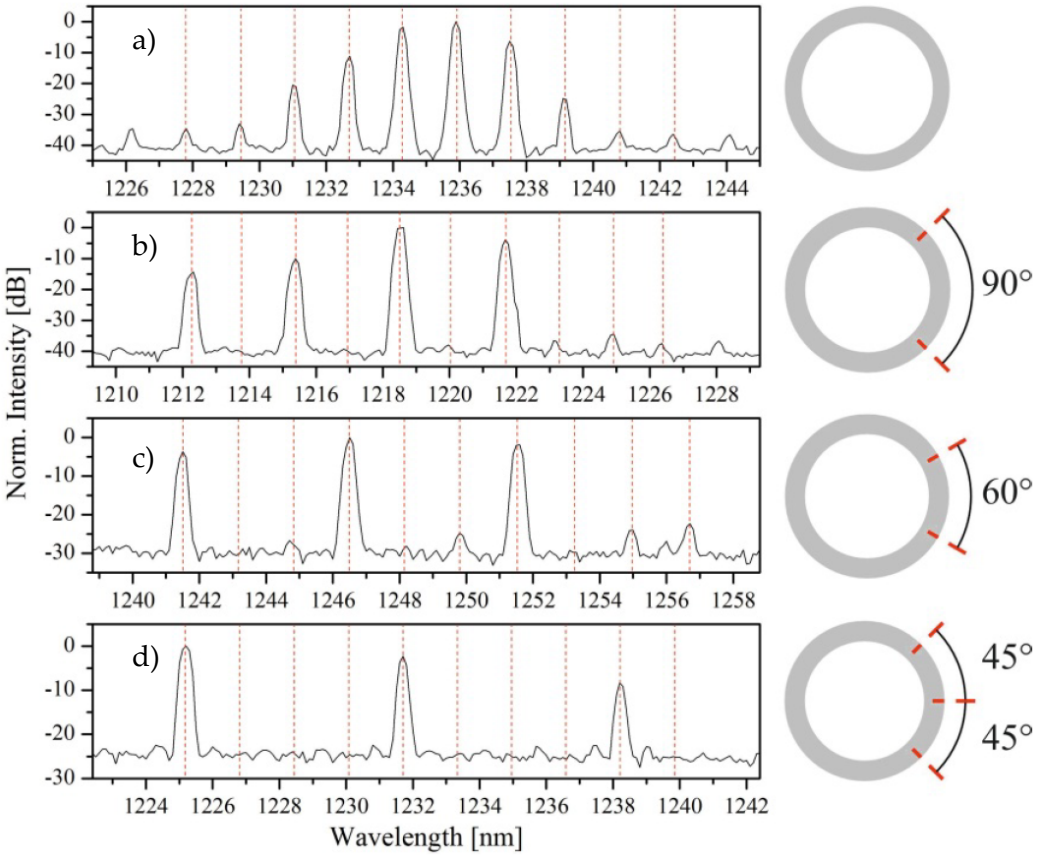

Figure 5.11: Comparison of room temperature spectra of 80 µm outer diameter rings with different notch symmetries taken at 10 mA injection current [127]. a) Unnotched reference spectrum; b) two notches with 90° offset angle; c) two notches with 60° offset angle; d) three notches with 45° offset angle.

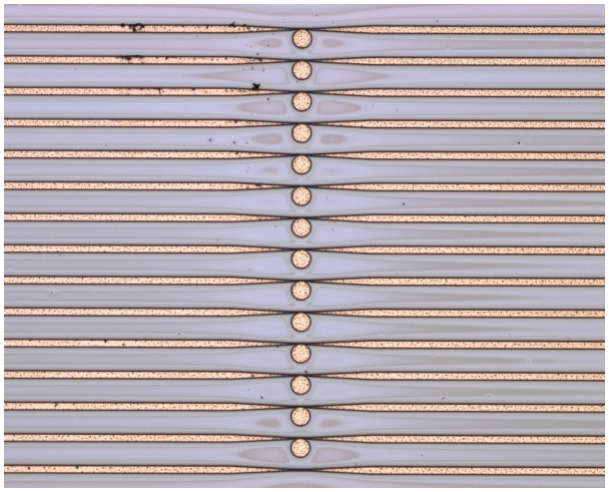

Figure 5.12: Optical microscope image of micro-cavities with integrated tapered coupling waveguides.

To validate the parameters used in the modeling, in parallel with the activities on the active devices, two series of passive test devices have been fabricated, to be characterized in the NIR and in the THz, respectively. Using such structures enables to neglect geometric and composition constraints dictated by phase-matching or heat-sinking issues, considerably reducing their fabrication complexity. The passive samples are grown by MBE according to the following vertical layout: 2505 nm of $Al_{0.8}Ga_{0.2}As$, 377 nm of $Al_{0.33}Ga_{0.67}As$, and 2453 nm of $Al_{0.8}Ga_{0.2}As$.

Passive samples

While sharing the same vertical structure, the samples used for the NIR characterization and the ones used for the THz characterization differ substantially.

In order to excite the NIR WGMs sustained by the cavities, integrated tapered waveguide are necessary (Fig. 5.12). The waveguide width and distance from the resonator are designed to obtain critical coupling for the pump modes, while the taper length is chosen to provide an adiabatic transition ($\sim 5\%$ of transmission losses).

The samples for the THz characterization, conversely, do not require coupling waveguides and need a double metallization for confining the THz modes. To this end, after the epitaxial growth, a gold mirror is deposited over the epitaxial layers and then epoxy bonded to a host substrate; the growth wafer is subsequently removed by mechanical and selective wet etching. The micropillars are finally defined by ECR plasma etching, using a second gold mirror deposited on top of the semiconductor layers and covered by a hard Ni mask.

5.5 Optical-Electrical-Thermal modeling

CEA – Study of the thermal effects

The comprehension of the thermal behavior of our structures plays a fundamental role for a good operation of the active device, since the phase-matching condition can be affected by the temperature dependence of the refractive indices. For this reason, thermal effects have been carefully studied at the CEA, by employing the commercial software SILVACO®.

The main lasing characteristics of the ring-like device of Figure 5.4 are reported in Fig. 5.13 (S on the graphs), where we compare them with those of two structures mounted n-side down, either identical to S (structure S_{inv}), or with a higher doping level (10^{17} cm^{-3}) in the cladding layers (structure $S_{2\mathrm{inv}}$) [128]. Currents in the few tens of mA range and output powers in the few tens of mW range can be obtained, although the bias is unusually large. As shown in Fig. 5.13, the p-side down mounting results in a better heat sinking: a total output power of 20 mW can be achieved for sample S, with a modest temperature raise of the active region (+35 K). This would not only enable a stable laser operation without mode jumps, but also a robust phase matching.

5.6 Summary

This chapter provided a general overview of the TREASURE project, whose final goal was the demonstration of THz Difference Frequency Generation at room temperature under electrical pumping.

After recalling the state-of-the-art for the THz sources, we described all the preparatory efforts required in terms of simulations and fabrication. For a better comprehension of our choices and for the sake of completeness, we also showed the intermediate structures that have led us to the final design of the device.

Concerning the activity carried out in the DON group, we reported on the modeling of a cylinder-like structure, highlighting the optimization steps in the choice of the device composition. Then we proposed the ring-like structure, discussing the advantages of this new kind of resonators with respect to the former geometry. Since the microring cavity finally turned out to be the best one in terms of performances, additional efforts were carried out to improve the THz emission and to understand the thermal behavior of the source.

In the next chapter we will show the results obtained from the characterization of the passive samples presented here, first step toward the fabrication of the final active source.

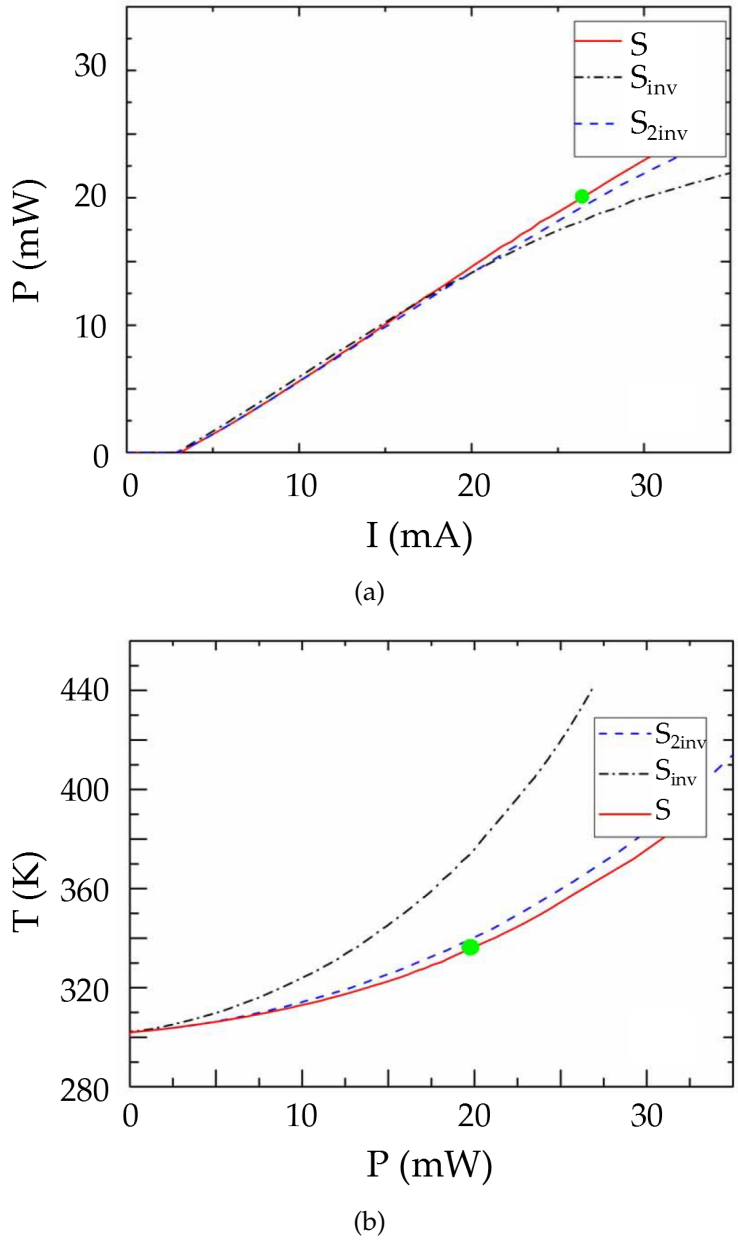

Figure 5.13: Calculated characteristic curves: (a) $P - I$, and (b) $T - P$ of structures S, S_{inv} and $S_{2\text{inv}}$ [128]. The green dot represents the expected operating point of the device.

Chapter 6

Near-IR and THZ characterization of passive microresonators

6.1 Introduction

This chapter is focused on the linear characterization of the passive WGM microresonators described in the previous chapter, at both NIR and THz frequencies. These measurements have been mandatory to test and understand the basic features of the TREASURE device while waiting for the active samples. We shall first discuss the linear characterization in the NIR performed by using the tapered fiber. Subsequently, we shall motivate the need for fabricating another kind of passive sample consisting of microresonators with integrated coupling waveguides, and we shall report its characterization. Finally, we shall describe the linear characterization in the THz range of double-metal microcavities. 2D arrays were probed with both Fourier-Transform Infra-Red (FTIR) and Time-Domain Spectroscopy (TDS) measurements. Note that, due to the difficulties related to the fabrication processes, the parameters for samples and modes (radii, wavelengths, order modes,...) are not exactly the same obtained from the simulations.

6.2 Linear characterization in the near-IR region

In this section we report on the linear optical characterization of passive microresonators in the NIR region. Moreover, we explain the drawbacks related to the tapered fiber technique, which have led us to design a new sample, composed of microcavities with integrated coupling waveguides.

6.2.1 Passive microresonators

At the beginning of the project, the first generation of passive samples (S1) quickly underwent heavy oxidation due to the use of Al-rich ternary AlGaAs alloy in the cladding layers of the microcylinders (Fig 6.1). The microcylinders became therefore unusable for evanescent fiber coupling.

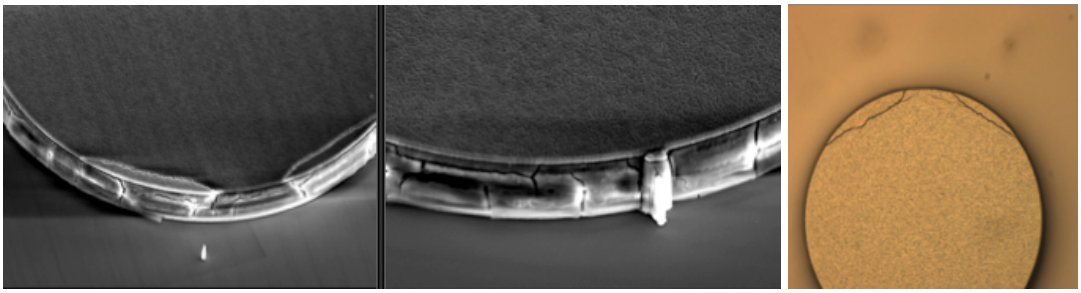

(a) (b)

Figure 6.1: SEM (a) and optical microscope (b) pictures of the oxidized microcylinders of S1.

To get rid of this issue, all the layers of the second generation of samples (S2) were grown with a digital GaAs/AlAs alloy. S2 is composed of 20 bars of about 20 microresonators with diameters ranging from 35 to 40 μm. The microcavities' vertical structure [1] and their radii are designed to sustain two WGMs with wavelengths around 1.3 μm, phase-matched to a THz WGM with frequency around 3 THz. To facilitate the positioning of the tapered fiber, and therefore adapt the sample to our experimental setup, the pillars on each bar are arranged on a line close to the bar edges. To do so, pairs of close pillars are defined during the etching step (Fig. 6.2a) and subsequently separated during the cleavage. Unfortunately, several pillars were damaged during this procedure and therefore were not measurable (Figure 6.2b).

S2: measurements and results

Experimental setup

The optical characterization of the passive microcavities contained in S2 is carried out via evanescent coupling technique, by using a tapered fiber, as described in chapter 4; the fiber SMF-28® is well suited for the wavelengths of interest (1280 nm $< \lambda <$ 1320 nm). All the measurements are performed with the setup sketched in Figure 6.3: the employed instrumentation is basically the same as for the SHG experiment. The sample and the tapered fiber are placed in front

1. S2 composition: GaAs substrate/ 2505 nm of $Al_{0.8}Ga_{0.2}As$ / 377 nm $Al_{0.33}Ga_{0.67}As$ / 2453 nm $Al_{0.8}Ga_{0.2}As$.

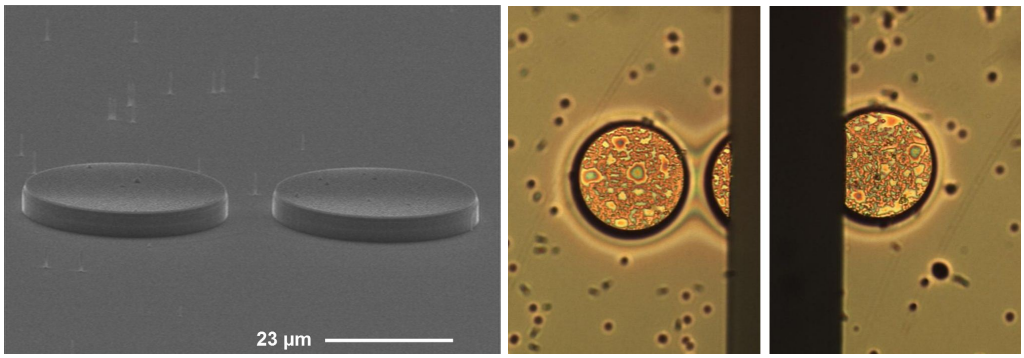

Figure 6.2: SEM (a) and optical microscope (b) pictures of S2 microcavities employed for the linear optical characterization in the NIR. (b) Damages caused by the cleavage.

of a microscope objective (×50, N.A. = 0.5) that is used for the alignment: the white light reflected by the sample is then redirected to a CCD camera connected to a computer, so as to image on a PC screen the sample with the fiber taper nearby and, therefore, ease the measurement performance. The entire system is enclosed in a Plexiglas® box to protect all the components from air currents, humidity, and dust. The box is also equipped with micro-positioning holders that allow full 3D adjustments of the system. Finally, piezoelectric actuators are used to finely change the position of the fiber with respect to the sample, which is a very critical step. In order to study the WGMs and their quality factors, we use a CW external-cavity tunable single-mode laser diode emitting from 1260

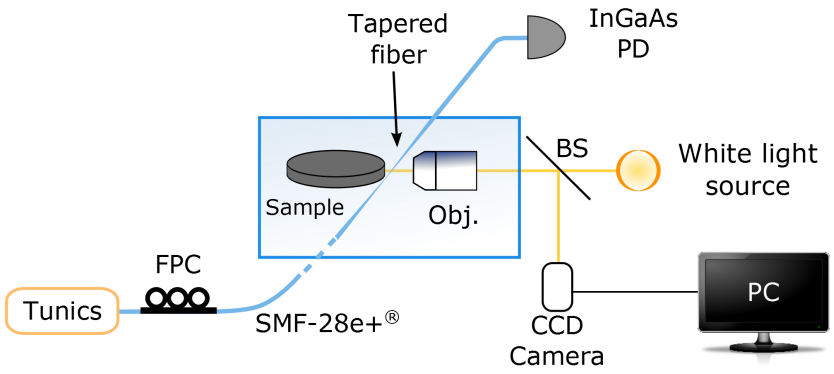

Figure 6.3: Schematic of the experimental setup used for the linear characterization of sample S2. FPC, fiber polarization controller; Obj., microscope objective; BS, beam splitter; PD, photodiode.

nm to 1360 nm with a maximal power of ∼10 mW (Tunics T100S from Yenista Optics); the transmission spectra are recorded via a fast InGaAs detector [2]. The polarization state of the radiation injected into the fiber can be varied with a three-paddle polarization controller.

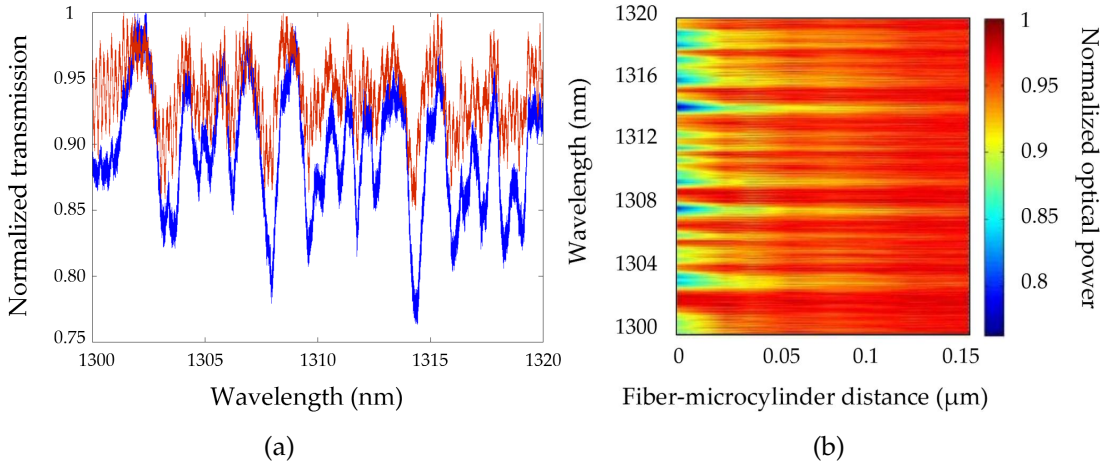

Figure 6.4: Transmission spectra for fiber-to-pillar distances $d = 0.05$ μm (red line) and $d = 0$ (blue line) (a); Transmitted optical power vs fiber-to-cylinder distance (b).

Linear characterization of S2

We perform a complete spectroscopy of the samples by recording transmission spectra for all the microcylinders contained in S2. To look for possible resonances, we perform a quick scan over the entire wavelength span via evanescent coupling. In all spectra and for each scan, the transmission of the fiber coupled to the microresonator is then normalized to the transmission of the fiber alone. Once the resonant WGMs have been singled out, a finer acquisition in proximity of the resonance wavelengths is carried out, to precisely determine their values and quality factors; after the measurement, our modeling helps us in labeling the resonant WGMs. Figure 6.4a shows two examples of such spectra: the red line corresponds to a fiber-to-pillar distance $d = 0.05$ μm, while the blue line to the case $d = 0$ (fiber in contact with the cavity sidewalls). Both spectra indicate a weak coupling of light from the fiber to the resonator. As far as the red curve is concerned, it is impossible to single out the resonant WGMs and perform a reliable mode labeling. On the other hand, we can identify a few resonances on the blue spectrum, but their quality factors are considerably lower than expected ($10^3 - 10^4$ versus 10^5). To figure out if the critical coupling regime is achieved ($Q^{\mathrm{cpl}} = Q^{\mathrm{intr}}$), we perform an additional set of measurements, by slightly changing the relative position between the fiber and the pillar at each

2. Wavelength range: 700 nm $< \lambda <$ 1800 nm; responsivity @ 1300 nm: 1.0 A/W.

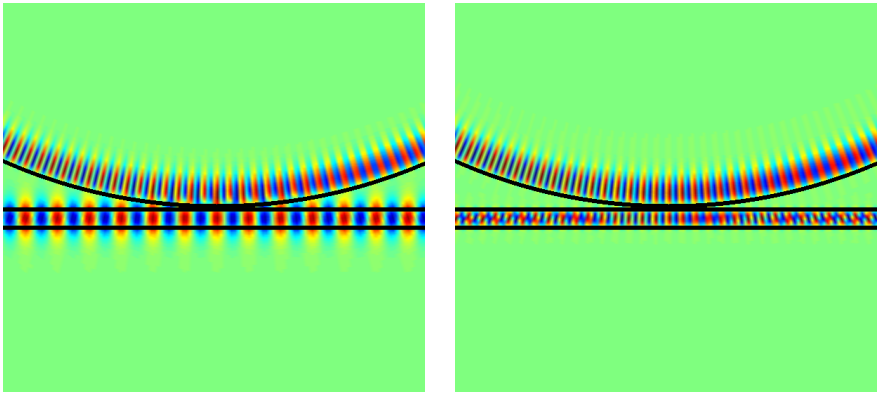

(a) (b)

Figure 6.5: Example of coupling from a fiber mode (a) and from a waveguide mode (b) to a microcylinder WGM. The cylinder radius is $R = 17.5$ μm, the fiber/waveguide width is $w = 1$ μm, and the distance from the fiber/waveguide to the cylinder is $d = 0.2$ μm.

scan. Figure 6.4b shows the results: the transmitted optical spectrum is plotted as a function of the fiber-to-cylinder distance, when the latter is varied from 0.15 μm to 0. We see that the transmission does not drop to zero (critical coupling condition), and this holds true even when the fiber touches the resonator.

The weak coupling between fiber modes and cylinder WGMs can be understood in terms of phase-velocity mismatch between them. In Figure 6.5 we plot the electric field of a WGM with radial and azimuthal number (p, m) = (1, 251), respectively, and λ = 1301.9 nm, plus the electric field of the fundamental mode of a fiber, which corresponds to our experimental conditions. As shown in Figure 6.5a, this configuration gives rise to a significant phase-velocity mismatch between the two modes, which results in weak coupling. On the other hand, in Figure 6.5b we show the same system where we replace the fiber with a waveguide, of the same vertical structure as the pillar. In this case, we can see that the phase velocities of the two modes are almost identical: this guarantees an efficient coupling from the waveguide to the resonator.

This difficulty was evident well before starting the linear characterization of our samples, but the extent of the problem was unclear. The fact that the phase velocities of the two modes need to be approximately equal holds strictly true only when the coupling is distributed over a large area: in this case it is simply a consequence of the translational invariance of the system, which requires momentum conservation. Bending the fiber and making a small loop with it [3]

3. After having tapered an optical fiber, it is possible to twist it so as to make a single-loop of ∼70 μm diameter. It can be used to characterize the samples as the straight fiber taper [99].

permits to relax the phase-matching requirement while dealing with small disks (pillar radius of a few microns). Unfortunately, as shown by the experimental results, this is not possible when the cavities are larger. In this case, only high-p WGMs can be excited with a tapered fiber. Besides the lack of interest for these modes due to the small nonlinear overlap integral they would give rise to, they still have low coupling efficiency (Fig. 6.4b). In fact, although phase matched with a fiber mode, high-p WGMs have their intensity maximum close to the pillar axis, and therefore their overlap with the exponential tail of the fiber mode is very low. Following these considerations, we design a new passive sample that includes coupling waveguides.

6.2.2 Passive samples with integrated waveguides

In light of the problems observed during the measurements on samples S2, a new sample has been designed. In Figure 6.6 we show the calculated coupling quality factor Q^{cpl} for the same WGM shown in Fig. 6.5a (i.e. $p = 1$, $m = 251$, $\lambda = 1301.9$ nm) as a function of the waveguide-to-pillar distance and waveguide width. The vertical layout of the pillars used in the simulations is the same as S2, and so is the radius ($R_{\mathrm{ext}} = 17.5$ μm). The results are obtained by following the CMT approach developed in Ref. [69]. The white lines correspond to $Q^{\mathrm{cpl}} = 10^5$ and $Q^{\mathrm{cpl}} = 10^6$. Since we expect resonators with intrinsic quality factors around $Q^{\mathrm{intr}} = 5 \times 10^5$, in order to attain the critical coupling regime, a waveguide close to 500 nm and a waveguide-to-pillar distance close to 150 nm seem to be reasonable.

Sample S3

Therefore, a preliminary sample has been fabricated according to the above guidelines (S3). It contains four groups of 16 rings with waveguides (same vertical structure as S2), with an external radius $R_{\mathrm{ext}} = 17.5$ μm and an internal radius $R_{\mathrm{int}} \sim 14$ μm (Figure 6.7a). The choice of rings instead of cylinders is simply due to the fact that, given the small waveguide-to-pillar distance, this geometry is easier to fabricate: using e-beam lithography to define a very small object (the waveguide taper) next to a very big one (the cylinder) is not easy due to proximity effects. Since we are interested only in the lowest radial order ($p = 1$) WGMs, a ring structure - with a not too big internal radius - is equivalent to a cylinder. As is evident from Fig. 6.7b, the fabrication of such structures is not trivial. Only in a few cases the actual spacing between the rings and the waveguides corresponds to the nominal value for efficient evanescent coupling. Moreover, surface roughness severely affect the quality of the sidewalls.

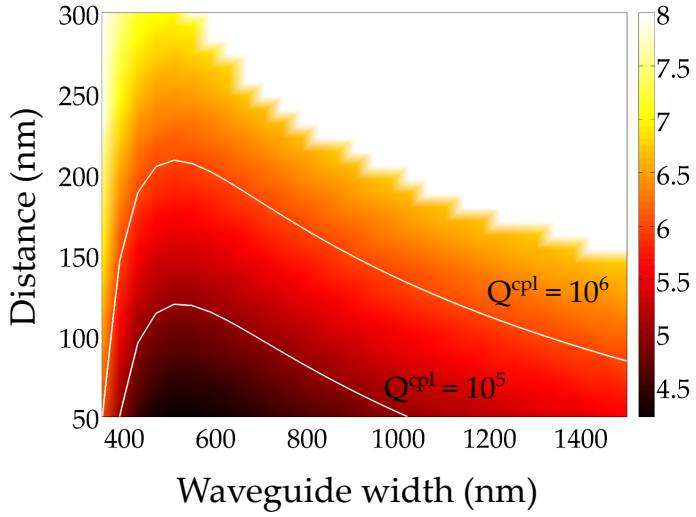

Figure 6.6: Logarithm of the calculated coupling quality factor Q^{cpl} for the WGM (p, m) = (1, 251), $\lambda = 1309.1$ nm, as a function of the waveguide width w and the waveguide-to-disk distance g, for a cavity of radius $R_{\mathrm{ext}} = 17.5$ µm.

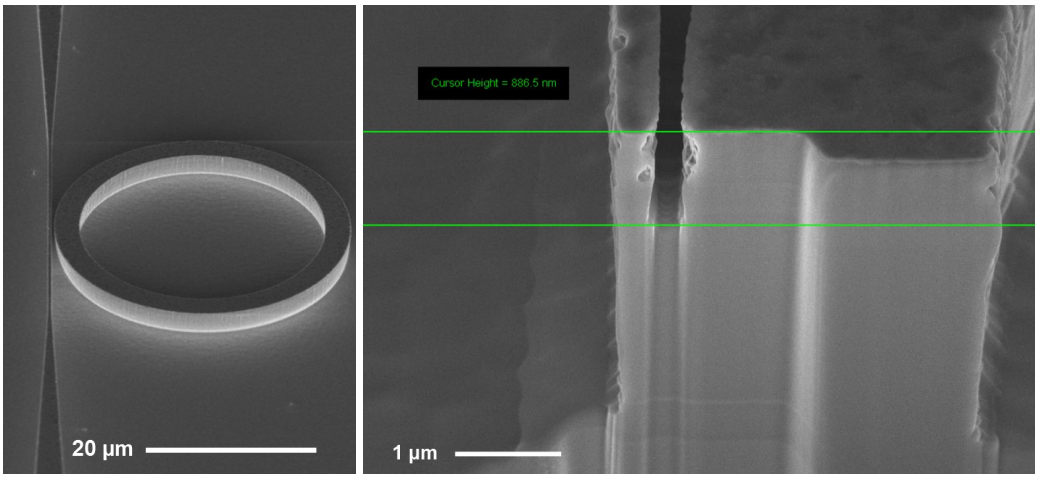

(a) (b)

Figure 6.7: SEM images of S3. (a) Microring and tapered waveguide; (b) Close-up of the coupling region (vertical cut). The sample has been fabricated at CEA.

S3: measurements and results

Experimental setup

Figure 6.8 shows the experimental setup needed for the characterization of S3. The sample is placed between a tapered microlensed fiber and a microscope objective (×50, N. A. = 0.82). The former is used to inject the light coming from the tunable laser (the same used for S2) into the waveguide, while the microscope objective is used to collect the output and redirect it onto a CCD

camera; the alignment is performed under an illuminated binocular magnifier. As in the previous section, micro-positioning holders and piezoelectric actuators are used to adjust the relative position between the fiber and the sample.

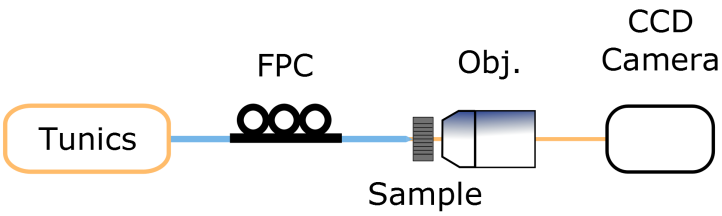

(a)

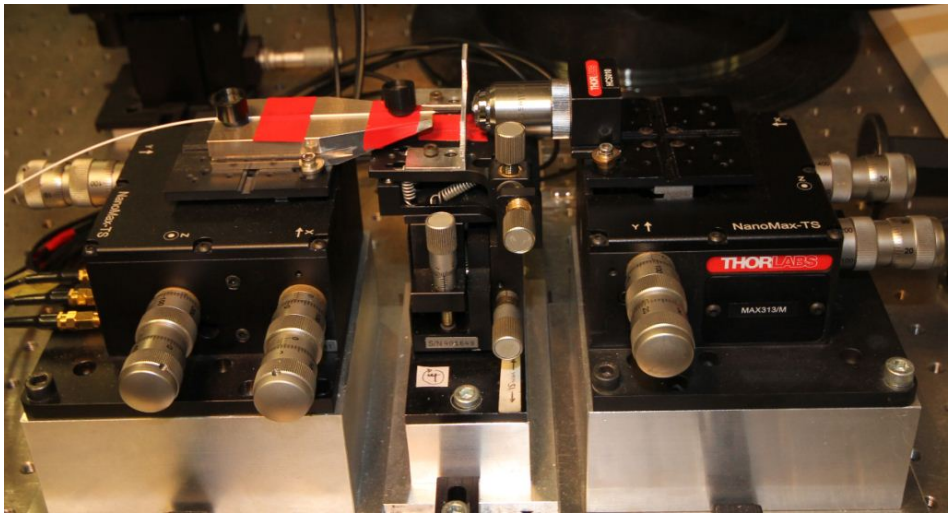

(b)

Figure 6.8: Experimental setup used for the characterization of the passive microresonators with integrated waveguides. FPC, fiber polarization controller; Obj., microscope objective.

An extensive characterization of the rings contained in S3 is carried out with several wavelength scans in order to single out possible resonances. Unfortunately, no signature of WGM excitation appears in the transmission spectra. To assess the quality of the sample, we therefore perform losses measurements. For this purpose we use the Fabry-Pérot technique [129] and obtain waveguide losses values considerably high (between 10 and 27 cm^{-1}). This could explain our inability to observe WGM resonance dips. It is worth stressing however, that S3 is a preliminary sample that has required technological steps not yet mastered by our partners (CEA and University of Würzburg).

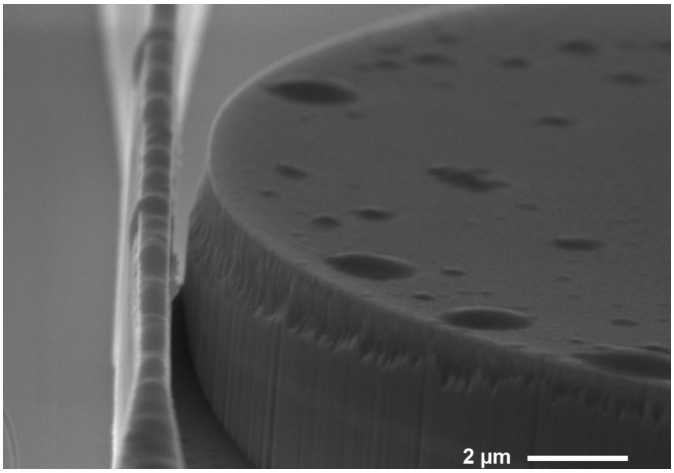

Figure 6.9: SEM picture showing the sample S4, fabricated at the University of Würzburg.

S4: measurements and results

Another sample, realized by using the high precision Focused Ion Beam (FIB) technique, has been fabricated. The new sample S4, shown in Figure 6.9, has the same vertical structure as S3.

In Figure 6.10 we show an example of transmission spectrum obtained from the linear characterization of S4. The high frequency oscillations correspond to the Fabry-Pérot fringe pattern due to the reflections at the waveguide facets. The resonances appearing on the graph correspond to the family of lowest radial order modes , and the Free Spectral Range can be estimated as:

$$\Delta\lambda = \frac{\lambda^2}{2\pi R n_g}\,, \tag{6.1}$$

where n_g is the WGM group index. At $\lambda = 1300$ nm it gives $\Delta\lambda \sim 4.55$ nm, instead of the experimental $\Delta\lambda^{\mathrm{exp}} \sim 4.61$ nm. This discrepancy is not expected to hinder THz DFG because the low THz quality factor provides a tolerance of about 140 GHz for fulfilling the phase matching.

6.3 Linear characterization in the THz region

For a further validation of the designed WGM modal structure, we proceed with the linear characterization in the THz range. The THz excitation of a single microresonator would be highly inefficient while the evanescent coupling technique is not applicable. We therefore perform reflectivity measurements on samples composed by 2D arrays of identical microcavities. Such measurements

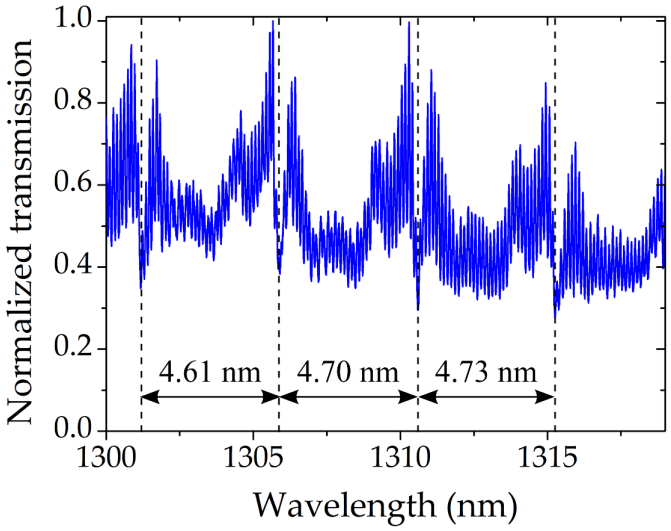

Figure 6.10: Transmission spectrum of a waveguide coupled to a resonator with radius $R = 17.5$ µm. The guide width is 500 nm in its narrowest part, while the guide-to-resonator distance is 350 nm.

are carried out both with a Fourier-Transform Infra-Red (FTIR) spectrometer at the University of Paris Diderot and with a Time-Domain Spectroscopy (TDS) system at the Danmarks Tekniske Universitet (DTU) in Copenhagen.

6.3.1 Passive samples

Samples S5 and S6

We have received two different samples from CEA, each including a 2D array of microcylinders.

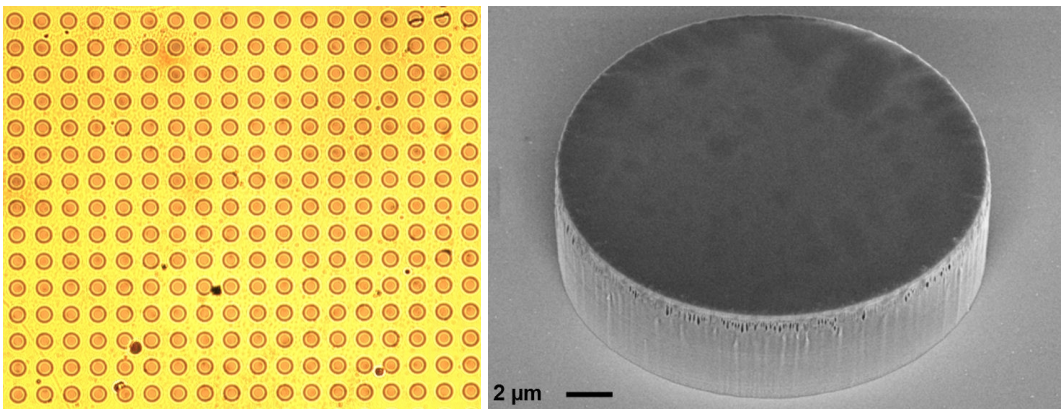

(a) (b)

Figure 6.11: Sample S6. (a) Optical microscope image of an array of microcylinders with radius $R = 20$ µm. (b) SEM close-up of a microresonator.

The epitaxial growth is the same as S2, although, in this case, the top and bottom metallic layers are needed in order to confine the THz WGMs. The first sample (S5) is composed of two matrices of microcylinders, with diameters of 20 μm (first matrix, MT1) and 40 μm (second matrix, MT2). MT1 contains a sufficient number of resonators and gives us clean experimental results. On the other hand, MT2 turns out to provide noisy spectra, probably due to the smaller number of cylinders (21×21 instead of 33×33 used for MT1). A second sample (S6) is therefore fabricated at CEA, with a larger area entirely covered by 40 μm diameter microcylinders (Fig. 6.11).

6.3.2 Fourier-Transform Infra-Red spectrometer measurements and results

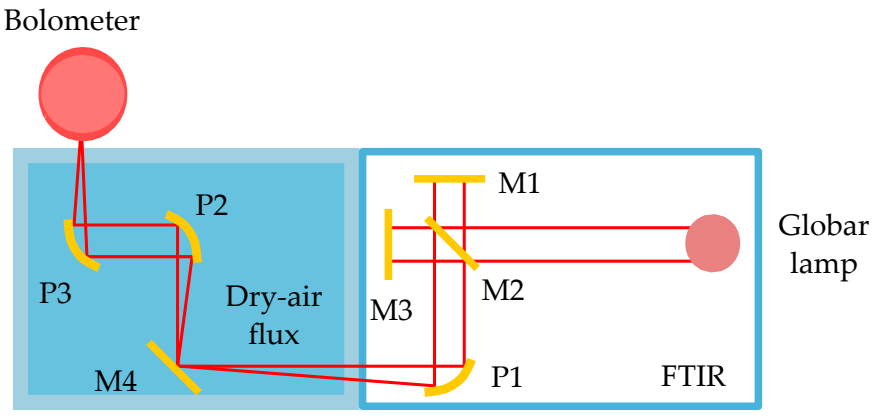

Figure 6.12: Schematic of the experimental setup for the FTIR characterization of the double-metal passive microresonators. M, mirror; P, parabolic mirror.

For the FTIR reflectivity measurements, the samples are kept into a PVC box to avoid absorption caused by humidity. For the same reason, the whole optical path (from the source to the detector) is enclosed in a water-vapor-poor environment, thanks to a continuous dry air purge. Figure 6.12 shows a schematic of the experimental setup. The incident light, emitted by a Globar lamp contained in the FTIR, is collimated onto the sample at the desired angle via a parabolic mirror.

FTIR: experimental setup

In Figure 6.13 we show the typical FTIR reflectivity spectra obtained by varying the incidence angle [130]: normal (a), 45° (b), and grazing (c). Each dip corresponds to the excitation of a different radial and azimuthal order cavity mode. The position and the width of the dips match very well the values expected from the modeling, as shown in Table 6.1.

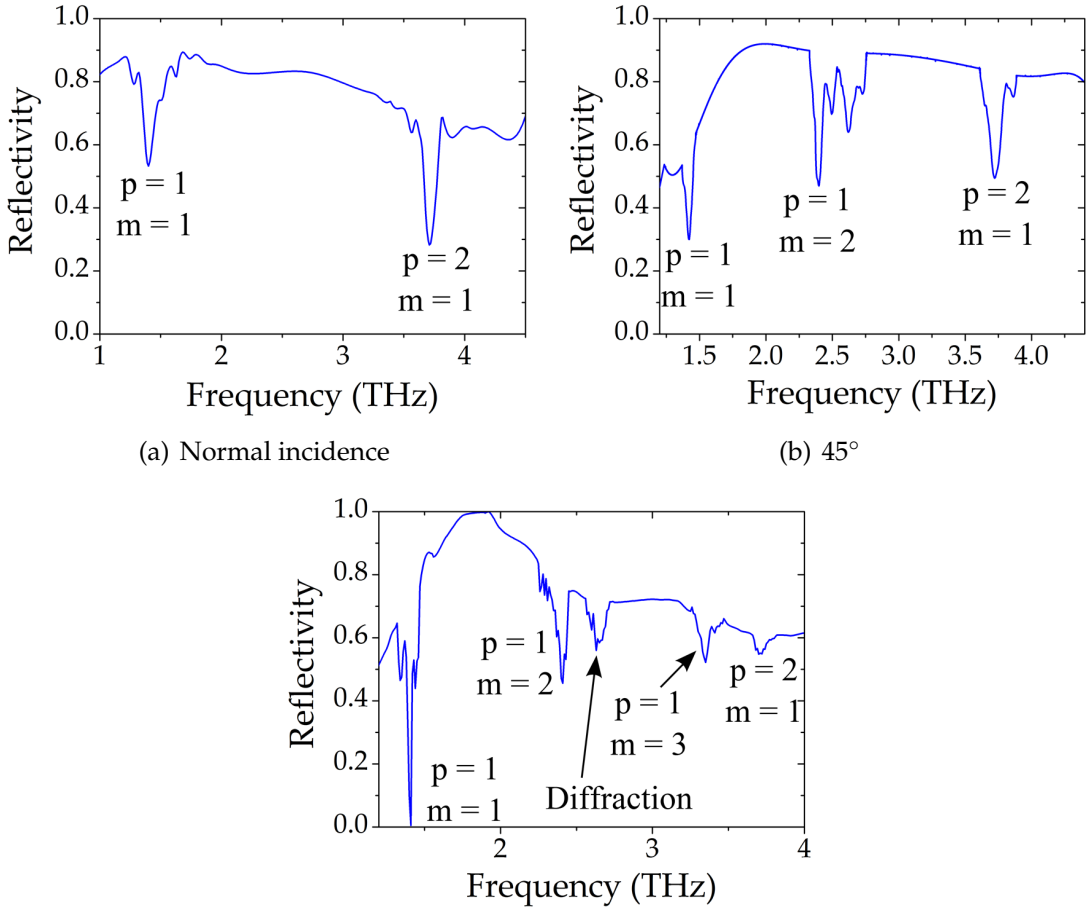

(a) Normal incidence

(b) 45°

(c) Grazing incidence

Figure 6.13: FTIR reflectivity spectra. All the spectra result from averaging approximately 200 measurements. The spectral resolution is about 7.5 GHz.

An interesting feature in these spectra is that, by varying the incidence angle, we are able to excite cavity modes with different radial and azimuthal orders. If we consider for example normal incidence (Fig. 6.13a), only WGMs with $m = 1$ - the dipole-like modes - appear on the spectrum. On the other hand, by exploiting non-vertical incidence angle, we can excite $m = 2$ modes (45° angle incidence), and $m = 3$ modes (grazing incidence). It is important to stress that the mode with (p, m) = (1, 3) is the THz WGM designed for the passive nonlinear source, which is nonlinearly phase matched with two pump WGMs around 1.3 μm. As a final remark, we note that the dip at 2.7 THz appearing in Fig. 6.13c does not correspond to a WGM, but it is due to diffraction.

		Modeling	
m	p	ν (THz)	Q
1	1	1.400	33
2	1	2.404	59
3	1	3.345	83
1	2	3.700	42

		Normal		45°		Grazing	
m	p	ν (THz)	Q^*	ν (THz)	Q^*	ν (THz)	Q^*
1	1	1.403 ± 0.007	17 ± 2	1.417 ± 0.007	32 ± 3	1.402 ± 0.007	23 ± 13
2	1	–	–	2.401 ± 0.007	59 ± 6	2.408 ± 0.007	47 ± 9
3	1	–	–	–	–	3.348 ± 0.007	41 ± 7
1	2	3.714 ± 0.007	45 ± 3	3.717 ± 0.007	47 ± 4	3.722 ± 0.007	30 ± 6

Table 6.1: Comparison between the results of our simulations and the experimental data. The experimental quality factors Q^* are estimated from the dips' FWHM.

6.3.3 Time-Domain Spectroscopy measurements and results

Samples S5 and S6 are also characterized via a fiber-coupled THz TDS system (Picometrix T-Ray 4000) with photoconductive switches for the generation and the detection of ultrashort THz transients [131] available at DTU. In fact, between 0 and 2 THz, the FTIR measurements are particularly noisy due to the presence of a filtering window on the bolometer. This is fortunately not the case for the TDS system.

TDS: experimental setup

The TDS system consists of a transmitter T and a receiver R, respectively emitting and detecting short picosecond pulses (Fig. 6.14). The sample is placed on a graduated wheel that enables to change the incidence angle α. At variance with the FTIR measurements, the focal length ℓ of the TDS system does not allow to perform measurements at normal incidence.

Reflectivity spectra are taken at various incidence angles and at frequencies between 0 and 2 THz. As an example, Fig. 6.15 shows the results obtained at 60° incidence. Since the system is not protected from humidity, several water-absorption lines are present. However, it is possible to observe the dip at 1.4 THz, as in the previous FTIR measurements.

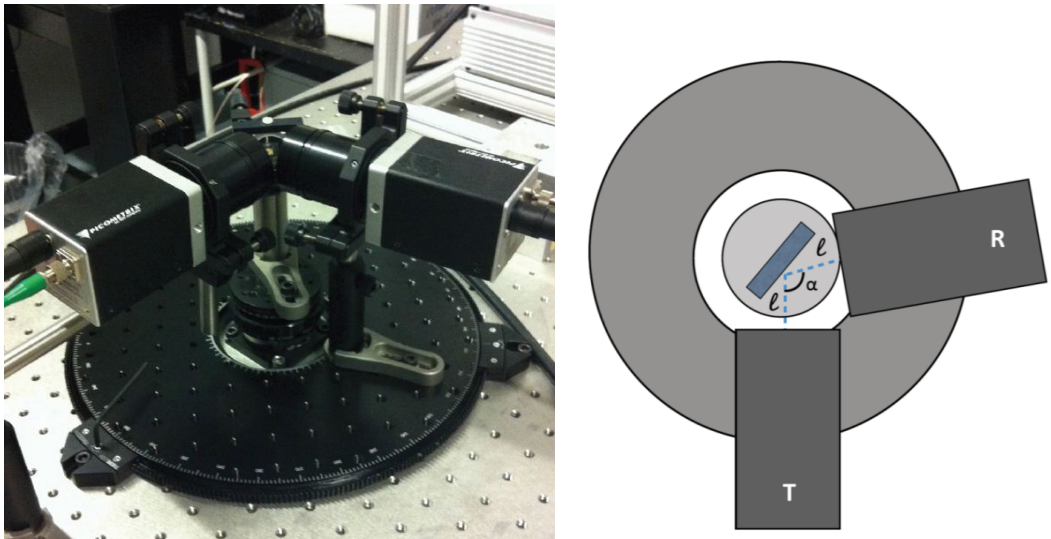

(a) (b)

Figure 6.14: Picture (a) and schematic representation (b) of the TDS system used for the THz characterization performed at DTU. T, transmitter; R, receiver; ℓ, focal length; α, incidence angle.

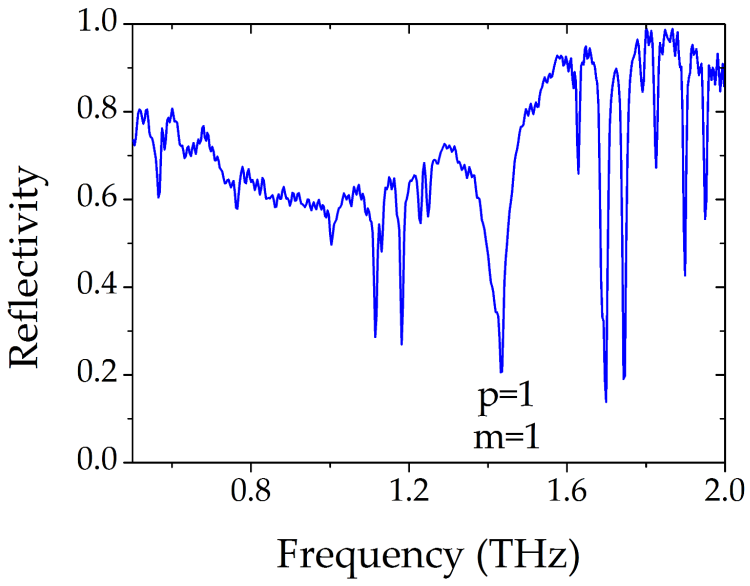

Figure 6.15: Experimental plot showing a TDS reflectivity spectrum performed at 60° incidence. The dip at 1.4 THz emerges from the water-absorption lines.

6.4 Summary

In this chapter we presented the experimental activity performed on passive microresonators in both near-IR and THz range, within the framework of the EU FET project TREASURE. From the linear measurements in the NIR, we noticed that the tapered fiber technique does not provide an efficient coupling for the large radii cylinders of interest for this project. We therefore designed samples with integrated coupling waveguides and characterized the first cavities sent by our partners. Due to the challenging technology associated to deeply etched WGM structures, there is still work to do for reducing waveguide losses and improving the quality of the cylinders sidewalls. Moreover, we performed reflectivity measurements to probe THz WGMs; the results obtained with both FTIR and TDS system agree very well with our modeling.

Right before the thesis deliver, we received the TREASURE active sample (Figure 6.16). Unfortunately, it will not be possible to characterize it before the end of my doctoral work. Nevertheless, the results obtained within the framework of this project are numerous and relevant. Finally, the collaborations and the efforts dedicated in developing codes and experiments have enabled the DON group to strongly progress on two crucial research domains for its ongoing research: nonlinear WGMphotonics and QD-based active nonlinear devices.

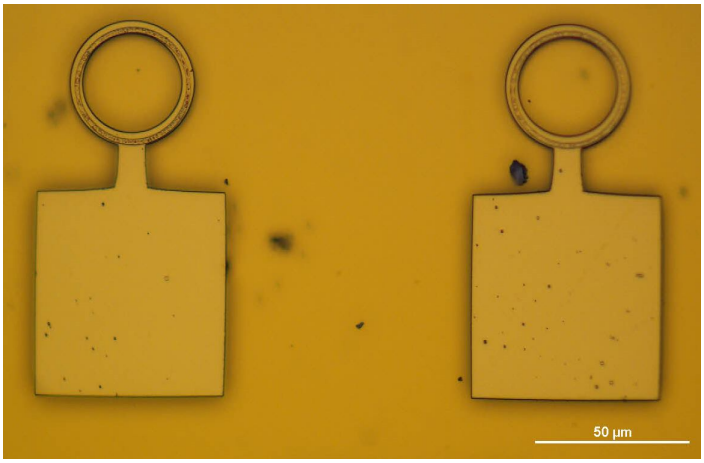

Figure 6.16: Optical microscope picture of the TREASURE active sample.

Conclusion

This doctoral work is the result of three years spent at the *Matériaux et Phénomènes Quantiques* Laboratory of the Univsersité Paris Diderot - Paris 7. In this manuscript, we reported on the design, fabrication and characterization of GaAs/AlGaAs WGM microresonators for nonlinear frequency generation.

In the **first part** of the thesis, we described our efforts in modeling and fabrication. The related work enabled us to perform optical measurements on AlGaAs WGM microdisks. The experiments carried out on the home-made fabricated samples brought us to the demonstration of SHG around 794 nm, with a pump wavelength around 1584 nm. The resulting efficiency is $\eta_{\mathrm{SHG}} = 0.7\times10^{-3}$ W^{-1}, comparable to the state of the art at $\lambda \sim 1.55$ μm, as shown in Table 6.2. This is a very encouraging result, especially if we consider that our microcavities

Technology	**L** (mm)	η (W^{-1})
$LiNbO_3$	60	14
GaP PhC wg	0.017	5×10^{-7}
Si PhC cav	N. A.	4×10^{-5}
GaN μ-ring	N. A.	2×10^{-4}
AlGaAs wires	1.5	2×10^{-3}
AlGaAs wg	2.2	7×10^{-3}
InGaP PhC wg	1.2	2×10^{-4}
this work	**N. A.**	$\mathbf{7 \times 10^{-4}}$

Table 6.2: Comparison of SHG in various integrated optics devices [40].

stem from a recent technology with considerable margin for improvements.

On a short-term perspective, our microdisks lend themselves to the demonstration of SPDC in the telecom band, with a potential impact on quantum optics applications. The highest quality factors exhibited by our microresonators [4]

4. See chapter 4, Table 4.2.

($Q_{\mathrm{FF}}^{\mathrm{intr}} \approx 5 \times 10^4$) are already sufficient for a SPDC experiment. However, it is mandatory to improve the fabrication reproducibility of our cavities in terms of both quality factors and small detunings $\Delta\lambda$ between the NIR and VIS resonances. By combining these two actions we should be able to considerably ameliorate the nonlinear performances of our device.

While the SHG experiments carried out so far were CW, the pulsed regime is more appropriate for SPDC. This would alleviate thermal issues in both fiber [5] and disks. In the DON group this kind of experiments is performed by using a Ti:Sapphire laser (MIRA from Coherent), with typical repetition rate $\tau_{\mathrm{rep}} =$ 1 MHz and pulse duration $\tau_{\mathrm{p}} = 3$ ps, respectively. Figure 6.17 reports our numerical prediction of SPDC power, for an input peak power $P_{\mathrm{peak}}^{\mathrm{in}} \approx 3$ kW, as a function of coupling and intrinsic quality factors, for the same cavity and modes employed for our SHG experiments. Since the Q factors observed in the NIR and VIS ranges differ by more than a factor 10, SPDC efficiency was calculated in two cases:

- $Q_{\mathrm{SH}}^{\mathrm{intr}} = Q_{\mathrm{SH}}^{\mathrm{cpl}} = 10^3$, with free variables $Q_{\mathrm{FF}}^{\mathrm{intr}}$ and $Q_{\mathrm{FF}}^{\mathrm{cpl}}$ (Figure 6.17a);
- $Q_{\mathrm{FF}}^{\mathrm{intr}} = Q_{\mathrm{FF}}^{\mathrm{cpl}} = 5{\times}10^4$, with free variables $Q_{\mathrm{SH}}^{\mathrm{intr}}$ and $Q_{\mathrm{SH}}^{\mathrm{cpl}}$ (Figure 6.17b).

Therefore, for an average input power $P_{\mathrm{avg}} = 10$ mW at λ_{SH}, we predict a SPDC degenerate power $P_{\mathrm{out}} \approx 2$ µW at λ_{FF}, when $Q_{\mathrm{FF}}^{\mathrm{intr}} = Q_{\mathrm{FF}}^{\mathrm{cpl}} = 5 \times 10^4$ and $Q_{\mathrm{SH}}^{\mathrm{intr}} = Q_{\mathrm{SH}}^{\mathrm{cpl}} = 1 \times 10^3$, which are the values that we should be able to obtain after slight sample improvements.

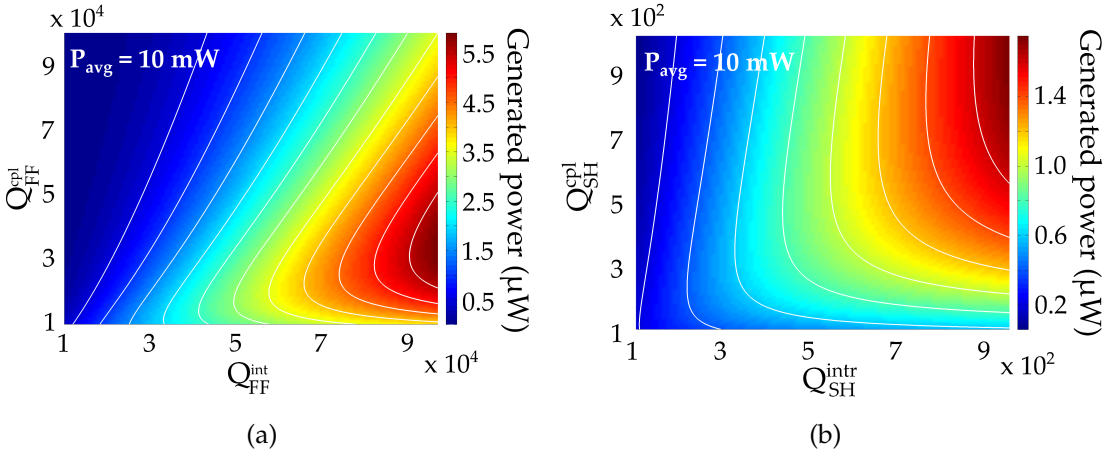

Figure 6.17: Estimate of the SPDC degenerate power, as a function of the intrinsic and coupling quality factors.

With a view on quantum optics experiments, let us express the SPDC effi-

5. The tapered fiber melts for CW input powers greater than ∼50 mW.

ciency in terms of photon pairs per pump photon:

$$\frac{N_{\text{pair}}}{N_{\text{pump}}} = \frac{P_{\text{out}}}{P_{\text{in}}^{\text{peak}}} = 0.6 \times 10^{-9} \text{ pairs/pump photon}\,. \tag{6.2}$$

This result is comparable with what observed in AlGaAs doped waveguides under optical pumping [132].

Of course, improving the samples means increasing the quality factors. Despite the higher losses experienced by AlGaAs microdisks with respect to GaAs ones, gaining more than a factor 10 on the Q factors at both wavelengths seems possible. To this end, the first mandatory step will be a further correction on the resist side. Its deposition and removal steps are critical, since this is the moment when the cavity takes shape. A resist reflow right after the development can help in reducing the possible roughness on the disk sidewall from the very beginning of the process. Morover, a comparison between the roughness caused by wet or dry etching will be another interesting test to make. Despite the general idea of obtaining smoothest cavities with the former technique, high-resolution SEM pictures of microresonators fabricated in the two different ways show comparable results with acid and ICP etching.

Other improvements concern the coupling of light to the microdisks. We saw in chapter 4 the issues linked to the tapered fiber technique. If we want to find the best coupling condition, the relative position between disk and fiber is certainly the most sensitive parameter. The random displacements of the fiber caused by air, thermal drift or fiber tension result in serious difficulties for the reproducibility of our measurements. An integrated waveguide would solve such a problem, at the expense of the flexibility provided by variable cavity-to-fiber distances. Various shapes of waveguides (straight, bent around one or both sides of the cavity, ...) are conceivable, and only fabrication and experimental efforts will proclaim the best one.

In the **second part** of the thesis we described the work carried out within the framework of a challenging project, aiming at an electrically pumped THz emitter working at room temperature, based on DFG in a WGM microresonator. In this case our task was to characterize in the near-IR and THz ranges the samples fabricated at CEA and at University of Würzburg. On the near-IR side, after receiving some samples that quickly underwent oxidation, we measured some new cavities from which we observed problems related to the fiber-coupling scheme again. Further measurement performed on microring-like samples with integrated waveguides have led to a more complete comprehension of the best resonator geometry to use. In the THz range the measurements carried out on mircroresonators arranged in 2D matrices with double-metal structure confirmed the results of our modeling. Unfortunately, the challenging technological development has required a huge effort, therefore the ongoing activities had

to slow down. Nevertheless, these measurements have provided causes for reflection on the features to gradually modify towards the final structure.

On a longer term perspective, the work done during these three years and its further possible developments might bring to customized integrated coherent sources for environmental sensing and spectroscopic applications, or also to the investigation of more exotics devices, such as comb generation [11, 12] and optical vortex beam emitters [133].

In particular, frequency combs have already been generated in silica and silicon nitride WGM resonators via Four-Wave Mixing (FWM). Analogous results in AlGaAs WGM microrings would take advantage from the excellent optical properties and long-standing development of the III-V platform.

FWM is enabled by the interplay between the $\chi^{(3)}$ nonlinearity and the group-velocity dispersion (GVD) in the microring. Specifically, the pump frequency has to lie within the anomalous-GVD bandwidth, so as to compensate for the nonlinear phase-mismatch and give rise to an efficient nonlinear process. By following Ref. [12], we have recently started to simulate the GVD for $Al_{0.2}Ga_{0.8}As$ microrings with different cross-sections. The curves of Figure 6.18 show that an appropriate choice of light polarization and microring dimensions might provide anomalous dispersion.

A further challenge to face will certainly be the integration of lasers within the nonlinear cavities. Good lasing performances and an efficient second-order

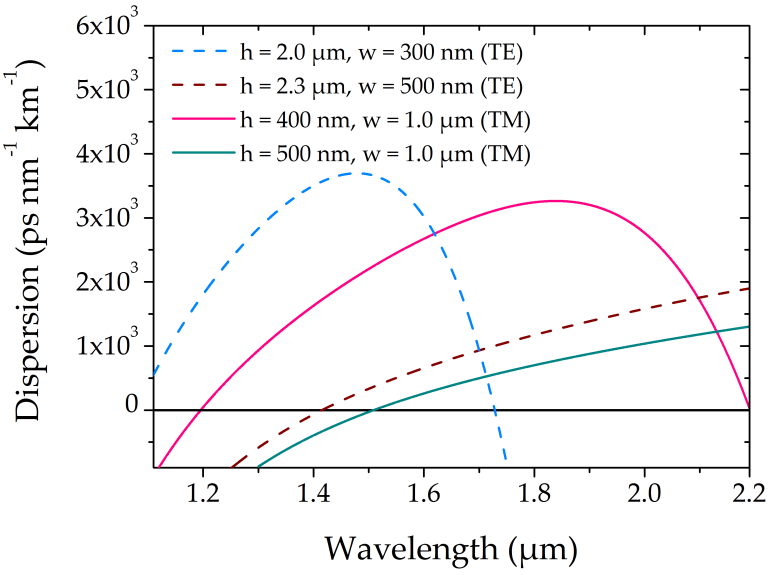

Figure 6.18: Dispersion vs. wavelength for the fundamental mode of an $Al_{0.2}Ga_{0.8}As$ microring.

nonlinear process at the same time are highly desirable for a good final device. To this end, the know-how acquired during this thesis work might allow Natalia Morais, the PhD student who will pursue this research activity in the next years, to converge on a WGM nonlinear microcavity with an integrated QD inter-band diode. Such a versatile device would draw on the results described in the two parts of the manuscript with the addition of the recent achievements of the QCL community [134, 48, 135]. In the wake of what demonstrated in Si coupled resonator optical waveguides (CROWs) [136, 137], it would also be possible to exploit different coupling configurations, passing from a stand-alone disk to a series of coupled microresonators with bus waveguides integrated on the same chip. This could favor the development of challenging projects on the III-V platform, without ceasing of taking advantage of the strong second-order nonlinearity of such materials.

Appendices

Appendix A

On quality factors

To estimate the intrinsic quality factors Q^{intr} of our resonant WGMs, we use standard Coupled-Mode Theory (CMT); the fiber transmission at resonance can be written as:

$$T = \left(\frac{1-K}{1+K}\right)^2 , \tag{A.1}$$

with $K = Q^{\text{cpl}}/Q^{\text{intr}}$, and where Q^{cpl} is the coupling quality factor of the WGMs. By solving Eq. A.1 for K, we get:

$$K = \frac{1-(\pm\sqrt{T})}{1+(\pm\sqrt{T})} , \tag{A.2}$$

where the sign choice corresponds to overcoupling or undercoupling.

As shown in chapter 1, the coupling quality factor is related to the loaded (measured) quality factor through:

$$\frac{1}{Q^{\text{intr}}} + \frac{1}{Q^{\text{cpl}}} = \frac{1}{Q} , \tag{A.3}$$

from which we get:

$$Q^{\text{cpl}} = \frac{Q^{\text{intr}} Q}{Q^{\text{intr}} - Q} . \tag{A.4}$$

From Eqs. A.2 and A.4, we get:

$$Q^{\text{intr}} = \left(1 + \frac{1}{K}\right) Q = \left(1 + \frac{1+(\pm\sqrt{T})}{1-(\pm\sqrt{T})}\right) Q . \tag{A.5}$$

Therefore, from the depth (T) and width (Q) of the measured resonance we can estimate the intrinsic (Eq. A.5) and coupling (Eq. A.4) quality factors. In the case of the measurements performed on the growth CAT104, we find $T_{\text{SH}} = 0.93$ and $T_{\text{FF}} = 0.95$, $Q_{\text{FF}} = 1.4 \cdot 10^4$ and $Q_{\text{SH}} = 4.9 \cdot 10^2$.

As far as the NIR mode is concerned, the first solution of Eq. A.5 gives: $Q^{\text{intr}}_{\text{FF}} = 7.86 \cdot 10^5$ and $Q^{\text{cpl}}_{\text{FF}} = 1.43 \cdot 10^4$. This is not possible since the calculated

radiation limited quality factor is $Q_{\mathrm{FF}}^{\mathrm{rad}} = 1.01 \cdot 10^5$. The other solution gives: $Q_{\mathrm{FF}}^{\mathrm{intr}} = 1.43 \cdot 10^4$ and $Q_{\mathrm{FF}}^{\mathrm{cpl}} = 7.86 \cdot 10^5$. This is acceptable and tells us that we are undercoupled ($Q^{\mathrm{cpl}} > Q^{\mathrm{intr}}$).

For the VIS mode, the first solution gives: $Q_{\mathrm{SH}}^{\mathrm{intr}} = 3.87 \cdot 10^4$ and $Q_{\mathrm{SH}}^{\mathrm{cpl}} = 4.96 \cdot 10^2$, while the second: $Q_{\mathrm{SH}}^{\mathrm{intr}} = 4.96 \cdot 10^2$ and $Q_{\mathrm{SH}}^{\mathrm{cpl}} = 3.87 \cdot 10^4$. From our measurements (transmission vs fiber-to-disk distance at the SH) it seems that the resonance contrast increases when the fiber gets closer to the disk. This points to undercoupling, which means that we should retain the second solution: $Q_{\mathrm{SH}}^{\mathrm{intr}} = 4.96 \cdot 10^2$ and $Q_{\mathrm{SH}}^{\mathrm{cpl}} = 3.87 \cdot 10^4$.

From the results provided by the measurements on both CAT104 and D8T157, it is clear that the intrinsic quality factors of the VIS WGM are lower than the ones in the NIR. This may be due to two main factors:

– surface roughness;
– Two-Photon Absorption (TPA).

A.1 Surface Roughness

If we assume Rayleigh-like scattering from roughness at the disk sidewalls we have:

$$\alpha_s = \frac{C(\lambda)}{\lambda^4}\,, \tag{A.6}$$

where $C(\lambda)$ depends on λ through the refractive index and the overlap integral between the field and the surface corrugations. We can simplify the calculation by assuming that the ratio $C(\lambda_{\mathrm{SH}})/C(\lambda_{\mathrm{FF}})$ is the same as the ratio of the fields (squared) at the interface of the disk. In other words:

$$\frac{C(\lambda_{\mathrm{SH}})}{C(\lambda_{\mathrm{FF}})} \sim \frac{|E(\lambda_{\mathrm{SH}}, \rho = R)|^2}{|E(\lambda_{\mathrm{FF}}, \rho = R)|^2} = 0.28\,, \tag{A.7}$$

where the last equality follows from simulations. Therefore we get:

$$\alpha_s(\lambda_{\mathrm{SH}}) \sim \frac{C(\lambda_{\mathrm{SH}})}{C(\lambda_{\mathrm{FF}})} \left(\frac{\lambda_{\mathrm{FF}}}{\lambda_{\mathrm{SH}}}\right)^4 \alpha_s(\lambda_{\mathrm{FF}}) = 4.5\, \alpha_s(\lambda_{\mathrm{FF}})\,. \tag{A.8}$$

If we calculate the intrinsic quality factor of the VIS field from this value, we get: $Q_{\mathrm{SH}}^{\mathrm{intr}} = 6.72 \cdot 10^3$. This is 10 times higher than what estimated in the previous section, so other loss mechanisms must be present.

A.2 TPA

From the quality factors estimated above, we can calculate the power circulating inside the disk for a given external power and estimate the TPA-limited

quality factor. By doing this, we find (for an external power of 4 mW, i.e. almost the max value in Fig. 4.6b):

$$Q_{\mathrm{TPA}} = 1.9 \cdot 10^7 \,.$$

This value is much higher than the value of the intrinsic quality factor that we have obtained, therefore TPA does not affect the quality factor of the VIS mode. This happens because the mode is undercoupled: with 4 mW of external power we have only 0.6 mW of power circulating inside the disk. This result is consistent with our measurements: we do not see any decrease of Q_{SH} while increasing the laser power.

We can conclude that TPA does not play any role neither for the NIR nor for the VIS (there is no TPA in the NIR, while the power circulating in the disk in the VIS is too low).

A.3 Nonlinear refraction

The resonance wavelength of a WGM can be roughly approximated through the relation:

$$2\pi R = m\frac{\lambda}{n} \,. \tag{A.9}$$

Nonlinear refraction can be described via:

$$n = n(\lambda, P_{\mathrm{circ}}) = n_0(\lambda) + n_2(\lambda)\frac{P_{\mathrm{circ}}}{\mathcal{A}_{\mathrm{eff}}} \,, \tag{A.10}$$

where n_0 is the power-independent refractive index (Gehrsitz model), n_2 the nonlinear refractive index, P_{circ} the WGM power circulating in the disk, and $\mathcal{A}_{\mathrm{eff}}$ the effective area of the mode. The power circulating in the disk is deduced from the CMT, and is related to the power in the fiber (P_{ext}) through the relation [61]:

$$P_{\mathrm{circ}} = \frac{2}{\pi m}\left(\frac{Q^{\mathrm{cpl}}}{(1+Q^{\mathrm{cpl}}/Q^{\mathrm{intr}})^2}\right) P_{\mathrm{ext}} \,. \tag{A.11}$$

By using Eq. A.9 together with Eqs. A.10 and A.11 we get:

$$\lambda = \frac{2\pi R}{m}\left(n_0(\lambda) + n_2(\lambda)\frac{2}{\pi m \mathcal{A}_{\mathrm{eff}}}\frac{Q^{\mathrm{cpl}}}{(1+Q^{\mathrm{cpl}}/Q^{\mathrm{intr}})^2}\right) P_{\mathrm{ext}} \,. \tag{A.12}$$

If we differentiate Eq. A.12 with respect to P_{ext} and assume that $\mathrm{d}n_0/\mathrm{d}\lambda \approx 0$ and $\mathrm{d}n_2/\mathrm{d}\lambda \approx 0$ (λ does not change very much, so this is not too inaccurate) we have:

$$\frac{\mathrm{d}\lambda}{\mathrm{d}P_{\mathrm{ext}}} = \frac{4Rn_2}{m^2\mathcal{A}_{\mathrm{eff}}}\frac{Q^{\mathrm{cpl}}}{(1+Q^{\mathrm{cpl}}/Q^{\mathrm{intr}})^2} \,. \tag{A.13}$$

Fundamental Frequency

According to Ref. [138], the nonlinear refractive index is $n_2 \approx 10^{-17}$ m^2/W for $Al_{0.36}Ga_{0.64}As$ and at $\lambda = 1.55$ μm. If we use this value (together with the Q-factors previously estimated) in Eq. A.12, we get $\mathrm{d}\lambda/\mathrm{d}P_{\mathrm{ext}} \approx 0.002$ nm/mW, which is quite smaller than the experimental value ($\mathrm{d}\lambda/\mathrm{d}P_{\mathrm{ext}} \approx 0.07$ nm/mW). Therefore it is not Kerr effect and we are left with an increase of temperature in the cavity.

Second Harmonic

When the wavelength approaches the bandgap, the nonlinear refractive index n_2 becomes negative [82, 139]. According to Eq. A.12, this should give a negative sign for $\mathrm{d}\lambda/\mathrm{d}P_{\mathrm{ext}}$ (Fig. 4.6b should have the opposite slope if nonlinear refraction played a role in our disk at the SH). The only thing that can explain the current slope of Fig. 4.6b seems (again) to be an increase of temperature (which increases the refractive index).

A.4 Summary

- TPA does not play any role neither for the FF nor for the SH (there is no TPA at the FF, while the power circulating in the disk at the SH is too low).
- Fig. 4.6 is not due to nonlinear refraction. It seems to be the result of some absorption/heating (maybe related to surface oxides).

Appendix B

List of Publications and Conferences

Publications and other communications

- A. Andronico, **S. Mariani**, F. Ghiglieno, J. Claudon, M. Munsch, J. M. Gérard, I. Favero, S. Ducci, and G. Leo, «Tuning of a nonlinear THz emitter», *Opt. Express*, Vol. 20, Issue 16, pp. 17678-17683 (2012).
- **S. Mariani**, A. Andronico, I. Favero, S. Ducci, Y. Todorov, C. Sirtori, M. Kamp, J. Claudon, J. M. Gérard, X. Wang, P. U. Jepsen, and G. Leo, «AlGaAs Micro-Pillars for THz Difference Frequency Generation», *IEEE Transactions on Terahertz Science and Technology*, Vol. 3, Issue 4, pp. 472-478 (2013).
- **S. Mariani**, A. Andronico, I. Favero, S. Ducci, Y. Todorov, C. Sirtori, M. Kamp, J. Claudon, J. M. Gérard, X. Wang, P. U. Jepsen, and G. Leo, «Quantum-dot micropillars for parametric THz emission», *Proceedings of SPIE*, Vol. 8631, pp. 86312B-86312B-8 (2013).
- **S. Mariani**, A. Andronico, O. Mauguin, A. Lemaître, I. Favero, S. Ducci, and G. Leo, «AlGaAs microdisk cavities for second-harmonic generation», *Opt. Lett.*, Vol. 38, Issue 19, pp. 3965-3968 (2013).
- **S. Mariani**, A. Andronico, A. Lemaître, I. Favero, S. Ducci, and G. Leo, «Second-harmonic generation in AlGaAs microdisks in the telecom range», *Opt. Lett.*, Vol. 39, Issue 10, pp. 3062-3065 (2014).

Conference presentations

- **S. Mariani***, F. Ghiglieno, A. Andronico, I. Favero, S. Ducci, Y. Todorov, C. Sirtori, M. Kamp, M. Munsch, J. Claudon, J. M. Gérard, and G. Leo, «Optical Characterization of AlGaAs Nonlinear THz Emitters», Semiconductor Sources and Detectors of Terahertz Radia-

tion, GDR-I Workshop, Avril 24−27, 2012, Tignes, France.

- **S. MARIANI***, F. GHIGLIENO, A. ANDRONICO, I. FAVERO, S. DUCCI, Y. TODOROV, C. SIRTORI, M. KAMP, M. MUNSCH, J. CLAUDON, J. M. GÉRARD, AND G. LEO, «Linear Characterization of THz DFG Emitters», 3rd EOS Topical Meeting on Terahertz Science & Technology (TST 2012), 17−20 June 2012, Prague, Czech Republic.
- **S. MARIANI**, F. GHIGLIENO, A. ANDRONICO*, I. FAVERO, S. DUCCI, Y. TODOROV, C. SIRTORI, M. KAMP, M. MUNSCH, J. CLAUDON, J. GÉRARD, AND G. LEO, «Optical Characterization of Nonlinear THz Emitters», Nonlinear Optics, 17−21 June 2012, Colorado Springs, USA.
- **S. MARIANI***, A. ANDRONICO, I. FAVERO, S. DUCCI, Y. TODOROV, C. SIRTORI, M. KAMP, J. CLAUDON, J. M. GÉRARD, AND G. LEO, «Linear Optical Characterization of AlGaAs Nonlinear THz Emitters», École résidentielle Nanoscience Île-de-France 2012, 24−29 June 2012, Le Tremblay-sur-Mauldre, France.
- **S. MARIANI**, A. ANDRONICO, I. FAVERO, S. DUCCI, Y. TODOROV, C. SIRTORI, M. KAMP, J. CLAUDON, J. M. GÉRARD, AND G. LEO*,«AlGaAs micropillars for THz DFG», (invited) NLO 50 International Symposium, 8−10 October 2012, Barcelona, Spain.
- **S. MARIANI**, A. ANDRONICO, I. FAVERO, S. DUCCI, Y. TODOROV, C. SIRTORI, M. KAMP, J. CLAUDON, J. M. GÉRARD, T. WANG, P. U. JEPSEN, AND G. LEO*, «Quantum-Dot Micropillars for Parametric THz Emission», Photonics West 2013, 2−7 March 2013, San Francisco, USA.
- **S. MARIANI**, A. ANDRONICO, I. FAVERO, S. DUCCI, Y. TODOROV, C. SIRTORI, T. WANG, P. U. JEPSEN, M. KAMP, J. CLAUDON, J. M. GÉRARD, AND G. LEO*, «Microring for DFG THz generation: concept and preliminary characterization», (invited) The 7th Terahertz Days / GDR-I Workshop, 25−27 March 2013, Cargèse, France.
- **S. MARIANI***, A. ANDRONICO, O. MAUGUIN, A. LEMAÎTRE, I. FAVERO, S. DUCCI, AND G. LEO, «Microcavités en AlGaAs pour la génération de second harmonique à 1.55 μm», Journées Nationales des Cristaux pour l'Optique (JNCO 2013), 10−12 June 2013, Cherbourg, France.
- G. LEO, **S. MARIANI**, A. ANDRONICO*, I. FAVERO, S. DUCCI, Y. TODOROV, C. SIRTORI, M. KAMP, J. CLAUDON, AND J. M. GÉRARD, «Microlaser à anneau pour la génération de fréquences THz», Journées Nationales des Cristaux pour l'Optique (JNCO 2013), 10−12 June 2013, Cherbourg, France.
- **S. MARIANI***, A. ANDRONICO, O. MAUGUIN, A. LEMAÎTRE, I. FAVERO, S. DUCCI, AND G. LEO, «Fabrication de mircodisques en AlGaAs pour le doublage de fréquence dans le proche IR», Journées Nationales d'Optique Guidée (JNOG 33), 8−11 July 2013, Villetaneuse, France.

– **S. MARIANI**, A. ANDRONICO*, Y. TODOROV, C. SIRTORI, I. FAVERO, S. DUCCI, M. KAMP, J. CLAUDON, J. M. GÉRARD, AND G. LEO, «Microcavités à modes de galerie pour la génération de THz», Journées Nationales d'Optique Guidée (JNOG 33), 8−11 July 2013, Villetaneuse, France.
– **S. MARIANI***, A. ANDRONICO, A. LEMAÎTRE, I. FAVERO, S. DUCCI, AND G. LEO, «AlGaAs microdisks for SHG in the telecom range», SPIE Photonics Europe 2014, 14−17 April 2014, Brussels, Belgium.
– **S. MARIANI***, A. ANDRONICO, J.M. GÉRARD, I. FAVERO, S. DUCCI, AND G. LEO, «Quantum dot diode optical parametric oscillator», SPIE Photonics Europe 2014, 14−17 April 2014, Brussels, Belgium.

Articles

In the following pages we include the papers reporting on the work presented in this doctoral thesis.

AlGaAs microdisk cavities for second-harmonic generation

Silvia Mariani,[1] Alessio Andronico,[1] Olivia Mauguin,[2] Aristide Lemaître,[2] Ivan Favero,[1] Sara Ducci,[1] and Giuseppe Leo[1,*]

[1]*Université Paris Diderot, Sorbonne Paris Cité, Laboratoire Matériaux et Phénomènes Quantiques, CNRS-UMR 7162, 10 rue Alice Domon et Léonie Duquet, 75013 Paris, France*

[2]*Laboratoire de Photonique et Nanostructures, CNRS, Route de Nozay, 91460 Marcoussis, France*

**Corresponding author: giuseppe.leo@univ-paris-diderot.fr*

Received July 23, 2013; revised August 30, 2013; accepted August 30, 2013; posted September 3, 2013 (Doc. ID 194327); published September 30, 2013

We report on the design, the fabrication, and the optical characterization of AlGaAs microdisks suspended on a GaAs pedestal, conceived for second-harmonic generation with a pump in the third telecom window. We discuss the results concerning the linear characterization of whispering gallery modes at fundamental and second-harmonic wavelengths, an essential step prior to the investigation of quasi-phase-matched processes in this type of microcavity.

OCIS codes: (190.4223) Nonlinear wave mixing; (140.3945) Microcavities; (220.4000) Microstructure fabrication.
http://dx.doi.org/10.1364/OL.38.003965

Semiconductor microresonators have already gained a prominent place in today's photonics, as an ideal environment for highly enhanced light-matter interactions like nonlinear wave mixing [1] and optomechanics. From low-threshold electrically injected optical parametric oscillators to high-speed nanosensors, a couple of materials and technologies promise a number of breakthrough applications at a chip scale. On the materials side, silicon and gallium arsenide are the most explored platforms in the telecom infrared to date: the former with its huge advantage in terms of monolithic CMOS integration, as well as with stimulated Raman [2] and $\chi^{(3)}$ processes [3]; the latter with its giant $\chi^{(2)}$ and the potential of laser integration associated to its direct gap [4]. With both material systems, microdisk and microring technology rivals photonic crystals, with a lower number of design options but a simpler fabrication.

While sharing the same whispering-gallery-mode (WGM) cavity physics, semiconductor microrings and suspended microdisks seem mostly suited for their robust heat sink and highly sensitive behavior, respectively. Microrings have been reported, e.g., in silicon as four-wave mixing sources [5] and Raman lasers [6], and in GaAs as quantum-dot lasers [7]. Microdisks have been demonstrated in both materials too, for example as high-frequency optomechanical resonators [8–11].

AlGaAs microdisks have also been proposed for second-harmonic generation (SHG), whose performances are granted by the high optical confinement and modal overlap between the interacting fields, as well as the effective quasi-phase matching in homogeneous WGM cavities [12,13]. More recently, AlGaAs microrings have also been suggested as terahertz emitters [14,15] or entangled photons sources [16]. To date, the only experimental demonstration of SHG in a semiconductor WGM cavity has been reported in a GaAs microdisk [17,18], with a pump wavelength around 2 μm. This wavelength choice is necessary to avoid linear absorption for the second-harmonic (SH) and two-photon absorption (TPA) for the fundamental frequency (FF) in this material.

With a view to possible applications, it would be certainly interesting to have the same device operating with a pump in the third telecom window. To this end, the WGM cavity should consist of an $Al_xGa_{1-x}As$ microdisk with $x > 0.28$, which has never been done to the best of our knowledge.

In this Letter, we report on the design, fabrication, and characterization of an $Al_{0.4}Ga_{0.6}As$ microdisk on a GaAs pedestal for frequency doubling at 1550 nm. For the modeling of disk resonances we used a 2D finite-difference frequency-domain code developed following [19]. In particular, we found that a cavity with a radius $R = 1.866$ μm and thickness $h = 150$ nm can be used to phase match a FF mode ($\lambda_{FF} = 1.5346$ μm, $m = 12$, $p = 1$) and a SH mode ($\lambda_{SH} = 0.7673$ μm, $m = 26$, $p = 2$), where $m(p)$ is the azimuthal (radial) modal order, respectively. The computed modal volumes are $V_{eff}(FF) = 0.76$ μm^3 and $V_{eff}(SH) = 0.55$ μm^3, while their nonlinear overlap integral is $I_{ov} = 75$ J$^{-1/2}$. The latter is defined as

$$I_{ov} = \int \varepsilon_0 \frac{\chi^{(2)}_{ijk}}{2} \frac{E_i^*(\lambda_{SH})}{\sqrt{U_{SH}}} \frac{E_j(\lambda_{FF}) E_k(\lambda_{FF})}{U_{FF}} dv, \quad (1)$$

where E is the electric field and U the WGM energy.

Moreover, for WGM quality factors of about $Q = 10^4$, we calculated a nonlinear conversion efficiency of 10^{-3}/mW, in agreement with what was reported in [18].

While $Al_{0.18}Ga_{0.82}As$ microdisks on $Al_{0.7}Ga_{0.3}As$ pedestals have been already reported [20], for the fabrication of our aluminum-rich cavities we had to resort to a new technological development to control their geometrical parameters. In fact, hydrobromic and hydrofluoric acids, which are widely used for the fabrication of GaAs or low-Al AlGaAs cavities, could not be employed in our case.

The microdisks, grown by molecular beam epitaxy on a GaAs substrate, consist of an AlGaAs layer lying on a GaAs sacrificial layer. In order to maximize the chances of meeting the phase-matching condition by systematically exploring several WGMs on the same sample, the top layer has a deliberate gradient for both the thickness

0146-9592/13/193965-04$15.00/0

(between 138 and 172 nm) and the Al concentration (between 39.1% and 47.4%).

We use e-beam lithography to draw the circular patterns with high accuracy and a two-step wet chemical etching for the definition of the cavities. The first etching step, requiring a nonselective solution composed of acetic acid, hydrobromic acid, and potassium dichromate [21], is used to reveal the GaAs layer. In the subsequent step, the latter is underetched with a NH_4OH-based solution to obtain the pedestals. Optical lithography followed by an additional step of wet chemical etching allows us to define a mesa to adapt the final shape of the sample to our experimental setup (Fig. 1). Following these guidelines, we fabricated disks with diameters ranging from 3660 to 3860 nm, and with a pedestal ~3 μm high and ~500 nm wide.

The WGMs excitation and the optical characterization of the AlGaAs microdisks were carried out via evanescent coupling with a silica tapered fiber [22]. The same fiber was used for the experiments at both FF and SH wavelengths. All the measurements were performed with the setup sketched in Fig. 2. The sample and the tapered fiber are placed in front of an objective, which is used for the alignment; white light reflected by the sample is redirected onto a CCD camera connected to a computer display, while an InGaAs detector is used to collect the fiber output. The entire system is enclosed in a transparent box to protect all the components from air currents, humidity, and dust. This box is also equipped with micropositioned holders that allow a full 3D alignment of the system. A piezo controller is used to finely adjust the relative position between the fiber and the sample. Finally, a half-wave plate and a polarizer allow to control and select the polarization of the light.

In order to investigate the spectral properties of our cavities, we measured two separate transmission spectra using two CW external-cavity tunable laser diodes emitting in the 1500–1600 nm and in the 755–785 nm range, respectively. In both cases, the first step is to perform a quick scan over the entire wavelength span, to check for the presence of possible resonances (Fig. 3). Then we carry out a finer acquisition around the resonance wavelength (insets in Fig. 3). In all spectra and for each scan, the transmission of the fiber coupled to the microdisk is normalized to the transmission of the fiber alone. Please note that, in the case of visible spectra we also need a polarization control to select the TM modes [Fig. 3(b)]. This is not necessary in the telecom band, since the disks do not support TM modes at these wavelengths.

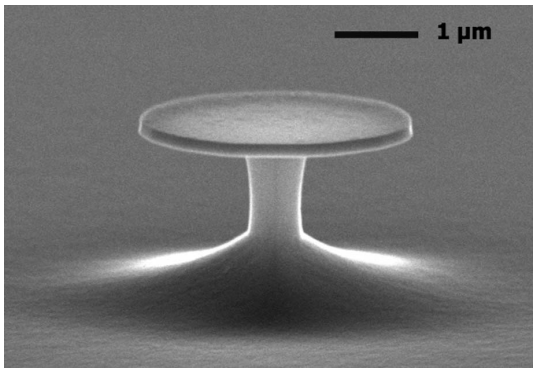

Fig. 1. Scanning-electron microscope side-view picture of an AlGaAs disk suspended over a GaAs pedestal.

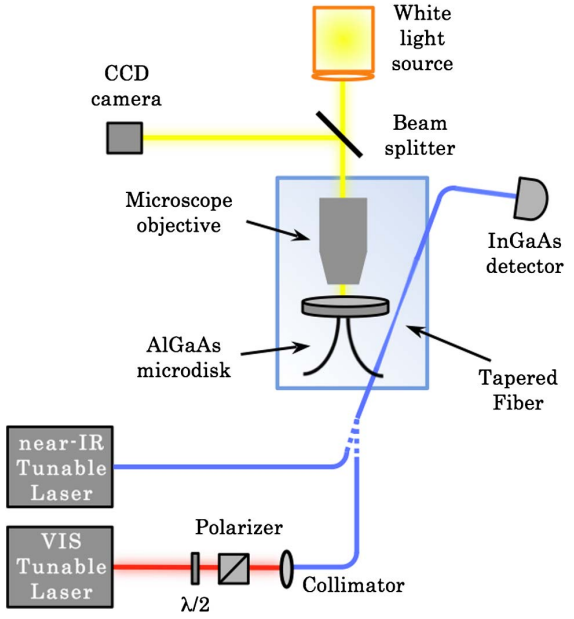

Fig. 2. Schematic of the experimental setup used for the characterization of the AlGaAs suspended microdisks.

The results of the measurements were compared to the values obtained from simulations, in order to identify the resonant WGMs and extract their m and p numbers. For a microdisk with radius $R = 1.85$ μm and $x = 47.4\%$, we were able to observe two adjacent TE-polarized modes at λ_{FF} and two adjacent TM-polarized modes at λ_{SH}. In the inset of Fig. 3(a), we show the resonance at $\lambda_{FF} = 1508.9$ nm, which corresponds to the WGM of interest for SHG ($p = 1$, $m = 12$) and has a loaded quality factor $Q_{FF} = 1.40 \times 10^4$. By repeating the same measurements for different fiber-to-disk distances [23], we were able to estimate its intrinsic quality factor, obtaining $Q^{int} = 1.43 \times 10^4$. In addition, in the inset of Fig. 3(b) we show the WGM at $\lambda_{SH} = 767.6$ nm (1534.84/2 nm), which corresponds to the ($p = 2$, $m = 26$) WGM and has a loaded quality factor $Q_{SH} = 4.90 \times 10^2$. In this case, the estimated intrinsic quality factor is $Q^{int} = 4.96 \times 10^2$.

Please notice that the discrepancy between λ_{FF} and $2\lambda_{SH}$ is due to a nonoptimal disk radius. This issue is linked to the difficulty of fabricating lines of disks having small radial variations (<20 nm), while the energy conservation is quite sensitive to the cavity radius ($d(\lambda_{FF} - 2\lambda_{SH})/dR = 0.18$, being $d\lambda_{FF}/dR = 0.62$ and $d\lambda_{SH}/dR = 0.22$).

A further series of measurements has been performed in order to study the behavior of the WGMs sustained by our cavities while increasing the input power. Once a resonance is singled out, we increase the injected power and monitor the displacement of the resonance wavelengths and the distortion of the transmission dips [9,24]. The first effect is shown in Fig. 4 for both λ_{FF} and λ_{SH}. According to our calculations, the linear dependence

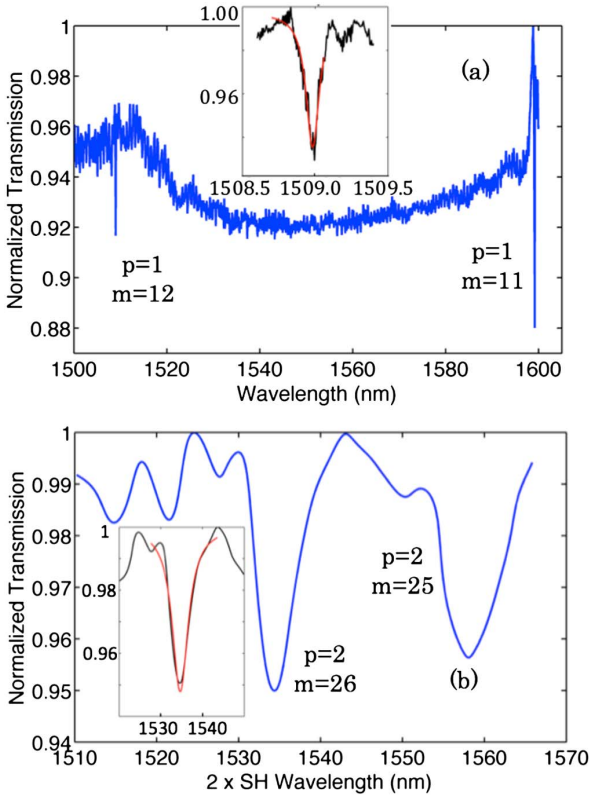

Fig. 3. Normalized transmission spectra for an AlGaAs microdisk with radius $R = 1.85$ μm, thickness $h = 155.4$ nm, and Al concentration of 47.4%. (a) Observed resonances between 1500 and 1600 nm. The dip at $\lambda_{FF} = 1508.9$ nm having a $Q_{FF} = 1.4 \times 10^4$ corresponds to the WGM with $p = 1$ and $m = 12$. (b) Observed resonances between 755 and 785 nm (1510/2 and 1570/2 nm). The dip at $2\lambda_{SH} = 1534.84$ nm having a $Q_{SH} = 4.9 \times 10^2$ corresponds to the WGM with $p = 2$ and $m = 26$. Both spectra cover the entire wavelength range available to our lasers.

observed in the figure cannot be ascribed either to the Kerr effect or to TPA. In fact, the Kerr effect gives rise to: (1) a wavelength shift at the FF of $d\lambda_{FF}/dP_{FF} \sim 0.002$ nm/mW, considerably smaller than what experimentally observed ($d\lambda_{FF}/dP_{FF} \sim 0.07$ nm/mW); and (2) a negative wavelength shift for the SH. On the other hand, TPA is absent for the FF, while giving rise to losses of about 25 cm^{-1}/W at the SH. However, due to the low power circulating in the disk, this has no measurable effect on the SH field. For these reasons, we believe that what is observed in Fig. 4 is related to the formation of surface oxides on the disk sidewalls. The effect of this oxide surface reconstruction layer has been already observed in our group for GaAs disks and could also explain the observed difference between the intrinsic quality factors at the FF and at the SH. A study on this issue goes well beyond the scope of the present article and will be developed in a subsequent publication.

From the data extracted from Fig. 4 we can deduce the sensitivities of the cavity temperature with respect to the input powers: $dT/dP_{FF} = 0.9$ K/mW and $dT/dP_{SH} = 9.4$ K/mW. Moreover, starting from the energy conservation relation ($|\lambda_{FF} - 2\lambda_{SH}| = \Delta$, where Δ is the SH

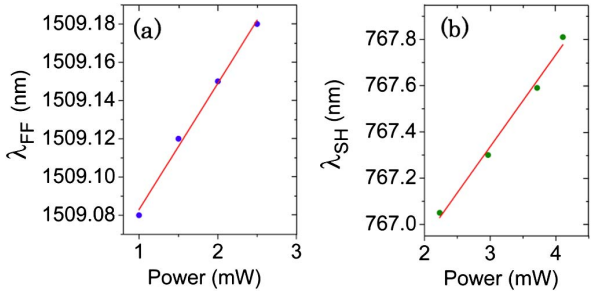

Fig. 4. Displacement of the resonance wavelengths as a function of the external power for (a) λFF and (b) λSH. From the linear fits we obtain the temperature dependence for both wavelengths.

resonance width) and differentiating, we can roughly estimate the external power at which thermal effects cause a roll-off in the SHG efficiency:

$$\left|\frac{d\lambda_{FF}}{dT} - 2\frac{d\lambda_{SH}}{dT}\right|\frac{dT}{dP}P_{max} \sim \Delta, \quad (2)$$

which gives $P_{max} \sim 8$ mW (corresponding to an internal power $P_{max,int} \sim 200$ mW), assuming the same fiber-to-disk distance (i.e., coupling) used for Fig. 4 and considering a SH quality factor $Q^{int} = 4.96 \times 10^2$.

In order to obtain cavities compatible with SHG and exhibiting higher quality factors, we are currently following several paths. On one side, we are exploring different disk parameters, such as diameter, thickness, and Al concentration. On the other side, sample quality optimization is under way. We also plan to endow our experimental setup with an efficient temperature control, in order to get an additional tuning parameter for the WGM resonances at both wavelengths.

In conclusion, we have designed a WGM AlGaAs microcavity for SHG with pump at 1.55 μm, and we have developed a specific technological protocol to fabricate the corresponding suspended microdisks. The latter were characterized at both near-IR and visible frequencies, providing a first important step toward nonlinear generation at 775 nm.

References

1. K. Rivoire, S. Buckley, and J. Vuckovic, Opt. Express **19**, 22198 (2011).
2. Y. Takahashi, Y. Inui, M. Chihara, T. Asano, R. Terawaki, and S. Noda, Nature **498**, 470 (2013).
3. J. Leuthold, C. Koos, and W. Freude, Nat. Photonics **4**, 535 (2010).
4. B. J. Bijlani, P. Abolghasem, A. Reijnders, and A. S. Helmy, *Conference on Lasers and Electro-optics 2011* (Optical Society of America, 2011), paper PDPA3.
5. S. Azzini, D. Grassani, M. Galli, L. Andreani, M. Sorel, M. Strain, L. Helt, J. Sipe, M. Liscidini, and D. Bajoni, Opt. Lett. **37**, 3807 (2012).
6. H. Rong, S. Xu, Y. Kuo, V. Sih, O. Cohen, O. Raday, and M. Paniccia, Nat. Photonics **1**, 232 (2007).
7. A. Schlehahn, F. Albert, C. Schneider, S. Höfling, S. Reitzenstein, J. Wiersig, and M. Kamp, Opt. Express **21**, 15951 (2013).
8. L. Ding, C. Baker, P. Senellart, A. Lemaitre, S. Ducci, G. Leo, and I. Favero, Phys. Rev. Lett. **105**, 263903 (2010).

9. L. Ding, C. Baker, P. Senellart, A. Lemaitre, S. Ducci, G. Leo, and I. Favero, Appl. Phys. Lett. **98**, 113108 (2011).
10. X. Sun, X. Zhang, and H. X. Tang, Appl. Phys. Lett. **100**, 173116 (2012).
11. W. C. Jiang, X. Lu, J. Zhang, and Q. Lin, Opt. Express **20**, 15991 (2012).
12. Y. Dumeige and P. Feron, Phys. Rev. A **74**, 063804 (2006).
13. A. Andronico, I. Favero, and G. Leo, Opt. Lett. **33**, 2026 (2008).
14. J. Bravo-Abad, A. W. Rodriguez, J. D. Joannopoulos, P. T. Rakich, S. G. Johnson, and M. Soljačić, Appl. Phys. Lett. **96**, 101110 (2010).
15. A. Andronico, S. Mariani, F. Ghiglieno, J. Claudon, M. Munsch, J. M. Gérard, I. Favero, S. Ducci, and G. Leo, Opt. Express **20**, 17678 (2012).
16. Z. Yang and J. E. Sipe, Opt. Lett. **32**, 3296 (2007).
17. P. S. Kuo and G. S. Solomon, *Conference on Lasers and Electro-optics 2012 Technical Digest*, San Jose, California, May 6–11, 2012, paper CW3K.
18. P. S. Kuo and G. S. Solomon, "Second-harmonic generation using 4-bar quasi-phasematching in a GaAs microdisk cavity," arXiv:1210.1984 (2012).
19. R. D. Kekatpure, J. Lightwave Technol. **29**, 253 (2011).
20. C. P. Michael, K. Srinivasan, T. J. Johnson, O. Painter, K. H. Lee, K. Hennessy, H. Kim, and E. Hu, Appl. Phys. Lett. **90**, 051108 (2007).
21. S. Adachi, J. Electrochem. Soc. **129**, 609 (1982).
22. L. Ding, C. Belacel, S. Ducci, G. Leo, and I. Favero, Appl. Opt. **49**, 2441 (2010).
23. L. Ding, P. Senellart, A. Lemaitre, S. Ducci, G. Leo, and I. Favero, Proc. SPIE **7712**, 771211 (2010).
24. T. Carmon, L. Yang, and K. J. Vahala, Opt. Express **12**, 4742 (2004).

Second-harmonic generation in AlGaAs microdisks in the telecom range

S. Mariani,[1] A. Andronico,[1] A. Lemaître,[2] I. Favero,[1] S. Ducci,[1] and G. Leo[1,*]

[1]*Université Paris Diderot, Sorbonne Paris Cité, Laboratoire Matériaux et Phénomènes Quantiques, CNRS-UMR 7162, 10 rue Alice Domon et Léonie Duquet, cc 7021, 75205 Paris cedex 13, France*

[2]*Laboratoire de Photonique et Nanostructures, CNRS, Route de Nozay, 91460 Marcoussis, France*

**Corresponding author: giuseppe.leo@univ-paris-diderot.fr*

Received February 24, 2014; revised March 31, 2014; accepted April 18, 2014; posted April 18, 2014 (Doc. ID 207009); published May 15, 2014

We report on second-harmonic generation in whispering-gallery-mode AlGaAs microcavities suspended on a GaAs pedestal. Frequency doubling of a 1.58 μm pump is observed with 7×10^{-4} W^{-1} conversion efficiency. This device can be integrated in a monolithic photonic chip for classical and quantum applications in the telecom band.

OCIS codes: (190.4223) Nonlinear wave mixing; (140.3945) Microcavities; (130.5990) Semiconductors.
http://dx.doi.org/10.1364/OL.39.003062

During the last few years, planar whispering-gallery-mode (WGM) resonators have undergone a revival of interest, after their introduction as add–drop filters [1] and microring lasers [2] two decades ago. Their present popularity stems from their high Q factors and promise of integrating novel functionalities on a photonic chip. Thanks to their versatility and high performance, they can be involved in a wide set of applications, such as quantum-dot lasers [3], optomechanics [4], nanosensing [5], and quantum optics [6].

For applications in the telecom band and in the optoelectronics industry, two alternatives stand out: the silicon (Si) platform and the III-V semiconductor family.

On the nonlinear optics side, Si compounds have a great deal to offer, thanks to their long-standing technological development and CMOS compatibility. Besides the demonstration of Raman lasing in a photonic crystal structure [7], several impressive results have been obtained in WGM resonators via $\chi^{(3)}$ nonlinear effects. For example, frequency comb generation has been reported in silica [8] and silicon nitride [9] microcavities, with the latter also exploited as frequency converters [10] and optical parametric oscillators [11]. Moreover, Si coupled resonator optical waveguides (CROWs) consisting of several cascaded microrings have been demonstrated for photon pair generation [12] and single-photon emission [13].

Analogous results for the III-V semiconductor family, and in particular for AlGaAs WGM microcavities, are still lacking, despite the advantages offered by this platform in terms of (1) fabrication of monolithic laser sources, (2) low losses and broad transparency window, and (3) high $\chi^{(2)}$. In fact, while AlGaAs waveguides have allowed the observation of, e.g., parametric oscillation [14] and generation of polarization-entangled photon pairs [15,16], the exploitation of quadratic nonlinear effects in AlGaAs WGM resonators is still in its infancy. A few years ago it was theoretically shown that, thanks to the azimuthal modulation of the effective second-order nonlinear coefficient, circular structures made of materials with the same crystallographic symmetry as AlGaAs allow one to attain quasi-phase matching without resorting to domain inversions [17].

Moreover, their high quality factors result in a strong field enhancement inside the cavity, possibly giving rise to efficient second-harmonic generation (SHG) [18], difference frequency generation [19], and entangled photon generation [20].

To date, the only experimental observation of SHG in III-V WGM microcavities has been reported very recently in a GaAs microdisk [21], with a fundamental frequency (FF) wavelength around 2 μm. Beyond this nice achievement for nonlinear optics, its reverse process, spontaneous parametric down-conversion (SPDC), would constitute a breakthrough for its possible impact as a quantum light source on-chip [22]. In this respect, it would be crucial to generate a signal–idler pair in the telecom band. However, GaAs does not allow for working with a pump in this wavelength range, since the second harmonic (SH) photons' energy would exceed the material bandgap. Moreover, the two-photon absorption coefficient is quite large up to 1800 nm, which represents a limit for application purposes. On the other hand, by using an $Al_xGa_{1-x}As$ microcavity with $x > 0.28$, these issues can be circumvented.

In this Letter, we report on the experimental observation of SHG in $Al_{0.4}Ga_{0.6}As$ microdisks suspended over a GaAs pedestal designed to operate with a pump wavelength in the third telecom window.

The vertical structure has been grown by molecular beam epitaxy and is composed of a 155 nm thick $Al_{0.4}Ga_{0.6}As$ layer on top of a GaAs sacrificial layer. We fabricated disks with radii ranging from 1.7 to 2.1 μm, and with a GaAs pedestal ~3 μm high and ~500 nm wide [Fig. 1(a)], following the protocol presented in [23].

The linear optical characterization of the AlGaAs microdisks and the SHG experiment are carried out via evanescent coupling with a tapered silica fiber having a typical diameter of about 1 μm [24]. The same fiber is used to couple the FF into the disks and to collect the generated SH. The experimental setup is shown in Fig. 1(b). Two CW external-cavity tunable laser diodes are used to perform the experiments, one emitting into a fiber in the near infrared (NIR) and the other emitting in air in the visible (VIS) range. The polarization state of the former can be varied with a three-paddle polarization

0146-9592/14/103062-04$15.00/0

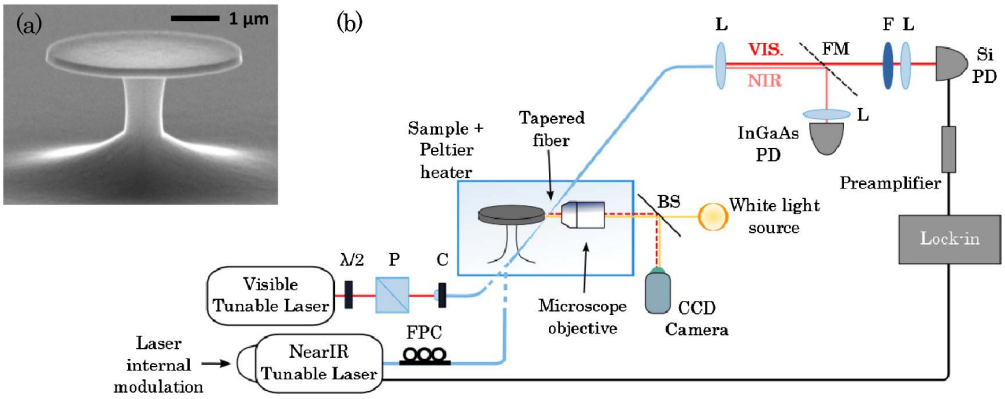

Fig. 1. (a) Scanning electron microscope side-view picture of an AlGaAs disk suspended over a GaAs pedestal. (b) Schematic of the experimental setup: $\lambda/2$, half-wave plate; P, polarizer; C, collimator; FPC, fiber polarization control; BS, beam splitter; L, lens; FM, flip mirror; PD, photodiode; F, bandpass filter.

controller, while a half-wave plate and a polarizer allow us to control and select the polarization of the latter. The tapered fiber and the sample are enclosed in a Plexiglas box to limit the fiber degradation caused by the external environment, while the microdisk temperature is controlled via a Peltier module. A microscope objective and a CCD camera connected to a PC screen are used for the alignment. The relative position between the fiber and the sample disk is then fully controlled via micropositioned holders and finely adjusted by means of a Piezo controller. At the output, the pump throughput is focused onto an InGaAs detector for the linear transmission measurements, while it is filtered out via a bandpass filter for the SHG measurements. The SH signal is focused onto a silicon photodiode and detected by a lock-in preceded by a low-noise transimpedance amplifier.

For the linear measurements, as first step, we perform two quick scans in the NIR and VIS ranges to identify the resonant wavelengths of our cavities. After comparing the experimental results to our simulations, we single out the resonances with radial and azimuthal numbers (p and m, respectively) fulfilling the phase-matching condition $\Delta m = m_{SH} - 2m_{FF} = \pm 2$ [17]. The experimental position of the resonances matches very well the results of our modeling. However, for some of the disks, the VIS resonance that satisfies the phase-matching condition lies outside of the wavelength range spanned by our laser (from 755 to 785 nm). In this case, the exact resonance position is not found via direct transmission measurements, but it is rather inferred by labeling all the WGMs in the above laser range and using the cavity free spectral range.

Then, to search for the SHG signal, we carry out a finer acquisition around the FF resonance wavelength. At this stage, we use the bandpass filter to reflect any radiation coming from the pump, while selecting only the SHG signal with wavelength between 700 and 1095 nm. Once the SH is detected, we adjust the fiber position to optimize the signal; please note that, in the present experiment, the maximum coupling and stability are found when the fiber is in contact with the disk sidewall.

For a microcavity with radius $R = 1.9$ μm, the linear measurements allow us to separately observe a TE-polarized WGM resonance at $\lambda_{FF}^{res} = 1584.29$ nm ($p_{FF} = 1$, $m_{FF} = 12$) and a TM-polarized WGM resonance at $\lambda_{SH}^{res} = 793.51$ nm ($p_{SH} = 2$, $m_{SH} = 26$); these are the only two modes fulfilling the phase-matching condition [23]. Their loaded quality factors, when the fiber is in contact with the disk, are $Q_{FF} = 1.5 \times 10^3$ (inset in Fig. 2) and $Q_{SH} = 3.2 \times 10^2$. By repeating the same measurements for different fiber-to-disk distances, we also estimate the intrinsic quality factors $Q_{FF}^i = 5.3 \times 10^3$ and $Q_{SH}^i = 5 \times 10^2$. The latter depends mostly on the fabrication process: while our best disks show Q^i around a few tens of 10^4, they exhibit an important detuning between the NIR and VIS resonances $\Delta\lambda = |\lambda_{FF}^{res} - 2\lambda_{SH}^{res}|$, resulting in low SHG efficiencies. This detuning can be controlled via the cavity radius and, for our sample, is minimized for the $R = 1.9$ μm disk ($\Delta\lambda = 2.73$ nm). According to our simulations, for a disk height $h = 155$ nm and $R = 1903$ nm, $\Delta\lambda$ should be zero. Unfortunately, with the wet-etching process, the minimal tolerance that we achieved for the cavity radii was around 20 nm, which constitutes our present limitation. Another way to reduce

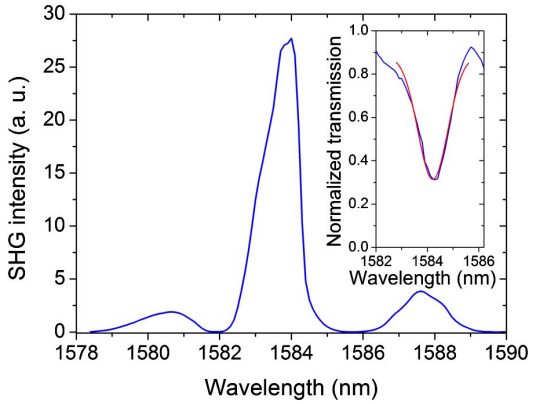

Fig. 2. SHG intensity versus pump wavelength. Inset, observed resonance at $\lambda_{FF}^{res} = 1584.29$ nm. The maximum of the generated nonlinear signal occurs when the FF dip and the SH peak are aligned at 1584 nm.

$\Delta\lambda$ could be using a SH mode with a radial number having the same parity as p_{FF}, in order to improve the overlap between the FF and SH fields. However, if we consider, for instance, $p_{SH} = 3$, according to our modeling, the only resonance which fulfills the phase-matching condition is the one with $\lambda_{SH}^{res} = 752.07$ nm, which corresponds to an even larger $\Delta\lambda$. Moreover, despite the parity matching, the corresponding nonlinear overlap integral turns out to be smaller.

The spectrum shown in Fig. 2 is obtained by monitoring the SH intensity while scanning the pump wavelength. The injected power and the optimal temperature are kept constant at $P_{FF} = 3.5$ mW and $T = 15°C$, respectively. Here, P_{FF} is the power inside the fiber when the latter is close to the disk, and it is estimated by taking into account the measured taper losses. As stated in [25], the maximum SH conversion takes place when (1) both modes are resonant within the cavity, (2) the two resonances are perfectly aligned ($\Delta\lambda = 0$), and (3) the critical coupling condition is achieved for both WGMs ($Q^i = Q^c$, where Q^c is the coupling quality factor). However, if the resonances are misaligned, it is possible to optimize the SH conversion when the cavity is over-coupled ($Q^i > Q^c$); this leads to a broadening of the resonance linewidth and to a better spectral overlap. Experimentally, we verify the assumption that, while the cavity is undercoupled for resonances in the visible region, it is overcoupled at the FF wavelength. This results in an increased SH signal that has its maximum in correspondence of the FF wavelength.

It is worth noticing that, during the data acquisition, we remarked on a slight blue shift of the resonances while the fiber approached the cavities. This effect depends on the fiber width and results in a NIR and VIS resonance wavelength shift of about 0.2%, close to our simulation predictions. However, all the data shown here have been taken during the same run of measurement, at constant fiber-to-disk distance and for a single fiber width, making the results self-consistent.

Figure 3 shows a logarithmic plot of the SH external power as a function of the FF external power. The slope of its linear part is 2.05 ± 0.07, matching the theoretical quadratic dependence. With this value, we extract the external conversion efficiency $\eta_{exp} = P_{SH}^{out}/(P_{FF}^{in})^2 = (7.04 \pm 0.07) \times 10^{-4}$ W^{-1}, with P_{SH}^{out} and P_{FF}^{in} being powers inside the fiber. Please note that the curve rolls off for $P_{FF} > 2$ mW due to the thermal shift of the FF resonance. In principle, this effect could be reduced via two main actions: (1) decreasing the Peltier module temperature, or (2) detuning the FF wavelength. However, in both cases, the resulting SHG efficiency decreases. This stems from the fact that the results of Fig. 3 correspond to an optimum at high power, with respect to Peltier temperature, FF wavelength, and fiber-to-disk coupling. In particular, as far as the temperature is concerned, Fig. 3 was obtained at $T = 15°C$, which is very close to the lowest temperature for which our microdisks behave correctly, before that water vapor condensation occurs on their surface. In the second case, two distinct regimes are observed: for a slight FF wavelength detuning of any sign, the SHG signal does not appreciably change; when such detuning gets more important, the fiber–disk coupling is affected. Unfortunately, the latter is extremely critical and cannot be adaptively changed to reoptimize each experimental point of the same curve.

In Fig. 4, we show the expected nonlinear efficiency (η_{NL}), calculated according to Ref. [25] and taking into account the measured quality factors. We report two curves for different detuning: the first one corresponds to the observed $\Delta\lambda = 2.73$ nm and has a maximum $\eta_{NL} = 3.31 \times 10^{-3}$ W^{-1}, in fair agreement with the experimental value; the second one represents the ideal case $\Delta\lambda = 0$, showing the maximum efficiency achievable with the current intrinsic quality factors and coupling conditions. The two peaks differ by less than a factor of 3, indicating that the present detuning is not limiting the nonlinear performance of our disks. Higher conversion efficiencies could be obtained by boosting the cavities' quality factors via an optimization of the fabrication process.

A further series of measurements has been performed in order to study the displacement of the NIR and VIS mode wavelengths versus temperature at fixed FF power

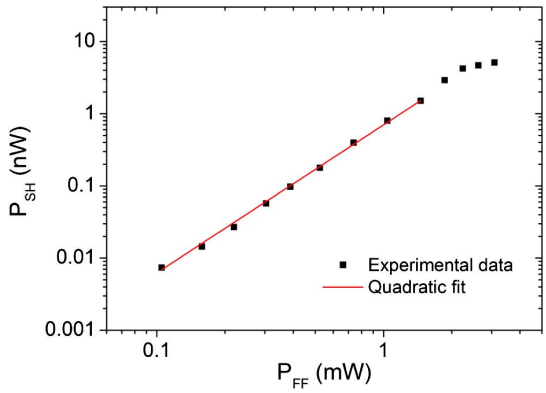

Fig. 3. Logarithmic plot of the SH power as a function of the FF power, having a slope of 2.05 ± 0.07. From the fit, we obtain an external conversion efficiency of $\eta_{exp} = (7.04 \pm 0.07) \times 10^{-4}$ W^{-1}.

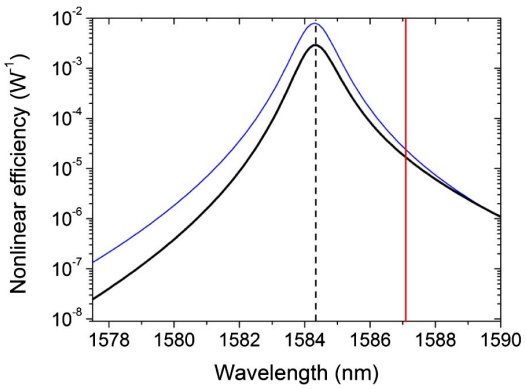

Fig. 4. Computed nonlinear efficiency for a detuning $\Delta\lambda = 2.73$ nm (thick black line) and $\Delta\lambda = 0$ (thin blue line). The dotted line corresponds to λ_{FF}^{res} while the solid red line corresponds to $2\lambda_{SH}^{res}$.

$P_{FF} = 1$ mW. For both λ_{FF}^{res} and $2\lambda_{SH}^{res}$, we observe a linear trend. When the fiber is not touching the disk sidewalls, the NIR resonance wavelength has a slope of 0.077 ± 0.008 nm/°C, while for the VIS WGM wavelength, we obtain 0.083 ± 0.004 nm/°C; these two values are close to the results of our simulations: 0.077 nm/°C for the NIR and 0.088 nm/°C for the VIS. This shows that the temperature can in principle be used as a fine-tuning parameter to compensate small detunings $\Delta\lambda$.

In conclusion, we have demonstrated SHG from 1.584 to 0.794 μm in $Al_{0.4}Ga_{0.6}As$ suspended microdisks. Even if we expect that this result will be improved by optimizing the fabrication process, the reported efficiency is already comparable with the state of the art at longer wavelengths [26]. We are currently working on the monolithic version of the present sample, consisting of disks with integrated waveguides. This evolution will alleviate our present difficulties in terms of reproducibility, related to the limited control of the fiber diameter and the fiber-to-disk distance. We believe that the present result is a significant step toward the fabrication of ultracompact SPDC sources in the telecom range.

S. M. acknowledges F. Boitier for helpful discussions.

References

1. B. E. Little, S. T. Chu, H. A. Haus, J. Foresi, and J.-P. Laine, J. Lightwave Technol. **15**, 998 (1997).
2. S. L. McCall, A. F. J. Levi, R. E. Slusher, S. J. Pearton, and R. A. Logan, Appl. Phys. Lett. **60**, 289 (1992).
3. F. Albert, T. Braun, T. Heindel, C. Schneider, S. Reitzenstein, S. Höfling, L. Worschech, and A. Forchel, Appl. Phys. Lett. **97**, 101108 (2010).
4. T. J. Kippenberg, H. Rokhsari, T. Carmon, A. Scherer, and K. J. Vahala, Phys. Rev. Lett. **95**, 033901 (2005).
5. J. Zhu, S. K. Ozdemir, Y. F. Xiao, L. Li, L. He, D. R. Chen, and L. Yang, Nat. Photonics **4**, 46 (2010).
6. J. U. Fürst, D. V. Strekalov, D. Elser, A. Aiello, U. L. Andersen, Ch. Marquardt, and G. Leuchs, Phys. Rev. Lett. **106**, 113901 (2011).
7. Y. Takahashi, Y. Inui, M. Chihara, T. Asano, R. Terawaki, and S. Noda, Nature **498**, 470 (2013).
8. T. J. Kippenberg, R. Holzwarth, and S. A. Diddams, Science **332**, 555 (2011).
9. Y. Okawachi, K. Saha, J. S. Levy, Y. H. Wen, M. Lipson, and A. L. Gaeta, Opt. Lett. **36**, 3398 (2011).
10. J. S. Levy, M. A. Foster, A. L. Gaeta, and M. Lipson, Opt. Express **19**, 11415 (2011).
11. J. S. Levy, A. Gondarenko, M. A. Foster, A. C. Turner-Foster, A. L. Gaeta, and M. Lipson, Nat. Photonics **4**, 37 (2010).
12. R. Kumar, J. R. Ong, J. Recchio, K. Srinivasan, and S. Mookherjea, Opt. Lett. **38**, 2969 (2013).
13. M. Davanço, J. R. Ong, A. B. Shehata, A. Tosi, I. Agha, S. Assefa, F. Xia, W. M. J. Green, S. Mookherjea, and K. Srinivasan, Appl. Phys. Lett. **100**, 261104 (2012).
14. M. Savanier, C. Ozanam, L. Lanco, X. Lafosse, A. Andronico, I. Favero, S. Ducci, and G. Leo, Appl. Phys. Lett. **103**, 261105 (2013).
15. A. Orieux, A. Eckstein, A. Lemaître, P. Filloux, I. Favero, G. Leo, T. Coudreau, A. Keller, P. Milman, and S. Ducci, Phys. Rev. Lett. **110**, 160502 (2013).
16. A. Vallés, M. Hendrych, J. Svozilík, R. Machulka, P. Abolghasem, D. Kang, B. J. Bijlani, A. S. Helmy, and J. P. Torres, Opt. Express **21**, 10841 (2013).
17. Y. Dumeige and P. Feron, Phys. Rev. A **74**, 063804 (2006).
18. Z. Yang, P. Chak, A. D. Bristow, H. M. van Driel, R. Iyer, J. S. Aitchison, A. L. Smirl, and J. E. Sipe, Opt. Lett. **32**, 826 (2007).
19. A. Andronico, J. Claudon, J.-M. Gérard, V. Berger, and G. Leo, Opt. Lett. **33**, 2416 (2008).
20. Z. Yang and J. E. Sipe, Opt. Lett. **32**, 3296 (2007).
21. P. S. Kuo, J. Bravo-Abad, and G. S. Solomon, Nat. Commun. **5**, 3109 (2014).
22. W. Chen, F. Sun, C. Zou, and G. Guo, J. Opt. Soc. Am. B **29**, 1884 (2012).
23. S. Mariani, A. Andronico, O. Mauguin, A. Lemaître, I. Favero, S. Ducci, and G. Leo, Opt. Lett. **38**, 3965 (2013).
24. L. Ding, C. Belacel, S. Ducci, G. Leo, and I. Favero, Appl. Opt. **49**, 2441 (2010).
25. P. S. Kuo and G. S. Solomon, Opt. Express **19**, 16898 (2011).
26. K. Lenglé, L. Bramerie, M. Gay, J.-C. Simon, S. Combrié, G. Lehoucq, and A. De Rossi, Appl. Phys. Lett. **102**, 151114 (2013).

Tuning of a nonlinear THz emitter

A. Andronico,[1] S. Mariani,[1] F. Ghiglieno,[1] J. Claudon,[2] M. Munsch,[2] J. M. Gérard,[2] I. Favero,[1] S. Ducci,[1] and G. Leo[1,*]

[1]*Univ. Paris Diderot, Sorbonne Paris Cité, Laboratoire MPQ, CNRS-UMR 7162 Case courrier 7021, 75205 Paris Cedex 13, France*

[2]*CEA-CNRS-UJF group "Nanophysique et Semiconducteurs," CEA, INAC, SP2M F-38054 Grenoble, France*

[*]*giuseppe.leo@univ-paris-diderot.fr*

Abstract: We numerically study a passive THz source based on difference frequency generation between modes sustained by cylindrical AlGaAs microcavities. We show that ring-like structures are advantageous in that they provide additional degrees of freedom for tuning the nonlinear process and for maximizing the nonlinear overlap integral and conversion efficiency.

OCIS codes: (190.2620) Harmonic generation and mixing; (190.4223) Nonlinear wave mixing; (190.4360) Nonlinear optics, devices.

References and links

1. M. Tonouchi, "Cutting-edge terahertz technology," Nat. Photon. **1**, 97–105 (2007).
2. E. R. Brown, K. A. McIntosh, K. B. Nichols, and C. L. Dennis, "Photomixing up to 3.8 THz in low-temperature-grown GaAs," Appl. Phys. Lett. **66**, 285–287 (1995).
3. R. Köhler, A. Tredicucci, F. Beltram, H. Beere, E. H. Linfield, A. G. Davies, D. A. Ritchie, R. C. Iotti, and F. Rossi, "Terahertz semiconductor-heterostructure laser," Nature **417**, 156–159 (2002).
4. M. A. Belkin, F. Capasso, F. Xie, A. Belyanin, M. Fischer, A. Wittmann, and J. Faist, "Room temperature terahertz quantum cascade laser source based on intracavity difference-frequency generation," Appl. Phys. Lett. **92**, 201101 (2008).
5. Q. Y. Lu, N. Bandyopadhyay, S. Slivken, Y. Bai, and M. Razeghi, "Room temperature single-mode terahertz sources based on intracavity difference-frequency generation in quantum cascade lasers," Appl. Phys. Lett. **99**, 131106 (2011).
6. J. Bravo-Abad, A. Rodriguez, P. Bermel, S. G. Johnson, J. D. Joannopoulos, and M. Soljačić, "Enhanced nonlinear optics in photonic-crystal microcavities," Opt. Express **15**, 16161–16176 (2007).
7. C. P. Michael, K. Srinivasan, T. J. Johnson, O. Painter, K. H. Lee, K. Hennessy, H. Kim, and E. Hu, "Wavelength- and material-dependent absorption in GaAs and AlGaAs microcavities," Appl. Phys. Lett. **90**, 051108 (2007).
8. L. Ding, C. Baker, P. Senellart, A. Lemaître, S. Ducci, G. Leo, and I. Favero, "High frequency GaAs nano-optomechanical disk resonator," Phys. Rev. Lett. **105**, 263903 (2010).
9. A. Andronico, J. Claudon, J.-M. Gérard, V. Berger, and G. Leo, "Integrated terahertz source based on three-wave mixing of whispering-gallery modes," Opt. Lett. **33**, 2416–2418 (2008).
10. J. Bravo-Abad, A. W. Rodriguez, J. D. Joannopoulos, P. T. Rakich, S. G. Johnson, and M. Soljačić, "Efficient low-power terahertz generation via on-chip triply-resonant nonlinear frequency mixing," Appl. Phys. Lett. **96**, 101110 (2010).
11. B. S. Williams, S. Kumar, H. Callebaut, Q. Hu, and J. L. Reno, "Terahertz quantum-cascade laser at $\lambda \approx 100\,\mu$m using metal waveguide for mode confinement," Appl. Phys. Lett. **83**, 2124–2126 (2003).
12. H. A. Haus, *Waves and Fields in Optoelectronics* (Prentice-Hall, 1984).
13. R. D. Kekatpure, "First-principles full-vectorial eigenfrequency computations for axially symmetric resonators," J. Lightwave Technol. **29**, 253–259 (2011).
14. F. Albert, T. Braun, T. Heindel, C. Schneider, S. Reitzenstein, S. Höfling, L. Worschech, and A. Forchel, "Whispering gallery mode lasing in electrically driven quantum dot micropillars," Appl. Phys. Lett. **97**, 101108 (2010).
15. M. Munsch, J. Claudon, N. S. Malik, K. Gilbert, P. Grosse, J.-M. Gérard, F. Albert, F. Langer, T. Schlereth, M. M. Pieczarka, S. Höfling, M. Kamp, A. Forchel, and S. Reitzenstein, "Room temperature, continuous wave lasing in microcylinder and microring quantum dot laser diodes," Appl. Phys. Lett. **100**, 031111 (2012).

#167987 - $15.00 USD Received 3 May 2012; revised 1 Jun 2012; accepted 8 Jun 2012; published 19 Jul 2012

1. Introduction

Despite the considerable demand in terms of applications [1], the current state of the art THz sources are still far from ideal. Photoconductive dipole antennas, for example, are very popular for generating and detecting broadband THz pulses, but they require the external excitation of femtosecond lasers. For Continuous-Wave (CW) sources, optical heterodyne mixing (photomixing) is still limited to output powers in the 100 nW range below 1 THz, quickly decreasing to few nW at about 2 THz [2]. THz Quantum Cascade Lasers (QCLs) can emit more than 50 mW (peak) in the pulsed regime, but they are poorly tunable and only operate at cryogenic temperatures [3].

The fabrication of a THz source that is, at the same time, compact, providing high output power, and operating at room temperature is still an unsolved challenge. In this context, nonlinear THz sources constitute a promising approach, but they are normally affected by two main drawbacks: 1) the required excitation of external (high-power) pump lasers; and/or 2) small conversion efficiencies.

The first problem can be circumvented by integrating laser pump sources and nonlinear medium. Although adding more constraints both in terms of design and technological processing, this provides considerable improvements in terms of ease of use for any applications. This approach is exemplified by the THz source based on Difference Frequency Generation (DFG) in dual-wavelength mid-IR QCLs reported in Refs. [4,5] and operating in pulsed regime up to room temperature.

The problem of small conversion efficiencies can be tackled by exploiting optical microcavities in order to boost the nonlinear phenomenon [6]. In this respect, Whispering Gallery Mode (WGM) resonators are promising candidates, because of their ultra-high quality factors. In particular, recent technological progress has allowed the fabrication of AlGaAs microdisks with Q factors exceeding 10^5 [7, 8]. These resonators could therefore be used for efficient frequency conversion sources based on DFG [9, 10].

High Q factors are desirable since they translate into long storage times and therefore into long interaction times between the modes involved in the nonlinear generation. However, they come at a price: the higher the Q factor, the smaller the width of the resonance. Therefore, the nonlinear process becomes extremely sensitive to even small changes of physical parameters and/or minimal fabrication imperfections.

It is clear that some degree of fabrication tolerance is highly desirable, and thus one needs to employ a well-controlled tuning parameter to compensate for any deviations with respect to the nominal design. Temperature is a classic example: by changing the temperature, the refractive index of the materials making up the cavity can be adjusted until the modes are brought into phase matching.

In this letter we numerically study an alternative and powerful tuning approach based on defining a hole in an AlGaAs WGM THz nonlinear microcavity source similar to the one we discussed in Ref. [9]. Interestingly, this opens the way for a second tuning parameter, provided by the height of a metallic tip positioned in the hollow part of the ring.

The paper is organized as follows: in Section 2, we present our design guidelines and briefly summarize the Coupled Mode Theory (CMT) results pertinent to a DFG process in a WGM cavity. In Section 3, we report the results of our analysis on ring resonators for THz generation by DFG. We show that ring-like cavities are advantageous over pillar-like structures not only in terms of tuning capabilities but also in terms of nonlinear conversion efficiencies.

2. Cavity design

As shown in Fig. 1(a), the vertical structure of our cavity is composed of AlGaAs layers placed between two gold mirrors. The central $Al_{0.34}Ga_{0.66}As$ slab sandwiched between $Al_{0.8}Ga_{0.2}As$

#167987 - $15.00 USD Received 3 May 2012; revised 1 Jun 2012; accepted 8 Jun 2012; published 19 Jul 2012

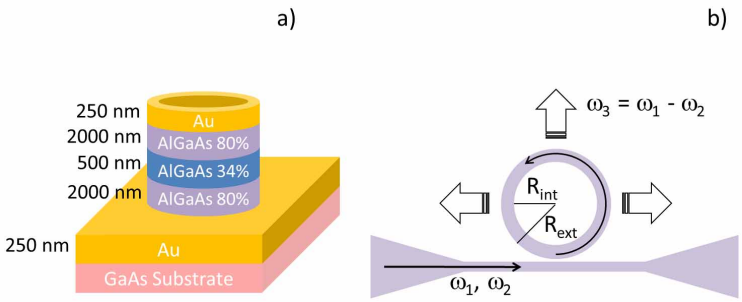

Fig. 1. Sketch of the nonlinear source studied in text (a). Schematic of the DFG process with pump fields injected via a tapered waveguide (b).

spacers provides dielectric guiding for two near-IR pump modes with wavelengths around 1.3 μm. The vertical confinement of the THz mode is made possible by the metallic layers, which create a double-metal waveguide similar to the one used for THz QCLs [11]. Please note that both the Al molar fraction and the pump wavelengths are chosen so to minimize the effect of two photon absorption.

By slightly changing the vertical design and by burying quantum dots in the cavity central layer, it should be possible to implement an active THz source. For the following however, we will limit our discussion to a passive structure.

A schematic of the DFG process is presented in Fig. 1(b): the circularly symmetric cavity is side-coupled to a tapered waveguide in order to excite the relevant pump WGMs. Due to the material nonlinearity, a third mode at the difference frequency is generated and radiated into free space.

Based on standard CMT [12], we have already described THz DFG in WGM cavities in Ref. [9]. Neglecting the pump depletion, the nonlinear efficiency of a passive emitter can be written as:

$$\eta = 4\frac{\omega_3}{\omega_1\omega_2}\frac{Q_3^{rad}}{(1+Q_3^{rad}/Q_3^{mat})^2}\prod_{i=1,2}\left[\frac{Q_i^{cpl}}{(1+Q_i^{cpl}/Q_i^{int})^2}\right]|I_{ov}|^2\frac{1}{(2\Delta\omega\, Q_3^{int}/\omega_3)^2+1} \qquad (1)$$

where Q_3^{rad} (Q_3^{mat}) is the optical (material) quality factor for the THz mode, Q_i^{int} (Q_i^{cpl}) is the intrinsic (coupling) quality factor for the i-th pump mode (i = 1,2), and I_{ov} is the nonlinear overlap integral. Moreover, the three modes need to fulfill the phase matching condition $\Delta m = m_1 - m_2 - m_3 = \pm 2$, where m_i is the azimuthal number of the mode i. The final Lorentzian factor (where $\Delta\omega = \omega_1 - \omega_2 - \omega_3$) expresses the relaxation of the energy conservation due to the short lifetime of the THz WGM.

According to Eq. (1), η is maximized when the critical coupling condition is obtained for the two pump fields, i. e. when $Q_i^{cpl} = Q_i^{int}$ (i = 1,2). This can be achieved by an appropriate choice of 1) the waveguide width; and 2) the waveguide to resonator distance.

3. Modeling and discussion

In Fig. 2 we report the calculated THz frequency (ν_3, solid black line) of a WGM with $m_3 = 2$ versus R_{int} for a ring cavity with $R_{ext} = 17.48$ μm - see Fig. 1(b) for the definition of internal (R_{int}) and external (R_{ext}) radii. The results were obtained with a fully-vectorial finite-difference frequency-domain code developed following the guidelines of Ref. [13].

#167987 - $15.00 USD Received 3 May 2012; revised 1 Jun 2012; accepted 8 Jun 2012; published 19 Jul 2012

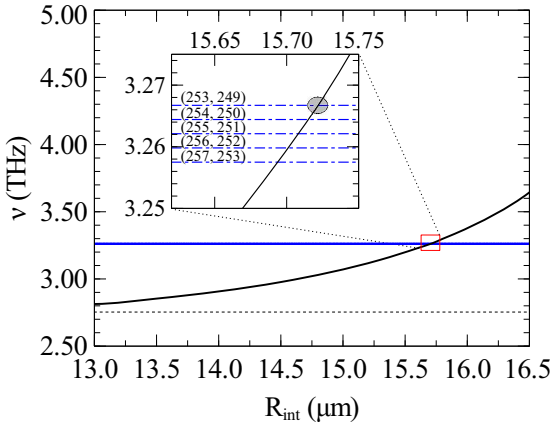

Fig. 2. THz WGM frequency ν_3 (solid black curve) and near-IR mode spacing $\Delta\nu$ (dash-dotted blue curves) versus internal radius of the ring. The black dotted line corresponds to the THz resonance frequency for a structure without hole. The inset is a zoomed-in view around $R_{int} = 15.7\mu$m.

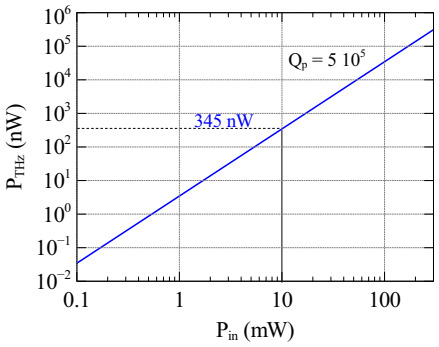

Fig. 3. THz output power (in nW) versus waveguide input power (in mW) calculated for a ring-like structure with internal radius $R_{int} = 15.72$ μm and external radius $R_{ext} = 17.48$ μm. Both pump modes are assumed to be critically coupled to the cavity.

The black dotted line represents the frequency of the mode for a cavity with no hole ($R_{int} = 0$) and radius $R = R_{ext} = 17.48$ μm. On the same plot we report, as blue dash-dotted lines, the frequency difference between pump modes $\Delta\nu = \nu_1 - \nu_2$ for a few different pairs of azimuthal numbers (m_1, m_2). Each pair and the THz WGM satisfy the phase-matching condition ($\Delta m = 2$). However, only the intersections between the dash-dotted curves and the solid black curve represent frequency triplets that strictly fulfill energy conservation. For example, if we consider a pillar with no hole (black-dotted line in Fig. 2), then the energy is strongly not conserved and DFG is inhibited.

By adjusting R_{int} we can fine tune the THz eigenfrequency - while leaving the pump modes unperturbed - so to enforce the energy conservation, and this can be done for different WGMs triplets. Therefore the central hole can be effectively used as a tuning parameter, with the possibility of implementing it - even after processing and testing the sample - via a Focused Ion Beam (FIB) session. While any treatments applied to the external semiconductor-air boundary

#167987 - $15.00 USD Received 3 May 2012; revised 1 Jun 2012; accepted 8 Jun 2012; published 19 Jul 2012

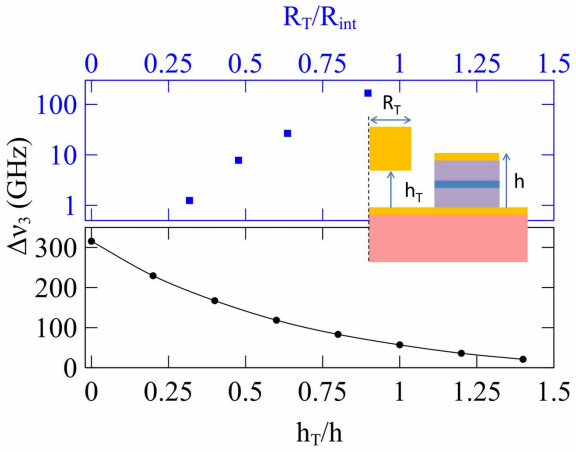

Fig. 4. Frequency shift of the THz WGM versus: the radius of a metallic tip placed at half pillar height (top panel); the height of a tip with fixed radius $R_T = 0.9\,R_{int}$ (bottom panel). Inset: sectional view of the tip and AlGaAs microring (the dashed line represents the axis of cylindrical symmetry).

would be detrimental for the quality factors of the pump WGMs involved in the DFG, the same does not hold for the internal radius. This is due to the fact that the pump WGMs have their maximum intensity at the periphery of the pillar, while they have negligible intensity close to the pillar axis.

Coming back to Fig. 2, if we restrict our attention to the pump modes ($m_1 = 249$, $m_2 = 253$), we find that the energy is strictly conserved for an internal radius $R_{int} = 15.72\ \mu$m (gray circle in the inset). Figure 3 shows the calculated THz output power provided by a ring with such internal radius and for pump quality factors $Q_p = 5\,10^5$, i. e. the current state of the art for AlGaAs cylindrical cavities. To obtain this figure, we assumed that both pump modes are critically coupled to the ring. Output powers of few hundred nW could be reached with input powers (inside the waveguide) ranging from 5 to 20 mW.

An additional benefit of the microring with respect to a structure without hole is the increase of the overlap integral between the three modes. This is due to the fact that the hole allows to squeeze the THz mode into a smaller volume, and it typically results in an efficiency increase of about 50%.

The exploitation of ring-like resonators provides more tuning options. In Fig. 4 we show the effect of a metallic tip placed in the hollow part of the above ring structure. In particular, the top panel shows the shift of the THz frequency due to a gold tip with varying radius (R_T) and height fixed at $h_T = h/2$, h being the height of the resonator (see inset). A shift close to 100 GHz (around 3% of the WGM original frequency) can be obtained by exploiting large tips (i.e. for $R_T > 0.8\,R_{int}$). On the other hand, the bottom panel of Fig. 4 shows the shift of the THz frequency due to a gold tip with radius $R_T = 0.9\,R_{int}$ and as a function of the relative tip height h_T/h. As we move the tip closer to the bottom mirror, the frequency of the THz WGM shifts up to 300 GHz (around 9% of the WGM original frequency).

The same principle can also be used with a non-metallic tip. For example, in Fig. 5, we show the shift of the THz mode resonance frequency versus h_T/h, for a GaAs tip with radius $R_T = 0.76\,R_{int}$. As expected, the shift is negative and decreases in modulus if we move the tip further away. Please note that, in this case, the tip radius must be smaller than $0.8\,R_{int}$ to avoid the leakage of the WGM.

#167987 - $15.00 USD Received 3 May 2012; revised 1 Jun 2012; accepted 8 Jun 2012; published 19 Jul 2012

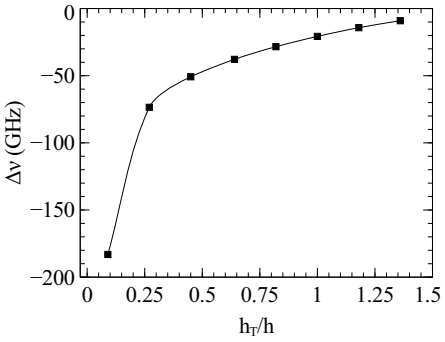

Fig. 5. Frequency shift of the THz WGM versus the height of a GaAs tip with fixed radius $R_T = 0.76 R_{int}$. The solid black line is a guide to the eye.

It is important to stress that the pump modes are localized close to the external ring periphery, and therefore they are not affected by the presence of the tip. This allows to have a powerful tuning mechanism for the DFG process.

4. Conclusion

In this letter we studied a passive THz source based on DFG between WGMs in semiconductor microcavities. We showed that ring-like resonators not only can be effectively used to introduce a tuning parameter (the pillar internal radius) that selectively acts on the THz WGM, but they also allow to increase the nonlinear efficiency of the DFG process. In particular, changing the ring internal radius allows to modify the frequency of the THz WGM (which is delocalized on the whole pillar volume) while not perturbing the frequencies of the pump modes (which are localized close to the periphery of the cavity). In this way, starting with a triplet satisfying the phase matching condition, we can exploit R_{int} to enforce the energy conservation.

Additionally, a controlled displacement of a non-absorbing tip in the hollow part of the ring, allows us an even finer tuning of the THz WGM frequency. The interest in this case is due to the fact that this fine tuning could also be performed while the source is operating. In the case of an active device, this would allow to compensate for e.g. temperature variations due to current injection. A piezo controller moving the tip could therefore be exploited to optimize the power emitted by the source. Moreover, the tip itself could be shaped so to act as a microantenna and increase the directivity of the extracted THz field.

Finally, the cavity considered here lends itself to pump laser integration by burying quantum dots in the central slab. In recent works the lasing action of WGMs sustained by electrically driven AlGaAs pillars has been demonstrated both at 10 K [14] and, more recently, at room temperature [15], a promising step towards the fabrication of the first electrically-pumped CW nonlinear THz emitter at room temperature.

Acknowledgments

The authors acknowledge the financial support of the Future and Emerging Technologies (FET) program within the 7th Framework Program for Research of the European Commission, under the FET-Open TREASURE project (grant number: 250056).

#167987 - $15.00 USD Received 3 May 2012; revised 1 Jun 2012; accepted 8 Jun 2012; published 19 Jul 2012

Microring Diode Laser for THz Generation

Silvia Mariani, Alessio Andronico, Ivan Favero, Sara Ducci, Yanko Todorov, Carlo Sirtori, Martin Kamp, Mathieu Munsch, Julien Claudon, Jean-Michel Gérard, Tianwu Wang, Peter Uhd Jepsen, *Member, IEEE*, and Giuseppe Leo

***Abstract*—We report on the modeling and optical characterization of AlGaAs/InAs quantum-dot microring diode lasers designed for terahertz (THz) difference frequency generation (DFG) between two whispering gallery modes (WGMs) around 1.3 μm. In order to investigate the spectral features of this active device in the two frequency ranges, we performed different measurements on ad hoc passive samples. For the study in the telecom range, we used transmission measurements on microcylinders with integrated coupling waveguides. For the analysis in the THz range, we used reflectivity spectra on 2D arrays of identical double-metal microcylinders. The good agreement that we demonstrate between experimental results and design parameters is crucial towards the achievement of active phase-matched THz emitters.**

***Index Terms*—Whispering gallery modes, nonlinear optics, optical harmonic generation, quantum dot lasers (QDLs).**

I. Introduction

THE THz frequency range has attracted a considerable interest in recent years due to its high potential impact on fields like biology and medical science [1], [2]. One of the key problems still waiting for a solution is the development of a compact and low-cost source operating at room temperature. For example, current photomixers are not able to generate significant output power beyond 2 THz [3], while THz quantum cascade lasers (QCLs) require cryogenic cooling [4]. Several nonlinear optics schemes have resulted in widely tunable sources with remarkable output levels [5], [6]. However, passive devices of this type cannot be considered compact because of the required excitation by bulky pump lasers.

In the context of nonlinear optics, DFG constitutes an appealing technique for the optical generation of THz, since it allows the fabrication of CW sources operating at room temperature. The toughest challenges related to such devices are: 1) the integration of the pump lasers; and 2) the maximization of the nonlinear conversion efficiency. In this respect, a successful approach based on dual-wavelength mid-IR QCLs has been demonstrated in [7]. More recently, this scheme has been strongly ameliorated by using a DFB grating for mid-IR mode purification [8] and Cherenkov phase-matching [9], [10] for minimizing free carrier absorption. This has resulted in 65 μW pulsed single-mode emission between 1 and 4.6 THz.

In this article we elaborate on an alternative electrically pumped DFG source with a low lasing threshold compatible with THz CW emission. We focus on a WGM cavity similar to the one that was proposed in [11], opting for a microring geometry because of its broader tunability with respect to microcylinders [12]. The device is based on AlGaAs non-resonant $\chi^{(2)}$, with the wavelengths of the pump modes ($\lambda \approx 1.3$ μm) and of the DFG modes ($\lambda \approx 75$–150 μm) lying on opposite sides of the Reststrahlen band.

In Section II we provide a refined design for an active source that incorporates quantum dots (QDs) as active medium. This design relies on a realistic estimate of the source operation, by taking into account two-photon absorption (TPA) for the pump fields, doping losses, and thermal effects. Due to the complexity of this active source, it is mandatory to validate material and design parameters via preliminary measurements on equivalent ad hoc passive samples. Their fabrication and linear optical characterization are therefore described in Sections III and IV.

II. Active Device Design

The active microring device is sketched in Fig. 1. Its vertical structure consists of a double-metal nested waveguide that allows the confinement of both near-IR and THz modes. The pump fields are provided by the simultaneous lasing of two near-IR WGMs excited by InAs QDs embedded in the two central GaAs layers [13], with no mode competition, while we aim at generating the THz mode through DFG.

Our design choices stem from several requirements related to the need of having: 1) an efficient nonlinear conversion; 2) a properly working near-IR dual-wavelength laser; and 3) physical parameters compatible with epitaxial growth and processing constraints.

In order to reduce the detrimental effect of TPA at the near-IR frequencies, the structure is mostly made by AlGaAs alloys with an Al composition above 40%, with a minimum use of GaAs. The latter is only employed for the ohmic contacts and for the barriers of the QDs, which are designed according to a dot-in-a-well scheme, with pure InAs dots embedded in an $In_{0.15}Ga_{0.85}As$ layer.

Manuscript received January 07, 2013; revised February 26, 2013; accepted March 13, 2013. This work was supported by the Future and Emerging Technologies (FET) program within the 7th Framework Program for Research of the European Commission, under FET-Open Grant 250056 (TREASURE).

S. Mariani, A. Andronico, I. Favero, S. Ducci, Y. Todorov, C. Sirtori, and G. Leo are with University Paris Diderot, Sorbonne Paris Cité, Laboratoire MPQ, CNRS-UMR 7162, 75013 Paris, France (e-mail: silvia.mariani@univ-paris-diderot.fr; alessio.andronico@univ-paris-diderot.fr; ivan.favero@univ-paris-diderot.fr;sara.ducci@univ-paris-diderot.fr; yanko.todorov@univ-paris-diderot.fr; carlo.sirtori@univ-paris-diderot.fr; giuseppe.leo@univ-paris-diderot.fr).

M. Kamp is with Technische Physik, Physikalisches Institut, University of Würzburg, Am Hubland, D-97074 Würzburg, Germany (e-mail: martin.kamp@physik.uni-wuerzburg.de).

J. Claudon, M. Munsch, and J.-M. Géraud are with CEA-CNRS-UJF group Nanophysique et Semiconducteurs, CEA, INAC, SP2M, F-38054 Grenoble, France (e-mail: julien.claudon@cea.fr; mathieu.munsch@cea.fr; jean-michel.gerard@cea.fr).

T. Wang and P. U. Jepsen are with the Department of Photonics Engineering, Technical University of Denmark, DK-2800 Kongens Lyngby, Denmark (e-mail: tianw@fotonik.dtu.dk; puje@fotonik.dtu.dk).

Color versions of one or more of the figures in this paper are available online at http://ieeexplore.ieee.org.

Digital Object Identifier 10.1109/TTHZ.2013.2255048

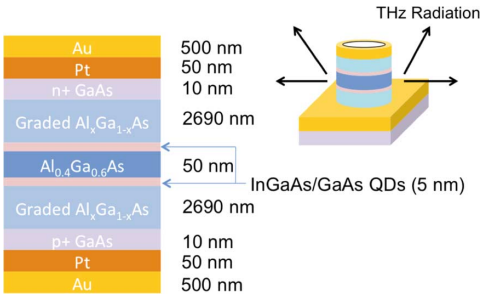

Fig. 1. Vertical layout of the active device. The graded AlGaAs regions have an Al concentration varying linearly from 40% (at the interface with the QD layers) to 80% (at the interface with the highly doped GaAs layers). Inset: 3D sketch of the double-metal microring resonator.

Concerning the cladding layers, a "flat GRINSCH" structure [14] is exploited to minimize the doping, which is kept heavy (10^{19} cm^{-3}) only at the ohmic contacts (10 nm of GaAs and the first 40 nm of the GRINSCH). The rest of the graded regions, with Al composition varying linearly between 0.8 and 0.4, have a $5 \cdot 10^{16}$ cm^{-3} doping, which is a reasonable compromise between the minimization of the series resistance and the maximization of laser power in the near-IR. Higher doping levels would result in very weak conversion efficiency (due to increased free carrier absorption for the THz mode), while lower levels would not permit to reach sufficient lasing power.

Also, a thin layer of Pt is needed between the semiconductor structure and the Au contacts in order to prevent diffusion of the gold into the semiconductor during contact annealing. However, the thickness of the Pt layer must be minimized, because it induces additional THz losses.

A. Expected Performance

With the above vertical structure, finite-difference frequency-domain simulations show that a ring with external (internal) radius $R_{\rm ext} = 18.88$ μm ($R_{\rm int} = 17.25$ μm) can sustain the following triplet of WGMs: ($\lambda_1 = 1.2458$ μm, $m_1 = 289$, $p_1 = 1$), ($\lambda_2 = 1.2618$ μm, $m_2 = 285$, $p_2 = 1$), ($\lambda_3 = 98.4$ μm, $m_3 = 2$, $p_3 = 1$). Here λ is the wavelength, and m (p) the WGM azimuthal (radial) number, respectively. Phase matching is fulfilled since $\Delta m = m_1 - m_2 - m_3 = 2$ [10]. For pump quality factors around $Q = 10^5$, we predict a nonlinear conversion efficiency $\eta \sim 20$ μW/W^2, which is close to the value $\eta \sim 30$ μW/W^2 reported, for pulsed operations, in [10].

The most relevant loss mechanism for the THz WGM are: 1) curvature (radiation) losses; 2) absorption losses in the metal layers; and 3) free carrier absorption. In our case we calculate $Q^{\rm rad} = 98$, $Q^{\rm met} = 54$, and $Q^{\rm FCA} = 61$, respectively.

Thermal management plays a fundamental role in the operation of such active device insofar phase-matching condition can be affected by the temperature dependence of the refractive indices. Therefore, in order to assess its realistic performance, we resorted to a full optical-electrical-thermal modeling, which we carried out with commercial software. For example, this analysis has shown that heat sinking is strongly improved if gold-on-gold bonding is used for the flip-chip fabrication of the double-metal structure of Fig. 1, instead of the simpler epoxy bonding. Moreover, as detailed below, the p-side down choice provides better heat sinking and lower operating temperature than the n-side down geometry.

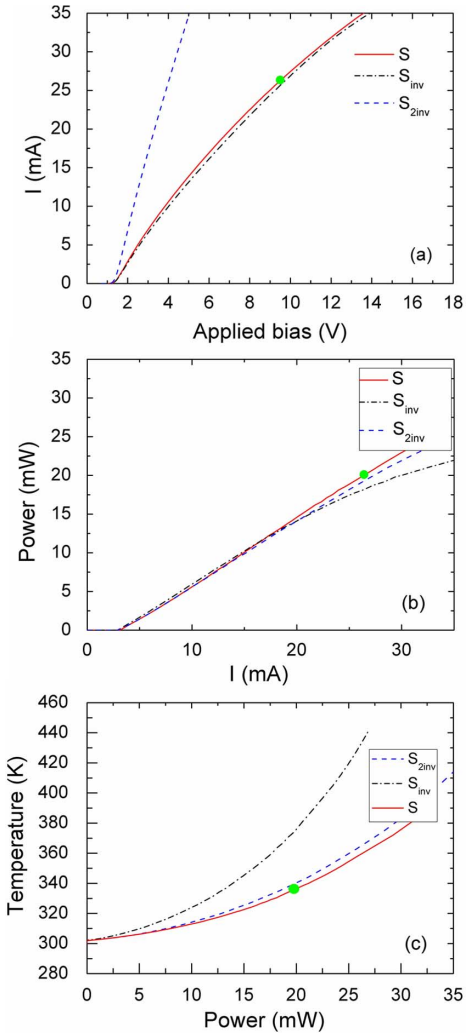

Fig. 2. Calculated characteristic curves: (a) I–V, (b) P-I, and (c) T-P of the structures S, $S_{\rm inv}$ and $S_{\rm 2inv}$. The expected operating point of the device is marked with a green dot.

The main characteristics of the device of Fig. 1 (S on the graphs) are reported in Fig. 2, where we compare them with those of two structures mounted n-side down, either identical to S (structure $S_{\rm inv}$), or with a higher (10^{17} cm^{-3}) doping level in the cladding layers (structure $S_{\rm 2inv}$).

Compared to standard GaAs laser diodes, these structures exhibit a large series resistance, due to their weakly doped flat GRINSCH. Nevertheless, currents in the few tens of mA range and output powers in the few tens of mW range can be obtained, albeit for unusually large bias.

As seen in Fig. 2(c), the p-side down mounting results in a much better heat sinking: a total output power of 20 mW can be achieved for sample S, with a modest temperature raise of the

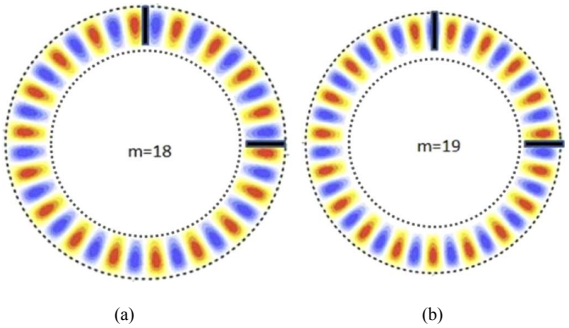

Fig. 3. Calculated field distribution of two WGMs in notched rings with 90° offset angle. The azimuthal numbers are (a) $m = 18$ (left) and (b) $m = 19$.

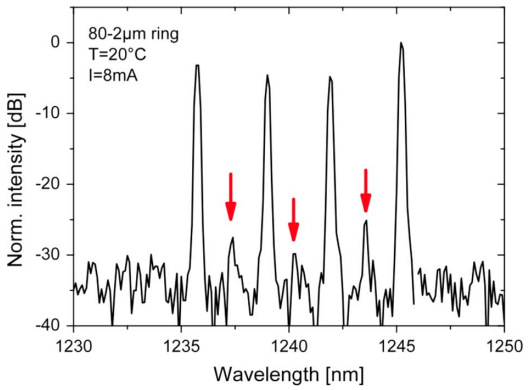

Fig. 4. Experimental emission spectrum of a QD ring laser with 80 μm diameter and 2 μm width, driven by a current of 8 mA.

active region (+35 K). This not only enables a stable laser operation without mode jumps, but also a robust phase matching.

Another point to observe is that, although providing a lower series resistance, the larger doping level of sample $S_{2\mathrm{inv}}$ does not bring a major advantage in terms of output power or temperature raise of the active layer, but it severely downgrades the THz output (simulations not shown here).

B. Mode Selection Mechanism

In order to have efficient DFG, the energy provided by the active medium should be funneled preferentially in the only two modes that contribute to the nonlinear process (i.e., in our case, the WGMs with azimuthal orders $m_1 = 289$ and $m_2 = 285$). This can be achieved by exploiting, as mode selection mechanism, a small number of notches etched along the external cavity sidewalls.

The concept is illustrated in Fig. 3, which shows the field distribution of two WGMs in a ring with two notches (black lines) placed at an angle of 90°. If the notches are small compared to the wavelength in the ring, the losses experienced by WGMs with even azimuthal number will be small. On the other hand, the losses for WGMs with odd m will increase, leading to a selection of every second mode in the laser spectrum.

Fig. 4 shows the effect of the notches on the experimental emission spectrum of a ring QD laser with a diameter $D = 80$ μm ($\mathrm{R_{ext}} = 40$ μm and $\mathrm{R_{int}} = 38$ μm). Every second mode (red arrows) is suppressed by the notch-induced losses.

The same idea can be extended to other angles between the notches. For example, if the notches are placed at an angle of 60 degree, every third mode will have little overlap with the notches and therefore contribute to the lasing spectrum.

For THz generation, lasing on two modes with a spacing of four times the free spectral range of the unmodified ring is required. This can be achieved by placing the notches at an angle of 45°. Moreover, since the notches are very small compared to the wavelength of the THz mode, the latter will not suffer from significant notch-induced losses.

The above discussion illustrates that the fabrication of the final active device is a challenging task. In order to validate the parameters used in the modeling, we therefore adopted a cautious approach and fabricated two simplified passive devices to be tested separately in the near-IR and in the THz. Using such structures allowed us to neglect geometric and composition constraints dictated by phase-matching or heat-sinking issues, thus reducing their fabrication complexity.

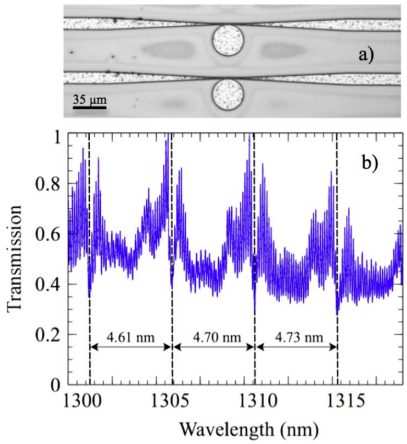

Fig. 5. (a) Optical microscope image of two micro-cavities with integrated tapered coupling waveguides. (b) Transmission spectrum of a waveguide coupled to a resonator with radius $R = 17.5$ μm. The guide width is 500 nm in its narrowest part, while the guide-to-resonator distance is 350 nm.

III. Passive Samples Fabrication

The passive samples were grown by MBE according to the following vertical layout: 2505 nm of $Al_{0.8}Ga_{0.2}As$, 377 nm of $Al_{0.33}Ga_{0.67}As$, and 2453 nm of $Al_{0.8}Ga_{0.2}As$. The three layers are sandwiched between two thin (69 nm) GaAs caps and lie on a sacrificial $Al_{0.8}$ $Ga_{0.2}$ As buffer (460 nm).

While sharing the same vertical structure, the samples used for the near-IR characterization and the ones used for the THz characterization differ substantially.

As shown in Fig. 5(a), in order to excite the near-IR WGMs sustained by the cavities, integrated tapered waveguide are necessary. The waveguide width and distance from the resonator are designed to obtain critical coupling for the pump modes [15], while the taper length is chosen to provide an adiabatic transition (∼5% of transmission losses). Please note that the required deep etching between the cavity and the waveguide considerably increases the difficulty of the fabrication.

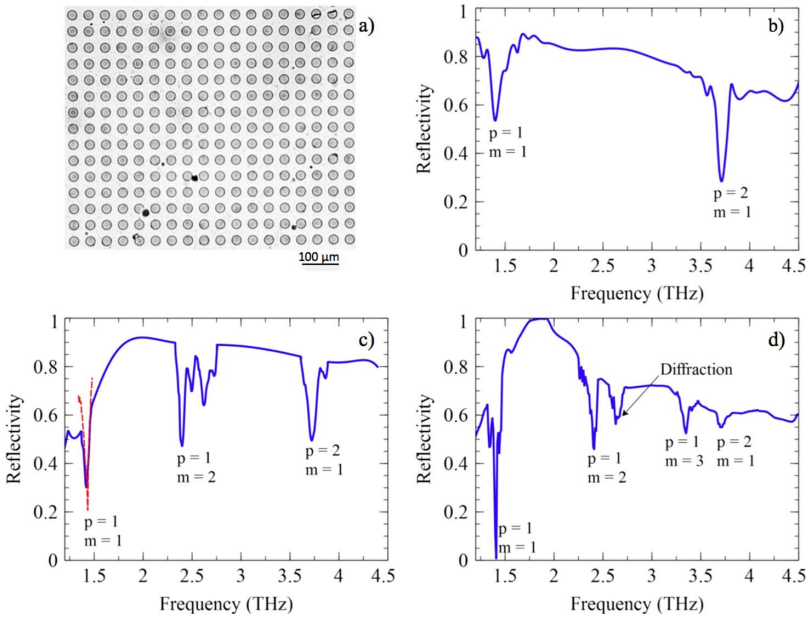

Fig. 6. (a) Optical microscope image of an array of micro-cylinders with radius $\mathrm{R} = 20\ \mu$m. FTIR reflectivity spectra obtained at (b) normal incidence; (c) 45° incidence angle; (d) grazing incidence. All spectra result from averaging approximately 200 measurements. The spectral resolution is about 7.5 GHz. The dashed line in Fig. 2(c) represents the reflectivity spectrum obtained with TDS measurements.

The samples for the THz characterization on the other hand do not require coupling waveguides, but they need a double metallization for confining the THz modes. To this end, after the epitaxial growth, we deposited a gold mirror over the epitaxial layers and epoxy bond the mirror to a host substrate; the growth wafer and the sacrificial layer were subsequently removed by mechanical and selective wet etching [16]. The micro-pillars were finally defined by electron–cyclotron—resonance plasma etching, using a second gold mirror deposited on top of the semiconductor layers and covered by a hard Ni mask.

IV. Experimental Results

A. Near-IR Characterization

For the characterization in the near-IR, light from a tunable laser is injected into the waveguide with a tapered micro-lensed fiber, while a microscope objective is used to redirect the transmitted field onto the detector. In Fig. 5(b) we show an example of transmission spectrum thus obtained, where the high frequency oscillations correspond to the Fabry–Pérot fringe pattern due to reflections at the waveguide facets. The resonances appearing on the graph correspond to the family of lowest radial order ($\mathrm{p} = 1$) modes, and the free-spectral range can be estimated as $\Delta\lambda = \lambda^2/(2\pi \mathrm{R} \mathrm{n_g})$, where $\mathrm{n_g}$ is the WGM group index. At $\lambda = 1300$ nm this gives $\Delta\lambda \sim 4.55$ nm, instead of the experimental value $\Delta\lambda \sim 4.61$ nm. This discrepancy is not expected to hinder THz DFG because the low THz quality factor provides a tolerance of about 140 GHz for fulfilling phase matching (although phase-matching acceptance, being dictated by the high quality factors at λ_1 and λ_2, is less than 5 GHz).

B. THz Characterization

In order to characterize the THz properties of the microresonators, we fabricated 2D arrays of identical pillars, where the cavities' radii range from 10 to 20 μm and the nearest-neighbor separation is 25 μm [see Fig. 6(a)]. We subsequently characterized their spectral features by using reflectivity measurements [17] performed with a Fourier transform infra-red spectrometer (FTIR). The THz radiation, provided by the Globar lamp included in the FTIR, is collimated onto the sample with a parabolic mirror and the reflected signal is collected by a bolometer. In order to avoid absorption caused by humidity, the samples are enclosed into a PVC box, and the whole optical path from source to detector is kept under a continuously flowing dry air purge.

In Fig. 6, we show a few FTIR reflectivity spectra obtained by varying the incidence angle: normal incidence (b), 45° angle incidence (c), and grazing incidence (d). Each dip, with the only exception of the one—due to grating diffraction—at 2.7 THz in Fig. 6(d), corresponds to the excitation of a cavity mode. The position and the width of the dips match very well the values expected from the modeling, as shown in Table I. An interesting feature emerging from these spectra is that, in analogy with results already reported in [17] for different cavities, by varying the incidence angle we are able to excite cavity modes with different azimuthal (m) and radial (p) orders. If we consider, for example, normal incidence (Fig. 5(b)), then we see that only WGMs with $m = 1$ (the dipole-like modes) appear on the spectrum. On the other hand, by exploiting non-vertical incidence angle, we can excite quadrupole-like modes ($m = 2$, 45° angle incidence), and hexapole-like modes ($m = 3$, grazing

TABLE I

		a		b		c		d	
m	p	ν (THz)	Q	ν (THz)	Q*	ν (THz)	Q*	ν (THz)	Q*
1	1	1.400	33	1.403 ± 0.007	17 ± 2	1.417 ± 0.007	32 ± 3	1.402 ± 0.007	23 ± 13
2	1	2.404	59	-	-	2.401 ± 0.007	59 ± 6	2.408 ± 0.007	47 ± 9
3	1	3.345	83	-	-	-	-	3.348 ± 0.007	41 ± 7
1	2	3.700	42	3.714 ± 0.007	45 ± 3	3.717 ± 0.007	47 ± 4	3.722 ± 0.007	30 ± 6

Comparison between the results of our simulations (a) and the experimental data obtained at normal incidence (b), 45° incidence (c), and grazing incidence (d). The experimental quality factors (Q* columns) are estimated from the dips' FWHM.

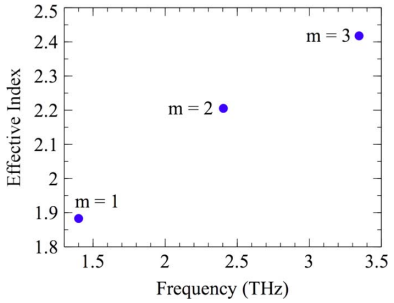

Fig. 7. Effective index of the THz WGMs with radial order $\mathrm{p} = 1$.

incidence). Sample 2D profiles of the corresponding WGMs are provided in [19].

Independent reflection measurements were also performed on the same samples with a fiber-coupled THz time-domain spectroscopy (THz-TDS) system (Picometrix T-Ray 4000) with photoconductive switches for generation and detection of ultrashort THz transients [18], to assess the accuracy of the results obtained between 1 and 2 THz, where the FTIR spectra are affected by higher noise due to the presence of the bolometer filtering window. As shown in Fig. 6(c) (dashed red curve), these additional experiments performed with an effective spectral resolution of approximately 6 GHz confirmed the spectral features observed in the FTIR spectra.

Finally, in Fig. 7 we report the inferred effective modal index for the THz WGMs with lowest radial order $(p = 1)$. This was obtained with the approximate relation: $n_{\mathrm{eff}} = m\lambda/(2\pi R)$. As seen in the figure, higher m modes have a higher effective index, indicating a stronger confinement inside the cavity.

V. Conclusion

We have reported on the design of a WGM QD laser microresonator, with the aim of achieving an electrically pumped CW THz source operating at room temperature, via triply-resonant DFG from near-IR pumps. In order to test our modeling tools and to extract physically sound parameters, we have also fabricated and linearly characterized passive ad hoc samples. The experimental data match very well the values obtained with our simulations, thus providing the necessary solid grounds for the fabrication and test of the first active device.

Acknowledgment

One of the authors, S. Mariani, acknowledges F. Ghiglieno for experimental help.

References

[1] P. H. Siegel, "Terahertz technology," *IEEE Trans. Microw. Theory Techn.*, vol. 50, pp. 910–928, 2002.
[2] M. Tonouchi, "Cutting-edge terahertz technology," *Nat. Photon.*, vol. 1, pp. 97–106, 2007.
[3] E. R. Brown, K. A. McIntosh, K. B. Nichols, and C. L. Dennis, "Photomixing up to 3.8 THz in low-temperature-grown GaAs," *Appl. Phys. Lett.*, vol. 66, pp. 285–287, 1995.
[4] R. Köhler, A. Tredicucci, F. Beltram, H. Beere, E. H. Linfield, A. G. Davies, D. A. Ritchie, R. C. Iotti, and F. Rossi, "Terahertz semiconductor-heterostructure laser," *Nature*, vol. 417, pp. 156–159, 2002.
[5] K. Kawase, H. Minamide, K. Imai, J. Shikata, and H. Ito, "Injection-seeded terahertz-wave parametric generator with wide tunability," *Appl. Phys. Lett.*, vol. 80, pp. 195–197, 2002.
[6] K. L. Vodopyanov, "Optical THz-wave generation with periodically-inverted GaAs," *Laser & Photon. Rev.*, vol. 2, pp. 11–25, 2008.
[7] M. A. Belkin, F. Capasso, F. Xie, A. Belyanin, M. Fischer, A. Wittmann, and J. Faist, "Room temperature terahertz quantum cascade laser source based on intracavity difference-frequency generation," *Appl. Phys. Lett.*, vol. 92, pp. 201101:1–201101:3, 2008.
[8] Q. Y. Lu, N. Bandyopadhyay, S. Slivken, Y. Bai, and M. Razeghi, "Room temperature single-mode terahertz sources based on intracavity difference-frequency generation in quantum cascade lasers," *Appl. Phys. Lett.*, vol. 99, pp. 131106:1–131106:3, 2011.
[9] K. Vijayraghavan, R. W. Adams, A. Vizbaras, M. Jang, C. Grasse, G. Boehm, M. C. Amann, and M. A. Belkin, "Terahertz sources based on Cherenkov difference-frequency generation in quantum cascade lasers," *Appl. Phys. Lett.*, vol. 100, pp. 251104:1–251104:4, 2013.
[10] Q. Y. Lu, N. Bandyopadhyay, S. Slivken, Y. Bai, and M. Razeghi, "High performance terahertz quantum cascade laser sources based on intracavity difference frequency generation," *Opt. Express*, vol. 21, pp. 968–973, 2013.
[11] A. Andronico, J. Claudon, J. M. Gérard, V. Berger, and G. Leo, "Integrated terahertz source based on three-wave mixing of whispering-gallery modes," *Opt. Lett.*, vol. 33, pp. 2416–2418, 2008.
[12] A. Andronico, S. Mariani, F. Ghiglieno, J. Claudon, M. Munsch, J. M. Gérard, I. Favero, S. Ducci, and G. Leo, "Tuning of a nonlinear THz emitter," *Opt. Express*, vol. 20, pp. 17678–17683, 2012.
[13] M. Munsch, J. Claudon, N. S. Malik, K. Gilbert, P. Grosse, J. M. Gérard, F. Albert, F. Langer, T. Schlereth, M. M. Pieczarka, S. Höfling, M. Kamp, A. Forchel, and S. Reitzenstein, "Room temperature, continuous wave lasing in microcylinder and microring quantum dot laser diodes," *Appl. Phys. Lett.*, vol. 100, pp. 031111:1–031111:4, 2011.
[14] W. T. Tsang, R. A. Logan, and J. A. Ditzenberger, "Ultra-low threshold, graded-index waveguide, separate confinement, CW buried-heterostructure lasers," *Electron. Lett.*, vol. 18, pp. 845–847, 1982.
[15] C. Baker, C. Belacel, A. Andronico, P. Senellart, A. Lemaître, E. Galopin, S. Ducci, G. Leo, and I. Favero, "Critical optical coupling between a GaAs disk and a nanowaveguide suspended on the chip," *Appl. Phys. Lett.*, vol. 99, pp. 151117:1–151117:3, 2011.
[16] J. Claudon, J. Bleuse, N. S. Malik, M. Bazin, P. Jaffrennou, N. Gregersen, C. Sauvan, P. Lalanne, and J. M. Gérard, "A highly efficient single-photon source based on a quantum dot in a photonic nanowire," *Nat. Photon.*, vol. 4, pp. 174–177, 2010.
[17] Y. Todorov, L. Tosetto, J. Teissier, A. M. Andrews, P. Klang, R. Colombelli, I. Sagnes, G. Strasser, and C. Sirtori, "Optical properties of metal-dielectric-metal microcavities in the THz frequency range," *Opt. Express*, vol. 18, pp. 13886–13907, 2010.

[18] P. U. Jepsen, D. G. Cooke, and M. Koch, "Terahertz spectroscopy and imaging—Modern techniques and applications," *Laser Photon. Rev.*, vol. 5, pp. 124–166, 2011.

[19] K. Iwaszczuk, C. Z. Bisgaard, A. Andronico, G. Leo, and P. U. Jepsen, "Numerical investigation of terahertz emission properties of microring difference-frequency resonators," *IEEE Trans. THz Sci. Technol.*, vol. 3, no. 2, pp. 192–199, Mar. 2013.

Silvia Mariani was born in Rome, Italy, in 1987. She received the Laurea degree (summa cum laude) in physics from the Italian University "La Sapienza", Rome, Italy, in July 2011, with a Laurea thesis performed at CERN, Geneva, Switzerland. In October 2011 she joined the TREASURE project as Ph.D. student, focusing her research interests on three-wave mixing in semiconductor whispering-gallery-mode resonators.

Alessio Andronico received the Laurea degree in physics in 2004, from the university La Sapienza, Rome, Italy and his Ph.D. in physics in 2008, from the University Paris Diderot, Paris, France.

He is currently a research scientist with the University Paris Diderot, Paris, France. His research interests include nonlinear optics and computational electrodynamics.

Ivan Favero received the Ph.D. degree in physics in 2005 for a research on Semiconductor Quantum dots carried-out at the physics department of the Ecole Normale Supérieure."

He has later been a Post-Doctoral fellow of the Von Humboldt foundation, Munich University LMU, where he was involved in pioneering research on the optomechanics of deformable optical cavities. In 2008, he joined the CNRS, France, within the MPQ laboratories at University Paris Diderot, where he launched a research activity on gallium–arsenide nano-optomechanical systems. His current interests include whispering gallery resonators, nanomechanics, sensors, quantum optics.

Sara Ducci was born in Montevarchi, Italy, in 1971. She received her Laurea degree (*summa cum laude*) and the Ph.D. degree in physics from the University of Florence, Italy.

After one year as Post-Doctorate at Laboratoire Kastler Brossel, Paris, France, during 2000–2001, and a one year as temporary assistant professor at Ecole Normale Supérieure Cachan (2001–2002).

In 2002, she has been appointed as Assistant Professor at the Université Paris Diderot, Paris, France, where she has become Full Professor in 2008. After her works on pattern formation in nonlinear optical systems and spatial quantum correlations in optical parametric oscillators, her present interests are focused on integrated quantum photonics for quantum information and optical parametric generation in AlGaAs heterostructures and microcavities. She is the head of the Master program 'Quantum Devices' of the University Paris Diderot and Ecole Polytechnique, member of the optics section of the National Council of the Universities, member of the Council of the Faculty of Physics and coordinator of the Photonic axe of the 'Laboratoire d'Excellence' SEAM (Science and Engineering of Advanced Materials and Photonic Devices.

Dr. Ducci is member of Institut Universitaire de France, since 2012.

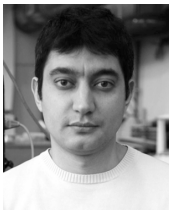

Yanko Todorov was born in Burgas, Bulgaria, in 1978. He received the Masters degree in physics from Ecole Normale Supérieure (rue d'Ulm), in 2003, and the Ph.D. degree in physics from Université Pierre et Marie Curie in 2006.

His Ph.D. work was carried in LPN/Marcoussis and concerned the study of the Purcell enhancement in electroluminescent quantum cascade devices in the THz frequency range. His Post-Doctoral research took place in MPQ Laboratory in University Paris 7, for studies on the strong light-matter coupling regime in the THz range. Since 2010 he is working as CNRS researcher in MPQ, working on the ultra-strong light matter coupling and electrical injection of intersubband polaritons. He is author or co-author of numerous publications in the field.

Carlo Sirtori received the Ph.D. degree in physics from the University of Milan in 1990.

Following his degree in 1990, he joined Bell Labs where he started his research career on quantum devices. At Bell Labs he made important contributions in the field of semiconductor quantum structures such as the invention and the development of the "Quantum Cascade Laser". In 1997, he joined the THALES Research & Technology (TRT) in France. In 2000, he was appointed head of the "Semiconductor Laser Group" at THALES. During this time he developed the first quantum cascade laser based on GaAs/AlGaAs and the concept of plasmonic waveguides for semiconductor lasers. Since 2002, he is Professor at the University Paris Diderot, where he pursues his research on unipolar quantum devices. In 2010, he became Director of the MPQ laboratories of Paris Diderot. One of his major research activities is, at present, the investigation of electrically injected devices operating in the light-matter strong coupling regime. Carlo Sirtori is the author of more than 210 articles in peer reviewed journals and has given some 80 invited talks at international conferences. He has received several prestigious awards such as the Fresnel Prize (European Physical Society) and various prizes in the USA, such as the "quantum devices award".

In 2010, Dr. Sirtori was awarded an ERC-advanced-grant for his pioneering research on quantum devices. He is presently a member of the Institut Universitaire de France.

Martin Kamp received the M.A. degree in physics from Stony Brook University, NY, USA, and the Ph.D. degree at the University of Würzburg in 2003 for his work on 'Laterally coupled semiconductor lasers'.

He is currently deputy chair of Technische Physik and head of the Microstructure Laboratory at the University of Würzburg. He is author or coauthor of over 150 papers relating to semiconductor nanostructures, optoelectronic devices and semiconductor spectroscopy. His current research interests include the investigation of light-matter interaction in semiconductor nanostructures and novel optoelectronic devices.

Mathieu Munsch was born in Mulhouse, France, in 1983. He received the Physics Engineer degree from INP Grenoble, France in 2006, the Masters degree in nanostructures, and the Ph.D. degree in physics from Université Joseph Fourier, Grenoble, France, in 2006 and 2009, respectively.

In 2010, he joined the Institute for Nanotechnology and Cryogenics (INAC) at CEA Grenoble as a Postdoc. Since May 2012, he has been in the Nano-Photonics group of the Physics Department of Basel Universität, Switzerland. His current research interests include generation of quantum light, spin coherence, spin-photon interface, nuclear magnetic resonance and nanostructures. He is a member of the QSIT program for the development of quantum science and technology in Switzerland.

Julien Claudon was born in France in 1978. In 2002, he received the M.Sc. degree in condensed matter physics jointly from the Ecole Normale Supérieure de Lyon and from the Joseph Fourier University , Grenoble, France, and the Ph.D. degree from the Joseph Fourier University in 2005, after a work on Josephson superconducting quantum circuits.

He is also Agrégé de Sciences Physiques, in 2001. Since 2006, he is a CEA researcher in the joint team CEA-CNRS, NanoPhysique et SemiConducteurs, Grenoble, France. He develops semiconductor nanophotonic structures, with an interest both in design and nanofabrication. His current research interests include one-dimensional photonic systems for quantum optics, the fast switch of optical microcavities and non-linear frequency conversion in whispering gallery mode resonators.

Jean-Michel Gérard was born in Chamalières, France, on October 2, 1962. He graduated from Ecole Polytechnique, Palaiseau, France, in 1985, and received the Ph.D. degree from Paris VI University, Paris, France, in 1990.

From 1986 to 2001, he was an engineer and scientific expert of the Délégation Générale pour l'Armement (DGA, French Ministry of Defense), affected for research purposes to the Centre National d'Etudes des Telecommunications in Bagneux(CNET). He joined the French Atomic Commission (CEA) in 2001 to become Head of the Nanophysics and Semiconductors CEA-CNRS joint Laboratory in Grenoble. Since 2005, he is in charge of the Service for Physics of Materials and Microstructures of the Institute for Nanoscience and Cryogeny (CEA/INAC/SP2M) in Grenoble, France. He has also been Professor of physics at Ecole Normale Supérieure de Techniques Avancées, Paris, from 1992 to 1997, and Associate Professor in physics at Ecole Polytechnique, Palaiseau, France, since 1997. His research interests include the physics of semiconductor nanostructures, optical microcavities, solid-state quantum optics, and nanotechnology. He authored more than 250 papers and book chapters, and 12 patents.

Dr. Gérard is a member of the French optical society (SFO) and French Physical Society (SFP). He received the young scientist award awarded by DGA in 1997, the Great Prize founded by the State from the French Academy of Sciences in 2005, and the Quantum Devices Award, sponsored by Eudyna Corporation, Japan, in 2008.

Tianwu Wang was born in Hei Longjiang Province, China, in 1984. He received his B.E. degree in optoelectric engineering and M.S. degree in optical engineering from National University of Defense Technology (NUDT), Changsha, China, in 2007 and 2009, respectively, and the Ph.D. degree from the Department of Optical Engineering, NUDT, in 2010. ow he is a Ph.D. student under the project of THz-BREW: Terahertz Broadband Relaxation dynamics of Electons in Water in the Department of Photonics Engineering, DTU.

In 2011, he joined the Department of Photonics Engineering, Technique University of Denmark (DTU), DK-2800 Kongens Lyngby, Denmark, as a guest Ph.D. student. He won the second award in 2007 China undergraduate Challenge Cup contest in Extracurricular Academic and Technology Works.

Peter Uhd Jepsen (M'11) received the M.Sc. in physics and chemistry in 1994 from Odense University, Denmark and the Ph.D. degree in natural sciences from Århus University, Denmark, in 1996.

He was at the University of Freiburg, Germany, from 1996 to 2004, working with terahertz time-domain spectroscopy. From 2005 he was Associate Professor at the Technical University of Denmark (DTU), and since 2008 Full Professor and Head of the Terahertz Technologies and Biophotonics group at DTU. He was visiting professor at Osaka University in 2008. His research areas include photonics-based THz technology, broadband spectroscopy, ultrafast lasers, time-resolved THz spectroscopy, and nonlinear THz science.

Giuseppe Leo received the M.Sc. degree (*summa cum laude*) in electrical engineering in 1990, La Sapienza University, Rome, Italy, and the Ph.D. degree in physics in 2001, from Paris-Sud University, Orsay, France.

Since 1992, he was Assistant Professor at Rome-3 University, where he became Associate Professor in 2002. Since 2004, he has been Full Professor at Paris Diderot University, and Head of the Nonlinear Devices group of MPQ Laboratory since 2006. His research areas include nonlinear optics and quantum optoelectronics, with a focus on AlGaAs platform. He has coordinated several research programs and published 67 articles, 9 book chapters, and >120 conference papers. He has also edited 1 one book and registered 3 patents.

Bibliography

[1] T. H. Maiman, *Stimulated optical radiation in ruby*, Nature **87**, 493 (1960).

[2] K. J. Vahala, *Optical microcavities*, Nature **424**, 839 (2003).

[3] L. Davidovich, A. Maali, M. Brune, J. M. Raimond, and S. Haroche, *Quantum Switches and Nonlocal Microwave Fields*, Phys. Rev. Lett. **71**, 2360 (1993).

[4] Q. A. Turchette, C. J. Hood, W. Lange, H. Mabuchi, and H. J. Kimble, *Measurement of Conditional Phase Shifts for Quantum Logic*, Phys. Rev. Lett. **75**, 4710 (1995).

[5] J. S. Foresi, P. R. Villeneuve, J. Ferrera, E. R. Thoen, G. Steinmeyer, S. Fan, J. D. Joannopoulos, L. C. Kimerling, H. I. Smith, and E. P. Ippen, *Photonic-bandgap microcavities in optical waveguides*, Nature **390**, 143 (1997).

[6] F. Albert, T. Braun, T. Heindel, C. Schneider, S. Reitzenstein, S. Höfling, L. Worschech, and A. Forchel, *Whispering gallery mode lasing in electrically driven quantum-dot micropillars*, Appl. Phys. Lett. **97**, 101108 (2010).

[7] T. J. Kippenberg, H. Rokhsari, T. Carmon, A. Scherer, and K. J. Vahala, *Analysis of Radiation-Pressure Induced Mechanical Oscillation of an Optical Microcavity*, Phys. Rev. Lett. **95**, 033901 (2005).

[8] J. Zhu, S. K. Ozdemir, Y. F. Xiao, L. Li, L. He, D. R. Chen, and L. Yang, *On-chip single nanoparticle detection and sizing by mode splitting in an ultrahigh-Q microresonator*, Nat. Photonics **4**, 46 (2010).

[9] J. U. Fürst, D. V. Strekalov, D. Elser, A. Aiello, U. L. Andersen, Ch. Marquardt, and G. Leuchs, *Quantum Light from a Whispering-Gallery-Mode Disk Resonator*, Phys. Rev. Lett. **106**, 113901 (2011).

[10] Y. Takahashi, Y. Inui, M. Chihara, T. Asano, R. Terawaki, and S. Noda, *A micrometre-scale Raman silicon laser with a microwatt threshold*, Nature **498**, 470 (2013).

[11] T. J. Kippenberg, R. Holzwarth, and S. A. Diddams, *Microresonator-Based Optical Frequency Combs*, Science **332**, 555 (2011).

[12] Y. Okawachi, K. Saha, J. S. Levy, Y. H. Wen, M. Lipson, and A. L. Gaeta, *Octave-spanning frequency comb generation in a silicon nitride chip*, Opt. Lett. **36**, 3398 (2011).

[13] J. S. Levy, M. A. Foster, A. L. Gaeta, and M. Lipson, *Harmonic generation in silicon nitride ring resonators*, Opt. Express **19**, 11415 (2011).

[14] J. S. Levy, A. Gondarenko, M. A. Foster, A. C. Turner-Foster, A. L. Gaeta, and M. Lipson, *CMOS-compatible multiple-wavelength oscillator for on-chip optical interconnects*, Nat. Photonics **4**, 37 (2010).

[15] M. Savanier, C. Ozanam, L. Lanco, X. Lafosse, A. Andronico, I. Favero, S. Ducci, and G. Leo, *Near-infrared optical parametric oscillator in a III-V semiconductor waveguide*, Appl. Phys. Lett. **103**, 261105 (2013).

[16] A. Orieux, A. Eckstein, A. Lemaître, P. Filloux, I. Favero, G. Leo, T. Coudreau, A. Keller, P. Milman, and S. Ducci, *Direct Bell states generation on a III-V semiconductor chip at room temperature*, Phys. Rev. Lett. **110**, 160502 (2013).

[17] A. Vallés, M. Hendrych, J. Svozilík, R. Machulka, P. Abolghasem, D. Kang, B. J. Bijlani, A. S. Helmy, and J. P. Torres, Opt. Express **21**, 10841 (2013).

[18] Z. Yang, P. Chak, A. D. Bristow, H. M. van Driel, R. Iyer, J. S. Aitchison, A. L. Smirl, and J. E. Sipe, *Enhanced second-harmonic generation in AlGaAs microring resonators*, Opt. Lett. **32**, 826 (2007).

[19] A. Andronico, I. Favero, and G. Leo, *Difference frequency generation in GaAs microdisks*, Opt. Lett. **33**, 2026 (2008).

[20] Z. Yang and J. E. Sipe, *Generating entangled photons via enhanced spontaneous parametric downconversion in AlGaAs microring resonators*, Opt. Lett. **32**, 3296 (2007).

[21] I. Shoji, T. Kondo, A. Kitamoto, M. Shirane, and R. Ito, *Absolute scale of second-order nonlinear-optical coefficients*, J. Opt. Soc. Am. B **14**, 2268 (1997).

[22] R. Miller, *Optical second harmonic generation in piezoelectric crystals*, Appl. Phys. Lett. **5**, 17 (1964).

[23] A.S. Helmy, P. Abolghasem, J. Stewart Aitchison, B.J. Bijlani, J. Han, B.M. Holmes, D.C. Hutchings, U. Younis, and S.J. Wagner, *Recent advances in phase matching of second-order nonlinearities in monolithic semiconductor waveguides*, Laser & Photon. Rev. **5**, 272 (2011).

[24] Y. Dumeige and P. Feron, *Whispering-gallery-mode analysis of phase-matched doubly resonant second-harmonic generation*, Phys. Rev. A **74**, 063804 (2006).

[25] S. L. McCall, A. F. J. Levi, R. E. Slusher, S. J. Pearton, and R. A. Logan, *Whispering-Gallery Mode Microdisk Lasers*, Appl. Phys. Lett. **60**, 289 (1992).

[26] B. E. Little, S. T. Chu, H. A. Haus, J. Foresi, and J.-P. Laine, *Microring resonator channel dropping filters*, J. Lightwave Technol. **15**, 998 (1997).

[27] V. S. Ilchenko, A. B. Matsko, A. A. Savchenkov, and L. Maleki, *Low-Threshold Parametric Nonlinear Optics with Quasi-Phase-Matched Whispering-Gallery Modes*, J. Opt. Soc. Am. B **20**, 1304 (2003).

[28] P. S. Kuo, and G. S. Solomon, *On- and off-resonance second-harmonic generation in GaAs microdisks*, Opt. Express **19**, 16898 (2011).

[29] S. Mariani, A. Andronico, O. Mauguin, A. Lemaître, I. Favero, S. Ducci, and G. Leo, *AlGaAs microdisk cavities for second-harmonic generation*, Opt. Lett. **38**, 3965 (2013).

[30] M. W. McCutcheon, J. F. Young, G. W. Rieger, D. Dalacu, S. Frederick, P. J. Poole, and R. L. Williams, *Experimental demonstration of second-order processes in photonic crystal microcavities at submilliwatt excitation powers*, Phys. Rev. B **76**, 245104 (2007).

[31] M. Galli, D. Gerace, K. Welna, T. F. Krauss, L. O' Faolain, G. Guizzetti, and L. C. Andreani, *Low-power continuous-wave generation of visible harmonics in silicon photonic crystal nanocavities*, Opt. Express **18**, 26613 (2010).

[32] A. Fiore, V. Berger, E. Rosencher, P. Bravetti, and J. Nagle, *Phase matching using an isotropic nonlinear optical material*, Nature **391**, 463 (1998).

[33] K. Moutzouris, S. Venugopal Rao, M. Ebrahimzadeh, A. De Rossi, V. Berger, M. Calligaro, and V. Ortiz, *Efficient second-harmonic generation in birefringently phase-matched GaAs/Al_2O_3 waveguides*, Opt. Lett. **26**, 1785 (2001).

[34] A. Fiore, V. Berger, E. Rosencher, S. Crouzy, N. Laurent, and J. Nagle, *$\Delta n = 0.22$ birefringence measurement by surface emitting second harmonic generation in selectively oxidized GaAs/AlAs optical waveguides*, Appl. Phys. Lett. **71**, 2587 (1997).

[35] G. Leo, M. Secondini, M. Morabito, A. De Rossi, G. Assantob, A. Fiore, V. Berger, M. Calligaro, and J. Nagle, *Birefringence evaluation of multimode multilayer AlGaAs/AlAs waveguides*, Appl. Phys. Lett. **78**, 1472 (2001).

[36] J. P. van der Ziel, R. C. Miller, R. A. Logan, W. A. Nordland Jr., and R. M. Mikulyak, *Phase-matched second-harmonic generation in GaAs optical waveguides by focused laser beams*, Appl. Phys. Lett. **25**, 238 (1974).

[37] S. Ducci, L. Lanco, V. Berger, A. De Rossi, V. Ortiz, and M. Calligaro, *Continuous-wave second-harmonic generation in modal phase matched semiconductor waveguides*, App. Phys. Lett. **84**, 2974 (2004).

[38] K. C. Rustagi, S. C. Mehendale, and S. Meenakshi, *Optical frequency conversion in quasi-phase-matched stacks of nonlinear crystals*, IEEE J. Quantum Electron. **18**, 1029 (1982).

[39] S. Yoo, R. Bhat, C. Caneau et M. Koza, *Quasi-phase-matched second-harmonic generation in AlGaAs waveguides with periodic domain inversion achieved by wafer-bonding*, Appl. Phys. Lett. **66**, 3410 (1995).

[40] K. Lenglé, L. Bramerie, M. Gay, J-C. Simon, S. Combrié, G. Lehoucq, and A. De Rossi, *Efficient second harmonic generation in nanophotonic waveguides for optical signal processing*, Appl. Phys. Lett. **102**, 151114 (2013).

[41] V. S. Ilchenko, A. A. Savchenkov, A. B. Matsko, and L. Maleki, *Nonlinear Optics and Crystalline Whispering Gallery Mode Cavities*, Phys. Rev. Lett. **92**, 043903 (2004).

[42] J. U. Fürst, D. V. Strekalov, D. Elser, M. Lassen, U. L. Andersen, C. Marquardt, and G. Leuchs, *Naturally Phase-Matched Second-Harmonic Generation in a Whispering-Gallery-Mode Resonator*, Phys. Rev. Lett. **104**, 153901 (2010).

[43] P. S. Kuo, J. Bravo-Abad, and G. S. Solomon, *Second-harmonic generation using $\bar{4}$-quasi-phasematching in a GaAs whispering-gallery-mode microcavity*, Nat. Commun. **5**, 3109 (2014).

[44] S. Mariani, A. Andronico, A. Lemaître, I. Favero, S. Ducci, and G. Leo, *Second-harmonic generation in AlGaAs microdisks in the telecom range*, Opt. Lett. **39**, 3062 (2014).

[45] T. W. Schlereth, C. Schneider, S. Höfling, and A. Forchel, *Tailoring of morphology and emission wavelength of AlGaInAs quantum dots*, Nanotechnology **19**, 045601 (2008).

[46] M. A. Belkin, F. Capasso, A. Belyanin, D. L. Sivco, A. Y. Cho, D. C. Oakley, C. J. Vineis, and G. W. Turner, *Terahertz quantum-cascade-laser source based on intracavity difference-frequency generation*, Nat. Photonics **1**, 288 (2007).

[47] Q. Y. Lu, N. Bandyopadhyay, S. Slivken, Y. Bai, and M. Razeghi, *Room temperature single-mode terahertz sources based on intracavity difference-frequency generation in quantum cascade lasers*, Appl. Phys. Lett. **99**, 131106 (2011).

[48] K. Vijayraghavan, R. W. Adams, A. Vizbaras, M. Jang, C. Grasse, G. Boehm, M. C. Amann, and M. A. Belkin, *Terahertz sources based on Čerenkov difference-frequency generation in quantum cascade lasers*, Appl. Phys. Lett. **100**, 251104 (2012).

[49] K. Vijayraghavan, Y. Jiang, M. Jang, A. Jiang, K. Choutagunta, A. Vizbaras, F. Demmerle, G. Boehm, M. C. Amann, and M. A. Belkin, *Broadly tunable terahertz generation in mid-infrared quantum cascade lasers*, Nat. Commun. **4**, 2021 (2013).

[50] G. Leo, J.-M. Gérard, S. Reitzenstein, P. U. Jepsen, *Towards a THz Terahertz room-temperature integrated parametric source*, Procedia Computer Science **7**, 205, Elsevier (2011).

[51] Q. Y. Lu, N. Bandyopadhyay, S. Slivken, Y. Bai, and M. Razeghi, *Continuous operation of a monolithic semiconductor terahertz source at room temperature*, Appl. Phys. Lett. **104**, 221105 (2014).

[52] P. A. Franken, A. E. Hill, C. W. Peters, and G. Weinreich, *Generation of optical harmonics*, Phys. Rev. Lett. **7**, 118 (1961).

[53] G. S. He, and S. H. Liu, *Physics of nonlinear optics*, World Scientific, 1999.

[54] R. Boyd, *Nonlinear optics*, Academic Press, 2008.

[55] D. Kleinman, *Nonlinear dielectric polarization in optical media*, Phys. Rev. **126**, 1977 (1962).

[56] A. Yariv, *Quantum Electronics*, Wiley (1984).

[57] V. Mizrahi and J. E. Sipe, *Phenomenological treatment of surface second-harmonic generation*, J. Opt. Soc. Am. B. **5**, 660 (1988).

[58] P. Curley, A. Ferguson, J. White, and W. Amos, *Application of a femtosecond self-sustaining mode-locked Ti:sapphire laser to the field of laser scanning confocal microscopy*, Opt. Quantum. Electron. **24**, 851 (1992).

[59] W. J. Kozlovsky, C. D. Nabors, and R. L. Byer, *Efficient second harmonic generation of a diode-laser-pumped CW Nd:YAG laser using monolithic MgO:LiNbO$_3$ external resonant cavities*, IEEE J. Quant. Electron. **24**, 913 (1987).

[60] C. Fischer, and M. Sigrist, *Mid-IR difference frequency generation*, in Solid-State Mid-Infrared Laser Sources (I. Sorokina et K. Vodopyanov, eds), Vol. 89 in Topics in Applied Physics, 99-143, Springer, 2003.

[61] A. Andronico, *Étude électromagnetique d'émetteurs intégrés infrarouges et terahertz en AlGaAs*, PhD Thesis, Université Paris VII - Paris Diderot, 2008.

[62] R. Sutherland, *Handbook of nonlinear optics*, Marcel Dekker, 1996.

[63] Lord Rayleigh, *Theory of Sound*, Editor MacMillan and Co., 1877.

[64] T. J. A. Kippenberg, *Nonlinear Optics in Ultra-high-Q Whispering-Gallery Optical Microcavities*, Ph.D. thesis, California Institute of Technology, 2004.

[65] M. Borselli, *High-Q Microresonators as Lasing Elements for Silicon Photonics*, Ph.D. thesis, California Institute of Technology, 2006.

[66] T. Tamir (Editor), *Guided-Wave Optoelectronics*, Springer-Verlag, Second Edition (1990).

[67] J. D. Jackson, *Classical Electrodynamics*, 2nd ed., John Wiley & Sons (1975).

[68] H. A. Haus, *Waves and fields in optoelectronics* **1**, Prentice-Hall (1984).

[69] C. Manolatou, M. Khan, S. Fan, P. R. Villeneuve, H. Haus, and J. Joannopoulos, *Coupling of modes analysis of resonant channel add-drop filters*, IEEE J. Quant. Electron. **35**, 1322 (1999).

[70] M. Borselli, T. J. Johnson, and O. Painter, *Beyond the Rayleigh Scattering Limit in High-Q Silicon Microdisk: Theory and Experiment*, Opt. Express **13**, 1515 (2005).

[71] J. A. Armstrong, N. Bloembergen, J. Ducuing et P. S. Pershan, *Interactions between light waves in a nonlinear dielectric*, Phys. Rev. **127**, 1918 (1962).

[72] L. A. Eyres, P. J. Tourreau, T. J. Pinguet, C. B. Ebert, J. S. Harris, M. M. Fejer, L. Becouarn, B. Gerard, and E. Lallier, *All-epitaxial fabrication of thick, orientation-patterned GaAs films for nonlinear optical frequency conversion*, Appl. Phys. Lett. **79**, 904 (2001).

[73] M. J. Angell, R. M. Emerson, J. L. Hoyt, J. F. Gibbons, L. A. Eyres, M. L. Bortz, and M. M. Fejer, *Growth of alternating <100>/<111>-oriented II-VI regions for quasi-phasematched nonlinear optical devices on GaAs substrates.* Appl. Phys. Lett. **64**, 3107 (1994).

[74] Y. Ueno, V. Ricci, and G. I. Stegeman, *Second-order susceptibility of $Ga_{0.5}In_{0.5}P$ crystals at 1.5 μm and their feasibility for waveguide quasi-phase matching*, J. Opt. Soc. Am. B **14**, 1428 (1997).

[75] T. Kondo, S. Koh, R. Ito, *Sublattice reversal epitaxy: a novel technique for fabricating domain-inverted compound semiconductor structures*, Sci. Technol. Adv. Mater. **1**, 173 (2000).

[76] W. Chen, F. Sun, C. Zou, and G. Guo, *Integrated entangled photons source from microcavity parametric down conversion*, J. Opt. Soc. Am. B **29**, 1884 (2012).

[77] J. T. Robinson, L. Chen, and M. Lipson, *On-chip gas detection in silicon optical microcavities*, Opt. Express **16**, 4296 (2008).

[78] B. Guha, B. Kyotoku, and M. Lipson, *CMOS-compatible athermal silicon microring resonators*, Opt. Express **18**, 3487 (2010).

[79] A. Turner, M. Foster, A. Gaeta, and M. Lipson, *Ultra-low power parametric frequency conversion in a silicon microring resonator*, Opt. Express **16**, 4881 (2008).

[80] W. C. Hurlbut, Yun-Shik Lee, K. L. Vodopyanov, P. S. Kuo, and M. M. Fejer, *Multiphoton absorption and nonlinear refraction of GaAs in the mid-infrared*, Opt. Lett. **32**, 6680 (2007).

[81] C. Bosio, J. L. Staehli, M. Guzzi, G. Hurri, and R. A. Logan, *Direct-energy-gap dependence on Al concentration in $Al_xGa_{1-x}As$*, Phys. Rev. B **38**, 3263 (1988).

[82] M. Sheik-Bahae, D. C. Hutchings, D. J. Hagan, and E. W. Van Stryland, *Dispersion of bound electronic nonlinear refraction in solids*, IEEE J. Quantum Electron. **27**, 1296 (1991).

[83] S. Gehrsitz, F. K. Reinhart, C. Gourgon, N. Herres, A. Vonlanthen, and H. Sigg, *The refractive index of $Al_xGa_{1-x}As$ below the band gap: Accurate determination and empirical modeling*, J. Appl. Phys. **87**, 7825 (2000).

[84] R. D. Kekatpure, *First-Principles Full-Vectorial Eigenfrequency Computations for Axially Symmetric Resonators*, J. Lightwave Technol. **29**, 253 (2011).

[85] Y.-R. Nowicki-Bringuier, J. Claudon, C. Böckler, S. Reitzenstein, M. Kamp, A. Morand, A. Forchel, and J.-M. Gérard, *High Q whispering gallery modes in GaAs/AlAs pillar microcavities*, Opt. Express **15**, 17291 (2007).

[86] L. Ding, C. Baker, P. Senellart, A. Lemaître, S. Ducci, G. Leo, and I. Favero, *High frequency GaAs nano-optomechanical disk resonator*, Phys. Rev. Lett. **105**, 263903 (2010).

[87] R. Dammel, *Diazonaphthoquinone-based Resists*, SPIE Press, 1993, p. 100.

[88] N. W. Parker, A. D. Brodie, and J. H. McCoy, *High-throughput NGL electron-beam direct-write lithography system*, Proc. SPIE **3997**, 713 (2000).

[89] T. Matsuoka, K. Takahei, Y. Noguchi, and H. Nagai, *1.5 micron region InP/GaInAsP buried heterostructure lasers on semi-insulating substrate*, Electron. Lett. **17**, 12 (1981).

[90] S. Adachi and K. Oe, *Chemical etching characteristics of (001) GaAs*, J. Electrochem. Soc. **130**, 2427 (1983).

[91] T. L. Koch, P. J. Corvini, and W. T. Tsang, *Anisotropically etched deep dratings for InP/InGaAsP optical devices*, J. Appl. Phys. **62**, 3461 (1987).

[92] S. Adachi, *Chemical etching of InP and InGaAsP/InP*, J. Electrochem. Soc. **129**, 609 (1982).

[93] I. Maximov, Q. Wang, M. Graczyk, P. Omling, L. Samuelson, W. Seifert, I. Shorubalko, K. Hieke, S. Lourdudoss, and E. R. Messmer, *Fabrication and characterization of 0.2-0.6 mm GaInAs/InP electron waveguides*, Proc. 11th International Conference on Indium Phosphide and Related Materials, 237 (1999).

[94] G. C. Desalvo, W. F. Tseng, and J. Comas, *Etch rates and selectivities of citric acid/H_2O_2 on GaAs, $Al_{0.3}Ga_{0.7}As$, $In_{0.2}Ga_{0.8}As$, $InGa_{0.53}Ga_{0.47}As$, $In_{0.52}Ga_{0.48}As$ and InP*, J. Electrochem. Soc. **139**, 831 (1992).

[95] R. A. Logan and F. K. Reinhart, *Optical waveguides in GaAs-AlGaAs epitaxial layers*, J. Appl. Phys. **44**, 4172 (1973).

[96] M.J. Parent, L. Zazzera, P. Rajtar, and F. Behr, *Low Surface Tension Etch Solutions for Silicon Dioxide Removal in Microelectromechanical Systems*, Microfabricated Systems and MEMS V, Electrochemical Society Proceedings (2000).

[97] T. A. Birks and Y. W. Li, *The shape of fiber tapers*, J. Lightw. Technol. **10**, 432 (1992).

[98] L. Bobb and P. Shankar, *Tapered optical biber components and sensors*, Microwave Journal **35**, 218 (1992).

[99] L. Ding, C. Belacel, S. Ducci, G. Leo, and I. Favero, *Ultralow loss single-mode silica tapers manufactured by a microheater*, Appl. Opt. **49**, 2441 (2010).

[100] J. D. Love, W. M. Henry, W. J. Stewart, R. J. Black, S. Lacroix, and F. Gonthier, *Tapered single-mode fibres and devices. I. Adiabaticity criteria*, IEEE Proc. J. of Optoelectron. **138**, 343 (1991).

[101] L. Ding, P. Senellart, A. Lemaître, S. Ducci, G. Leo, and I. Favero, *GaAs micro-nanodisks probed by a looped fiber taper for optomechanics applications*, Proc. SPIE **7712**, 771211 (2010).

[102] T. Carmon, L. Yang, and K. J. Vahala, *Dynamical thermal behavior and thermal self-stability of microcavities*, Opt. Express **12**, 4742 (2004).

[103] R. M. Camacho, J. Chan, M. Eichenfield, and O. Painter, *Characterization of radiation pressure and thermal effects in a nanoscale optomechanical cavity*, Opt. Express **17**, 15726 (2009).

[104] V. R. Almeida and M. Lipson, *Optical bistability on a silicon chip*, Opt. Lett. **29**, 2387 (2004).

[105] F. G. Della Corte, G. Cocorullo, M. Iodice, and I. Rendina, *Temperature dependence of the thermo-optic coefficient of InP, GaAs, and SiC from room temperature to 600 K at the wavelength of 1.5 μm*, Appl. Phys. Lett. **77**, 1614 (2000).

[106] S. Matsuura, M. Tani, and K. Sakai, *Generation of coherent terahertz radiation by photomixing in dipole photoconductive antennas*, Appl. Phys. Lett. **70**, 559 (1997).

[107] E. R. Brown, K. A. McIntosh, K. B. Nichols, and C. L. Dennis, *Photomixing up to 3.8 THz in low-temperature-grown GaAs*, Appl. Phys. Lett. **66**, 285 (1995).

[108] S. Verghese, K. A. McIntosh, S. Calawa, W. F. Dinatale, E. K. Duerr, and K. A. Molvar, *Generation and detection of coherent terahertz waves using two photomixers*, Appl. Phys. Lett. **73**, 3824 (1998).

[109] R. Köhler, A. Tredicucci, F. Beltram, H. E. Beere, E. H. Linfield, A. G. Davies, D. A. Ritchie, R. C. Iotti, and F. Rossi, *Terahertz semiconductor-heterostructure laser*, Nature **417**, 156 (2002).

[110] D. Mittleman, ed., *Sensing with Terahertz Radiation*, Springer-Verlag (2003).

[111] R. L. Aggarwal, B. Lax, and G. Favrot, *Noncollinear phase matching in GaAs*, Appl. Phys. Lett. **22**, 329 (1973).

[112] T. Yajima, and N. Takeuchi, *Far-infrared difference-frequency generation by picosecond laser pulse*s, Jpn. J. Appl. Phys. **9**, 1361 (1970).

[113] K. H. Yang, P. L. Richards, and Y. R. Shen, *Generation of Far-Infrared Radiation by Picosecond Light Pulses in $LiNbO_3$*, Appl. Phys. Lett. **19**, 320 (1971).

[114] Y.-S. Lee, T. Meade, V. Perlin, H. Winful, T. B. Norris, and A. Galvanauskas, *Generation of narrow-band terahertz radiation via optical rectification of femtosecond pulses in periodically poled lithium niobate*, Appl. Phys. Lett. **76**, 2505 (2000).

[115] K. L. Vodopyanov, M. M. Fejer, X. Yu, J. S. Harris, Y.-S. Lee, W. C. Hurlbut, V. G. Kozlov, D. Bliss, and C. Lynch, *Terahertz-wave generation in quasi-phase-matched GaAs*, Appl. Phys. Lett. **89**, 141119 (2006).

[116] V. Berger and C. Sirtori, *Non-linear phase matching in semiconductor waveguides*, Semicond. Sci. Technol. **19**, 964 (2004).

[117] K. L. Vodopyanov and Y. H. Avetisyan, *Optical terahertz wave generation in a planar GaAs waveguide*, Opt. Lett. **33**, 2314 (2008).

[118] K. L. Vodopyanov, *Optical THz-wave generation with periodically-inverted GaAs*, Laser & Photon. Rev. **2**, 11 (2008).

[119] Ioffe Institute database: `www.ioffe.ru/SVA/NSM/Semicond/`.

[120] SNLO nonlinear optics code available from A. V. Smith, AS-Photonics, Albuquerque, NM.

[121] K. Matsuda, K. Ikeda, T. Saiki, H. Tsuchiya, H. Saito and K. Nishi, *Homogeneous linewidth broadening in a $In_{0.5}Ga_{0.5}As$/GaAs single quantum dot at room temperature investigated using a highly sensitive near-field scanning optical microscope*, Phys. Rev. B **63**, 121304 (2001).

[122] E. D. Palik (Editor), *Handbook of Optical Constants of Solids*, Academic Press, San Diego (1998).

[123] W. T. Tsang, R. A. Logan, and J. A. Ditzenberger, *Ultra-low threshold, graded-index waveguide, separate confinement, CW buried-heterostructure lasers*, Electron. Lett. **18**, 845 (1982).

[124] E. Rosencher, B. Vinter, *Optoelectronics*, Cambridge University Press, Cambridge (2002).

[125] A. Andronico, S. Mariani, F. Ghiglieno, J. Claudon, M. Munsch, J.-M. Gérard, I. Favero, S. Ducci, and G. Leo, *Tuning of a nonlinear THz emitter*, Opt. Express **20**, 17678 (2012).

[126] M. Munsch, J. Claudon, N. S. Malik, K. Gilbert, P. Grosse, J.-M. Gérard, F. Albert, F. Langer, T. Schlereth, M. M. Pieczarka, S. Höfling, M. Kamp, A. Forchel, and S. Reitzenstein, *Room temperature, continuous wave lasing in microcylinder and microring quantum dot laser diodes*, Appl. Phys. Lett. **100**, 031111 (2012).

[127] A. Schlehahn, F. Albert, C. Schneider, S. Höfling, S. Reitzenstein, J. Wiersig, and M. Kamp, *Mode selection in electrically driven quantum dot microring cavities*, Opt. Express **21**, 15951 (2013).

[128] S. Mariani, A. Andronico, I. Favero, S. Ducci, Y. Todorov, C. Sirtori, M. Kamp, M. Munsch, J. Claudon, J.-M. Gérard, T. Wang, P. U. Jepsen, and G. Leo, *Microring Diode Laser for THz Generation*, IEEE Trans. THz Sci. Technol. **3**, 472 (2013).

[129] A. De Rossi, V. Ortiz, M. Calligaro, L. Lanco, S. Ducci, V. Berger, and I. Sagnes, *Measuring propagation loss in a multimode semiconductor waveguide*, J. Appl. Phys. **97**, 073105 (2005).

[130] Y. Todorov, L. Tosetto, J. Teissier, A. M. Andrews, P. Klang, R. Colombelli, I. Sagnes, G. Strasser, and C. Sirtori, *Optical properties of metal-dielectric-metal microcavities in the THz frequency range*, Opt. Express **18**, 13886 (2010).

[131] P. U. Jepsen, D. G. Cooke, and M. Koch, *Terahertz spectroscopy and imaging - Modern techniques and applications*, Laser Photon. Rev. **5**, 124 (2011).

[132] F. Boitier, A. Orieux, C. Autebert, A. Lemaître, E. Galopin, C. Manquest, C. Sirtori, I. Favero, G. Leo, and S. Ducci, *Electrically Injected Photon-Pair Source at Room Temperature*, Phys. Rev. Lett. **112**, 183901 (2014).

[133] X. Cai, J. Wang, M. J. Strain, B. Johnson-Morris, J. Zhu, M. Sorel, J. L. O'Brien, M. G. Thompson, S. Yu, *Integrated Compact Optical Vortex Beam Emitters*, Science **338** (6105), 363 (2012).

[134] Q. Y. Lu, N. Bandyopadhyay, S. Slivken, Y. Bai, and M. Razeghi, *Widely tuned room temperature terahertz quantum cascade laser sources based on difference-frequency generation*, Appl. Phys. Lett. **101**, 251121 (2012).

[135] G. Fasching, Ch. Deutsch, A. Benz, A. M. Andrews, P. Klang, R. Zobl, W. Schrenk, G. Strasser, P. Ragulis, V. Tamošiūnas, and K. Unterrainer, *Electrically controllable photonic molecule laser*, Opt. Express **17**, 20321 (2009).

[136] R. Kumar, J. R. Ong, J. Recchio, K. Srinivasan, and S. Mookherjea, *Spectrally multiplexed and tunable-wavelength photon pairs at 1.55 μm from a silicon coupled-resonator optical waveguide*, Opt. Lett. **38**, 2969 (2013).

[137] M. Davanço, J. R. Ong, A. B. Shehata, A. Tosi, I. Agha, S. Assefa, F. Xia, W. M. J. Green, S. Mookherjea, and K. Srinivasan, *Telecommunications-band*

heralded single photons from a silicon nanophotonic chip, Appl. Phys. Lett. **100**, 261104 (2012).

[138] J. E. Heebner, N. N. Lepeshkin, A. Schweinsberg, G. W. Wicks, R. W. Boyd, R. Grover, and P.-T. Ho, *Enhanced linear and nonlinear optical phase response of AlGaAs microring resonators*, Opt. Lett. **29**, 769 (2004).

[139] M. J. LaGasse K. K. Anderson, C. A. Wang, H. A. Haus, and J. G. Fujimoto, *Femtosecond measurements of the nonresonant nonlinear index in AlGaAs*, Appl. Phys. Lett. **56**, 417 (1990).